Technical Report Documentation Page

1. Report No. FHWA/TX-08/0-4875-1	2. Government Accession No.	3. Recipient's Catalog No.
4. Title and Subtitle Highway Drainage at Superelevation Transitions		5. Report Date March 2008 6. Performing Organization Code
7. Author(s) Randall J. Charbeneau, Jaehak Jeong, Michael E. Barrett		8. Performing Organization Report No. 0-4875-1
9. Performing Organization Name and Address Center for Transportation Research The University of Texas at Austin 3208 Red River, Suite 200 Austin, TX 78705-2650		10. Work Unit No. (TRAIS) 11. Contract or Grant No. 0-4875
12. Sponsoring Agency Name and Address Texas Department of Transportation Research and Technology Implementation Office P.O. Box 5080 Austin, TX 78763-5080		13. Type of Report and Period Covered Technical Report September 2004 to December 2007 14. Sponsoring Agency Code
15. Supplementary Notes Project performed in cooperation with the Texas Department of Transportation and the Federal Highway Administration.		
16. Abstract This research has addressed issues associated with highway drainage at superelevation transitions. A physical modeling experimental program focused on the effects of surface roughness and rainfall intensity on the hydraulic behavior of stormwater runoff from pavement surfaces. A diffusion wave numerical model was developed to simulate stormwater runoff at superelevation transitions. The model was applied to evaluate the influence of longitudinal grade on maximum ponding depth. Conclusions from the modeling program are that maximum ponding depth does not depend significantly on longitudinal grade, but the location of maximum ponding depth is very sensitive to longitudinal grade, moving from the outside pavement edge for small longitudinal slope, to the center of the roadway for moderate slope, and to the inside pavement edge for large longitudinal grade.		
17. Key Words Stormwater drainage, sheet flow, Manning equation, diffusion wave models, superelevation transition	18. Distribution Statement No restrictions. This document is available to the public through the National Technical Information Service, Springfield, Virginia 22161; www.ntis.gov.	

19. Security Classif. (of report)	20. Security Classif. (of this page)	21. No. of pages	22. Price
Unclassified	Unclassified	180	

Form DOT F 1700.7 (8-72) Reproduction of completed page authorized

Highway Drainage at Superelevation Transitions

Randall J. Charbeneau
Jaehak Jeong
Michael E. Barrett

CTR Technical Report:	0-4875-1
Report Date:	March 2008
Project:	0-4875
Project Title:	Minimum Longitudinal Grade at Zero Cross Slope in Superelevation Transition
Sponsoring Agency:	Texas Department of Transportation
Performing Agency:	Center for Transportation Research at The University of Texas at Austin

Project performed in cooperation with the Texas Department of Transportation and the Federal Highway Administration.

Center for Transportation Research
The University of Texas at Austin
3208 Red River
Austin, TX 78705

www.utexas.edu/research/ctr

Disclaimers

Author's Disclaimer: The contents of this report reflect the views of the authors, who are responsible for the facts and the accuracy of the data presented herein. The contents do not necessarily reflect the official view or policies of the Federal Highway Administration or the Texas Department of Transportation (TxDOT). This report does not constitute a standard, specification, or regulation.

Patent Disclaimer: There was no invention or discovery conceived or first actually reduced to practice in the course of or under this contract, including any art, method, process, machine manufacture, design or composition of matter, or any new useful improvement thereof, or any variety of plant, which is or may be patentable under the patent laws of the United States of America or any foreign country.

Engineering Disclaimer

NOT INTENDED FOR CONSTRUCTION, BIDDING, OR PERMIT PURPOSES.

Project Engineer: Randall J. Charbeneau
Professional Engineer License Number: Texas No. 56662
P.E. Designation: Research Supervisor

Acknowledgments

The authors would like to express appreciation to Sam Talje, TxDOT project director for this study, for his guidance, support and continued interest in this research. The authors also wish to thank Julien Villard, Lauren Schneider, Emily Reeder, and Wa Seong (Andy) Chan for their significant contributions to this research.

Table of Contents

List of Figures

List of Tables

Chapter 1. Introduction

This research program addresses issues associated with stormwater drainage at superelevation transitions. Within superelevation transitions the roadway cross slope changes from negative to positive, and the size of the region with small pavement cross-slope depends on the longitudinal grade. The amount of ponding on pavement surfaces in areas of transition from normal crown to fully-superelevated roadway sections depends on longitudinal slope and other factors. The effects of longitudinal slope on highway drainage at superelevation transitions have been investigated through this research effort, and design guidance on longitudinal grade is developed.

1.1 Background and Significance of Work

Design speed and highway curvature are important issues in design of longitudinal roadway alignment. Centrifugal forces are developed as vehicles move through curved highway sections, and these forces may be controlled through use of limits on curve radius and through superelevation of highway lanes. At superelevation transitions, the outside lane cross-slope is rotated from negative cross slope at normal crown conditions, to positive cross slope at fully superelevated conditions. Figure 1.1 shows the longitudinal alignment of a roadway section at a 45-degree curve (Microstation GEOPAK representation). At stations A and E the roadway cross section has normal crown. At station C the roadway cross section is fully superelevated. Superelevation transitions occur at stations B and D, which are relatively short in longitudinal length.

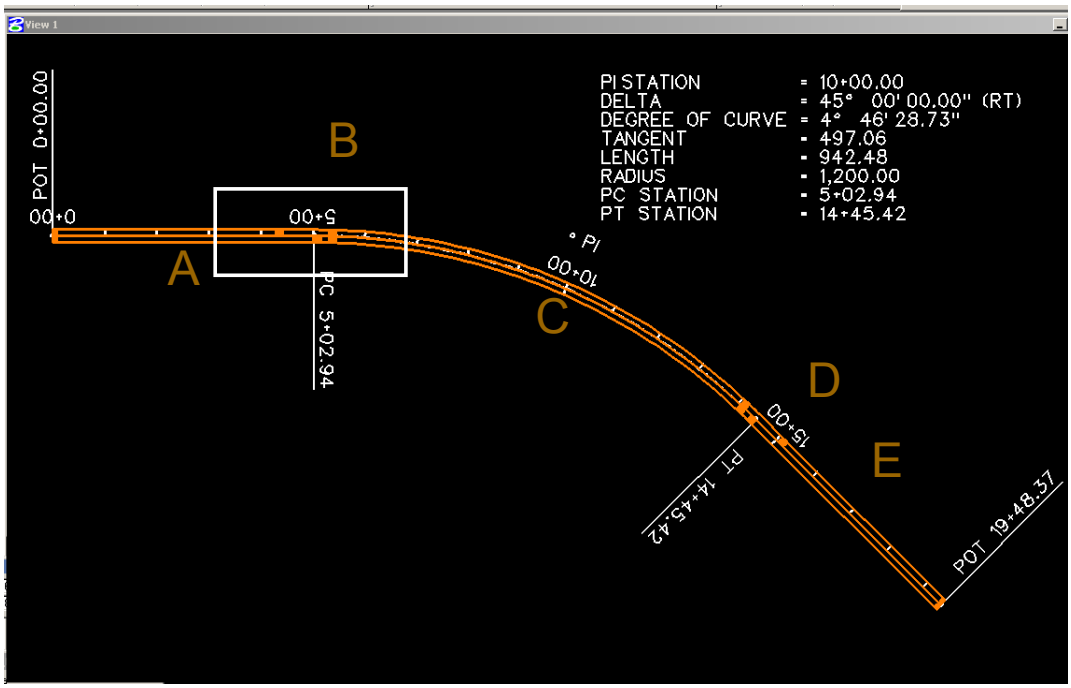

Figure 1.1: Microstation GEOPAK representation of longitudinal alignment for a 45-degree curve including two superelevation transitions at stations B and D

The sequence for change in cross slope at superelevation transition B in Figure 1.1 is shown in Figure 1.2. Location 1 has normal crown. The outside lane is rotated and has zero cross slope at location 2. By location 3 the cross slope is uniform across the roadway, and the entire cross section continues to rotate reaching fully superelevation conditions at location 4. Roadway alignment at superelevation transitions is described in greater detail in Section 2.6. The pattern of drainage at superelevation transitions depends on the combination of the change in cross slope plus the longitudinal grade.

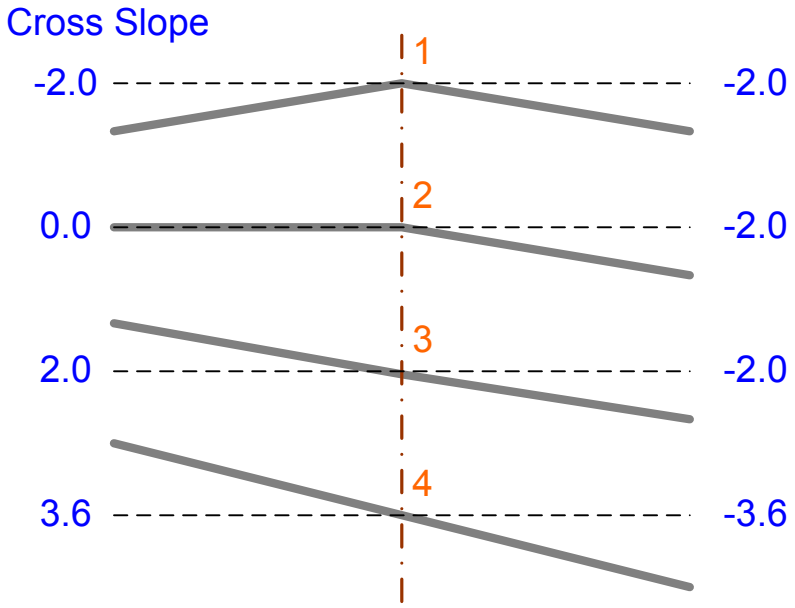

Figure 1.2: Sequence of changing cross slope at superelevation transition

1.1.1 Drainage at Superelevation Transitions

Control of water on pavement surfaces is essential for maintenance of highway safety and service. The presence of water slows traffic and contributes to accidents from hydroplaning and loss of visibility from splash and spray. Ponded water may also result in dangerous torque levels on vehicles and ultimate loss of vehicle control (FHWA HEC-12). In order to promote drainage from highway surfaces, pavements generally have a cross slope of up to two percent from the highway crown towards the shoulder or gutter.

In superelevation transitions leading to curved alignments, the inward travel lane edge is lowered in elevation while the outer travel lane edge is raised. This means that travel lanes on the outward side of the radius of curvature must pass from a negative cross slope to a positive cross slope. This transition in cross slope means that there must be a section of pavement with zero cross slope. Furthermore, AASHTO provides design recommendations on the maximum relative gradient that limit the rate (with respect to longitudinal distance) at which the outer travel lane elevation can be raised or lowered, and the maximum relative gradient decreases with increasing vehicle design speed. This means that for highway sections with larger design speeds, the length of highway pavement with near-zero cross slope will increase. To prevent ponding of water from rainfall, the pavement in these segments with near-zero cross slope must maintain a longitudinal slope. The TxDOT Roadway Design Manual notes that “Special care should be given to ensure that the zero cross slope in the superelevation transition does not occur at the flat portion of the

crest or sag vertical curve. A plot of roadway contours can identify drainage problems in areas of superelevation transition." However, no guidance is provided on the minimum necessary longitudinal gradient, and how this relates to the maximum relative gradient, pavement width, or design rainfall. Furthermore, through roadway segments with near-zero cross slope, increasing the longitudinal slope will increase the drainage path length and could result in increased ponded water depths over parts of the roadway surface.

A schematic plan view of a superelevation transition is shown in Figure 1.3. In this figure it is assumed that the highway crown serves as the axis of rotation for the warped section leading to the superelevated highway section (the curvature of the highway is not shown). The elevation of the travel lane edge increases along the highway longitudinal length, but at a limited rate. The pavement cross section slope changes from negative (outward) to positive near the entrance to the transition. The zero cross slope station is shown in the figure. Normally a roadway shoulder or gutter will be present with a drainage inlet located immediately upslope of the zero cross slope station to capture and remove stormwater runoff; otherwise such runoff would flow across the pavement surface down slope through the transition entrance section. Figure 1.3 shows the stormwater runoff drainage path length with maximum length. This path originates near the highway crown at a location upslope from the zero-slope station. Because of the negative cross slope, the drainage path is initially directed towards the outer travel lane edge. However, the cross slope superelevation results in the drainage path turning inward towards the inside pavement edge. The path with maximum drainage path length should be tangent to the outer travel lane edge near the station with zero cross slope. The drainage path will cross the traffic lanes again and will also cross the traffic lanes on the inside of the transition. The direction of the drainage path is "down slope" because gravity is the primary force causing overland flow. Increasing the longitudinal slope will increase the drainage path length by increasing the length in the longitudinal direction. Rainfall will increase the discharge along the path length, and may result in increased ponding along pavement travel surfaces. Decreasing the longitudinal slope will result in a shorter path length. This will also result in a smaller path slope (S_o) and smaller drainage rates (q). The smaller drainage rates increase the pavement drainage time, and may result in increased ponding depths due to continued addition of rainfall. Thus it appears that for a given rainfall intensity, there may be an "optimal" longitudinal pavement slope leading to and from superelevation transitions. Here, "optimal" may refer to controlling the maximum ponding depth, or the size of the ponding region, or other factors, under design rainfall conditions.

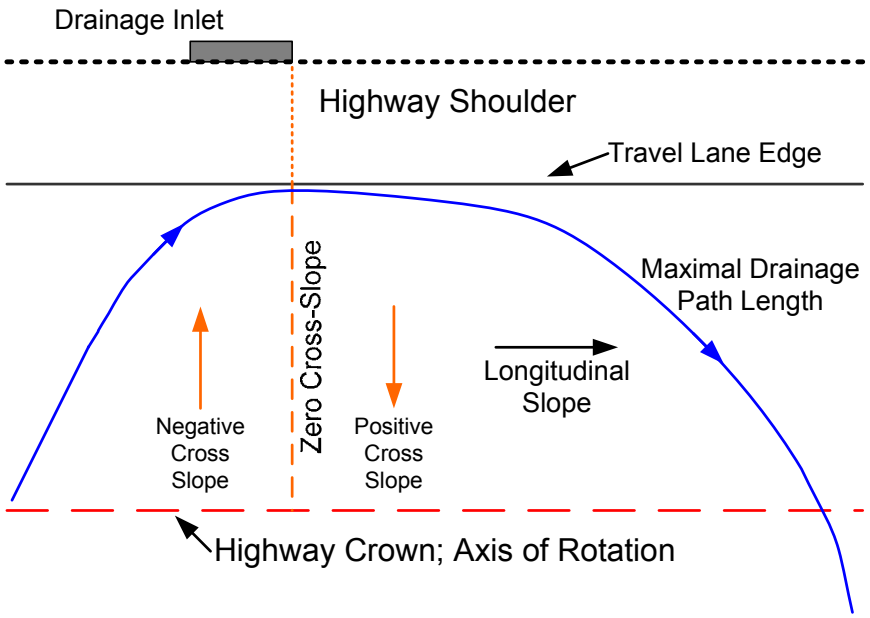

Figure 1.3: Schematic plan view of pavement cross and longitudinal alignment near superelevation transition showing the drainage path with maximal length

Procedures for locating highway inlets must also be modified for superelevation transitions. For a four-lane highway, inlet spacing is based on drainage of two lanes, with inlets placed within the gutters along both sides of the roadway. In a superelevation section, all four lanes would drain to one side of the roadway, and the inlet spacing must be modified accordingly. Spatially varied flow through the transition section is significant, and special design procedures may be required for determining inlet spacing.

1.1.2 Hydroplaning Potential

Vehicle speed at incipient hydroplaning (HPS) depends on stormwater runoff depth, tire pressure, tire tread depth, average pavement texture depth, and other factors (Huebner et al., 1986). Stormwater runoff depth (water film thickness, WFT) is the primary variable. Figure 1.4 shows results from model equations of HPS as a function of WFT. There is a great deal of uncertainty associated with the curve shown in Figure 1.4. Furthermore, with regard to vehicle safety at superelevation transitions, it is not clear whether the magnitude of WFT or changes in WFT in the longitudinal and lateral directions are the more critical variables. The model equations suggest that HPS is very sensitive to WFT values up to approximately 2.4 mm.

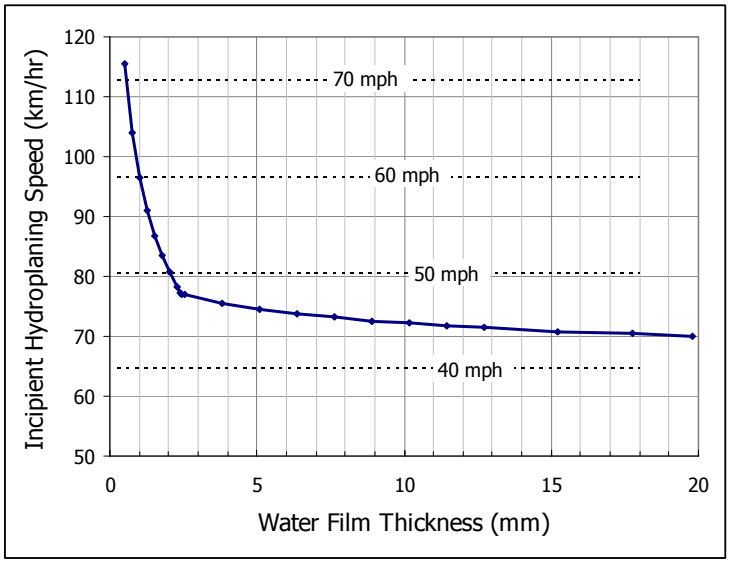

Figure 1.4: Vehicle speed at incipient hydroplaning (based on Huebner et al., 1986)

1.2 Study Objectives

The primary objective of this research program is to identify the effects of longitudinal grade on stormwater drainage at superelevation transitions as a function of relative gradient through superelevation transitions, pavement width, design rainfall, and other significant factors. Positive research results will build confidence in TxDOT design procedures, increase safety through control of hydroplaning and differential torque on vehicles, and reduced risk to TxDOT from litigation.

The specific objectives that are addressed through this research are as follows.

1. Determine the applicability of literature characterization of sheet flow mechanics and select appropriate models for roadway drainage at superelevation transitions.
2. Develop and test kinematic and diffusion wave models for highway drainage.
3. Determine the pattern of pavement drainage at superelevation transitions as a function of longitudinal grade.
4. Apply models to develop guidance on longitudinal grade effects at superelevation transitions.

1.3 Overview

There is much literature dealing with overland flow and highway drainage. However, there is scant literature dealing with issues associated with highway drainage at superelevation transitions. Relevant literature on sheet flow mechanics and potential models for simulation of highway drainage at superelevation transitions are presented in Chapter 2. Chapter 3 describes the experimental program for assessment of sheet flow mechanics on rough surfaces with simulated rainfall. Chapter 4 provides the model development for roadway drainage at superelevation transitions, including the framework for model grid generation, and the diffusion-wave model formulation for highway drainage. Chapter 5 describes model application and development of design guidelines, while Chapter 6 provides a summary and conclusions.

Chapter 2. Literature Review

This literature review is divided into two main areas of research focus. The first area of interest deals with experimental investigations of overland flow (sheet flow) mechanics, especially as they relate to flow on pavement surfaces, effects of rainfall and surface roughness, and possible effects of pavement slope. The second significant area of interest concerns (numerical) modeling of overland flow, gutter flow and pavement drainage. Necessary background information is presented first, followed by discussions of the experimental and mathematical modeling programs. The final subsection addresses the geometry of supercritical transitions in greater detail, compared with Chapter 1.

2.1 Hydraulics Background

Sheet flow can be either laminar or turbulent, and either subcritical or supercritical. On a single surface all conditions can occur simultaneously. Important parameters that have been used to characterize sheet flow are the Reynolds number (*Re*), Froude number (*Fr*), Darcy friction factor (*f*), and Manning coefficient (*n*). The Reynolds number is the ratio of inertial to viscous forces. Definition of the appropriate Reynolds number for sheet flow varies in the literature, and some care must be taken when evaluating data from different sources. For sheet flow the most convenient form of the Reynolds number is based on the flow depth (*h*), which is the same as the hydraulic radius ($R_h = h$), and depth-average velocity (*V*). This definition is

$$Re = \frac{Vh}{\nu} = \frac{q}{\nu} \tag{2.1.1}$$

In equation (2.1.1) q = discharge per unit width (unit discharge) (L^2/T) and ν = kinematic viscosity. Values of *Re* from equation (2.1.1) are smaller than conventional values used for pipe flow by a factor of 4.

For open channel flow problems, the Froude number is defined as the ratio of the speed of water flow to the speed (celerity) of disturbances (waves) on the free surface. The Froude number is specified by

$$Fr = \frac{V}{\sqrt{gD_h}} = \frac{V}{\sqrt{gh}} = \frac{q}{\sqrt{gh^3}} = \frac{\nu\,\mathrm{Re}}{\sqrt{gh^3}} \tag{2.1.2}$$

In equation (2.1.2) D_h = hydraulic depth, which for an open channel is defined as the ratio of cross-section area to top width, and is equal to the flow depth and hydraulic radius for sheet flow.

The friction factor, *f*, is introduced to parameterize bed (surface) shear, and thus the variables *f*, τ_o and S_f are interrelated, where τ_o = wall or bed shear stress and S_f = friction slope (slope of the energy grade line). The definition consistent with the Darcy-Weisbach equation is as follows:

$$h_f = f\frac{L}{(4R_h)}\frac{V^2}{2g} \quad \rightarrow \quad S_f = \frac{f\,V^2}{8\,g\,h} = \frac{f\,q^2}{8gh^3} \equiv \frac{\tau_o}{\rho\,g\,h} \tag{2.1.3}$$

If *h* and *q* are measured, the friction factor is calculated using

$$f = \frac{8gS_f h^3}{q^2} \quad \rightarrow \quad f = \frac{8gS_o h^3}{q^2} \tag{2.1.4}$$

As suggested by the arrow, when equation (2.1.4) is used in analysis of data, the friction slope is usually assumed equal to the slope of the surface, S_o. For laminar flow without rainfall, both theory and experiment give (Horton et al., 1934)

$$f = \frac{24}{Re} = \frac{24\nu}{q} \tag{2.1.5}$$

With this result, equation (2.1.4) is written

$$q = \frac{gS_o h^3}{3\nu} \quad \leftrightarrow \quad h = \left(\frac{3\nu q}{gS_o} \right)^{1/3} \tag{2.1.6}$$

Equation (2.1.6) represents a prototype equation for analysis of sheet flow. More generally, for laminar flow on a rough surface, or laminar flow with rainfall, equation (2.1.5) is written

$$f = \frac{K}{Re} = \frac{K\nu}{q} \tag{2.1.7}$$

The value of the parameter K in equation (2.1.7) must be greater than 24.

For turbulent flow (higher Re) on a smooth surface, the Blasius equation (Monin and Yaglom, 1971) gives

$$f = \frac{C}{Re^{0.25}} = C\left(\frac{\nu}{q} \right)^{1/4} \tag{2.1.8}$$

For the Blasius equation, $C = 0.223$. Combining equations (2.1.4) and (2.1.8) gives

$$q = \left(\frac{8gS_o}{C\nu^{0.25}} \right)^{4/7} h^{12/7} \quad \leftrightarrow \quad h = \left(\frac{C\nu^{1/4} q^{7/4}}{8gS_o} \right)^{1/3} \tag{2.1.9}$$

A more general form of equation (2.1.8) that is useful for analysis of experimental data is the following

$$f = \frac{C}{Re^b} \tag{2.1.10}$$

In analysis of experimental data using equation (2.1.10), the parameter values should be compared with their prototype values $C = 0.223$ and $b = 0.25$ from the Blasius equation.

The *Manning equation* is commonly used to describe the relationship between channel geometry, friction slope, and flow rate for open channel flow. For sheet flow, this equation may be written

$$q = \frac{1}{n} h^{5/3} S_f^{1/2} \quad \leftrightarrow \quad h = \left(\frac{nq}{\sqrt{S_f}} \right)^{0.6} \tag{2.1.11}$$

In equation (2.1.11) n is the Manning (channel resistance) coefficient. When h and q are measured, the Manning coefficient is calculated using

$$n = \frac{S_f^{1/2} h^{5/3}}{q} \quad \rightarrow \quad n = \frac{\sqrt{S_o}\, h^{5/3}}{q} \tag{2.1.12}$$

Combining equation (2.1.4) and (2.1.11) to eliminate the unit discharge gives

$$n = \sqrt{\frac{f}{8g}}\, h^{1/6} \quad \leftrightarrow \quad f = \frac{8gn^2}{h^{1/3}} \tag{2.1.13}$$

Equation (2.1.13) is useful in analysis of experimental data.

The hydraulic behavior of flow near a rough boundary depends on the magnitude of the shear Reynolds number (Monin and Yaglom, 1971), which may be defined by

$$Re_* = \frac{u_* k_s}{\nu} \quad ; \quad u_* = \sqrt{\frac{\tau_o}{\rho}} \tag{2.1.14}$$

In equation (2.1.14) u_* = shear velocity, k_s = size of the roughness elements (Nikuradse's equivalent sand roughness), ν = kinematic viscosity, τ_o = boundary shear stress, and ρ = fluid density. When Re_* is small (less than 4 or 5) then the roughness elements are embedded within the viscous sublayer, the surface is hydraulically smooth, and flow resistance is associated primarily with viscous forces. If Re_* is large (greater than 70 to 100), the surface is hydraulically rough, and flow resistance is associated primarily with form drag on the roughness elements and the magnitude of k_s determines surface resistance. Manning's equation should apply for hydraulically rough conditions with a constant value of the Manning coefficient. Intermediate values of Re_* are associated with transition of flow behavior from hydraulically smooth to rough conditions. For open channel flow, Henderson (1966) combines equation (2.1.14) with Strickler's equation, which relates the Manning coefficient to the 1/6-power of the roughness element size and $\tau_o = \rho g h S_f$ to provide the following condition for hydraulically rough flow:

$$n^6 \sqrt{h S_f} \geq 1.9 \times 10^{-13} \tag{2.1.15}$$

Equation (2.1.15) is based on a critical Re_* = 100 for rough flow conditions, kinematic viscosity = $1.2(10^{-5})$ ft^2/s, and h measured in feet. Henderson (1966) notes that when the condition specified by equation (2.1.15) is not met, then the Manning coefficient will also depend on the Reynolds number Re in addition to surface roughness.

2.2 Experimental Investigation of Sheet Flow Mechanics

Overland flow, or sheet flow, has been of interest to engineers, hydrologists, and geomorphologists because of the role it plays in stormwater runoff and landform evolution. The literature dealing with overland flow is vast. Of interest for this research are the experimental methods that have been used to measure sheet flow and the results from different experimental programs. The different methods for measuring sheet flow variables are considered first. The primary variables are the flow depth (h), depth-average velocity (V), surface velocity (u_s), and unit discharge (q). These variables are dependent because the product of the depth and average velocity is equal to the unit discharge ($V\ h = q$) and the depth-average velocity and surface velocity are directly related for different flow regimes.

2.2.1 Indirect Measurement Methods using Hydrographs

Izzard (1944) determined the average depth on a surface from the difference in inflow and outflow hydrographs, divided by the surface area, and relates the average depth to the runoff from the end of the plot. The resistance coefficient (skin-friction coefficient) was calculated using the recession flow when rainfall influences were absent. An increase in discharge immediately at cessation of rainfall was noted and was associated with the removal of the

resistance created by rainfall disturbances. Similar types of analyses were carried out by Hicks (1944). Katz et al. (1995) measured detention storage from the volume under the falling limb hydrograph. Engman (1986) applied a hydrograph analysis technique to estimate detention storage and Manning's n for a variety of agricultural-type land covers.

2.2.2 Measurement of Flow Depth

The depth of sheet flow has been measured in the laboratory using point gages, piezometers, and indirectly by weight. Izzard (1944) reports on a series of experiments where steady uniform flow was introduced to a 1.8 meter (6-ft) wide channel over a series of stilling pools so that about 15 meters (50 ft) of length was available to establish normal flow with depth measurements made using two point gages at the quarter-points of the channel. Robertson et al. (1966) used point gages to measure depth of flow at multiple stations along the length of a 29 meter (96-ft) long, 0.9 meter (3-ft) wide channel with 5 percent slope and gravel (2.77, 4.06 and 5.56 mm diameter) fixed to the concrete base. Measurements were made for experiments with constant flow introduced at the upstream end, simulated rainfall along the length of the channel, and a combination of both. Rainfall discharge was measured using an orifice meter in the inflow pipe, with spray falling outside the channel captured and measured and subtracted from the total. Discharge at the end of the channel was measured using an H-flume. Depth measurements were made using a point gage. Because size of the pea gravel was a considerable portion of the flow depth, determination of the channel bottom received considerable attention. Two different methods were used. The first method was to average a series of point gage readings on the gravel tops across the channel ("measured bottom"). The second method was to find a "hydraulically effective bottom" by plotting the reading of flow depth (measured using a point gage located in a stilling well) against $q^{0.6}$, where q is the unit discharge, and determining the effective bottom from the $q = 0$ intercept. This approach is based on use of Manning's equation. Generally good agreement was found between the measured and effective bottom elevations (effective bottom elevation giving a slightly larger value for depth), and the measured bottom elevation was used in depth determinations (corresponding to the top of the gravel). Emmett (1970) carried out both laboratory and field measurements of overland flow on hillslopes. Only the laboratory measurements are of interest to this present study. The flume used in his study was 1.2 meter (4-ft) wide by 4.8 meter (16-ft) long. The slope was adjustable by hydraulic jacks. Nine series of measurements were made in Emmett's study in which five series were performed on a smooth surface and four were on a roughened surface. The roughened surface was covered with sand of median grain size close to 0.50 mm (45% by weight of sand finer than 0.50 mm). Uniform flow as well as artificial rainfall could be produced. The depth of water flow on the smooth surface was measured by a point gage placed on a "precision leveled carriage" independent of the flume structure. The depth is calculated as the difference between the water surface and the flume floor. For the roughened surface, flume floor elevation was taken as the top of the roughness elements by placing a ¾-inch-wide blade to the tip of the point gage when taking the bottom depth measurements. No correction was applied for flow depth. An interesting conclusion from this analysis is the indication that the mean texture depth of the surface was about the same as the height of the roughness elements, as the smooth and roughened velocity ratios came out to be similar. Yoon and Wenzel (1971) measured water depth using a point gage with resistance meter so that the meter oscillated with the wave crest was reached, and a steady reading was achieved when the wave trough was reached by the point gage. The average was used as the depth measurement. Anderson et al. (1998) investigated drainage of pavement surfaces and distinguish

between the total flow depth (y), water film thickness (WFT), and mean texture depth (MTD), with y = WFT + MTD. They measure the WFT by placing a 25-mm circular disk on the pavement surface, using the point gage to measure the water depth above the disk, and then WFT = depth above disk plus disk thickness. Lawrence (2000) measured the (nominal) flow depth between large-scale roughness elements using a point gage. Channel discharge was measured volumetrically, and the (nominal) flow velocity was then determined from the discharge and depth.

Robertson et al. (1966) also measured the depth of flow in their channel using piezometer taps connected along the base of the channel to a stilling well with Styrofoam float attached to a linearly variable differential transformer with recorder. Shen and Li (1973) used piezometer taps coupled with a pressure transducer to measure depths (within +/- 0.25 mm) in a channel with Plexiglass side walls and stainless steel plate base.

Savat (1977) determined the *average* depth of flow on a plastic surface from the weight of water flowing in a channel divided by the flow area (channel length = 2.05 meter, width = 0.10 meter). Various corrections account for 1) raindrop impact, 2) splattered raindrops, 3) change in depth due to acceleration of flow near the channel entrance to reach the steady-state depth, and 4) overall acceleration of the flow from zero velocity at the channel entrance. Savat (1980) used a similar weighing measurement method for flow channels with different applied surface roughness.

2.2.3 Measurement of Flow Velocity

Jeffreys (1925) measured the discharge to a 10.2 cm wide, 364 cm long painted wooden trough and assumed q was uniform. Depth measurement was difficult (to within 1 mm) because of surface waves (average depth about 5 mm). Surface velocity was measured using floats or the leading edge of (ink) tracer. Use of tracers for measurement of sheet flow velocity has been used by many other investigators. Most studies timed the leading edge of the dye tracer instead of the centroid, and the leading edge velocity is treated as the maximum velocity, or the surface velocity. The mean velocity is determined by multiplying the maximum velocity by 0.67 when flow is laminar, 0.7 when transitional, and 0.8 when turbulent. This was proposed by Horton et al. (1934). The value of 0.67 of laminar flow was derived from the theoretical velocity profile of such flow regime. Emmett (1970) measured surface velocity values by timing the movement of dye and non-wetting colored powder tracers between marked stations along the channel. The leading edge of the tracer was monitored. Emmett also investigated the relationship between depth-average velocity (V) and surface velocity (u_s). While the relationship $\alpha = V/u_s = 2/3$ was found appropriate for smooth surfaces under expected laminar flow conditions ($Re < 500$), the value of α was found to be smaller for roughened surfaces under the same flow regime. For $Re >$ 1250 the relationship $\alpha = 0.8$ was found for all surfaces. Luk and Merz (1992) performed field as well as laboratory experiments on sheet flow. Again, only laboratory experiments are of interest in the present research. The laboratory flume measured 5 m long by 0.2 m wide covered with a smooth sheet metal bed with no simulated rainfall. Just like Emmitt (1970), Luk and Merz used salt as tracer in their experiments. However, they performed a comparison between dye and salt tracer. They compared the maximum velocity of both forms of tracers in the velocity range of 4 to 48 cm/s. The data points from both field and laboratory experiments were fit to the one-to-one line fairly well. They concluded that salt and dye tracing techniques were compatible, though the dye tracing method appeared to underestimate the maximum velocity at low flow rates. They stated the difficulty of accurately timing the dye tracer arrival time due to substantial dilution as

the reason for the underestimation. The sheet flow experiments ran by Luk and Merz in the laboratory ranged between $450 < Re < 2700$. The measured velocity ratios (α) varied from 0.612 to 0.863 with an average of 0.746 in 21 samples. This value was between 0.7 of transitional flow and 0.8 of turbulent flow proposed by Horton et al. It was also lower than the 0.8 found by Emmitt in turbulent flow. This was probably due to the mix of different flow regimes of both low and high Reynolds numbers, which lowered the average. They also found that the effect of raindrop impact and overestimation of surface (maximum) velocity caused error in dye tracing. They calculated from Emmitt's data that the velocity ratio dropped 9% with rain compared with no rain conditions on a smooth surface. In their own study the reduction was as high as 22%. Katz et al. (1995) sprayed a narrow streak of fluorescent dye across the channel and timed the movement of the leading edge of the dye (rather than the centroid). This gives a measure of the maximum (or surface) velocity. To calculate the average velocity, the maximum velocity was multiplied by a correction factor, α, so that $V = \alpha\ u_s$. They assumed that $\alpha = 2/3$, which corresponds to the laminar flow velocity distribution. Li et al. (1996) and Li and Abrahams (1997) have also investigated the relationship between velocity ratio and Reynolds number for sheet flow under both sediment-laden and sediment-free conditions. Barros and Colello (2001) determined the overland flow velocity using a chemical tracer (sodium bromide) introduced to the channel and concentration measured using an ion-sensitive electrode. Peak concentration values were used to determine the mean travel time.

Yoon and Wenzel (1971) measured sheet flow on a smooth surface with simulated rainfall. Point mean velocity measurements were made using a boundary layer hot-film sensor having a sensitive length of 0.01 inches (2 mm). Their measurements on a smooth surface show velocity profiles that are influenced by rainfall with the surface velocity retarded by rainfall impact.

Phelps (1975) performed experiments in a channel 32-ft long and 3-ft wide. Roughness elements (sand grains or glass spheres approximately 1 mm diameter) were attached to a glass surface using sprayed polyurethane lacquer. The coverage was very sparse, with the ratio of area covered by roughness elements to total area approximately equal to 0.1. Small aluminum particles (of diameter less than 0.025 mm) were introduced into the water. The particles were viewed through a rotating prism with the aid of a microscope that provides a strobe system so that particle velocities can be related to the rotational speed. The depths of the particles were determined by the depth of focus of the microscope. This method allows velocity profiles, $u(z)$, and height to be accurately determined. Measurements confirm the parabolic velocity profile leading to equation (2.1.5) for locations away from roughness elements, and that the velocity profile is distorted in the immediate vicinity of such elements.

2.2.4 Discussion of Measurement Methods

Measurements of sheet flow variables have primarily used point gages for flow depth and tracers for flow velocity. No literature has been identified that uses local measurements of unit discharge; when unit discharge values are used in analysis, the total channel discharge is measured through gage measurements at the channel end, and the unit discharge is calculated from the total discharge and channel width assuming uniform cross-section flow. There are considerable uncertainties with these measurements including the effects of simulated rainfall on depth measurements from point gages when surface waves are present, and differences and relationship between depth-average and surface velocity as a function of flow regime and

channel roughness. The measurement program described in Chapter 3 attempts to circumvent some of these issues.

2.3 Experiment Results from Previous Investigations

Experimental results from investigations of sheet flow mechanics are often expressed in terms of Darcy-Weisbach friction factor (*f*) or Manning's coefficient (*n*). Summary results from the literature are presented in this chapter.

2.3.1 Smooth Surfaces

Yoon and Wenzel (1971) and Shen and Li (1973) have investigated the mechanics of sheet flow over a smooth surface under simulated rainfall, with rates ranging from 0 to 460 mm/hr (18 in/hr). Slopes of 0.1, 0.5, 1, and 3 percent were investigated. Results show that for laminar flow conditions, *f* increases with rainfall intensity and decreases with increasing *Re*. For larger *Re* values, *f* approaches the Blasius curve for smooth surfaces (equation 2.1.8). The velocity distributions measured using hot-film sensors show resistance associated with rainfall inflow near the surface, with the peak velocity occurring at a relative depth approximately 0.8 (*z/h* = 0.8). However, it is observed that the location of measured peak velocity from experiments with zero rainfall is also below the water surface, suggesting that the measured velocity distributions using hot-film techniques is influenced by the presence of the free surface. The effect of rainfall (vertical) impact velocity was not found to be significant. The data from Yoon and Wenzel (1971) and Shen and Li (1973) were analyzed by Shen and Li, who present the following model for $Re < 900$:

$$f = \frac{24 + 27\, r^{0.4}}{Re} = \frac{24}{Re}\left(1 + 1.125\, r^{0.4}\right) \qquad (2.3.1)$$

In equation (2.3.1) the rainfall intensity *r* is in inches per hour. Equation (2.3.1) was also used by Chow and Yen (1976) [as cited by Chow et al., 1988]. At a Reynolds number of about 1000 the flow becomes turbulent and the data for different rainfall intensities converge toward the Blasius curve for turbulent flow in a smooth pipe. For Re > 2000, Shen and Li found that the friction factor varies according to

$$f = \frac{C}{R_e^{\,0.25}} \qquad (2.3.2)$$

They suggest that C = 0.262 for 0.5 < r < 17.5 in/hr, while C = 0.25 for r = 0. From this they speculate that rainfall with intensity somewhere below 0.5 in/hr would begin to increase the flow resistance, and once the flow resistance is increased by the rainfall, the amount of increase would be constant and independent of any further increase of rainfall. Equation (2.3.2) is the *Blasius equation* (2.1.8) with different *C* parameter value.

2.3.2 Rough Surfaces

In the experiments of Robertson et al. (1966), they attached three different gravel sizes (average diameters 2.77, 4.06 and 5.56 mm) to a 30-meter long concrete slab with 5 percent slope. They measured the depth of flow at a number of stations for simulated rainfall at a rate of approximately 150 mm/hr (6 in/hr). Depth measurements were made using a point gage and from float elevation measurements in a stilling well connected to the plane surface through piezometer ports. Depth uncertainty was approximately +/- 1.2 mm. Because size of the pea gravel was a

considerable portion of the flow depth, determination of the channel bottom received considerable attention. Three methods were considered: 1) adding the average gravel diameter, or some fraction thereof, to the concrete bottom, 2) average a series of point gage readings on the gravel tops across the channel ("measured bottom"), and 3) find a "hydraulically effective bottom" by plotting the gage reading depth against $q^{0.6}$, and determining the effective bottom from the q = 0 intercept. Generally good agreement was found between the measured and effective bottom elevations (effective giving a larger value), and the measured bottom elevation was used in depth determinations (corresponding to the top of the gravel). Based on uniform flow experiments (without rainfall) they estimated the friction factor using a model form $f = C/Re^b$ (equation 2.1.10) where the coefficients C and b had values C = 0.74, 4.22, and 2.91, and b = 0.20, 0.39 and 0.31 for the three gravel sizes. Re ranged from about 400 – 4000.

The investigation of Anderson et al. (1998), funded through NCHRP, is most relevant to the current research. They evaluated methods for improved surface drainage of highway pavements and developed a mathematical model (PAVDRN) for prediction of drainage depth on different types of pavement surfaces. As shown in Figure 2.1 (from Anderson et al., 1998), they separate the drainage depth into a lower section within the Mean Texture Depth (MTD) and a flowing section designated the Water Film Thickness (WFT). Through method of measurement, the WFT is the flow depth above the elevation of the top of surface roughness elements. Anderson et al. (1998) apply Manning's equation to characterize sheet flow on pavement surfaces. As an example of their analysis for Portland cement concrete (PCC) surface, they first apply regression analysis to measured data to relate unit discharge q (m^2/s), flow depth h (m) and slope S_o through the following equation [as shown in Figure 2.1, they use the symbol y to designate the total flow depth while this same variable is designated as h in the current work]

$$h = \frac{127 q^{0.312}}{S_o^{0.285}} \tag{2.3.3}$$

They then use this result along with equation (2.1.12) to estimate the dependency of the Manning coefficient on the unit discharge (Reynolds number) resulting in the following set of equations:

$$n = \frac{0.388}{R_e^{0.535}} \quad ; \quad 0 < R_e < 240$$

$$n = \frac{0.345}{Re^{0.502}} \quad ; \quad 240 < Re < 500$$

$$n = \frac{0.319}{Re^{0.480}} \quad ; \quad 500 < Re < 1000$$

$$n = 0.012 \quad ; \quad Re > 1000 \tag{2.3.4}$$

The results from this model set of equations are shown in Figure 2.2. For comparison, results presented by Charbeneau et al. (2007) for a similar surface type (Surface 1 discussed in Chapter 3) are also shown. The model result presented by Charbeneau et al. is

$$n = \frac{7.5}{Re} + 0.0122 \tag{2.3.5}$$

It is of interest that there is large scatter of data for both model equations shown in Figure 2.2.

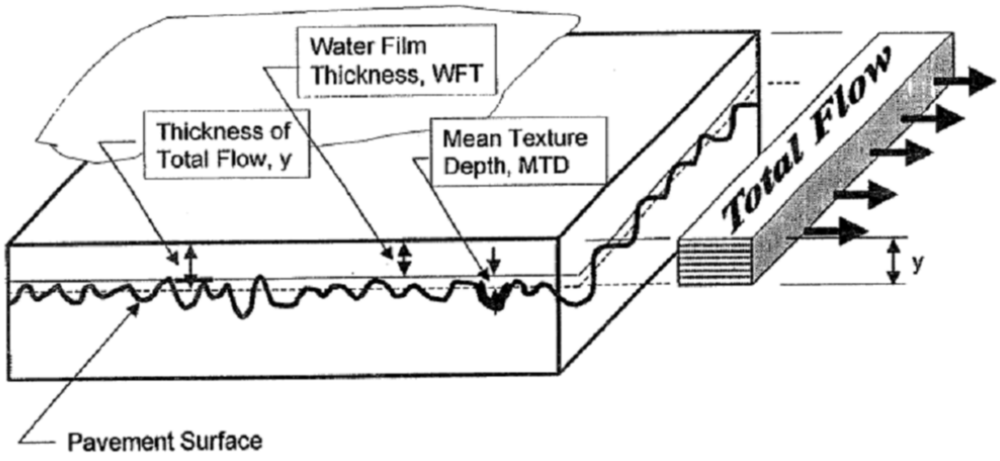

Figure 2.1: Definition of water film thickness, mean texture depth, and total flow (from Anderson et al., 1998)

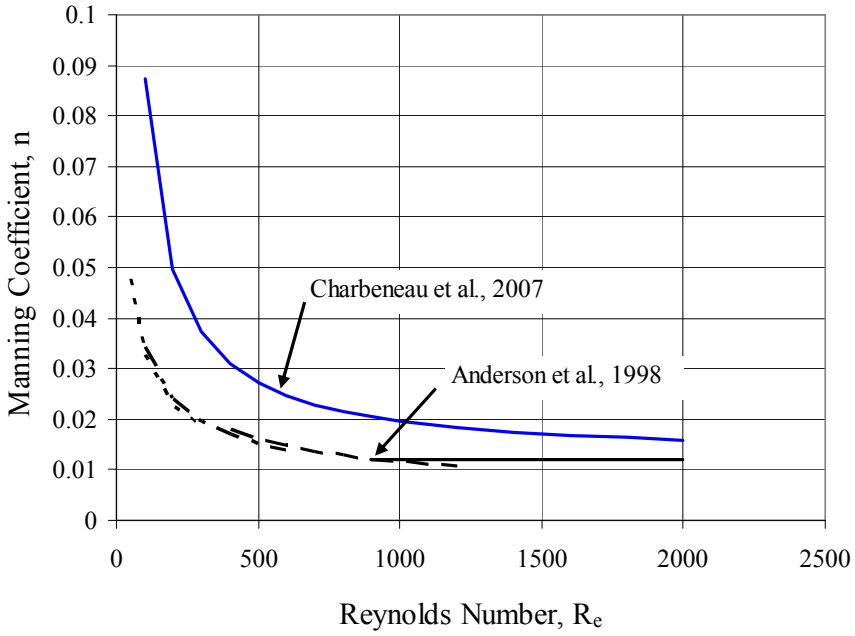

Figure 2.2: Manning coefficient as a function of Reynolds number

2.3.3 Rainfall Effects

Yoon and Wenzel (1972) and Shen and Li (1973) have shown that for smooth surfaces, rainfall increases the magnitude of the Darcy friction factor, resulting in an increase in flow depth with reduced velocity for a given discharge. They found that the mass inflow rate from rainfall, rather than rainfall velocity, was the significant factor. Katz et al. (1995) have found that for low Reynolds number flows ($Re < 160$) surface roughness has a significant effect on flow

velocity while rainfall intensity has a smaller but still discernable effect. For a larger range in Reynolds number, Robertson et al. (1966) also found that surface roughness has a significant effect on sheet flow behavior, but they did not identify a significant influence from rainfall intensity. Similarly, Savat (1977) found that on a smooth surface, rainfall impacts were significant only for small flow rates, but decreased with increasing discharge and slope.

2.4 Models for Surface Runoff (Sheet Flow) Mechanics

Surface runoff models are generally categorized in two groups: empirical models and hydrodynamic models. Empirical models simplify hydrologic processes by introducing empirical parameters and employing a one-dimensional treatment. The Soil Conservation Service (SCS) method developed for computing abstractions from storm rainfall has been popularly used since it was introduced in 1972. The surface runoff at the outlet of a watershed is estimated using an empirical relationship between rainfall excess and curve number that represents the degree of surface infiltration. On the other hand, the rational method is widely used for sewer design because of its simplicity (Chow et al., 1988). In this method, the rate of peak discharge, which occurs at the time of concentration, is estimated by the watershed area, rainfall intensity, and an empirical runoff coefficient that represents surface characteristics. Because the runoff coefficient is empirically determined and the nature of watershed surfaces is complex, the accuracy of the model application is heavily dependent on expertise for choosing a reasonable runoff coefficient. The unit hydrograph proposed by Sherman (1932) is a simple linear model that predicts direct runoff and stream flow hydrographs. The assumptions and limitations of this model are described by Chow et al. (1988). Empirical models are simple and easy to apply to estimate the runoff of a watershed at the outlet such as a gage station. However, the simplicity of the model makes it inapplicable for estimating the flow responses within the flow domain.

The equations of continuity and momentum for gradually varied unsteady shallow water flow are often referred to as the Saint Venant equations. Hydrodynamic models, which consist of the dynamic wave model, the diffusion wave model, and the kinematic wave model, solve the flow dynamics represented by the Saint Venant equations to estimate the runoff and flow responses in a watershed. The dynamic wave model takes into account the full Saint Venant equations for flow routing. The origin of the name “dynamic wave” is from the fact that the model includes the convective inertial terms in the momentum equation. Based on the data taken from an actual river in steep alluvial terrain, Henderson (1966) proposed that on steep slopes only the surface slope terms need to be retained in the momentum equation, and on very flat slopes the bed slope and the pressure gradient terms need to be retained.

Keulegan (1944) was the first to use the concepts of conservation of mass and momentum to analyze overland flow. A detailed discussion of these equations and their different formulations is provided in Singh (1996). Consider sheet flow over a surface where no infiltration occurs, as shown in Figure 2.3. The depth of the sheet flow is relatively small compared with the width and length of the stream. Therefore it is reasonable to assume that the vertical component of the sheet flow momentum is negligible. Furthermore, it is assumed that rainfall is uniform in space and vertical in direction.

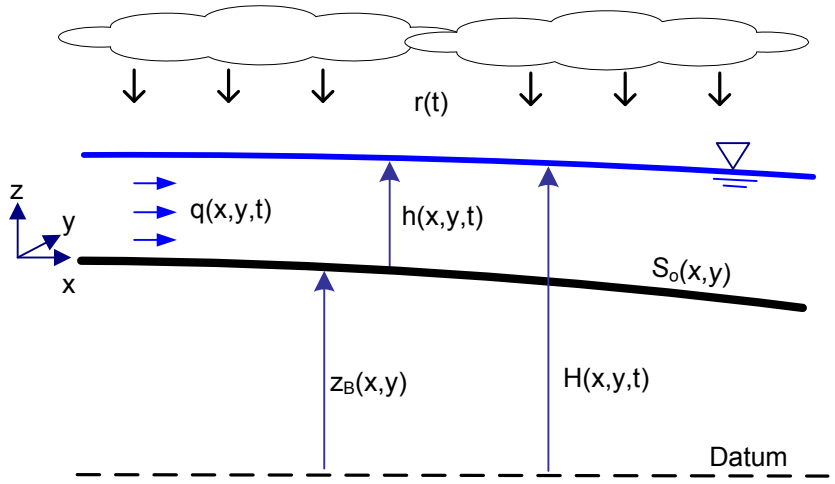

Figure 2.3: Overland flow over a plane

The surface slope, S_o, is defined as positive for a down slope $S_{oi} = -\partial z_B / \partial x_i$ and the total head $H(x,y,t) = h(x,y,t) + z_B(x,y)$ is the main variable of the mathematical model for which a set of nonlinear differential equations is solved. The general constitutive equations for 2D flow include the continuity equation and two full momentum equations

$$\frac{\partial H}{\partial t} + \frac{\partial q_x}{\partial x} + \frac{\partial q_y}{\partial y} - r = 0 \qquad (2.4.1)$$

$$\frac{\partial q_x}{\partial t} + \frac{\partial}{\partial x}\left(\frac{q_x^{\,2}}{h}\right) + \frac{\partial}{\partial y}\left(\frac{q_x q_y}{h}\right) + gh\left[\frac{\partial h}{\partial x} + S_{fx} - S_{ox}\right] = 0 \qquad (2.4.2)$$

$$\frac{\partial q_y}{\partial t} + \frac{\partial}{\partial y}\left(\frac{q_y^{\,2}}{h}\right) + \frac{\partial}{\partial x}\left(\frac{q_x q_y}{h}\right) + gh\left[\frac{\partial h}{\partial y} + S_{fy} - S_{oy}\right] = 0 \qquad (2.4.3)$$

The first three terms of the momentum equations (2.4.2) and (2.4.3) represent fluid inertia. The depth gradient term represents the fluid lateral pressure gradient. The last two terms represent the friction slope due to viscous and turbulent bed resistance and the gravitational gradient, respectively. To simplify notation, the inertial terms may be written in the following form:

$$A_x = \frac{1}{gh}\left(\frac{\partial q_x}{\partial t} + \frac{\partial}{\partial x}\left(\frac{q_x^{\,2}}{h}\right) + \frac{\partial}{\partial y}\left(\frac{q_x q_y}{h}\right)\right)$$

$$A_y = \frac{1}{gh}\left(\frac{\partial q_y}{\partial t} + \frac{\partial}{\partial y}\left(\frac{q_y^{\,2}}{h}\right) + \frac{\partial}{\partial x}\left(\frac{q_x q_y}{h}\right)\right) \qquad (2.4.4)$$

With this notation the momentum equations may be interpreted such that the friction slope is the summation of the bed slope, depth gradient, and the inertial terms.

$$S_{fx} - S_{ox} + \frac{\partial h}{\partial x} + A_x = 0$$

$$S_{fy} - S_{oy} + \frac{\partial h}{\partial y} + A_y = 0 \qquad (2.4.5)$$

If the full set of equations (2.4.5) is solved, then the model constitutes a dynamic wave model. If the inertial terms are neglected, then the model is a diffusion wave. If the friction slope is set equal to the bed slope, then the model is a kinematic wave.

Lighthill and Whitham (1955) developed a theory for the kinematic wave model. They used the kinematic wave theory for flood routing in long rivers. They showed that at the low Froude numbers appropriate to flood waves of a river, the dynamic waves were rapidly attenuated and the main disturbance was carried downstream by the kinematic waves. Henderson and Wooding (1964) applied the kinematic wave theory to the problem of overland flow and groundwater flow on a sloping plane. They found good agreement between the kinematic wave solution and experimental measurements for overland flow, while significant differences were found in the groundwater flow, possibly due to the existence of slope of groundwater surface. They concluded that the buildup and decay of the groundwater surface led the problem to a nonlinear diffusion wave model problem. Woolhiser and Liggett (1967) applied the kinematic wave theory to model unsteady one-dimensional overland flow. They used the method of characteristics to find the flow response of the rising portion of a hydrograph. Iwagaki (1955) developed an approximation method to compute unsteady flow in open channels of any cross-sectional shape with lateral inflows using the method of characteristics. His research is restricted to rivers with steep slopes.

The question of criteria for use of different types of wave models has been of considerable interest in the literature. In this regard, the Froude number at the downstream end of a flow path is often used in characterizing sheet flow (Liggett and Woolhiser, 1967; Govindaraju et al., 1988a, 1988b; Woolhiser and Liggett, 1967). The kinematic wave number K reflects the effects of the length and slope of the plane as well as the normal flow depth and velocity. The kinematic wave number may be defined as follows.

$$K = \frac{S_o L_0}{h_0 Fr_0^{\,2}} \tag{2.4.6}$$

In equation (2.4.6) the variables with the subscript "0" are the values at the downstream end. Woolhiser and Liggett (1967) showed that the kinematic wave approximation is not appropriate for the value of K smaller than 10 but is good for $K > 20$ and $Fr_0 > 0.5$ based on numerical experimentation on rising hydrographs at the downstream end of a plane. If the flow near the downstream boundary is subcritical, a numerical problem may arise near the boundary due to the backwater effect. Singh and Aravamuthan (1996) investigated errors in hydrodynamic models for one-dimensional steady state overland flow. They found that the percentage error in water depth over dimensionless distance of the kinematic wave model varied from 6% ($K=30$, $Fr_0=1.0$) to 100% ($K=3$, $Fr_0=0.1$). The error increased near the upstream end and gradually decreased toward the downstream end. The error was large for small K, but it was lower than 10% at the downstream end with large K, and became negligible when $K=\infty$ regardless of the value of the Froude number, and was relatively small in the diffusion wave model. For example, the error in the diffusion wave model ranged from 0.39% ($K=30$, $Fr_0=1.0$) to 9% ($K=3$, $Fr_0=0.1$) for variable conditions. It should be noted that most of the error occurred near the upstream end. They concluded that the error of the diffusion wave model was considerably lower than the kinematic wave model for low KFr_0^2; therefore, the diffusion wave model was preferred over the kinematic wave model for small values of KFr_0^2.

Dalus Vieira (1983) compared the solutions of the Saint-Venant equations with those of the kinematic, diffusion, and gravity wave approximation, for a range of constant Froude and kinematic wave numbers for one-dimensional shallow surface water flow. Two different types of

downstream boundary conditions were used: (1) critical flow and (2) zero depth gradient condition. By comparing the solutions of hydrodynamic models made for more than 150 K-Fr_0 pairs, Dalus Vieira was able to draw a contour map representing the values of surface slope, $S_x(Fr_0, K)$, in the Fr_0 - K field. The contour line corresponding to $S_x = 0.005$ is shown in Figure 2.4. In case of smooth urban slopes where the value of K generally ranges from 5 to 20, the kinematic or diffusion wave model may be used depending on the value of Fr_o where the critical value of Fr_o is about 0.5 in the figure. The full dynamic wave model must be used for low values of K (<5). Ponce (1990) developed a linearized diffusion wave model for different cases, which include full inertial, local inertial, convective inertial, and non-inertial. In his numerical experiments, the non-inertial model showed good approximation to the full inertial model for low Froude number flows. Therefore he concluded that the non-inertial diffusion wave model was a better approximation to the full inertial model than either local or convective inertial models.

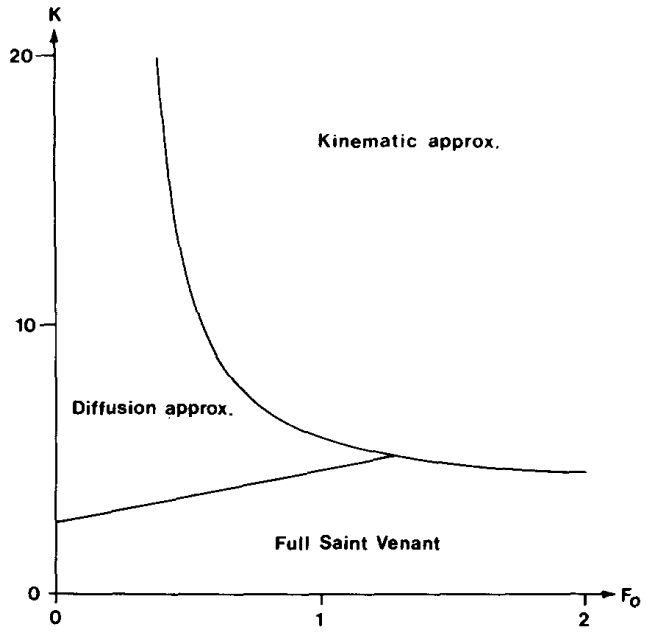

Figure 2.4: Partition of the K, Fr_0 field into three zones for zero-depth-gradient downstream boundary conditions.
Note: Contours correspond to longitudinal slope Sx = 0.005 (from Dalus Vieira, 1983)

2.5 Numerical Simulation of Overland Flow

The theories for the kinematic wave model mentioned in this section are mostly for one-dimensional problems. The knowledge gained from the kinematic wave theories is crucial for developing a proper sheet flow model. Even though the kinematic wave model is widely used by many researches on various topics (Cristina and Sansalone, 2003; Akan et al., 2000; Tisdale et al., 1999; Tsai and Yang, 2005), it must be noted that most hydrologic processes occur in two-dimensional space and with a temporal variation. Over-simplification in a physically based model may result in failing in representation of the parameters that should be evaluated in a required spatial and temporal resolution (Grayson et al., 1992). Therefore, the kinematic wave

model may not be applicable to urban flood analyses including sheet flow on impervious pavement surfaces. Backwater effects, ponding, flow over adverse slope, and other flow effects associated with flood control systems must be considered in modeling sheet flow on urban pavement surfaces. The full dynamic wave model would be the best option when it comes to the accuracy of the solution. However, the numerical difficulties and computation cost compromise the benefit of the model, and the necessary condition for using the full dynamic wave model ($K<5$) rarely occurs in rivers and overland flows. Therefore, researchers (Feng and Molz, 1997; Jain and Singh, 2005; Hromadka and Yen, 1986; Lal, 1998) showed that the diffusion wave model is the best model to apply for this purpose. It not only inherits the advantages of the kinematic wave model but also works well for most realistic hydrologic processes.

There have been a few research efforts on modeling stormwater runoff from highway surfaces. Cristina and Sansalone (2003) developed a 1D kinematic wave model of urban pavement rainfall-runoff subject to traffic loadings. They compared the time of concentrations predicted with a kinematic wave model with field measured data. The difference is empirically modeled to an adjusted runoff coefficient. Even though their research is valuable for predicting the amount of stormwater for designing drainage inlets, the model is not able to predict the spatial variation of the stormwater spread within the domain. Anderson et al. (1998) conducted a comprehensive research for improved surface drainage of pavements. The topics encompass various experimental studies and computer modeling. However, they did not develop a proper numerical model for simulating sheet flow on road surfaces due to the difficulties such as computational cost, convergence, and computational errors but ended up with a 1D kinematic wave model.

The relative magnitude of the terms in the momentum equation is important for choosing a wave model. Henderson (1966) computed the relative magnitude of momentum equation terms for a steep alluvial channel with a fast rising hydrograph. He concluded that the discharge can be computed as in uniform flow (kinematic wave approximation) suggesting that the relative magnitude of bed slope is 100 times larger than the inertial terms in order of magnitude in the momentum equation. He also noted that the depth gradient term may well be of the same order as the bed slope when the bed slope is very flat. Yu and McNown (1964) considered use of Keulegan's equation for calculation of runoff from the end of a pavement section. They concluded that the gravity and bed resistance terms were larger than others by a factor of 100, and thus a kinematic model could be used based on the continuity equation and a resistance equation. Due to model simplicity, the computation cost and difficulty in model development for kinematic wave models are significantly lower than full dynamic or diffusion wave models while the computed results are fairly accurate. A 1D sheet flow simulation computed with the kinematic wave model under a constant rainfall and surface slope at steady state is compared with the diffusion wave model result in Figure 2.5 (diffusion wave model development is described in Chapter 4). The curve with circled marker represents the kinematic wave solution, and the triangle shows the diffusion wave solution. There is no apparent difference observed between the solutions.

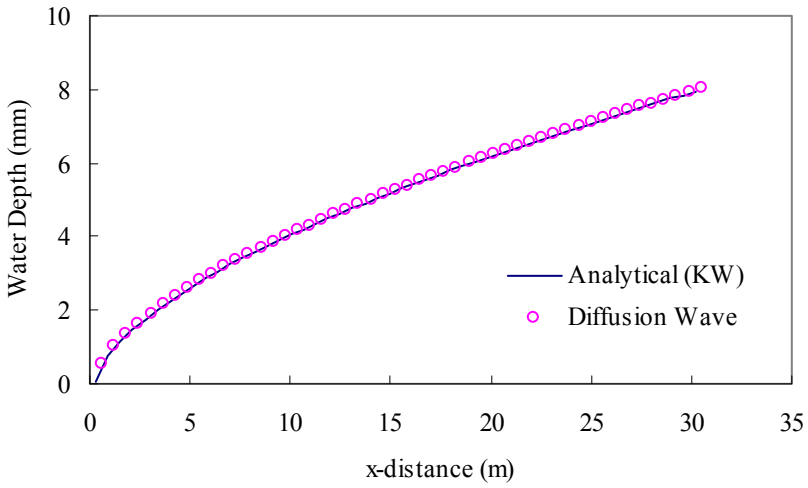

Figure 2.5: 1D flow under constant rainfall at steady state

However, the application of the kinematic wave model is limited for domains that have areas 1) where bed slope is zero or 2) where there is significant pressure gradient. Due to the fact that the surface slope is the only term that contributes to friction slope, zero slopes within a domain will result in discontinuity in the solution. Figure 2.6 shows a 2D sheet flow under constant rainfall with change in cross slope. A stream tube method with kinematic wave approximation was used to compute water depth at steady state. The streamlines head to the left side near the upstream, but the direction gradually changes to inside domain as they go downstream. There exists a clear discontinuity in the water depth between streamlines that barely touch the left side boundary forming a long flow path, and streamlines that begin on the side of the domain. As streamlines head back to the domain, new streamlines begin at the nearby side boundary. If surface slope is the only term in the equation of motion, the difference of water depth on these streamlines cannot be counted appropriately resulting in a sharp decrease in water depth.

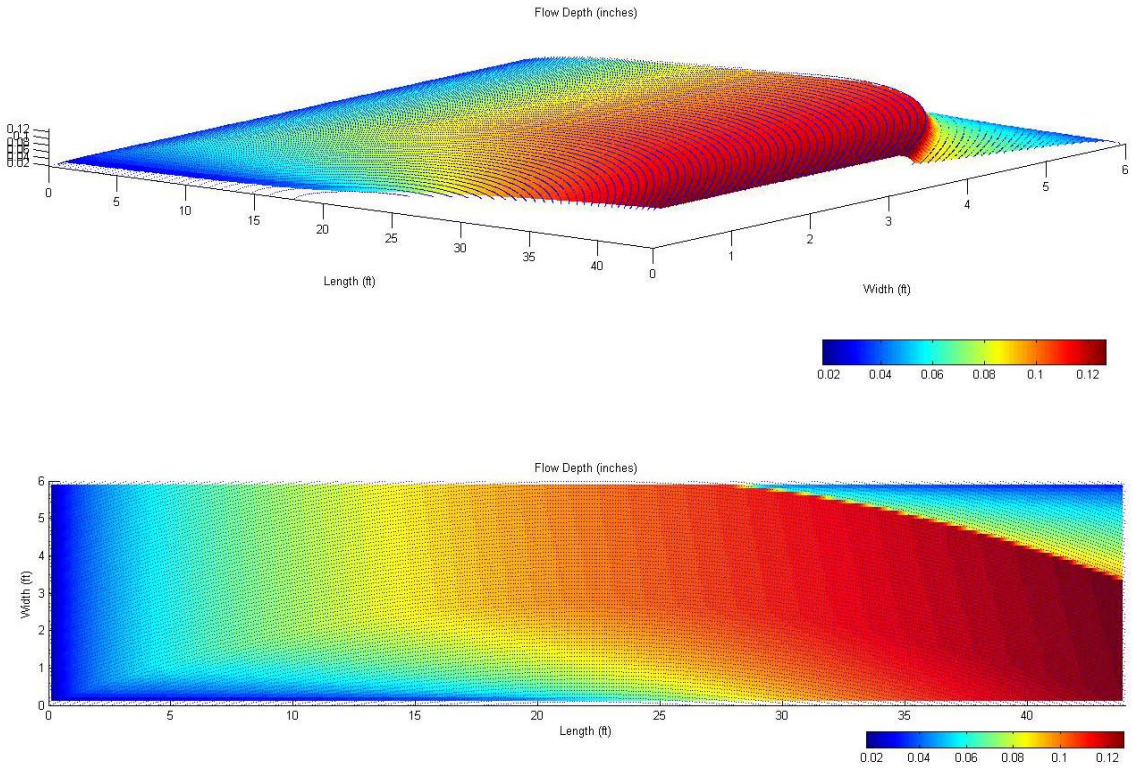

Figure 2.6: Kinematic wave solution for a 2D flow

The flow pattern shown in Figure 2.6 is typical on a superelevation transition area, which means the head gradient term in the momentum equation cannot be neglected. Therefore, the kinematic wave model is not adequate for the domains with this kind of irregular topography. As a result, a diffusion wave model is considered to be the one that gives a fairly accurate solution without a discontinuity contributed by topography, and the one that significantly saves numerical computation cost compared with a full dynamic wave model.

2.6 Geometry of Superelevation Transitions

Design speed and highway curvature are important issues in design of horizontal roadway alignment. Centrifugal forces are developed as vehicles move through curved highway sections, and these forces may be controlled through use of limits on curve radius and through superelevation of highway lanes. Through superelevation transitions, the curve outside-lane cross slope is rotated from negative cross slope at normal crown conditions, to positive cross slope at fully superelevated conditions. TxDOT generally follows AASHTO recommendations (A Policy on Geometric Design of Highways and Streets, 2001) in design of superelevation transitions. The length of roadway needed to accomplish the change in outside-lane cross slope from zero to fully-superelevated (e_s) is called the superelevation runoff (L_2). The tangent runout (L_1) is the length of roadway that is necessary to accomplish the change in outside-lane cross slope from normal crown (e_n) to zero. Both of these lengths are shown in Figure 2.7. The upper part of this

figure is a plan view of the pavement surface, while the lower part shows the cross slope as a function of longitudinal station. A linear longitudinal change in cross slope is shown.

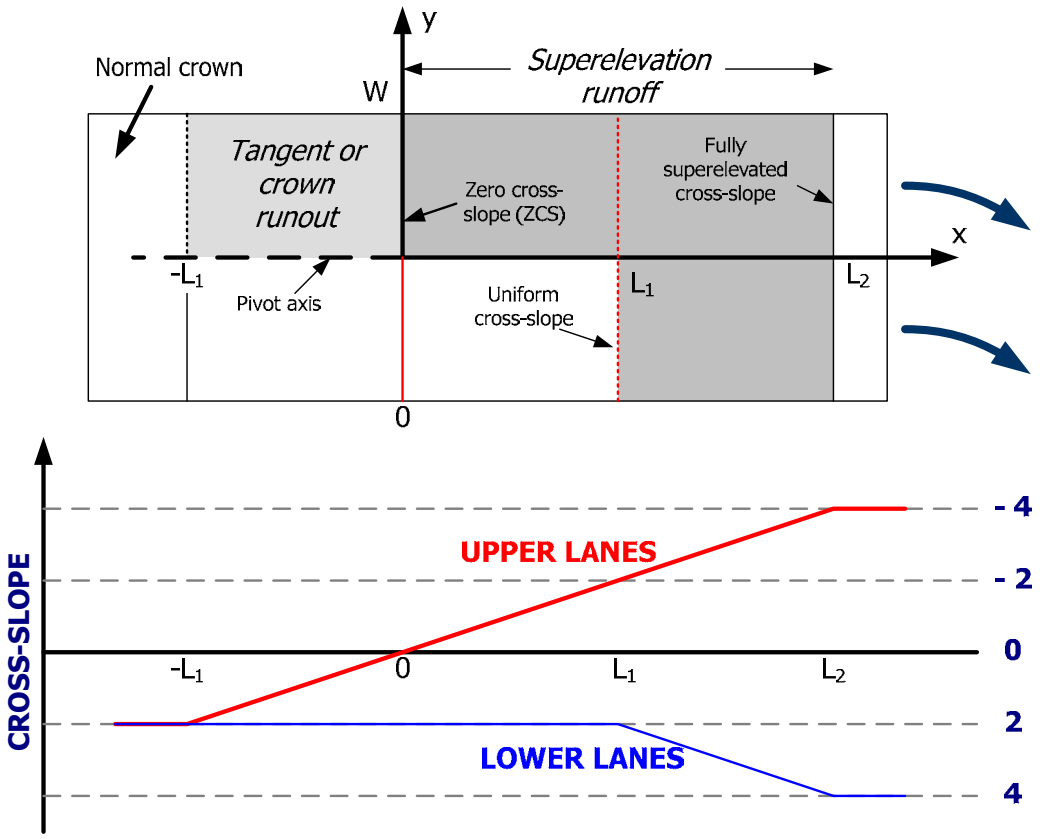

Figure 2.7: Lateral alignment at superelevation transition with superelevation cross slope = 4%

Roadway alignment is based on design guidance for maximum longitudinal rate of rotation of pavement slope, as a function of vehicle design speed, as provided in the TxDOT Roadway Design Manual (October, 2006), Chapter 2 (Basic Design Criteria), Chapter 4 (Horizontal Alignment). The minimum superelevation runoff travel length depends on the width of travel lanes, the design superelevation cross slope, and the relative gradient (G) that depends on the vehicle design speed (TxDOT, 2006, Table 2.8 shows that G varies from 0.8 percent at design speed 20 km/hr to 0.35 percent at design speed 130 km/hr). The tangent runout (L_1) and superelevation runoff (L_2) are calculated using

$$L_1 = \frac{e_n W}{G}$$
$$L_2 = \frac{e_s W}{G} \qquad (2.6.1)$$

AASHTO guidance includes an additional factor that depends on the number of travel lanes, which allows reduction of the minimum superelevation runoff length. In general practice the "1/3 rule" states that 2/3 of the superelevation should be obtained before the beginning of the

horizontal curve (Anderson, et al., 1998). Thus the roadway horizontal alignment near the zero cross slope (ZCS) station is straight.

The relative gradient (G) is the primary determinant of alignment near superelevation transitions; the superelevation runoff length depends directly on the design superelevation cross slope, but the roadway configuration near the zero cross slope station does not depend on the superelevation cross slope. It is the drainage characteristics near the ZCS station that are most critical for hydroplaning potential.

For design of all roadways, TxDOT requires use of the GEOPAK software package that runs on MicroStation CAD software. GEOPAK defines the horizontal and vertical alignment of a roadway and includes cross slope, superelevation, and superelevation transitions. While GEOPAK does not specifically address issues of highway drainage, data available through GEOPAK design can be processed to analyze hydraulic performance of roadway design for selected design rainfall. Analysis tools developed through this research project use output files generated by the GEOPAK software package.

2.6.1 Geometric Description of Roadway Surface and Kinematic Flow Paths

The geometric description of the roadway surface is based on Figure 2.7. The roadway centerline is the pivot axis. The roadway centerline forms the x-axis while the station with zero cross slope (ZCS) forms the y-axis. The cross slope is designated e. In decimal form, $e = S_y(x)$, which is a function of longitudinal station, where S_y is the cross slope. The convention used is that if the elevation decreases in the direction away from the x-axis, then the cross slope is positive; under normal crown conditions, the cross slope $e = e_n$ is positive for both positive and negative y-directions. The longitudinal slope along the roadway centerline, S_{x0}, is assumed constant (either positive or negative, depending on whether the roadway surface elevation decreases or increases in the longitudinal x-direction). At stations $x < -L_1$ the roadway has normal crown. The designations e_n and $e_{s(oi)}$ represent the cross slope at normal crown and superelevation, respectively, with the designation $e_{s(oi)}$ being negative for the outside-lanes of a curve and positive for the inside-lanes of a curve. Starting at station $x = -L_1$ the outside-lanes cross slope decreases from e_n to 0 at station $x = 0$. From station $x = 0$ to $x = L_1$, the outside-lanes cross slope decreases from 0 to $-e_n$. At station $x = L_1$ the roadway cross slope is uniform across both the outside and inside travel lanes. From stations $x = L_1$ to L_2 the cross slope decreases for the outside-lanes and increases for the inside-lanes at a uniform rate from e_n to e_s (with appropriate sign). For stations beyond $x = L_2$, the roadway is fully superelevated with constant cross-slope $-e_s$ for the outside-lanes and e_s for the inside-lanes. The station lengths L_1 and L_2 are calculated using equation (2.6.1).

It is of interest to develop an algebraic expression giving the roadway surface elevation as a function of location based on geometric parameters describing the superelevation transition. Assuming a linear variation in lateral alignment, as shown in the lower part of Figure 2.7, the roadway surface elevation, Z_s, through the transition section is described by

$$Z_s(x, y) = z_0 - S_{x0}\, x - e_{s(oi)} \frac{x}{L_2} |y| \qquad (2.6.2)$$

In this expression z_0 is the elevation at the coordinate origin. With regard to Figure 2.7, equation (2.6.2) is valid for the regions [$-L_1 < x < L_2$, $y > 0$] and [$L_1 < x < L_2$, $y < 0$]. For the inside-lanes section that remains at normal crown slope the corresponding equation is

$$Z_n(x, y) = z_0 - S_{x0}\, x - e_n |y| \qquad (2.6.3)$$

Assuming kinematic (gravity) drainage, the hydraulic gradient and streamline paths coincide, and the hydraulic gradient is calculated as

$$\vec{I}_s = -\nabla Z_s = \left(S_{x0} + \frac{e_{s(oi)}}{L_2}|y| \right) \hat{i}_x + \left(\frac{e_{s(oi)} x}{L_2} \text{sgn}(y) \right) \hat{i}_y \tag{2.6.4}$$

$$\vec{I}_n = -\nabla Z_n = S_{x0} \hat{i}_x + e_n \, \text{sgn}(y) \hat{i}_y \tag{2.6.5}$$

In equations (2.6.4) and (2.6.5) the function sgn(y) is the generalized function that takes the value 1 for $y > 0$ and -1 for $y < 0$. Equations (2.6.4) and (2.6.5) can be used to determine the drainage flow paths under specific conditions.

Example: Consider the alignment shown in Figure 2.7 with W = 10 m, G = 0.0045, e_n = 0.02, e_s = 0.04, and S_{x0} = 0.01. Calculate the limiting streamline path suggested in Figure 1.3.

For this data equation (2.6.1) and (2.6.2) give L_1 = 44.4 m and L_2 = 88.8 m. The drainage streamline equation for the outside-lanes ($y > 0$; $e_{s(oi)} = -e_s$) is determined from equation (2.6.4) as follows.

$$\frac{dy}{dx} = \frac{e_{s(oi)} x \, \text{sgn}(y) / L_2}{S_{x0} + e_{s(oi)} |y| / L_2} = \frac{-e_s x / L_2}{S_{x0} - e_s y / L_2} \equiv \frac{x}{y - A} \tag{2.6.6}$$

Equation (2.6.6) can be integrated to give

$$x^2 = y^2 - 2Ay + C \tag{2.6.7}$$

In equation (2.6.7) $A = \frac{S_{x0} L_2}{e_s}$ and C = constant of integration (which is determined by the location of a single point along a streamline). Equation (2.6.7) shows that the flow drainage paths are represented through a family of hyperbolas. The limiting streamline passes through the point (x,y) = (0,10 m) and with the given data, A = 22.2 m. Using these values in equation (2.6.7) gives $C = 0^2 - 10^2 + 2(22.2)(10) = 344$ m^2. The streamline equation within the outside lanes is: $x^2 = y^2 - 44.4y + 344$. This streamline contacts the roadway centerline (y = 0) at locations $x = \pm\sqrt{344} = \pm 18.5$ m. The streamline originates along the roadway centerline at location (-18.5 m, 0), flows towards the outside late edge and turns at the ZCS station, reaches the roadway centerline again at location (18.5 m, 0), and then crosses the inside-lanes under normal crown slope moving in a straight line with slope $y/x = -e_n/S_{x0}$. This streamline curve is shown in Figure 2.8.

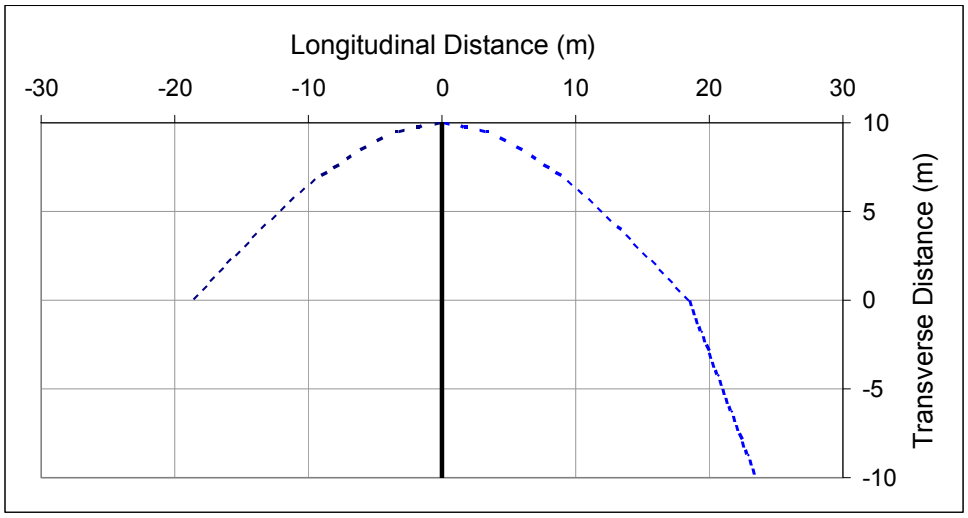

Figure 2.8: Drainage path for limiting streamline based on gravity (kinematic) drainage

2.6.2 Existence of Drainage Stagnation Points on Roadway Surface

One interesting feature that appears directly from examination of the drainage surface geometry is the potential presence of drainage stagnation points on the roadway surface. At a stagnation point the hydraulic gradient vanishes. Equation (2.6.5) makes it clear that this can never happen under normal crown conditions. However, within the outside-lanes near a superelevation transition, equation (2.6.4) shows that the lateral gradient vanishes at the ZCS station ($I_{sy}(0,y) = 0$). The longitudinal gradient will vanish on the outside-lanes ($e_{s(oi)} = -e_s$) at a location where $|y| = \frac{S_{x0} L_2}{e_s}$, and only if $S_{x0} > 0$. Comparison with equation (2.6.1) shows that this can be written

$$|y| = \frac{S_{x0}}{G} W \qquad (2.6.8)$$

Equation (2.6.8) implies that a drainage stagnation point can exist on the roadway surface only if $S_{x0} < G$ and $S_{x0} > 0$. The requirement that $S_{x0} < G$ is understood to mean that the outside edge of pavement is increasing in elevation at a rate that is greater than the overall decrease in elevation associated with the centerline longitudinal slope. The existence of drainage stagnation points could be significant in accumulation of ponding depth during stormwater runoff from pavement surfaces.

Chapter 3. Experimental Program

3.1 Experiment Set-up

A rainfall simulator and roadway model were constructed to investigate sheet flow behavior on rough impervious surfaces during storm events. The primary structure consists of a platform with supports that allow adjustment of the longitudinal and lateral slope. A secondary platform that served as the 'roadway' surface was constructed on top of the primary platform. The secondary platform (elevated plywood structure) has size 13.4 meters by 2.5 meters and was coated with granular material and resin to provide the desired surface roughness.

Suspended from the support structure is a PVC pipe system with nozzles spaced in a rectangular array at 1 meter intervals that sprayed water downward at an angle of 60 degrees from the nozzle centerline. To enhance the spatial uniformity of rainfall, the entire rainfall simulating system rotates at 0.25 revolutions per second with a 30-cm rotation arm. This configuration was selected by first measuring the spray intensity beneath an individual nozzle, then evaluating the average rainfall intensity that would occur beneath a system of nozzles being rotated with an arm of given radius. Evaluating the resulting intensity distribution for different arm radii, maximum uniformity was found to occur with an arm radius of 30 centimeters. Furthermore, a head box installed on the upstream end of the roadway provides the roadway surface with longitudinal inflow for simulation of large flow events. With this setup, different experiments can be performed with just the head box, just the rainfall simulator, or with both. This allows testing to occur under a wide range of conditions. A schematic view of the experiment setup is shown in Figure 3.1, while a picture taken from the downstream end of the setup is shown in Figure 3.2. In Figure 3.2 one may note three sample ports located near the downstream end of the secondary platform, and an inclined manometer board shown on the right-hand side of the figure. Details on construction of the experimental facility are provided by Villard (2005).

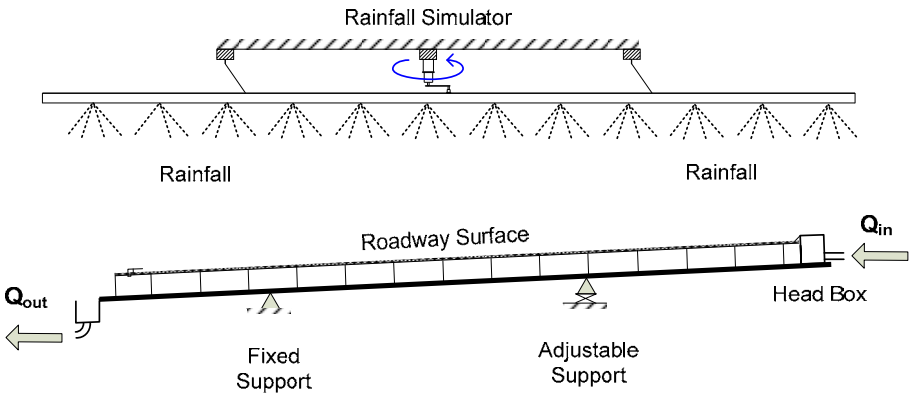

Figure 3.1: Schematic view of physical model

Figure 3.2: Picture of physical model viewed from downstream end showing rainfall simulator, three sample ports located near end of model surface, and inclined manometer board located to the right side of the surface platform

Spatial uniformity of the rainfall intensity was of great concern for constant rainfall simulation. The coefficient of uniformity (CU) defined by Christiansen (1942) was used as an index. A CU value of 100 implies an absolutely uniform distribution in space. The rainfall simulator with its unique rotating structure provides rainfall intensity in the range of 9 cm/hr to 15 cm/hr with no less than 85 CU. Investigations of rainfall intensity and distribution for this experimental setup are described in detail by Schneider (2006).

Three different surfaces were created to simulate the roughness of concrete and asphalt type pavements. These surfaces were developed by first coating the plywood surface with resin, and then applying granular material by hand uniformly over the surface, and finally spraying a coat of resin to seal and affix the material. The first surface used fine-grain sand material with grain size distribution shown in Figure 3.3. Grain size was measured by sieving. The mean grain size for Surface 1 is d_{50} = 1.22 mm. After the experiments with Surface 1 were completed, coarser-grain material was applied to the existing surface and fixed with resin. The grain-size distribution for Surface 2 is also shown in Figure 3.3 with mean grain size d_{50} = 3.33 mm. Finally, to create a surface with intermediate roughness, fine-grain material (similar to that used for Surface 1) was added to the experiment surface platform and sealed with resin. The only

physical characterization of Surface 3 is estimation of mean texture depth using ASTM (2006). The estimated mean texture depth in front of each sample port and at other locations on the platform surface was 2.2 mm. Hydraulic characterization of each surface is provided through estimation of an effective surface roughness k and Manning coefficient, as described in the following section.

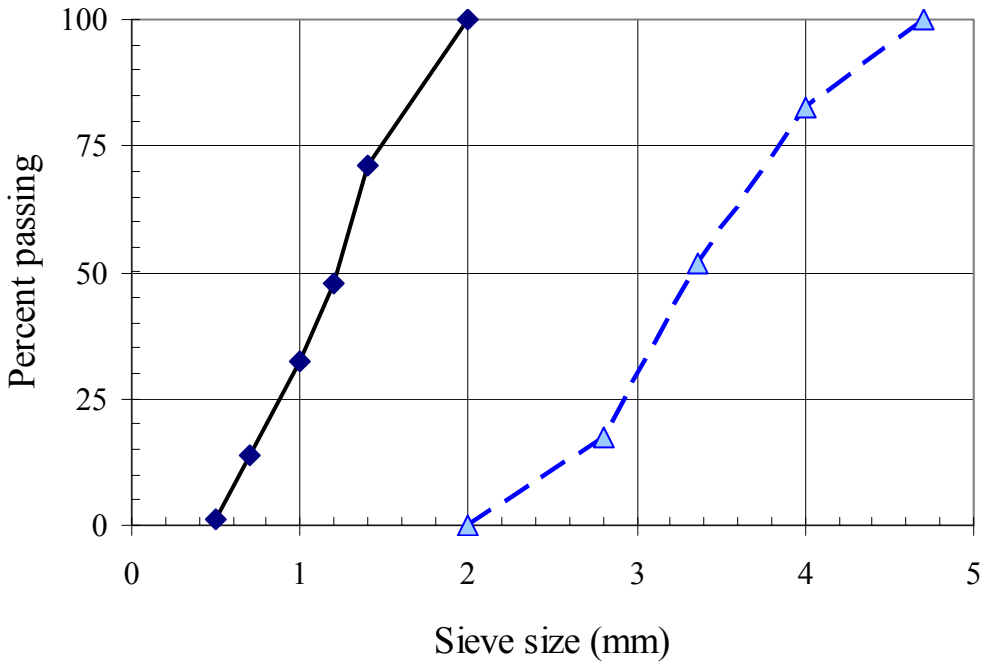

Figure 3.3: Grain-size distribution curves for material applied to Surface 1 (diamond) and Surface 2 (triangle)

Characterization of sheet flow hydraulics requires the relationship between the surface roughness, flow rate (velocity or unit discharge), flow depth, and rainfall intensity. For these experiments, the surface roughness is fixed by construction. The rainfall intensity can be controlled within a limited range and measured independently. This leaves measurement of the velocity u (m/s), unit discharge q (m^2/s), and depth h (m). These values are related through $q = uh$, so that only two of the variables need be measured independently. A number of alternative measurement methods was investigated, with the following method selected. A detailed discussion of evaluation of the different measurement methods is presented by Schneider (2006).

The flow measurement system consists of independent measurements of the flow depth (h) and unit discharge (q). The flow depth is measured using a piezometer tap located on the roadway surface and attached through tubing to an inclined monometer board. The unit discharge is measured by direct capture of discharge from the roadway surface. The setup for this measurement system is shown in Figure 3.4. As shown in the figure, the manometer opening (piezometer tap) on the roadway surface is shaded by the cab of a shield box to prevent rain drops from impacting on the opening. The elevation of water level in the slanted manometer tube is 3 times more sensitive than the vertical depth on the roadway. For flow depth measurement, the water level with flow is recorded first; then, with no flow on the roadway surface, the

manometer tube is flushed by water and the water level is recorded again after the water level is stabilized. Water depth is computed by subtracting the water depth with no-flow condition from the condition with flow. The discharge collected by the collection hole (sampling port) is measured directly with a container and a stopwatch. Three sets of this measurement system were installed near the downstream end of the roadway section on the centerline and 60 cm from both sides. The surface slope of the roadway model was varied from one to three percent.

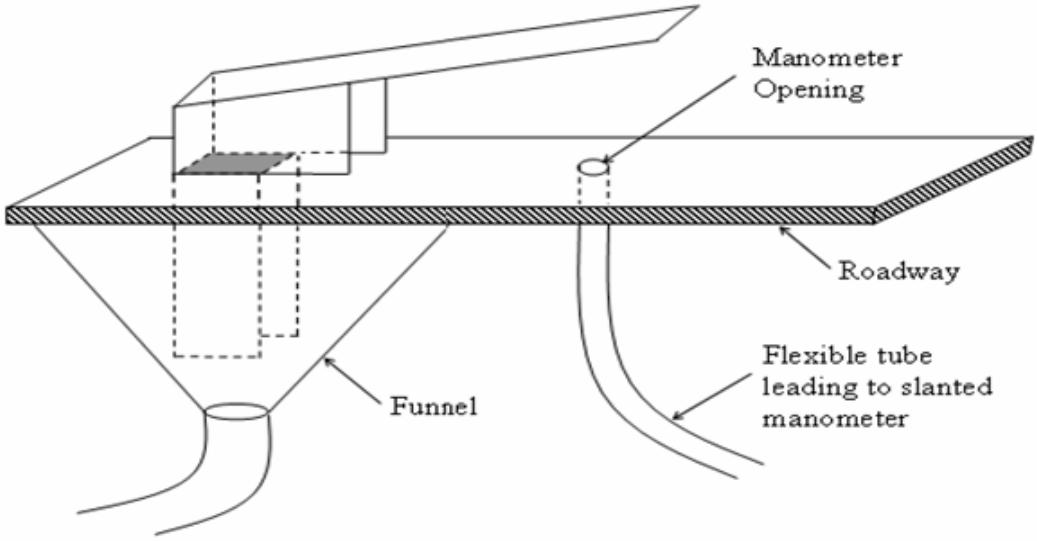

Figure 3.4: Flow and depth measurement system

3.2 Experiment Data

The experiment data consists of measurement of depth from the piezometer tap/manometer board apparatus and discharge from the sample ports, along with temperature for determination of water viscosity. For each experiment (slope, rainfall rate, head-box flow rate), three separate measurements of depth and unit discharge were obtained from the three sampling ports located near the ends of the roadway section. Measurements were made in triplicate and data were averaged (for each sample port separately). Experiments were performed on three different surfaces, with three different slopes (1, 2, and 3 percent), and under conditions with and without the rainfall simulator operating. For the "no rain" (*NR*) conditions, the sheet flow is established using the head-box alone. For "rain" (*R*) conditions, experiments were performed using just the rainfall simulator and combination of the rainfall simulator plus the head-box. The entire data set for all surfaces and all conditions is shown in Figure 3.5. The measured depth ranges from nearly zero to almost 3 cm. The measured unit discharge ranges from nearly zero to approximately 0.02 m^2/s. The wide range of data scatter reflects the individual effects of surface roughness and slope, and to a lesser extent, *R* versus *NR* condition. The individual data sets are described in greater detail later in this chapter.

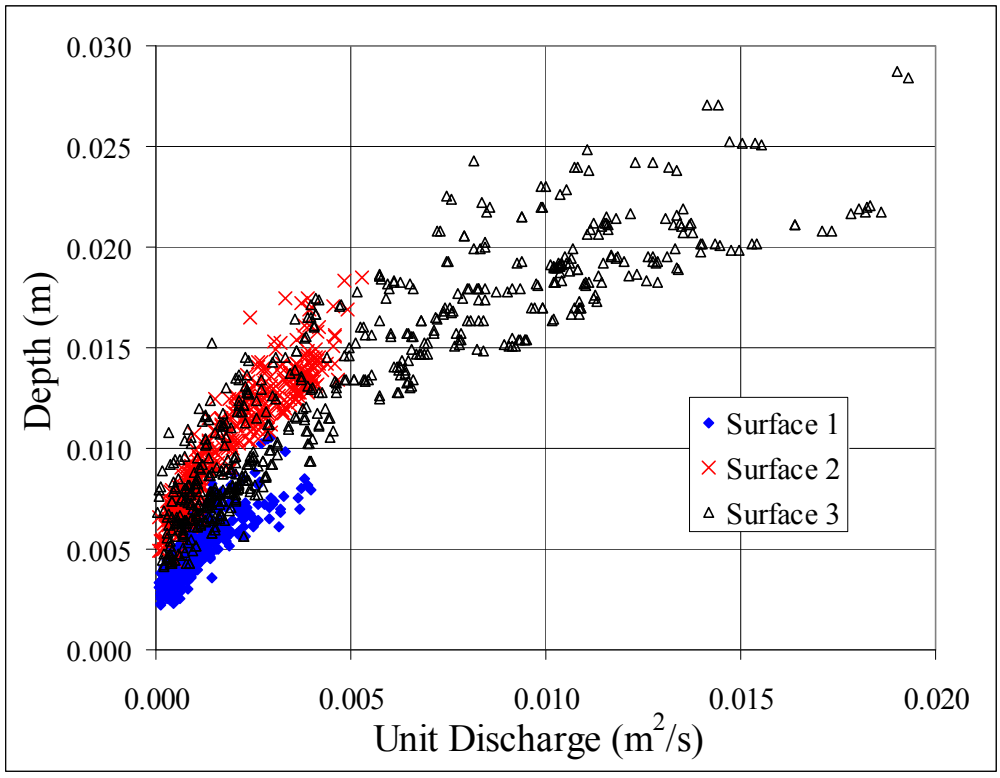

Figure 3.5: Data sets for Surface 1 (diamond), Surface 2 (cross), and Surface 3 (triangle) for all slope and rainfall conditions

The number of data for each surface and *NR/R* subset is shown in the first column of Table 3.1. The overall data set has $N = 1432$ data. The experiment data are presented in Figures 3.6, 3.7 and 3.8 for the three different surfaces. The range in unit discharge is much larger for Surface 3. For this setup the size of the sample ports and collection tubing was increased to allow measurement of larger flow rates. From the basic data presented in Figure 3.5 (or Figures 3.6 to 3.8), a number of informative statistics can be calculated without further analysis. With equations (2.1.1), (2.1.2) and (2.1.12) one may calculate values of Reynolds number (*Re*), Froude number (*Fr*) and Manning coefficient (*n*) corresponding to each data. The ranges in calculated results are listed in Table 3.1. Figure 3.9 shows the relationship between Froude number and Reynolds number for the three data sets. The Froude number clearly increases with increasing Reynolds number for all three surfaces. Based on equation (2.1.2), this shows that the flow rate (corresponding to *Re*) increases at a faster rate than $h^{3/2}$. The rate of increase in *Fr* with *Re* is greater for smoother surfaces (Surface 1 versus Surface 2). For Surfaces 1 and 3, the data exhibit both subcritical and supercritical conditions.

Table 3.1: Data Summary

Surface/*N* *NR/R*	*Re*	*Fr*	*n*(*h*)	*K*	$N_H = n^6 (hS_o)^{0.5}$
1/442 183/259	80-[840]-5080	0.12-[0.78]-2.17	0.008-[0.021]-0.102	8-[74]-2700	2.3E(-15)-[8.3E(-13)]-6.5E(-9)
2/375 201/174	110-[2420]-6520	0.06-[0.53]-0.96	0.020-[0.035]-0.247	14-[73]-7890	6.4E(-13)-[2.5E(-11)]-1.8E(-6)
3/615 345/270	50-[3090]-17690	0.02-[0.91]-1.85	0.011-[0.023]-0.583	3-[27]-33700	1.9E(-14)-[2.5E(-12)]-3.2E(-4)

Note: *N* = number of data, *NR* = number of no-rain data, *R* = number of rain data, *Re* = Reynolds number, *Fr* = Froude number, *n*(*h*) = Manning coefficient based on measured depth *h*, *K* = kinematic wave number, and N_H = (Henderson) roughness number (dimensional). Data format: minimum-[median]-maximum

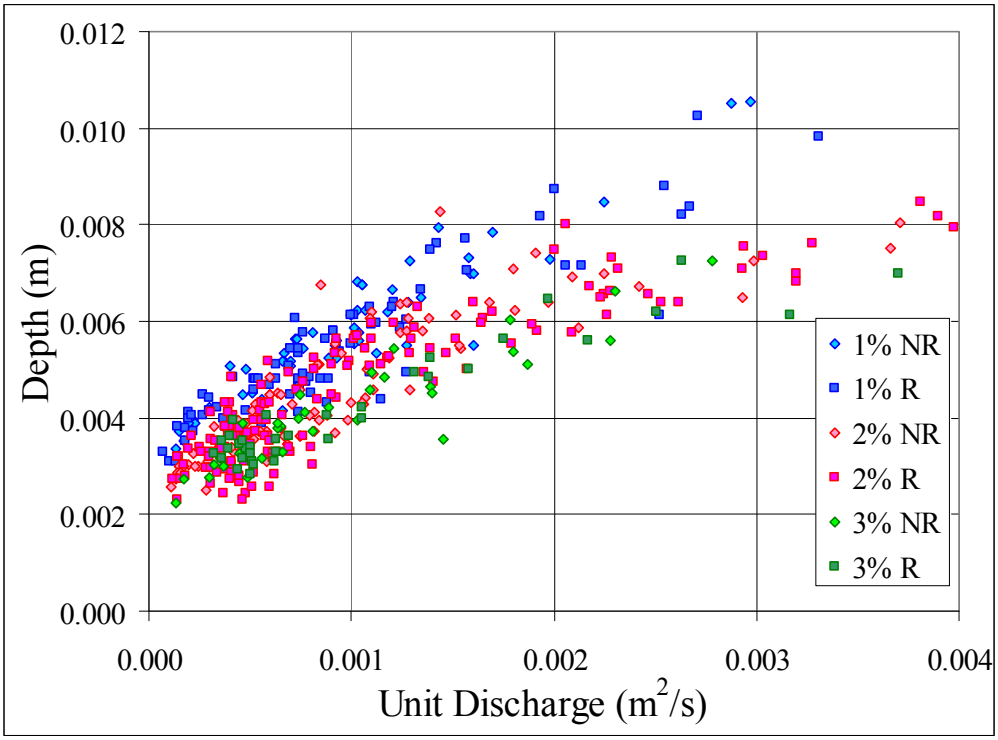

Figure 3.6: Data set for Surface 1

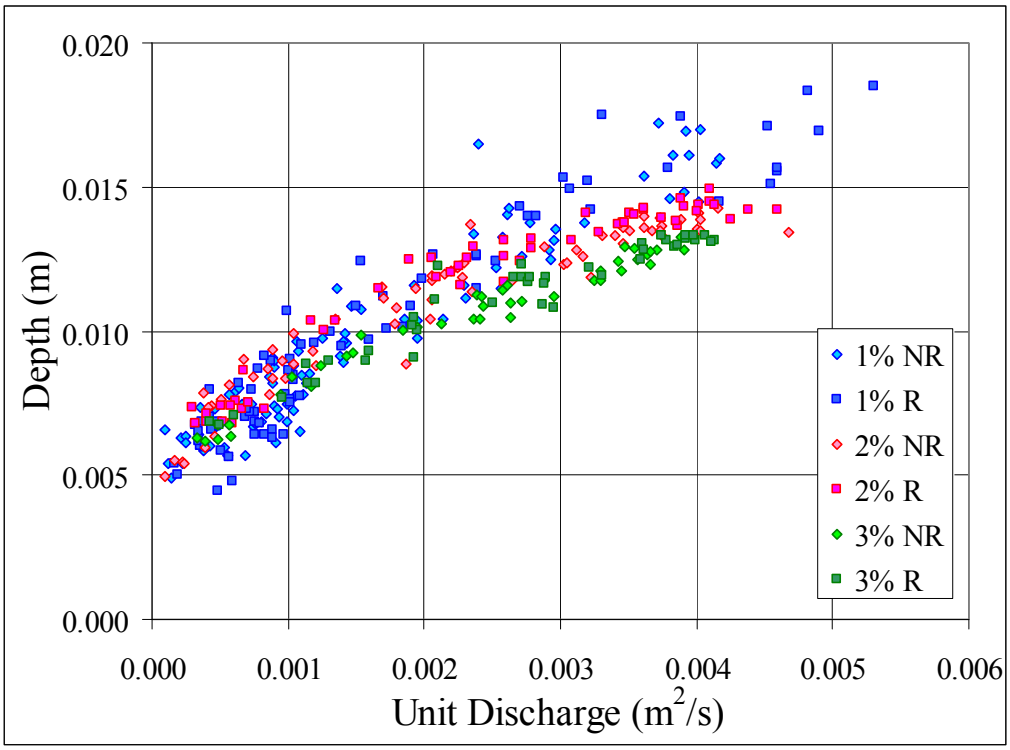

Figure 3.7: Data set for Surface 2

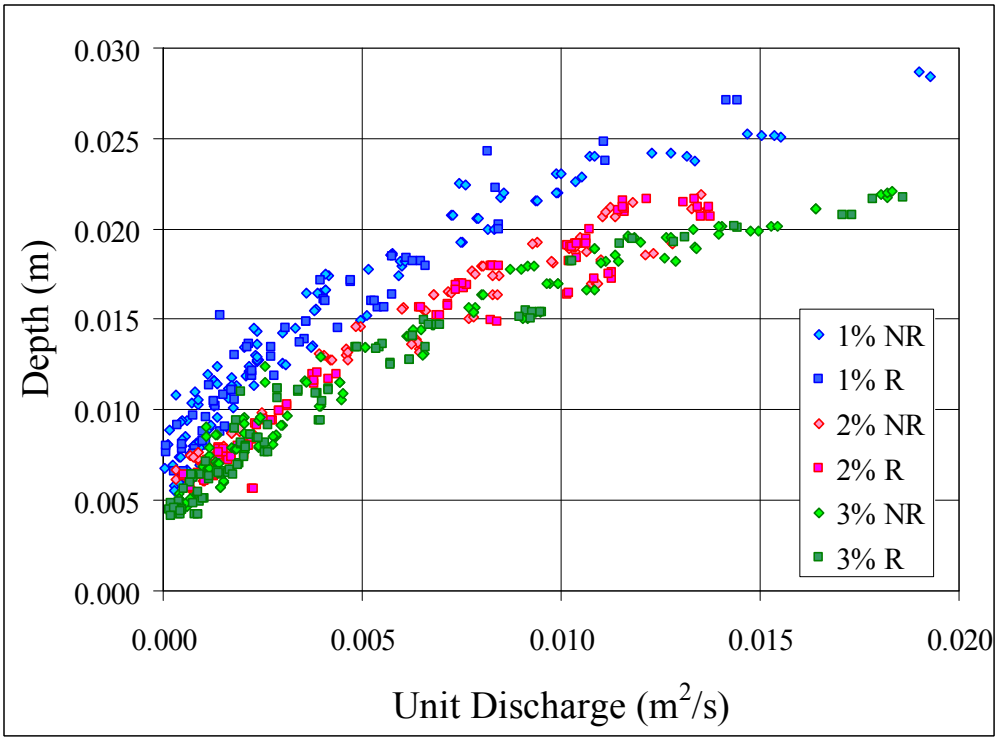

Figure 3.8: Data set for Surface 3

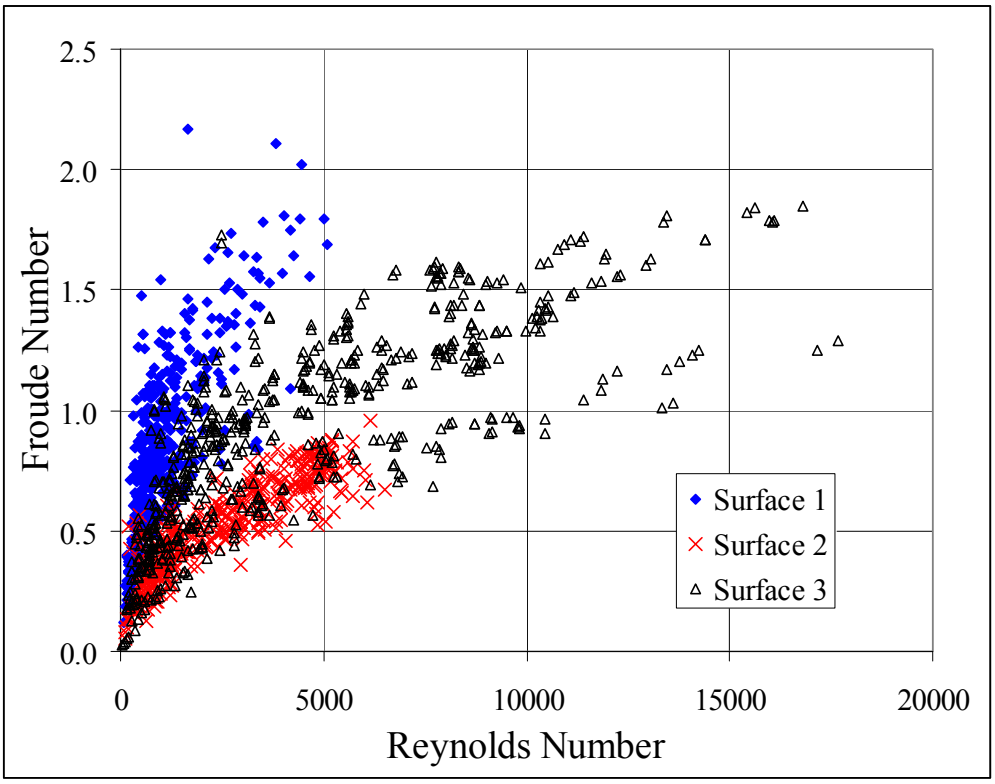

Figure 3.9: Froude number versus Reynolds number for three surface data sets with Surface 1 (diamond), Surface 2 (cross), and Surface 3 (triangle) for all slope and rainfall conditions

Figure 3.10 shows calculated values of Manning's coefficient as a function of Reynolds number. The Manning coefficient is calculated using equation (2.12) based on the total measured flow depth *h*. Use of effective flow depth is discussed later in this chapter. For all surfaces the Manning coefficient value decreases with increasing flow rate and appears to approach an asymptotic value at larger *Re*.

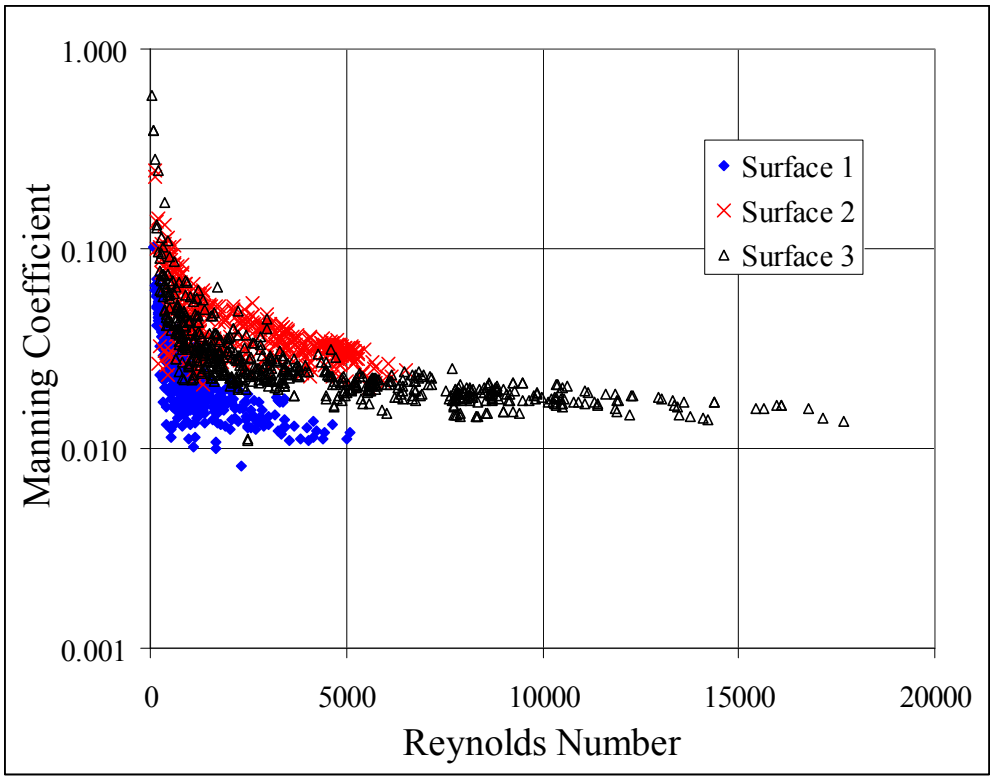

Figure 3.10: Manning coefficient versus Reynolds number for three surface data sets with Surface 1 (diamond), Surface 2 (cross), and Surface 3 (triangle) for all slope and rainfall conditions

With equation (2.4.6) one may calculate the kinematic wave number for each data. The results for the three surfaces are shown in Figure 3.11. The kinematic wave number decreases with increasing flow rate (Reynolds number). For a given *Re*, the values of *K* increase with surface roughness. This parameter is of interest because it provides guidance on whether application of kinematic wave theory is appropriate, and thus whether point measurements of depth and unit discharge can be used to characterize flow behavior under gradually varied flow conditions. Woolhiser and Liggett (1967) suggest that the kinematic wave approximation is not appropriate for $K < 10$ but is good for $K > 20$ and $Fr > 0.5$. Other authors have suggested modification to these limits (see Singh, 1996). For example, Daluz Vieira (1983) suggests that the kinematic wave approximation is appropriate for $KFr^2 > 5$ and $Fr < 2$ (see Figure 2.4). Based on the data range shown in Table 3.1, it would appear that data for Surface 3 is most questionable in terms of application of kinematic wave theory. Further analysis of data for Surface 3 shows that only the 1% slope data is of concern, and that for all of this data, when $Fr < 0.5$, $K > 20$. As a working model it is assumed that point measurements of depth and unit discharge can be used for surface characterization even under conditions of nonuniform flow.

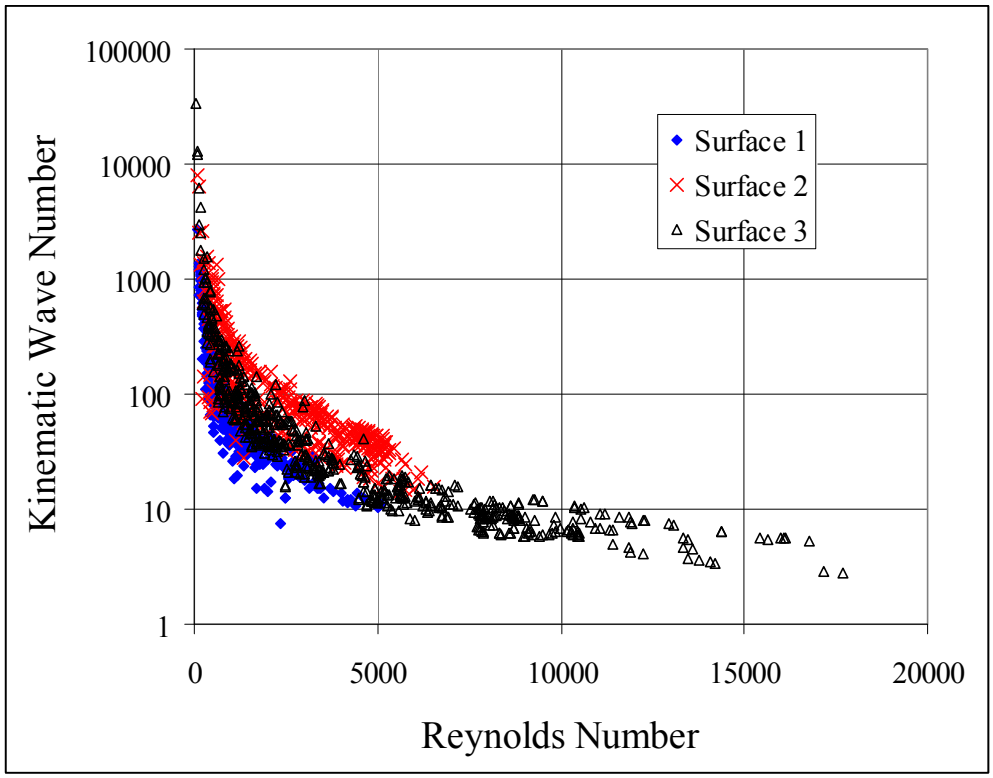

Figure 3.11: Kinematic wave number versus Reynolds number for three surface data sets with Surface 1 (diamond), Surface 2 (cross), and Surface 3 (triangle) for all slope and rainfall conditions

The Manning equation is appropriate for use in open channel flow analysis, including analysis of overland flow, when the flow conditions are fully rough. Equation (2.1.15) provides criteria for assessment of fully rough conditions. This function is plotted as a function of Reynolds number in Figure 3.12. For $Re_* > 70$, $\nu = 10^{-6}$ m^2/s, and h measured in meters, the critical value of $n^6(h\,S_o)^{0.5} = 8(10^{-14})$. Data for Surface 2 and Surface 3 lay above the criteria limit corresponding to shear Reynolds number $Re^* = 70$. However, some of the data for Surface 1 appears to lie in the region corresponding to boundary layer transition where flow resistance should be a function of Reynolds number as well as surface roughness. Use of Manning's equation for data analysis would appear to be most questionable for Surface 1.

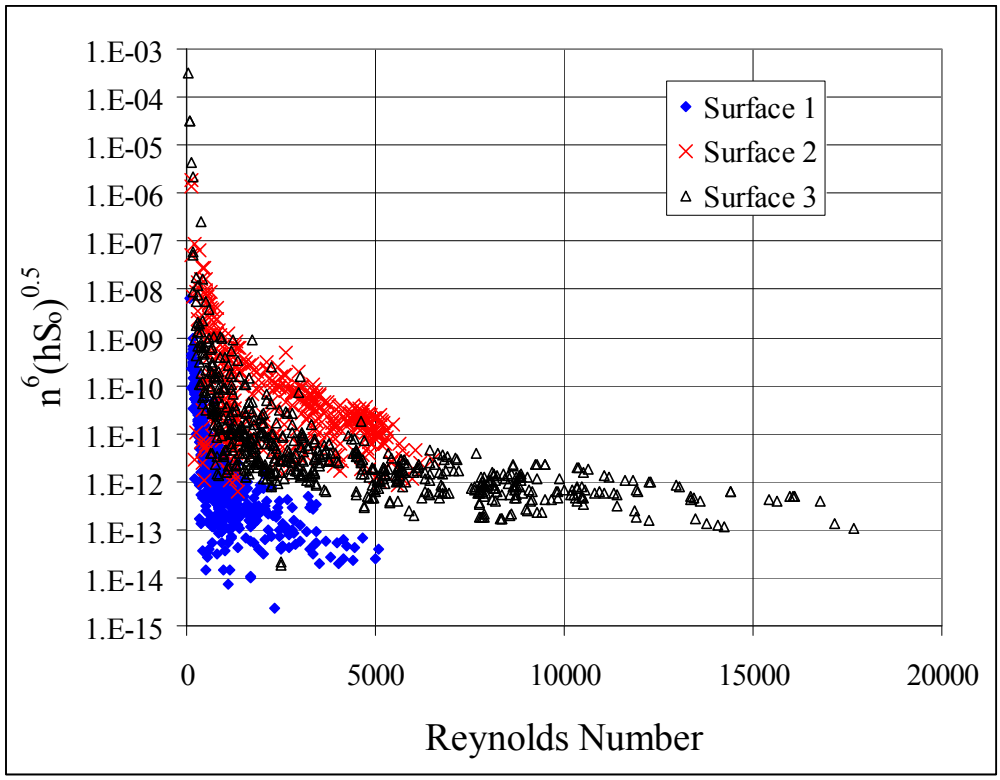

Figure 3.12: Criteria for fully rough flow versus Reynolds number for three surface data sets with Surface 1 (diamond), Surface 2 (cross), and Surface 3 (triangle) for all slope and rainfall conditions.
Note: For $Re_* > 70$, $\nu = 10^{-6}$ m^2/s, and h measured in meters, the critical value of the Henderson roughness parameter is 8E(-14)

3.3 Data Analysis

Analysis of data from sheet flow experiments is presented in three steps. First, theory of a logarithmic boundary layer (LBL) on a rough surface is applied to relate flow depth and unit discharge, and to characterize the roughness of each surface. Next, analyses based on Manning's equation are applied to develop model equations that are easier to use in numerical simulation of sheet flow on rough surfaces. Finally, results from statistical analysis of the data are presented to characterize the effects of rainfall.

3.3.1 Logarithmic Boundary Layer for a Rough Surface

Theory for the logarithmic boundary layer (LBL) near a rough surface is based primarily on the theoretical work of Prandtl and Karman and the experimental results presented by Nikuradse (Schlichting, 1968; Monin and Yaglom, 1971; Yalin, 1977). The velocity distribution is shown schematically in Figure 3.13. In this figure h = flow depth measured from a base datum and z = elevation above this same datum. The parameter k = roughness height. The form of the logarithmic velocity law for a rough surface is written

$$\frac{u(z)}{u_*} = \frac{1}{\chi}\ln\left(\frac{z}{k}\right) + B = \frac{1}{\chi}\ln\left(\frac{z}{z_1}\right) \tag{3.3.1}$$

In equation (3.3.1) u_* = shear velocity (defined shortly), χ = von Karman constant (χ = 0.40) and $z_1 = k\, e^{-\chi B}$. The parameter B is generally a function of Reynolds number. Einstein and El-Samni (1949) have shown that for a rough surface, a surface datum must be selected for the velocity distribution to be logarithmic. This surface datum is designated z_0 in Figure 3.13. Thus the effective depth y is defined as

$$y = h - z_0 \tag{3.3.2}$$

The second parameter z_1 is also related to surface roughness (Monin and Yaglom, 1971, pg. 287). The parameter z_1 may be interpreted as the depth (measured from z_0) at which the extrapolated logarithmic velocity distribution reaches zero velocity. With these parameters the velocity distribution takes the form

$$u(z) = \frac{u_*}{\chi}\ln\left(\frac{z - z_0}{z_1}\right) \tag{3.3.3}$$

Equation (3.3.3) may be integrated from $z = z_1 + z_0$ (where $u(z) = 0$) to $z = h = y + z_0$ to give

$$q = \frac{u_*}{\chi}\left(y\ln\left(\frac{y}{z_1}\right) - y + z_1\right) \tag{3.3.4}$$

In general, $z_1 << y$, equation (9) can be written as follows.

$$q = \frac{u_* y}{\chi}\left(\ln\left(\frac{y}{z_1}\right) - 1\right) \tag{3.3.5}$$

$$\frac{V}{u_*} = \frac{1}{\chi}\left(\ln\left(\frac{y}{z_1}\right) - 1\right) \tag{3.3.6}$$

In equation (3.3.6), which was presented by Keulegan (1938), V = depth-average velocity = q/y.

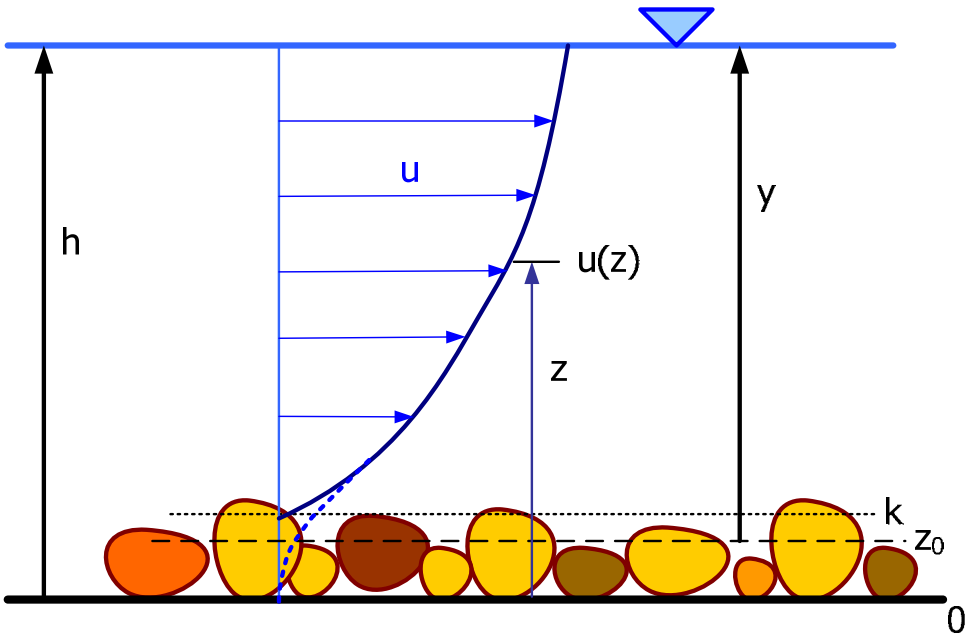

Figure 3.13: Schematic view of the logarithmic velocity distribution on a rough surface

Discussion of Parameters

The shear velocity is used to characterize the wall shear stress. For open channel flow the shear velocity is (Keulegan, 1938; Henderson, 1967; Sturm, 2001)

$$u_* = \sqrt{gS_f R_h} \qquad (3.3.7)$$

In equation (3.3.7) S_f = hydraulic gradient and R_h = hydraulic radius. For sheet flow on a plane surface the hydraulic radius is the same as the effective flow depth, y, and it is assumed that the surface slope is the same as the hydraulic gradient; these allow equation (3.3.7) to be represented as follows:

$$u_* = \sqrt{gS_o y} \qquad (3.3.8)$$

Based on Nikuradse's data, as long as the friction or shear Reynolds number, $Re_* = u_* k/\nu > 70$, $B = 8.5$. When $Re_* < 70$, $B(Re_*)$ is a function of the shear Reynolds number as shown in Figure 3.14 from Yalin (1977) with change in notation. For the range $14.1 < Re_* < 70$, Prandtl and Schlichting (in Goldstein, 1938, pg. 381) suggest

$$B = 11.50 - 1.62\log_{10}\left(\frac{u_* k}{\nu}\right) \quad ; \quad 14.1 < \frac{u_* k}{\nu} < 70 \qquad (3.3.9)$$

Equation (3.3.9) is used with the data for Surface 1. For most of the experimental data on Surface 2 and Surface 3, $Re_* > 70$ ("completely rough" conditions) and $B = 8.5$. None of the data corresponds to the hydraulically "smooth" region ($Re_* < 5$). Other investigators (see Schlichting, 1968; Hinze, 1975; Yalin, 1977) have shown that parameter curves such as shown in Figure 3.14 depend on the type of surface roughness (this figure corresponds to uniform and sand-grain roughness). While the general pattern of the curve is expected to remain consistent, the level (B-values) will vary with different types of surface roughness.

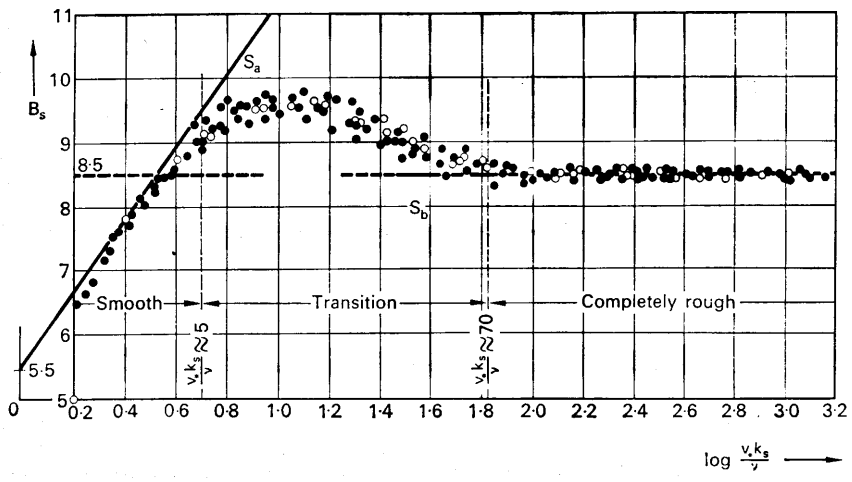

Figure 3.14: Parameter B as a function of shear Reynolds number $Re_* = u_* k/\nu$ (from Yalin, 1977)

Equation (3.3.5) has two parameters related to surface roughness, k and z_0. However, the relationship between these parameters is not clear. Estimation of z_0 has been discussed by Einstein and El Samni (1949), Monin and Yaglom (1971), Bayazit (1976), and Chien and Wan (1999). Einstein and El Samni suggest that the displacement distance z_0 is located a distance 0.2 k below a plane parallel to the top of the roughness elements. Other authors suggest values ranging from 0.15 k to 0.35 k (see Bavazit, 1976). To help fix these parameter values the following assumptions are made:

$$k = z_0 + z_1 \tag{3.3.10}$$

$$z_0 = k\left(1 - e^{-\chi B}\right) \tag{3.3.11}$$

$$z_1 = k\, e^{-\chi B} \tag{3.3.12}$$

With these parameters, equation (3.3.5) can be written

$$q(h) = \frac{\sqrt{gS_o}}{\chi}\left(h - k\left(1 - e^{-\chi B}\right)\right)^{3/2}\left(\ln\left(\frac{\left(h - k\left(1 - e^{-\chi B}\right)\right)}{k\, e^{-\chi B}}\right) - 1\right) \tag{3.3.13}$$

Two approximate forms of equation (3.3.13) are used in analysis of experiment data. A one-parameter version of the model is derived by assuming equivalent sand-grain roughness and completely rough conditions. For fully rough flow ($Re_* > 70$, $B = 8.5$, $e^{-\chi B} = 1/30$), equation (3.3.13) takes the following approximate form.

$$q(h) = \frac{\sqrt{gS_o}}{\chi}(h - k)^{3/2}\left(\ln\left(\frac{30(h - k)}{k}\right) - 1\right) \tag{3.3.14}$$

In equation (3.3.14), the roughness height k is the only parameter. A second, somewhat more general form for a model equation allows the parameter B as a variable for each surface (similar to k). The corresponding model takes the approximate form

$$q(h) = \frac{\sqrt{gS_o}}{\chi}(h - k)^{3/2}\left(\ln\left(\frac{e^{\chi B}(h - k)}{k}\right) - 1\right) \tag{3.3.15}$$

The physical interpretation of this two-parameter (k and B) model is that effective flow depth is measured from the top of the roughness element height ($z = k$) and that the extrapolated logarithmic velocity distribution has zero velocity at an elevation $z = k\,(1 + e^{1-\chi B})$.

Model Calibration

The model equations (3.3.14) and (3.3.15) are calibrated against the experiment data for each surface by selecting the parameter k (and B), which minimizes the standard error of prediction. Either depth or unit discharge could be used as the regression variable. For this investigation, use of flow depth as the regression variable is considered appropriate. In model application the unit discharge is determined by roadway geometry and rainfall intensity, and one is interested in predicting the flow depth corresponding to an estimated discharge value. The standard error is defined by

$$SE = \sqrt{\frac{1}{(N-p)}\sum_{i=1}^{N}\left(h_{data} - h_{model}\right)^2} \qquad (3.3.16)$$

In equation (3.3.16) N = number of data in each set and p = number of model parameters. The difficulty with applying equation (3.3.16) is that either equation (3.3.14) or (3.3.15) must be inverted to find h_{model} from measured q_{data}. This is done iteratively using

$$\left(h_{j+1} - k\right) = \left(\left(\frac{\chi\, q_{data}}{\sqrt{g\, S_o}}\right) \Big/ \left(\ln\left(\frac{e^{\chi B}\left(h_j - k\right)}{k}\right) - 1\right)\right)^{2/3} \qquad (3.3.17)$$

Equation (3.3.17) is found to converge rapidly starting for $j = 0$ with $h_j = (5/3)\,k$. The regression results are summarized in Table 3.2.

Table 3.2: Summary Results from Model Equations (3.3.14) and (3.1.15) Calibration

Surface	1-Parameter Model (B = 8.5)		2-Parameter Model		
	k (mm)	SE (mm)	k (mm)	B	SE (mm)
1	1.0	0.68	1.6	12.9	0.62
2	3.5	1.04	3.0	7.2	1.03
3	2.5	1.36	3.3	10.5	1.32

While the relative magnitudes of the calculated values of the parameter k are consistent with expectations, it is difficult to draw quantitative conclusions relating k and surface roughness texture. For Surface 1 the magnitude of k for the 1-parameter and 2-parameter models is approximately equal to the d_{35} and d_{75} values, respectively, as shown in Figure 3.3. For Surface 2 the corresponding magnitudes are approximately d_{60} and d_{30}. There is no data to directly assess the roughness size for Surface 3 because the granular material is a combination of Surfaces 1 and 2, along with additional resin. The calculated magnitudes of k are somewhat larger than the measured Mean Texture Depth for this surface (2.2 mm). The larger SE values for Surface 3 are expected as the range in unit discharge and flow depth is much larger for this surface. The overall decrease in SE in going from use of a 1-parameter model to a 2-parameter model is small,

and the relative changes suggest that the parameters k and B are positively correlated (k increases or decreases as B with little change in SE).

Figures 3.15, 3.16, and 3.17 compare the measured data with the model equation (3.3.15) predictions with parameter values shown in Table 3.2. The general fit for all surfaces is considered sufficiently adequate to suggest that the measured data sets provide data that is consistent with rough surface logarithmic boundary layer theory. Examination of regression residual errors is discussed following consideration of Manning's equation.

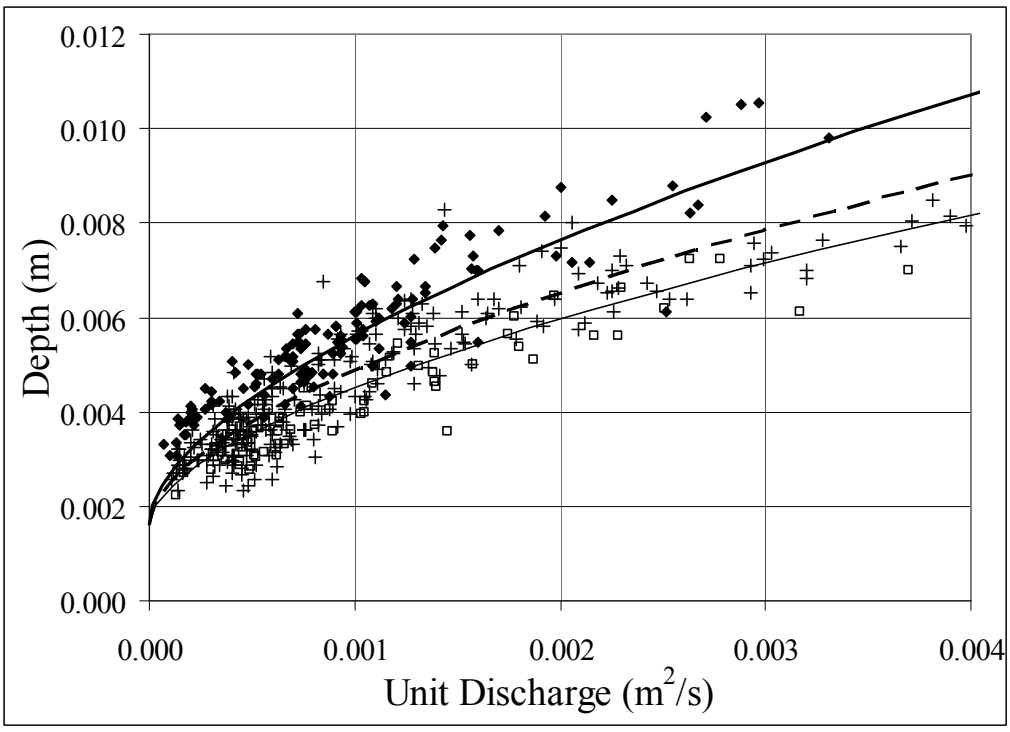

Figure 3.15: Comparison of experiment data and model formulation for Surface 1. 1% slope (diamond, heavy solid line), 2% slope (plus, dashed line), 3% slope (box, light solid line)

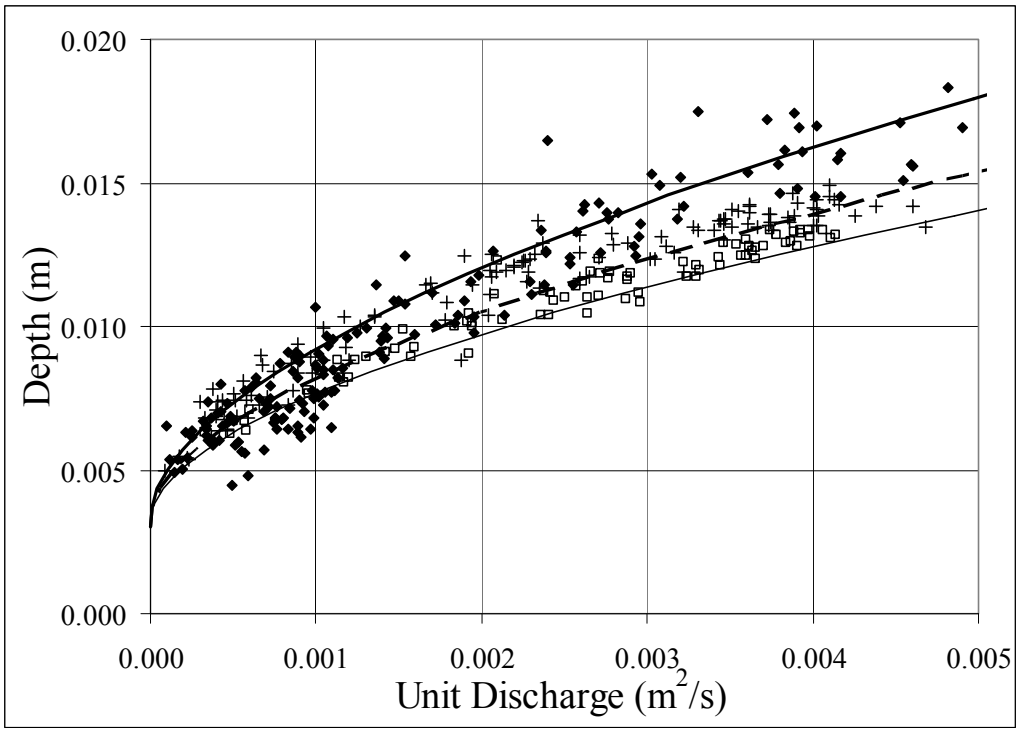

Figure 3.16: Comparison of experiment data and model formulation for Surface 2. 1% slope (diamond, heavy solid line), 2% slope (plus, dashed line), 3% slope (box, light solid line)

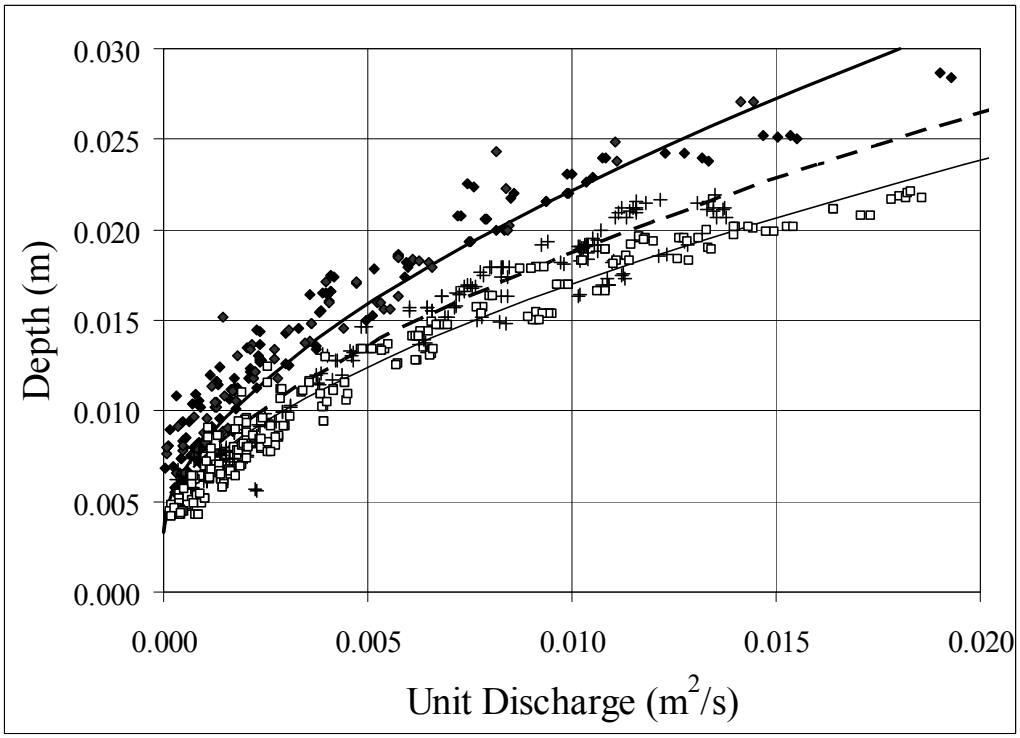

Figure 3.17: Comparison of experiment data and model formulation for Surface 3. 1% slope (diamond, heavy solid line), 2% slope (plus, dashed line), 3% slope (box, light solid line)

Model equations (3.3.14) and (3.3.15) appear to be useful for predicting the relationship of unit discharge to flow depth. The parameter k is directly related to surface roughness while the parameter B characterizes effective location of the boundary layer relative to the roughness element height. However, for some applications, the model form is too complex. In particular, function inversion is difficult; as noted earlier, evaluation of $h = f(q)$ requires numerical solution. Furthermore, applications towards roadway drainage must consider gutter flow in addition to sheet flow, and flow in roadway gutters is usually modeled using Manning's equation. Because of these issues, the same data set is evaluated using Manning's equation.

3.3.2 Manning's Equation

Manning's equation may also be used in the data analysis. For this purpose the Manning equation is written in the form of a linear regression model:

$$h = z_0 + c_1\left(\frac{q}{\sqrt{S_o}}\right)^{0.6} + e \qquad (3.3.18)$$

The intercept parameters z_0 corresponds to the "hydraulically effective bottom" elevation considered by Robertson et al. (1966), the slope parameter c_1 is related to the Manning coefficient, and e = regression error. The relationship between the slope term and Manning coefficient is

$$n = (c_1)^{5/3} \qquad (3.3.19)$$

Using equation (3.3.18) as Manning's equation requires the assumption that the Manning coefficient is constant. With the linear regression model, parameter confidence intervals can also be estimated. This allows different subsets of the data to be evaluated and parameter values compared statistically.

Figure 3.18 shows the data for all three surfaces plotted in the form suggested by equation (3.3.18). The intercept is much smaller for Surface 1 while it is approximately the same for Surface 2 and Surface 3. The slope increases in order from Surface 1 to Surface 3 to Surface 2, with the slope being directly related to the magnitude of the Manning Coefficient. Table 3.3 shows regression results from Manning's equation for the cases where the entire data set is combined for each surface. The resulting z_0 parameter values are generally larger but comparable to those presented in Table 3.2 for the roughness parameter k. The Manning coefficient values calculated from equation (3.3.19) are also shown in the table. Model-data comparison graphs for Manning's equation look essentially the same as Figures 3.15 – 3.17. There is no significant difference in the capabilities of the two different model equations (logarithmic boundary layer theory and Manning's equation) to represent the measured data. The standard error values are the same. The overall comparison between the two model formulations and for all three surfaces gives an average result that $z_0 = 1.16\ k$. For Manning's equation, z_0 is the depth at which significant sheet flow commences. For comparison, with the logarithmic boundary layer model (equation 3.3.14), sheet flow commences when $h > (1 + e/30)k \sim 1.091\ k$.

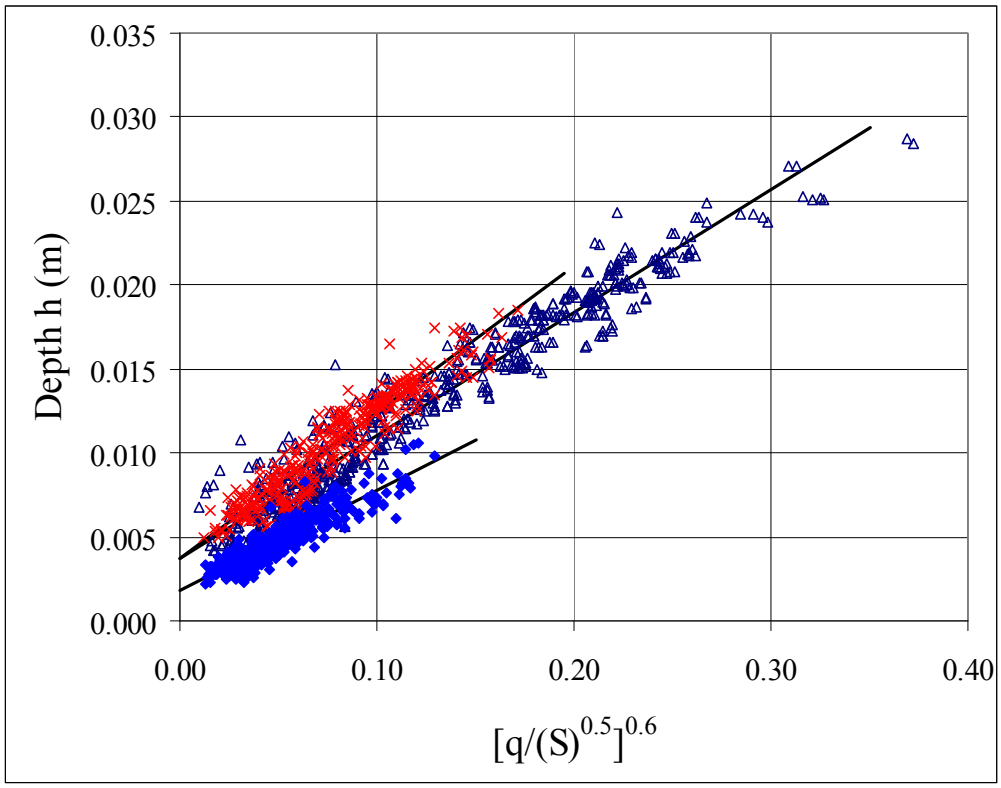

Figure 3.18: Experiment data plotted in form suggested by Manning's equation for linear regression (h-Regression using equation 3.3.18). Surface 1 (diamond), Surface 2 (cross), Surface 3 (triangle)

Table 3.3: Summary Results from Regression Analysis for Surfaces 1, 2, and 3 Using Manning's Equation

Surface	z_0 (mm)	n	SE (mm)
1	1.82	0.0091	0.62
2	3.73	0.0170	1.03
3	3.70	0.0129	1.32

Discussion

For use of the Manning equation there is an implicit assumption that the Manning coefficient is constant. With measured h and q, Manning coefficient values are calculated using

$$n = \frac{(h - z_0)^{5/3}\sqrt{S_o}}{q} \qquad (3.3.20)$$

Graphs of Manning coefficient versus Reynolds number are shown in Figures 3.19 to 3.21, where the regression values of z_0 from Table 3.3 have been used. There is very large variability for small Re, but there is no apparent trend in n versus Re. This is confirmed by regression analysis, except for Surface 1, which shows a trend of slightly decreasing n with increasing Re

within the range of data considered. Overall, the assumption of constant 'average' Manning coefficient is confirmed. If one averages the calculated values of the Manning coefficient for each surface, one finds $n = 0.0094$ for Surface 1, $n = 0.0177$ for Surface 2, and $n = 0.0138$ for Surface 3. For all cases the values are larger than found from regression. This is associated with the very large values calculated at small *Re*.

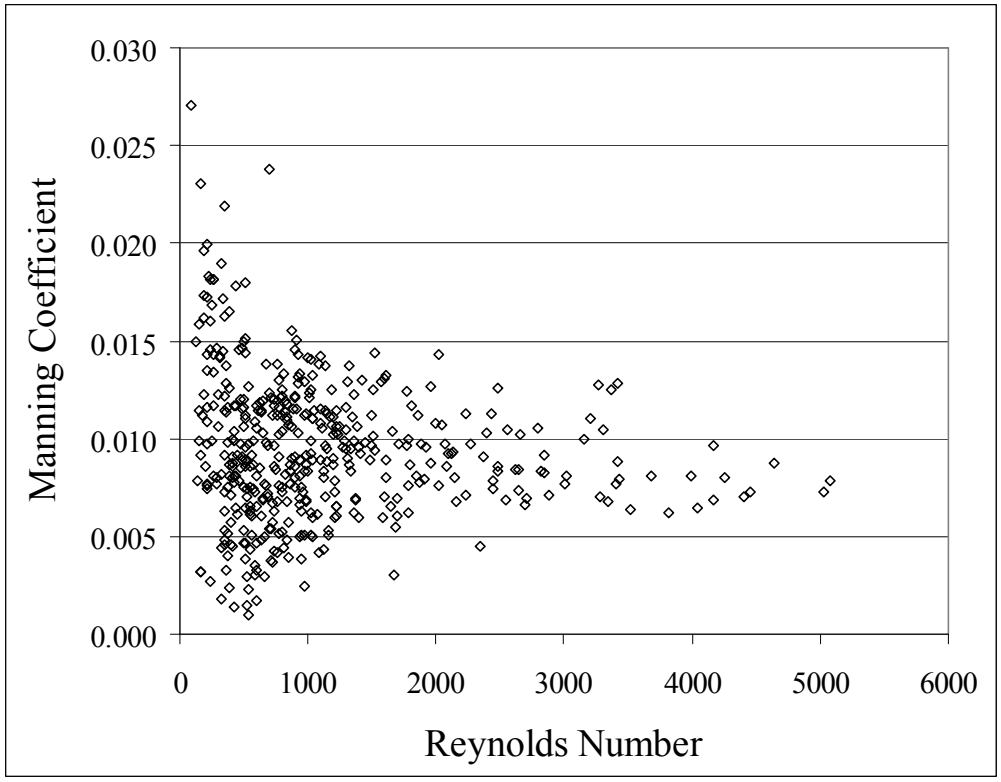

Figure 3.19: Manning coefficient as a function of Reynolds number for Surface 1

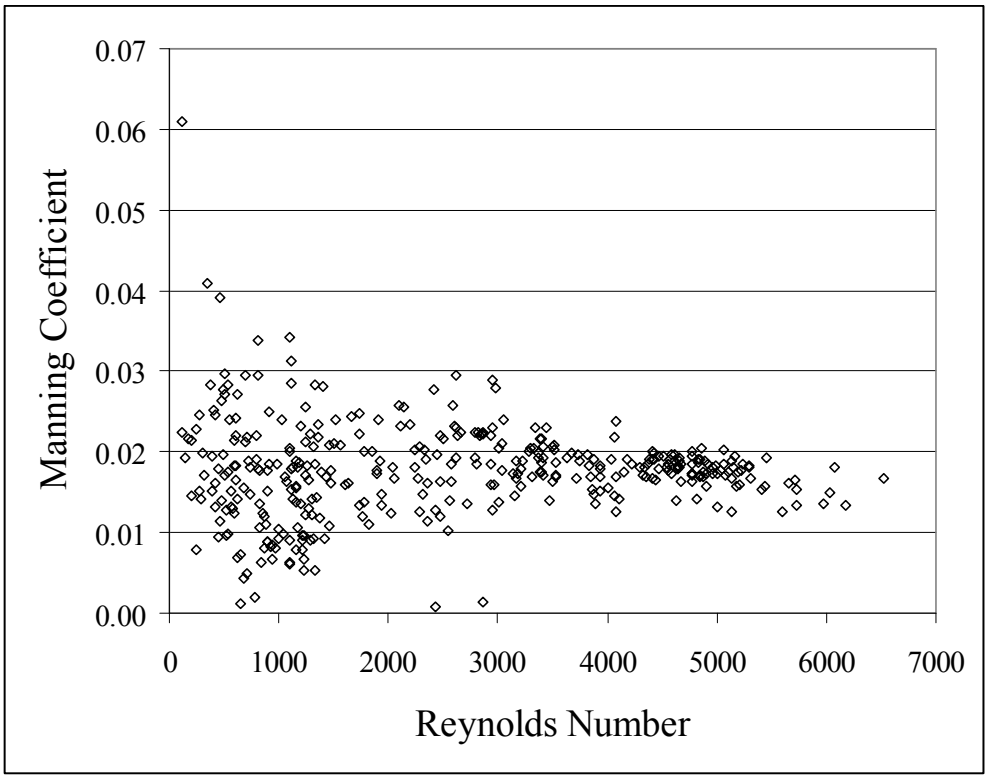

Figure 3.20: Manning coefficient as a function of Reynolds number for Surface 2

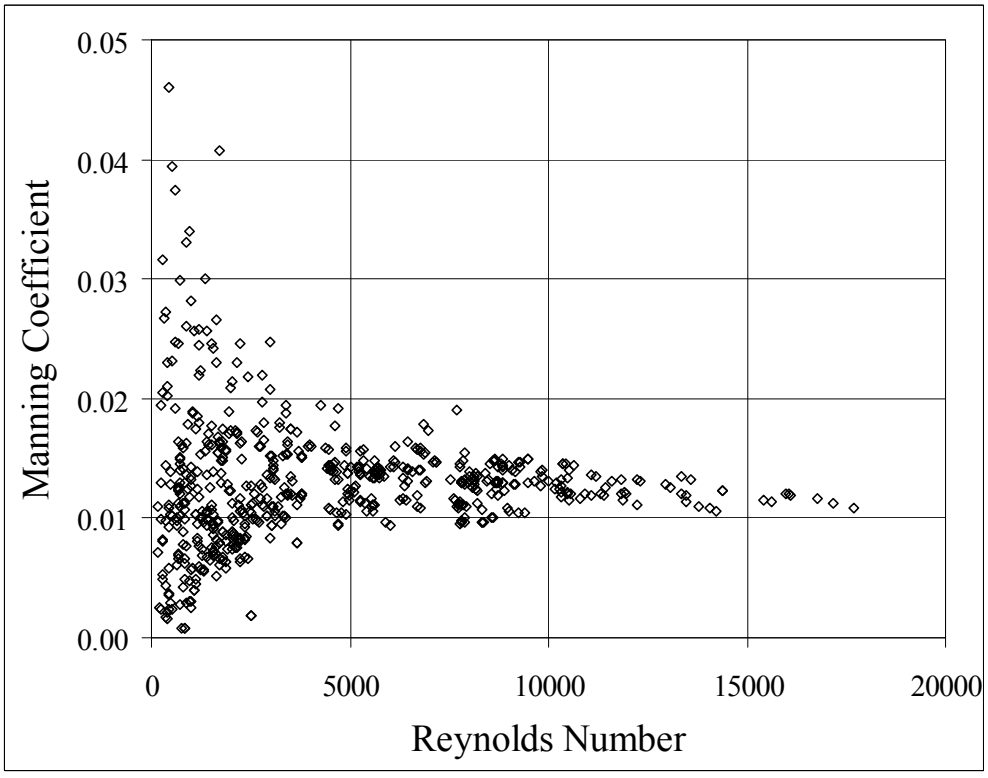

Figure 3.21: Manning coefficient as a function of Reynolds number for Surface 3 (extreme high values at very low Re are not shown within the abscissa range)

3.3.3 Examination of Regression Residual-Error Values

There are a number of ways to evaluate results from regression models. The model parameters k and z_0 are consistent in magnitudes in Tables 3.2 and 3.3, and they are consistent with expectations based on the material grain size used to establish surface roughness. In addition, the *SE* values are fairly small for all models. A useful test is to examine whether the residual errors ($e = h_{data} - h_{model}$) are correlated with variable magnitude. This may be evaluated visually from Figures 3.15-3.17 for the LBL model; the magnitude of e is the vertical distance between the model curve and data. Throughout the range of data there is no apparent bias.

For comparison purposes it is useful to show the residual regression error in a normalized fashion as the ratio of the residual error to the standard error: e/SE. This allows one to use Chauvenet's criterion (Taylor, 1982) to identify possible outliers. According to this criterion, individual data are considered outliers if the normalized error e/s (where s is the standard deviation of the error measurements – the standard error) exceeds a certain magnitude determined by the number of data in the set. If u is a unit variate and $\eta(u)$ the standard normal distribution function, then an individual value is a suspected outlier if it falls outside of the range

$$\left|\frac{e}{SE}\right| < u^C = -\eta^{-1}\left(\frac{1}{4N}\right) \qquad (3.3.21)$$

In equation (3.3.21) $\eta^{-1}(\ )$ is the inverse standard unit normal function [the Excel function NORMSINV( ) may be used for this evaluation] and N is the number of data in the set. For the three surfaces the critical Chauvenet values are u^C = 3.26, 3.21, and 3.35, respectively, based on the number of data within each set. The normal residual data and Chauvenet criteria values for the three surfaces are shown in Figures 3.22 – 3.24. The normal residual error data for both the LBL model and Manning equation model are shown.

In reviewing Figures 3.22 to 3.24, both identification of possible outliers and trends are of interest. The number of potential outliers for Surface 1, Surface 2, and Surface 3 are 3, 1, and 2, respectively. With regard to trends, Surfaces 1 and 3 have consistently negative residuals for larger flow rates (*Re*). The calibrated model equations appear to over-predict the flow depth at larger flow rates for these surfaces. However, the residual plots show no strong bias and do not suggest concern with the regression models and parameters.

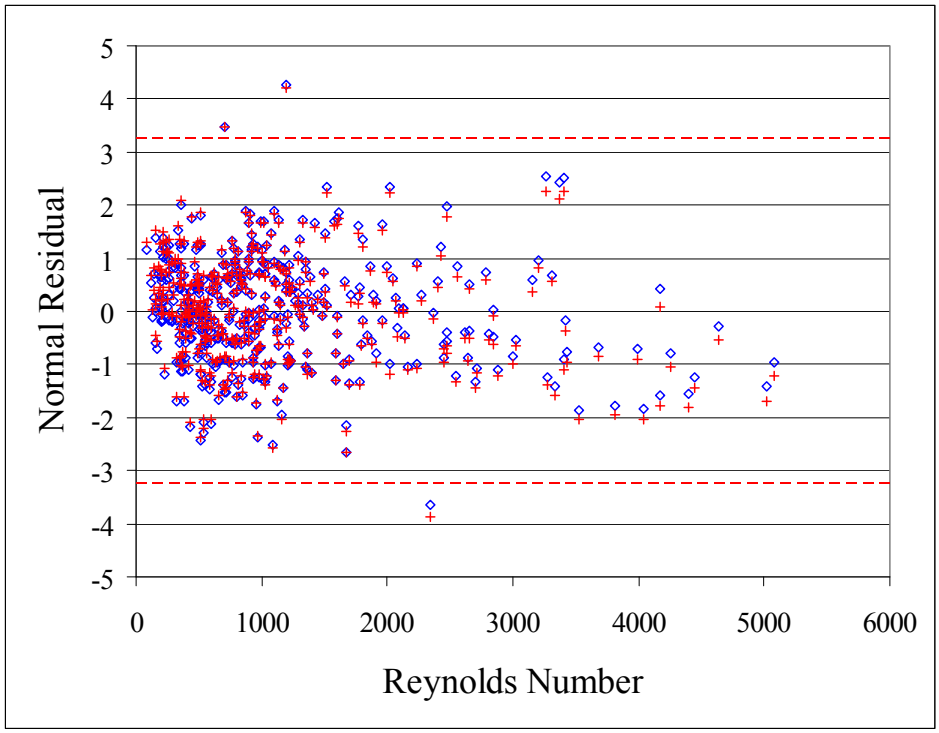

Figure 3.22: Normal residual error as a function of flow rate for Surface 1. LBL model (diamond) and Manning equation model (plus). Chauvenet criterion $u^C = 3.26$

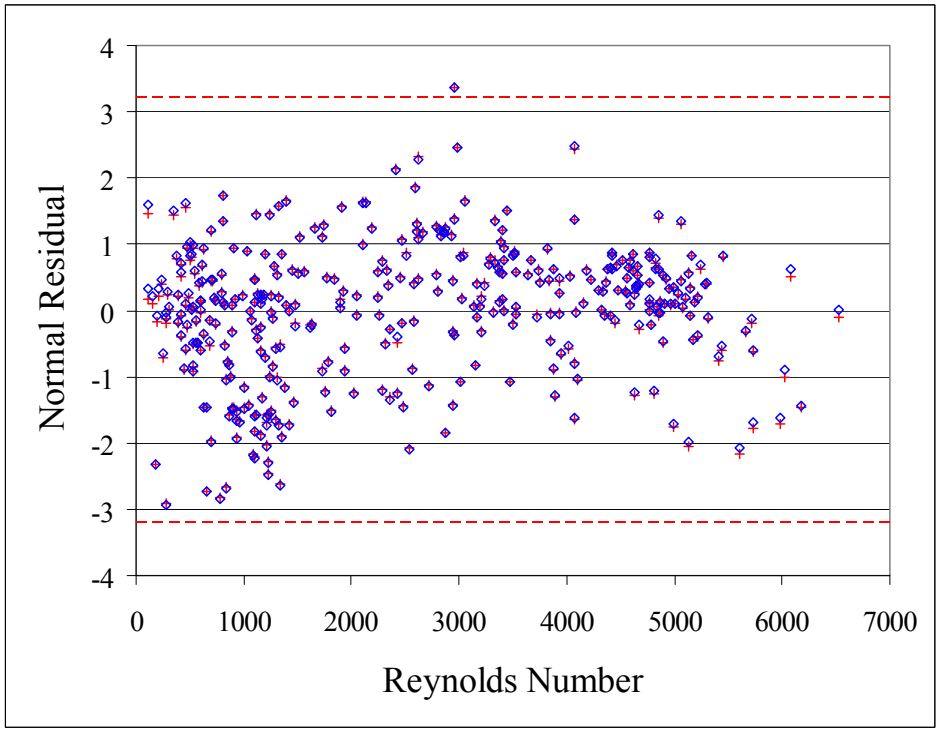

Figure 3.23: Normal residual error as a function of flow rate for Surface 2. LBL model (diamond) and Manning equation model (plus). Chauvenet criterion $u^C = 3.21$

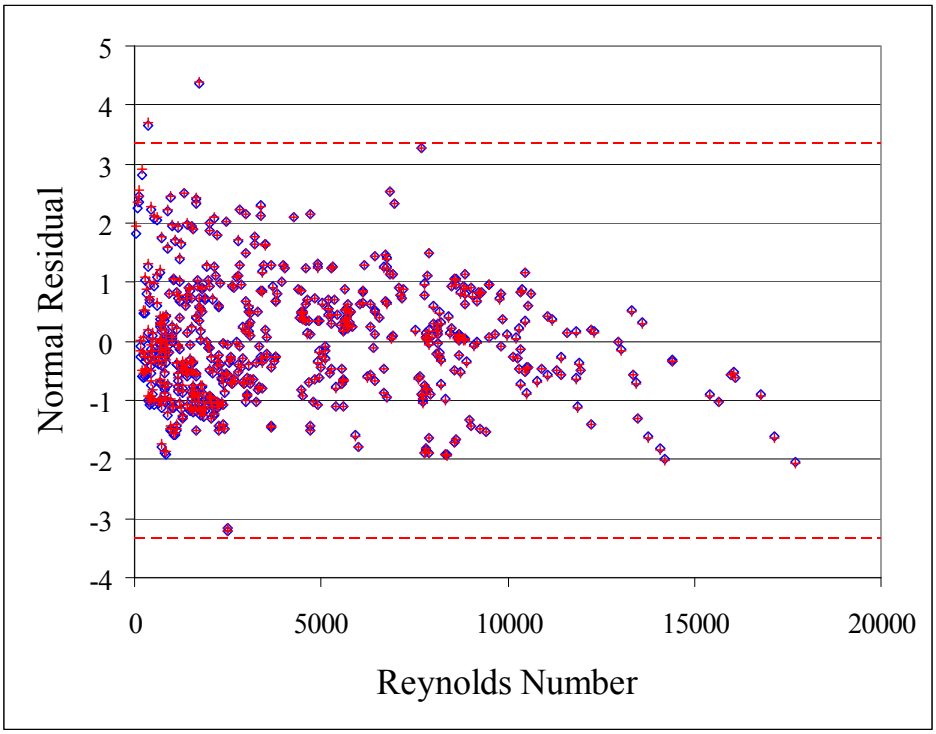

Figure 3.24: Normal residual error as a function of flow rate for Surface 3. LBL model (diamond) and Manning equation model (plus). Chauvenet criterion $u^C = 3.35$

3.3.4 Hydraulic Effects of Rainfall over Rough Surfaces

As noted in Chapter 2, other investigators have shown that rainfall increases runoff hydraulic resistance when applied over smooth surfaces. The situation for rough surfaces is less clear. For the present research this issue is addressed by comparing regression results from analysis of data sets with and without rainfall. The linear regression model with Manning's equation (equation 3.3.18) is used. Data sets with only the rainfall simulator and with the rainfall simulator plus head box are combined. Separate analyses have shown no statistical difference between these data sets (which are limited to low *Re* because of the capacity limitations of the rainfall simulator). Results from statistical analysis of these data are shown in Table 3.4. Rainfall impacts are assessed by comparing the parameter range of 95-percent confidence intervals for the *NR* and *R* conditions. As shown in this table, the CI range overlaps for z_0 and c_1 for both Surface 1 (most smooth) and Surface 2 (most rough). On this basis one cannot statistically distinguish the effects of rainfall on model parameter values. Both Surface 1 and Surface 2 show an increase in z_0 values with rainfall. However, the Manning coefficient (as reflected by c_1) decreases with rainfall for Surface 1 but increases with rainfall for Surface 2. The situation is quite different for Surface 3 (intermediate roughness), which shows a large decrease in z_0 with rainfall and large increase in Manning coefficient (c_1). At the 95-percent confidence range, these differences are significant. To highlight the difference, the data for *NR* and *R* are shown in Figure 3.25 along with their corresponding trend lines. There is no difference between the data sets within the intermediate range. The overall conclusion from this comparison is that the effects of rainfall are small compared with other factors and can be excluded in model applications.

Table 3.4: Summary Results from Regression Analysis for Surfaces 1, 2, and 3 Using Model Equation (3.3.18) under No Rainfall (*NR*) and Rainfall (*R*) conditions.

Surface	z_0 (m)	c_1	R^2	*SE* (m)	95% *CI* (z_0)		95% *CI* (c_1)	
1-*NR*	0.00170	0.0636	0.839	0.00061	0.00148	0.00193	0.0595	0.0677
1-*R*	0.00187	0.0576	0.842	0.00061	0.00170	0.00204	0.0545	0.0607
2-*NR*	0.00385	0.0844	0.882	0.00101	0.00349	0.00420	0.0801	0.0887
2-*R*	0.00362	0.0890	0.893	0.00106	0.00322	0.00403	0.0844	0.0937
3-*NR*	0.00422	0.0709	0.945	0.00130	0.00394	0.00450	0.0690	0.0727
3-*R*	0.00309	0.0766	0.945	0.00127	0.00279	0.00340	0.0744	0.0788

Note: R2 = R-squared Statistic; SE = Standard Error; CI = Confidence Interval

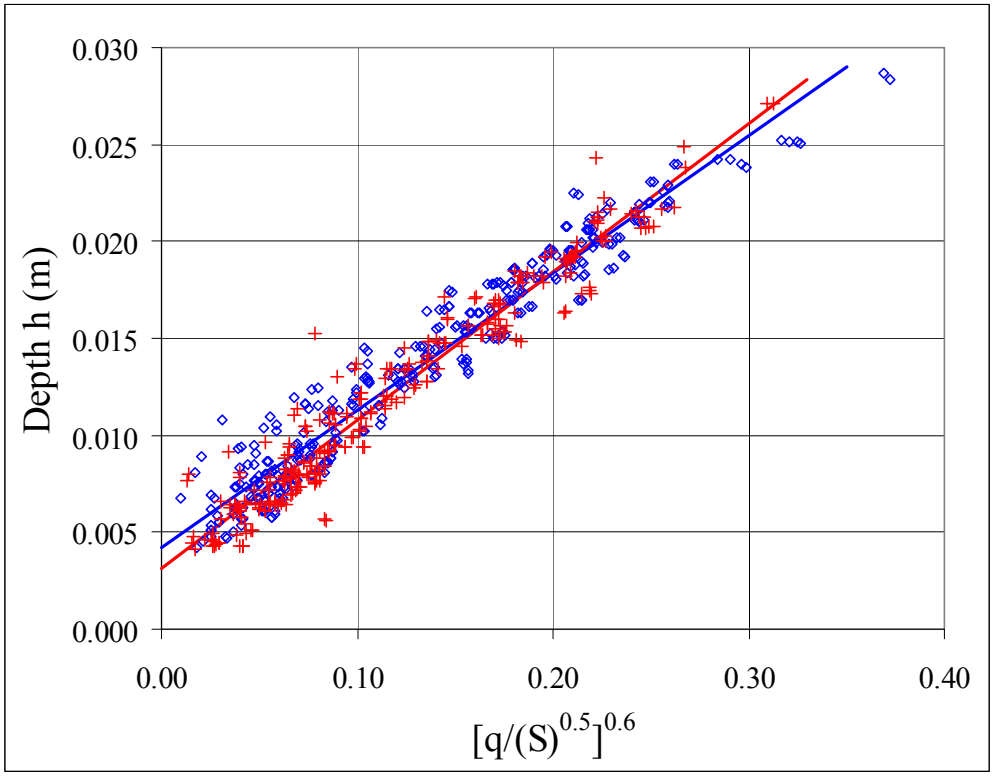

Figure 3.25: Surface 3 data for NR (diamond) and R (plus) conditions with corresponding trend lines

3.3.5 Discussion

Both models (LBL and Manning) discussed in this chapter are able to represent the essential characteristics of the measured data sets for sheet flow over rough surfaces. The

logarithmic boundary layer model has a strong foundation in fluid mechanics, while the model based on Manning's equation is easier to apply. Comparison of the model curves for the three surfaces are shown in Figures 3.26 to 3.28 for slope values 1, 2, and 3 percent. Parameter values are presented in Tables 3.2 and 3.3. The largest difference between the models is shown for Surface 1. In particular, the 1-Parameter LBL model predicts a larger flow depth for given unit discharge, except for very low discharge values. For the three surfaces, there is essentially no difference between these model curves for the 2-Parameter LBL and Manning equation models. From this physical modeling research it can be confirmed that sheet flow over rough surfaces behaves in accordance with logarithmic boundary layer theory. Roughness parameter values correspond to physical measurements in terms of size of roughness elements. There is little difference between model results using LBL theory and Manning's equation. Finally, the Manning coefficient may be treated as a constant determined by surface roughness and independent of rainfall rate.

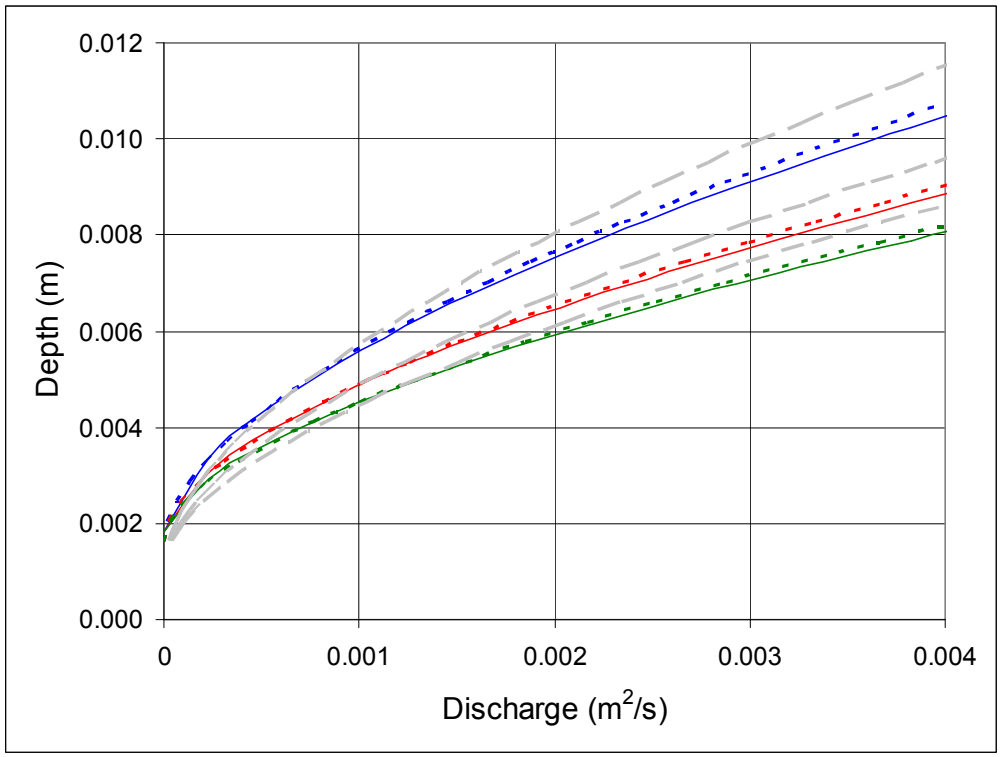

Figure 3.26: Comparison of Manning (solid), LBL 2-Parameter (dotted), and LBL 1-Parameter (light-dashed) models for Surface 1

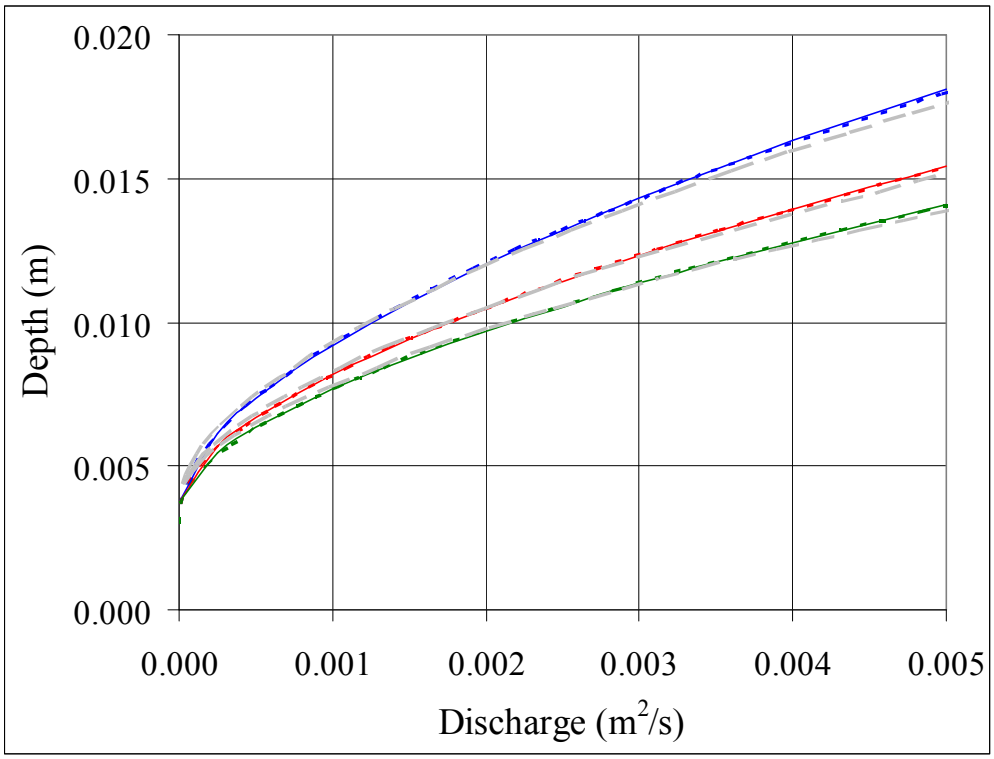

Figure 3.27: Comparison of Manning (solid), LBL 2-Parameter (dotted), and LBL 1-Parameter (light-dashed) models for Surface 2

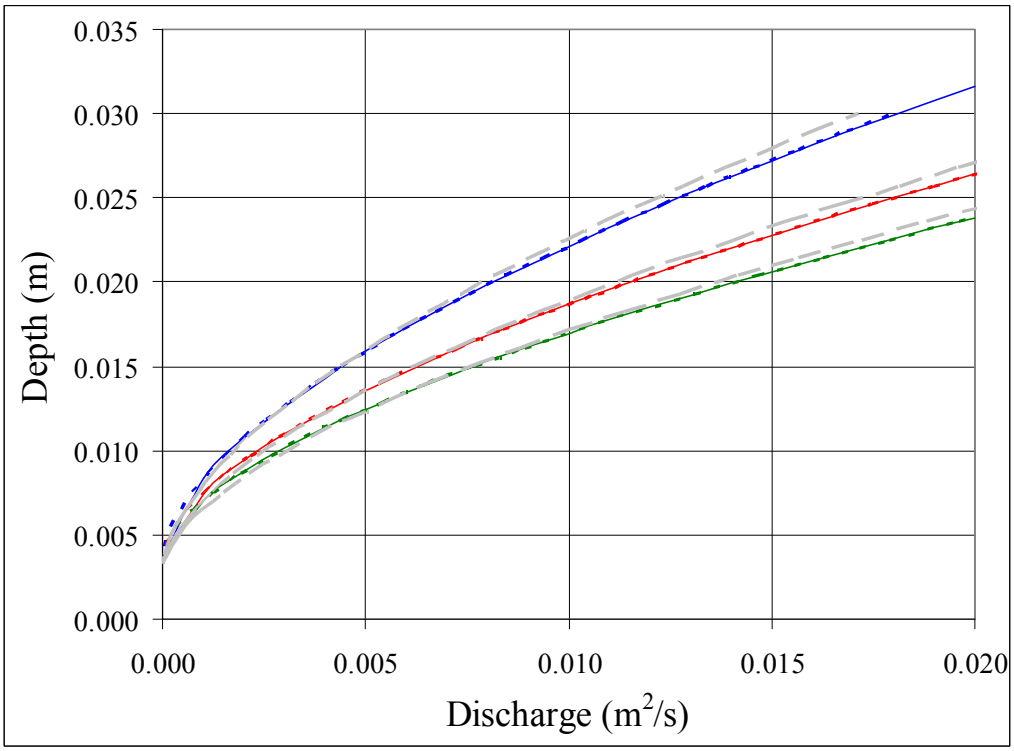

Figure 3.28: Comparison of Manning (solid), LBL 2-Parameter (dotted), and LBL 1-Parameter (light-dashed) models for Surface 3

Chapter 4. Numerical Model Development and Testing

4.1 Grid Generation

Simulation of sheet flow is sensitive to the domain geometry; therefore it is important to precisely represent the pavement surface near superelevation transition for the numerical model. An interface model is developed for the model to read geometric information in a Digital Terrain Model (DTM) and to create a computational grid space. The mathematical algorithms described in this chapter are presented to create a structured curvilinear grid space based on the DTM. Grid points are defined through a parametric mapping of domain surface for both linear and curved roadway sections. Further details on grid generation are presented by Jeong (2008).

4.1.1 Geometry Data from GEOPAK

Bentley's GEOPAK® Civil Engineering Suite is a modular software package for roadway design that is widely used by Departments of Transportation in the United States. GEOPAK calculates superelevation transition for any chain stored in the coordinate geometry database. Because GEOPAK uses coordinate geometry tools to calculate and store design elements, it can provide precise information on the geometry for a complex roadway surface at stations. For the roadway surface profile, one can generate a digital terrain model (DTM) data file in which the three dimensional (3D) geometric profile of a roadway is described. The DTM data file is in ASCII format so it may be readily used by other program modules.

A GEOPAK DTM has the information of x-, y-, and z-coordinates of a roadway surface at the center and the end of all traffic lanes with a constant interval along the roadway. Figure 4.1 shows the format from a DTM data file. The second column represents the x-coordinate; the third column the y-coordinate; the forth column the elevation; and the last column represents the station number. Three rows are allotted to one station as shown in the last column. At each station, the first row represents the left end point; the second row the center point; and the third row the right end points. One may notice that the DTM in Figure 4.1 is for a roadway with one traffic lane in each direction so there are only 3 points at a station (center, left, and right ends). As the number of traffic lanes increases or decreases, the number of rows for each station also increases or decreases, respectively.

```
1          2174158.52          7126640.20          892.29      // 61+75.01 R 1
1          2174180.47          7126641.63          893.51      // 61+75.01 R 1
1          2174202.43          7126643.05          894.66      // 61+75.01 R 1
1          2174156.82          7126664.97          891.68      // 62+00.01 R 1
1          2174178.76          7126666.57          892.96      // 62+00.01 R 1
1          2174200.70          7126668.16          894.23      // 62+00.01 R 1
1          2174154.92          7126689.73          891.10      // 62+25.01 R 1
1          2174176.85          7126691.50          892.40      // 62+25.01 R 1
1          2174198.78          7126693.26          893.69      // 62+25.01 R 1
1          2174152.84          7126714.48          890.51      // 62+50.01 R 1
1          2174174.75          7126716.41          891.81      // 62+50.01 R 1
1          2174196.67          7126718.34          893.11      // 62+50.01 R 1
1          2174150.57          7126739.21          889.90      // 62+75.01 R 1
1          2174172.47          7126741.30          891.20      // 62+75.01 R 1
1          2174194.37          7126743.40          892.50      // 62+75.01 R 1
```

Figure 4.1: An example of geometric information of a roadway in the DTM data file

4.1.2 Curvature Geometry

The interface model stores the coordinates of center and side ends of a roadway section. From here one may take a sequence of points $\vec{x}_i = (x_i, y_i)$ that specify the roadway centerline, which has curvilinear length ξ_c, as shown in Figure 4.2. The radius of curvature and center of curvature for each point can be identified based on locations of neighboring points. The geometry for the computational algorithm is shown in Figure 4.3.

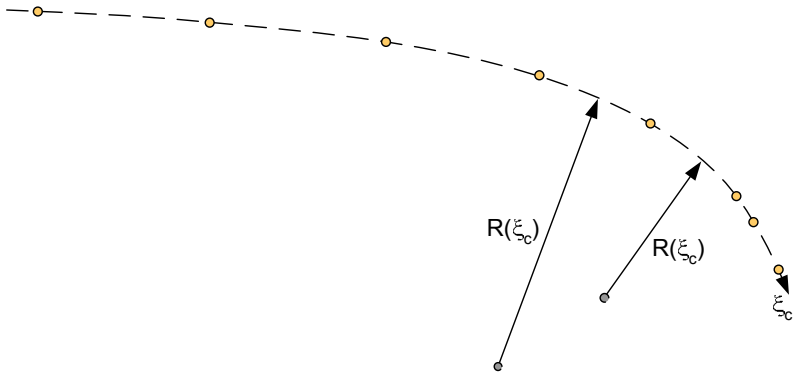

Figure 4.2: Sequence of centerline points with radius of curvature $R(\xi_c)$

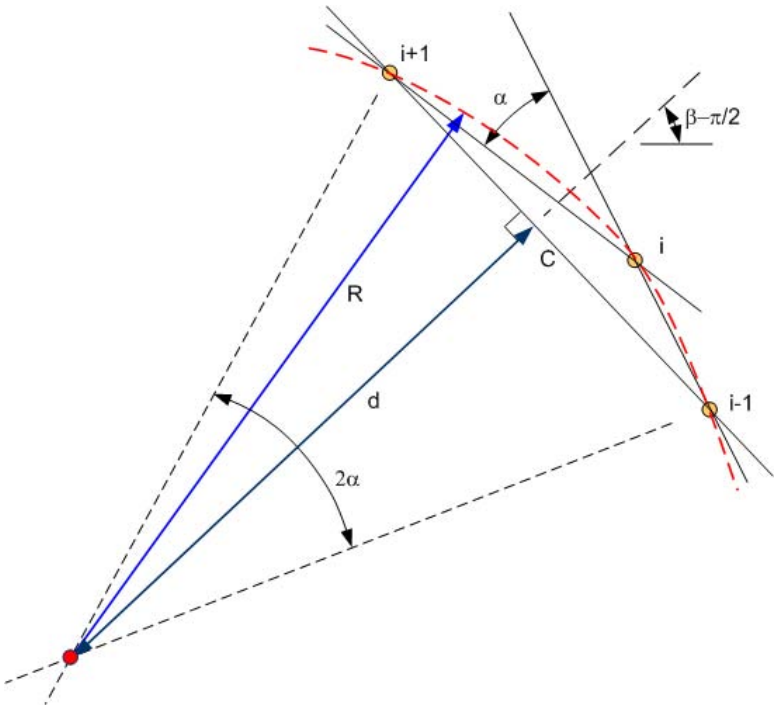

Figure 4.3: Geometry for curvature algorithm

The algorithm for finding the roadway centerline radius of curvature and center of curvature proceeds as follows. The change in direction through neighboring points may be found using

$$\alpha_i = \tan^{-1}\left(\frac{y_{i+1}-y_i}{x_{i+1}-x_i}\right) - \tan^{-1}\left(\frac{y_i-y_{i-1}}{x_i-x_{i-1}}\right) \tag{4.1.1}$$

The direction of the curvature may be determined from the sign of the alpha values. A positive α_i means that the roadway is curved 'counter-clockwise' and a negative value denotes 'clockwise.' The total angle of the sector between rays through points (i-1) and (i+1) is equal to $2\alpha_i$. The length of the chord between these points is

$$C_i = \sqrt{(x_{i+1}-x_{i-1})^2 + (y_{i+1}-y_{i-1})^2} \tag{4.1.2}$$

With the central angle and chord length, the radius of curvature is

$$R_i = \frac{C_i}{2\left|\sin(\alpha_i)\right|} \tag{4.1.3}$$

The center of the chord, angle of the chord segment, and distance from the center of the chord to the center of curvature are calculated using the following:

$$(x_c, y_c)_i = \left(\frac{x_{i+1}+x_{i-1}}{2}, \frac{y_{i+1}+y_{i-1}}{2}\right) \tag{4.1.4}$$

$$\beta_i = \tan^{-1}\left(\frac{y_{i+1}-y_{i-1}}{x_{i+1}-x_{i-1}}\right) \tag{4.1.5}$$

$$d_i = R_i\left|\cos(\alpha_i)\right| \tag{4.1.6}$$

Because the angle β_i defines the direction of the curvature by taking the inverse tangent of two points, it needs to be modified in the following case:

$$\beta_i = \beta_i + \pi, \quad if\ x_{i-1} > x_{i+1} \tag{4.1.7}$$

d_i in Equation 4.6 is a scalar, so it takes an absolute value of a cosine. With these values the center of curvature is

$$(x_{cc}, y_{cc})_i = (x_c, y_c)_i - (d_i\cos(\gamma_i), d_i\sin(\gamma_i)) \tag{4.1.8}$$

The position of the center of curvature depends on the direction to which the curve rotates.

$$\gamma_i = \beta_i - \pi/2 \ \ for\ \alpha_i < 0$$
$$\gamma_i = \beta_i + \pi/2 \ \ for\ \alpha_i > 0 \tag{4.1.9}$$

4.1.3 Grid Generation for Curvature

A DTM data file may have an interval of 3 meters (10 feet) or 30 meters (100 feet) between stations, depending on how it is specified. Therefore an objective of grid generation is to refine the coarse DTM grids into reasonably spaced grids for numerical simulation. The algorithm developed up to this point can read the DTM and compute geometric variables that define the centerline curvature. Given the center line geometry through a series of points $(x_c,y_c)_i$ along the roadway centerline with a corresponding series of center of curvature points $(x_{cc},y_{cc})_i$, radius of curvature R_i, and angles θ_i, one may define the locations of (N-1) points along the centerline through curvilinear interpolation using equal "increments" as shown in Figure 4.4. This implies that the distance between points is larger in regions with larger radius of curvature.

The direction of the radius of curvature is important because it is later used to determine the placement of the interpolated grid points

$$\theta_i = \tan^{-1}\left(\frac{y_c - y_{cc}}{x_c - x_{cc}}\right)_i \qquad (4.1.10)$$

The module defines θ_i to range from zero to 2π so that it can represent the direction of the roadway curvature. The value calculated by equation (4.10) is modified accordingly (addition of π or 2π) depending on the relative locations of the roadway centerline and center of curvature (see Jeong, 2008).

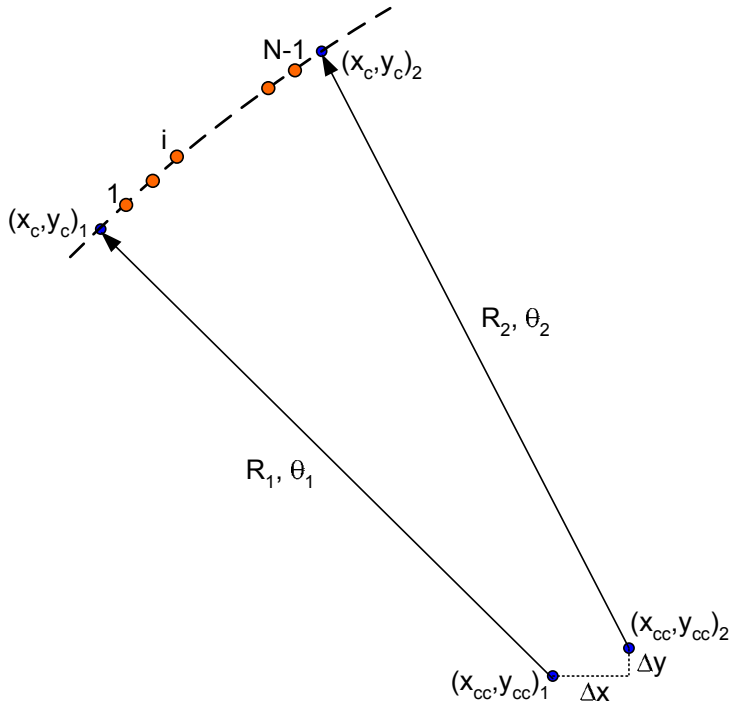

Figure 4.4: Geometry for grid point generation algorithm

In Figure 4.4, the increment of x in the Cartesian coordinate is computed by

$$\Delta x = x_{cc2} - x_{cc1} \qquad (4.1.11)$$

The increments Δy, ΔR, and $\Delta\theta$ are computed similarly. Then the location of i^{th} grid point in Figure 4.4 may be determined using the following

$$\begin{aligned} x_c(\xi) &= (x_{cc1} + \xi\Delta x) + (R_1 + \xi\Delta R)\cos(\theta_1 + \xi\Delta\theta) \\ y_c(\xi) &= (y_{cc1} + \xi\Delta y) + (R_1 + \xi\Delta R)\sin(\theta_1 + \xi\Delta\theta) \end{aligned} \qquad (4.1.12)$$

In equation (4.12) the variable ξ ranges from 0 to 1, representing the fractional increment (i/N) between endpoints along the curve. This algorithm can be generalized to a curved section of roadway (prototype data space). If W is the roadway width, then a parameter η can be introduced to parameterize the entire roadway as follows

$$\begin{aligned} x(\xi,\eta) &= (x_{cc1} + \xi\Delta x) + (R_1 + \xi\Delta R + (\eta - 0.5)W)\cos(\theta_1 + \xi\Delta\theta) \\ y(\xi,\eta) &= (y_{cc1} + \xi\Delta y) + (R_1 + \xi\Delta R + (\eta - 0.5)W)\sin(\theta_1 + \xi\Delta\theta) \end{aligned} \qquad (4.1.13)$$

Equation (4.13) is a parametric mapping of a section of the roadway onto a unit square. In these equations the parameters range $0 < \xi < 1$; $0 < \eta < 1$. The roadway centerline corresponds to $\eta = 0.5$, while the outer curb and inner curb correspond to $\eta = 1$ and $\eta = 0$, respectively. The resulting grid in prototype space is shown schematically in Figure 4.5.

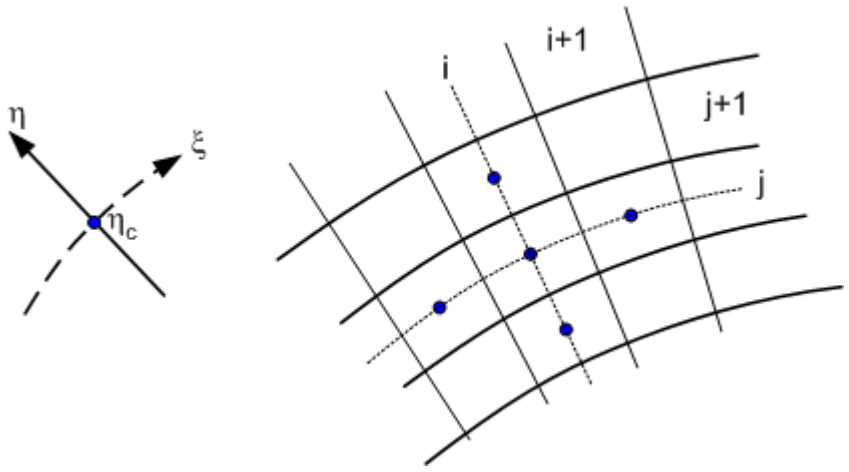

Figure 4.5: Model grid in prototype data space

4.1.4 Characterization of the Parametric Mapping

The transformation between the Cartesian coordinate (x,y) and a curvilinear coordinate system (ξ,η) requires the partial derivatives of the coordinate transformation functions. Differentiating equation (4.13) with respect to ξ and η one gets

$$\frac{\partial x}{\partial \xi} = \Delta x + \Delta R\cos(\theta_1 + \xi\Delta\theta) - \Delta\theta\left(R_1 + \xi\Delta R + (\eta - 0.5)W\right)\sin(\theta_1 + \xi\Delta\theta)$$

$$\frac{\partial y}{\partial \xi} = \Delta y + \Delta R\sin(\theta_1 + \xi\Delta\theta) + \Delta\theta\left(R_1 + \xi\Delta R + (\eta - 0.5)W\right)\cos(\theta_1 + \xi\Delta\theta)$$

$$\frac{\partial x}{\partial \eta} = W\cos(\theta_1 + \xi\Delta\theta)$$

$$\frac{\partial y}{\partial \eta} = W\sin(\theta_1 + \xi\Delta\theta) \qquad (4.1.14)$$

The parametric representation of the coordinate system is useful because length and area transformations can be calculated. The length scaling for segments associated with changes in ξ and η are

$$L_\xi(\xi,\eta) = \sqrt{\left(\frac{\partial x}{\partial \xi}\right)^2 + \left(\frac{\partial y}{\partial \xi}\right)^2}$$

$$L_\eta(\xi,\eta) = \sqrt{\left(\frac{\partial x}{\partial \eta}\right)^2 + \left(\frac{\partial y}{\partial \eta}\right)^2} = W \qquad (4.1.15)$$

The total length of a segment can be found by integrating the length scaling.

$$\xi_{Length} = \int_0^1 L_\xi(\xi,\eta)\, d\xi \tag{4.1.16a}$$

$$\eta_{Length} = \int_0^1 L_\eta(\xi,\eta)\, d\eta \tag{4.1.16b}$$

Note that equation (4.16a) is for the interval between stations at η position and equation (4.16b) is the same as the total width of the roadway. The size of a grid cell can be computed similarly.

$$\ell(\xi,\eta) = L_\xi(\xi,\eta)\Delta\xi$$
$$w(\xi,\eta) = W\,\Delta\eta \tag{4.1.17}$$

In equation (4.17) $\Delta\xi = 1/N_\xi$, $\Delta\eta = 1/N_\eta$, where N_ξ and N_η are the number of grid cells within the sector in each local coordinate direction. The area increments transform according to the Jacobian defined as

$$J(\xi,\eta) = \begin{vmatrix} \partial x/\partial\xi & \partial y/\partial\xi \\ \partial x/\partial\eta & \partial y/\partial\eta \end{vmatrix} = \left(\frac{\partial x}{\partial\xi}\right)\left(\frac{\partial y}{\partial\eta}\right) - \left(\frac{\partial y}{\partial\xi}\right)\left(\frac{\partial x}{\partial\eta}\right) \tag{4.1.18}$$

Within the Cartesian coordinate system the unit vectors along the ξ and η curves are calculated as follows:

$$\hat{u}_\xi = \frac{1}{L_\xi}\frac{\partial x}{\partial\xi}\hat{i} + \frac{1}{L_\xi}\frac{\partial y}{\partial\xi}\hat{j}$$
$$\hat{u}_\eta = \frac{1}{L_\eta}\frac{\partial x}{\partial\eta}\hat{i} + \frac{1}{L_\eta}\frac{\partial y}{\partial\eta}\hat{j} \tag{4.1.19}$$

The inner product of these unit vectors represents the cosine of the angle between these unit vectors.

$$\cos(\omega) = \hat{u}_\xi \cdot \hat{u}_\eta \tag{4.1.20}$$

With equation (4.19), equation (4.20) takes an algebraic form

$$\cos(\omega) = \frac{1}{L_\xi}\left(\Delta x\cos(\theta_1 + \xi\,\Delta\theta) + \Delta y\sin(\theta_1 + \xi\,\Delta\theta) + \Delta R\right) \tag{4.1.21}$$

It is only for the special case $\cos(\omega) = 0$ that the parametric curves are orthogonal. Figure 4.6 shows an example of a computed curvilinear grid based on the equations (4.13) to (4.21). In this figure, the solid circles correspond to the roadway centerline. The solid diamonds correspond to the refined grid points on the domain. Between the stations *i*-1 and *i,* the spacing in the ξ-direction is visually non-uniform, as expected because of the rapidly increasing radius of curvature.

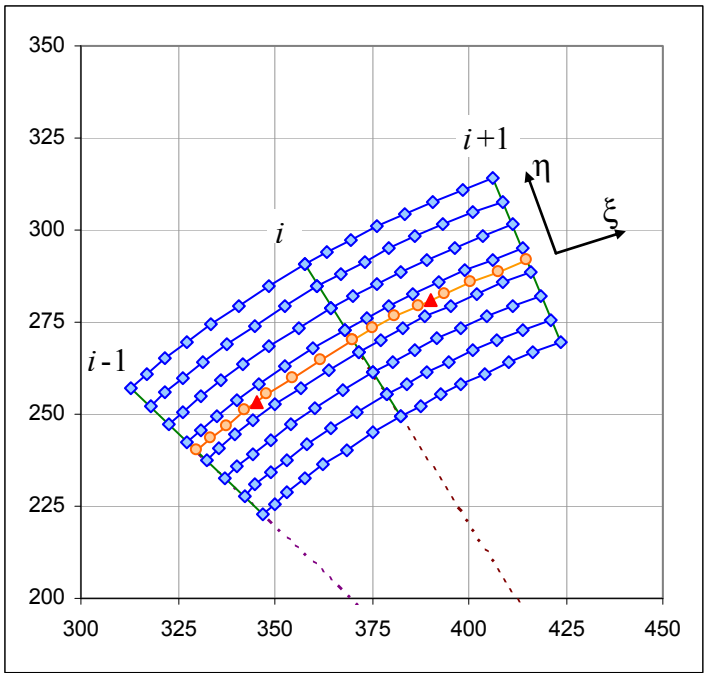

Figure 4.6: Grid layout for a domain with a curved roadway

In order to evaluate the sensitivity of the transformation, a 6 m (20 ft) long and 7.3 m (24 ft) wide curved sector with the design speed of 96.5km/hr (60 mi/hr) is considered. At the center of the sector ($\xi = 0.5$), the radius of curvature is R = 365m (1200 ft). This sector has $\Delta\theta$ = 0.01667 radian. The radii of the outer and inner curb are R_o = 369.4 m and R_i = 362.1 m. Using standard cylindrical coordinate formula, the area of the section is $A = 0.5\Delta\theta\,(R_o^2 - R_i^2)$ = 44.602 m^2. Evaluating the Jacobian at the center (treating the entire sector as one grid cell) gives A = J(0.5,0.5) = 44.5935 m^2. Using a 5x5 division of the unit area gives A = (1/5) (J(1/10, 1/10) + J(1/10, 3/10) + … + J(9/10, 9/10)) = 44.5935 m^2. Clearly the area transformation is well behaved and the section area is approximately A = 44.5935 m^2. Application of the Jacobian to any sub-area will give results of equal or increased accuracy.

4.1.5 Geometry Data Screening

The numerical model recognizes the roadway shape with the sign of the angle shown in equation (4.1). If α_i is zero, the shape of the roadway at the station i is linear; if α_i is non-zero then it is curved. Whereas the precision of a DTM can be controlled manually up to 4 digits after the decimal, it turned out that the accuracy of the data is not enough to use raw values. The data points in a DTM have significant 'noise' that may cause the interface model to fail to read the geometric information from the DTM correctly. For instance, a line-curve-line shaped domain may have α_i's at stations as shown in Figure 4.7. In this figure, the hollow circles represent the alpha values of the roadway center curve with original geometry data, and the solid squares are filtered values. The existence of noise is apparent in the data and causes error in determining the roadway direction and resulting grid layout. A filtering technique that decreases data-noise effects is developed: alpha values are computed for the roadway sides as well as at the center of the domain, and the average of these values rounded up at 0.001 represents the direction of the roadway at each station. The results from such filtering are shown with blue squares in Figure

4.7. The filtered data is reasonable to represent the original shape of the domain; α_i's are zero for the linear sections and are constant with a non-zero value (0.012) throughout the curved section with two exceptional points at transitions.

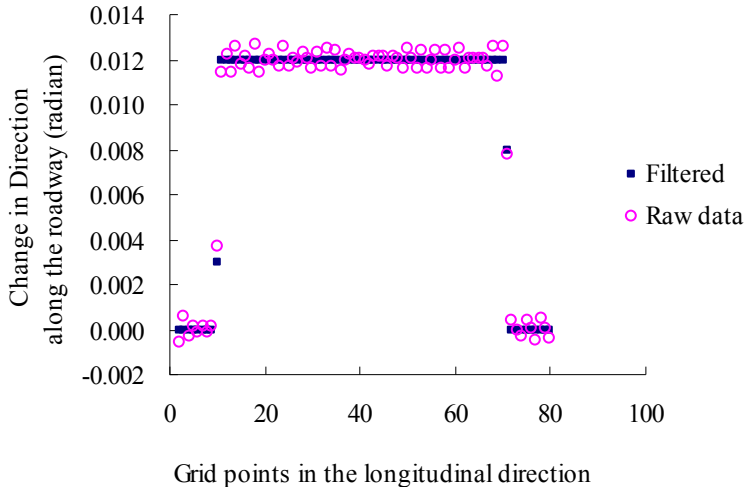

Figure 4.7: Use of filtering to minimize 'data-noise' in roadway direction

Grid interval can be defined differently in the ξ– and η–directions. A grid with large $\Delta\xi$ and small $\Delta\eta$ for a long and narrow curved roadway section can save computation costs without undermining the reliability of the result. The algorithm defines grid points at the center of grid cells. Surface elevation is linearly interpolated from the DTM at the corners of cells then the values at corners of a cell are averaged to get the elevation at the center.

4.2 Numerical Simulation Model Formulation

As noted in Chapter 2, a simplified form of the Saint-Venant equations based on diffusion wave formulation may be used to model sheet and gutter flow on complex pavement surfaces. This subsection outlines the development of a diffusion wave model for sheet flow, development of appropriate boundary conditions, and model testing. The Manning equation is used to define the hydraulic friction slope. A set of finite volume based discrete equations is solved implicitly by a general conjugate gradient method with incomplete Cholesky decomposition.

4.2.1 Diffusion Wave Model Equation (with Manning's Equation)

Highway drainage is usually modeled using a combination of Manning's equation and kinematic wave theory for estimation of the time of concentration (Brown et al., 2001). However, because of the nonuniform drainage flow paths through superelevation transitions, diffusion wave models are employed, allowing for the effects of lateral pressure gradients to be included. Manning's equation is retained because of its prevalent use for both sheet flow and gutter flow. The continuity and Manning's equation (vector form) are

$$\frac{\partial h}{\partial t} + \nabla \cdot \vec{q} = r \qquad (4.2.1)$$

$$\vec{q} = \frac{h^{5/3}}{n\sqrt{S_f}}\vec{S}_f \tag{4.2.2}$$

In equations (4.2.1) and (4.2.2) h = flow depth, $\vec{q}$ = unit discharge vector, r = rainfall intensity, n = Manning coefficient, S_f = magnitude of friction slope, $\vec{S}_f = -\nabla H = \vec{S}_o - \nabla h$ = friction slope vector, $H = z + h$ = water surface elevation, and z = elevation of the pavement surface. Equation (4.2.2) may be written as a diffusion volume flux as follows

$$\vec{q} = -D_h \nabla H \tag{4.2.3}$$

In equation (4.2.3) the nonlinear diffusion coefficient is defined by

$$D_h = \frac{h^{5/3}}{n\sqrt{S_f}} \tag{4.2.4}$$

Combining equations (4.2.1) and (4.2.3) yields the diffusion equation written in Cartesian form as

$$\frac{\partial h}{\partial t} = \frac{\partial}{\partial x}\left(D_h \frac{\partial H}{\partial x}\right) + \frac{\partial}{\partial y}\left(D_h \frac{\partial H}{\partial y}\right) + r \tag{4.2.5}$$

In formulating the numerical model using the finite volume method, equation (4.2.5) is not used directly. Instead, each grid cell is considered as a control volume, and the continuity equation is applied for each cell. The resulting system of equations is combined to yield a domain equation to solve for either the flow depth h or water surface elevation H as a function of time.

4.2.2 Initial and Boundary Conditions

Initial Conditions

It is assumed that there is no ponding of water on the domain before rain starts. Therefore a 'dry' initial condition is set for the model,

$$h_{i,j}^0 = 0 \tag{4.2.6}$$

Equation (4.2.6) is equivalent to stating that the initial water surface elevation is the same as the elevation of the pavement surface, $H_{i,j}^0 = z_{i,j}$.

Kinematic Boundary Conditions

Kinematic boundary conditions are applied using the method of characteristics (MOC) on both the upstream and downstream ends of the grid where the roadway surface has a normal crown or is plane and in superelevation. Outflow kinematic boundary conditions are also applied along the sides of the roadway when no curbs are present. The methods of implementation for inflow and outflow boundary conditions are different. In one case, the characteristic curves approach the boundary from outside of the domain. In the second case, the characteristic curves approach the boundary from within the domain. These two cases are shown in Figure 4.8.

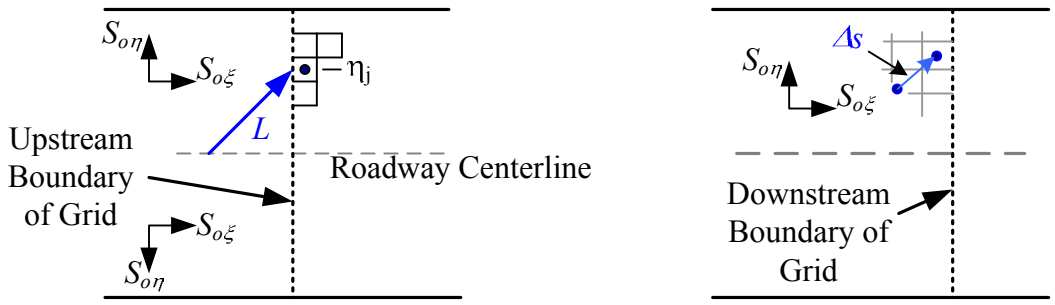

Figure 4.8: Implementation of kinematic boundary conditions when characteristics arrive at the boundary from outside (left) of the domain and within (right) the domain

First consider the case shown to the left of Figure 4.8. The base characteristic that reaches the domain boundary at location η_j leaves the roadway centerline (crown) at a location determined by the pavement longitudinal and cross slope $S_{o\xi}$ and $S_{o\eta}$. Recalling that the roadway centerline corresponds to $\eta = 0.5$ and that the length scale ratio from equation (4.1.15) equals the width of the roadway (W), the drainage path length (L_d) from the roadway crown to the boundary is equal to

$$L_d = \left|\eta_j - 0.5\right| W \frac{S_o}{S_{o\eta}} \tag{4.2.7}$$

With this drainage path length and a constant rainfall rate starting at time zero, the unit flux at the grid boundary reaches its maximum value at the time of concentration for this drainage path. These values of maximum unit discharge and time of concentration are given by

$$q_{\max}(\eta_j) = r \left|\eta_j - 0.5\right| W \frac{S_o}{S_{o\eta}} \tag{4.2.8}$$

$$T_c = \left(\frac{nL_d}{\sqrt{S_o}}\right)^{0.6} \left(\frac{1}{r}\right)^{0.4} \tag{4.2.9}$$

The MOC equations provide the depth and unit flux at the boundary for time $t < T_c$.

$$h_B(\eta_j, t) = r\, t \quad ; \quad t \le T_c \tag{4.2.10}$$

$$q_B(\eta_j, t) = \frac{\sqrt{S_o}}{n} (r\, t)^{5/3} \quad ; \quad t \le T_c \tag{4.2.11}$$

The flow rate is applied as a Neumann boundary condition through an incremental addition to the rainfall intensity of the boundary cell. The normal component of the flow across the boundary is calculated as q_B ($S_{o\xi}/S_o$). Assuming that the boundary corresponds to the first column ($i = 1$) and that the cell column width is $\Delta\xi_1$, then the incremental rainfall added to the boundary cell is

$$\Delta r_{1,j} = \frac{q_B(\eta_j, t)}{L_\xi(\xi_1, \eta_j)\Delta\xi_1} \frac{S_{o\xi}}{S_o} \tag{4.2.12}$$

Figure 4.9 shows a plot of incremental rainfall on the upstream boundary for half of a normal crowned roadway (center to side end). The variables are normalized by largest values. As η increases the time of concentration also increases. Once the time reaches T_c, the rainfall loading becomes steady (equation 4.2.11). Thus, the steady state for the incremental rainfall loading on

the upstream boundary begins from the roadway center (η=0.5) at t=0 (theoretically $L_{d,center}$=0) and propagates to the side of the roadway (η=1).

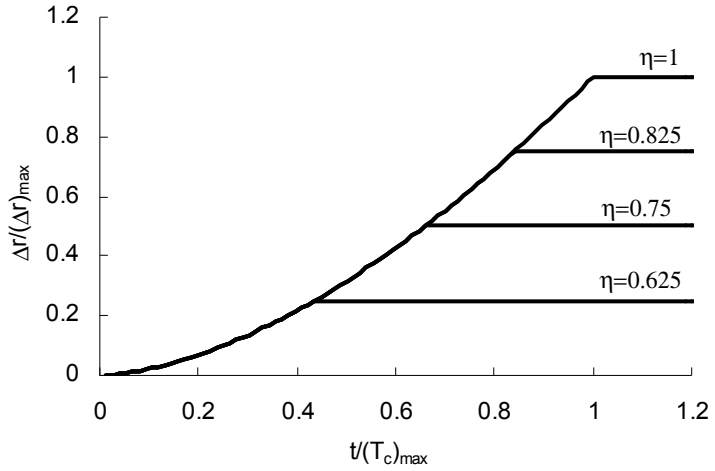

Figure 4.9: Incremental rainfall loading on the upstream boundary.
($S_{o\xi}$ = 2%, $S_{o\eta}$ = 2%, W = 7.3m, $\Delta x = \Delta y$ = 0.3m, r = 125mm/hr, n = 0.015)

For the case shown on the right side of Figure 4.8, the characteristic curve arrives at the boundary from within the domain. For this case, the objective is to apply the kinematic boundary condition as a Dirichlet condition at time level k+1 with depth interpolated from the depth values at time level k and updated using the characteristic equations. The algorithm is best presented in a general setting with point 2 downstream of initial point 1 along a characteristic curve. For point 2, located at the center of a boundary cell, h_2^{k+1} can be predicted given the numerical solution at time level k. As the roadway surface is plane and uniform near the domain boundary, the kinematic wave model is the one-dimensional form of equation (4.2.1) (Henderson and Wooding, 1964). The MOC solution can be formulated either in terms of depth or unit discharge. For each formulation the MOC solution gives

$$h = h_2^{\,k} + r\tau \tag{4.2.13}$$

$$q = q_1^{\,k} + r(s - s_1) \tag{4.2.14}$$

In equations (4.2.13) and (4.2.14), τ refers to time ($\tau = t - t^k$) and s to distance along a characteristic curve. The selection of 'initial conditions' is determined through the following discussion. If $c(h) = dq/dh$ is the characteristic celerity, then the base characteristic equation gives

$$\frac{ds}{d\tau} = c(h) = \frac{dq}{dh} = \frac{5}{3}\frac{\sqrt{S_o}}{n} h^{2/3} \tag{4.2.15}$$

Combining equations (4.2.13) and (4.2.15) and integrating over the time increment $\Delta t = t^{k+1} - t^k$ gives

$$\Delta s = \frac{\sqrt{S_o}}{n r}\left[\left(h_2^{\,k} + r\Delta t\right)^{5/3} - \left(h_2^{\,k}\right)^{5/3}\right] \tag{4.2.16}$$

Equation (4.2.16) gives the distance moved along the base characteristic B shown in Figure 4.10 during the time increment $t^k \rightarrow t^{k+1}$. The increase in unit discharge along this flow path is

$\Delta q = r\,\Delta s$. It is assumed that the same distance is traversed along the characteristic A shown in Figure 4.10, and use of equation (4.2.14) results in the following algorithm (when combined with the Manning equation)

$$h_2^{\,k+1} = \left(\left(h_1^{\,k}\right)^{5/3} + \left(h_2^{\,k} + r\Delta t\right)^{5/3} - \left(h_2^{\,k}\right)^{5/3} \right)^{0.6} \qquad (4.2.17)$$

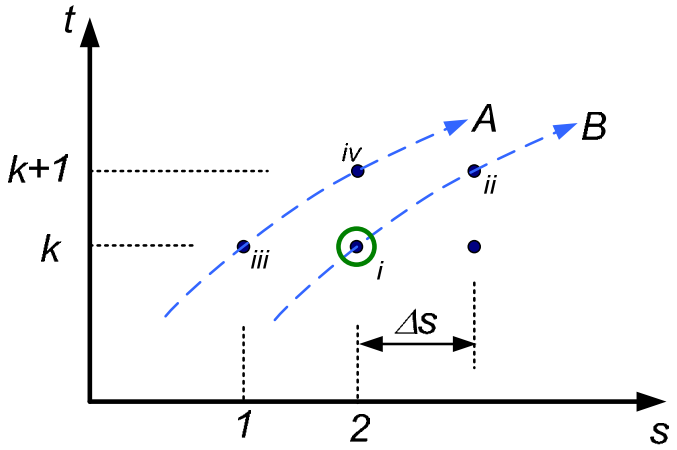

Figure 4.10: Schematic view of computational grid for outflow kinematic boundary condition

Specifically, with reference to Figure 4.10, the point correspondence is $i \rightarrow h_2^{\,k}$, $ii \rightarrow h_2^{\,k} + r\Delta t$, $iii \rightarrow h_1^{\,k}$, and $iv \rightarrow h_2^{\,k+1}$. The algorithm is applied by first using equation (4.2.16) to determine the distance upstream from point 2 to point 1, then interpolating between cell values using the numerical solution at time t^k, and finally using the interpolated value as $h_1^{\,k}$ in equation (4.2.17) to determine the Dirichlet boundary value for the boundary cell.

No-flow (Neumann) Boundary Conditions

Highways with curbs have closed boundaries on the roadsides. A no-through flow boundary condition applies to these boundaries. In this boundary condition, water surface is forced to be flat transverse to the boundary by setting zero-transverse-gradient in total head near the boundary.

$$\frac{\partial H_{i,j}^{n}}{\partial \eta} = 0 \quad ; \quad j = 1, N_y \qquad (4.2.18)$$

This boundary condition also holds for curb-less roadside where the cross slope is uphill toward the boundary so water flows from the boundary toward the road center. Another Neumann-type B.C. is the zero water-depth gradient condition. This boundary condition defines the normal flow condition where water depth is constant through the boundary. For cases with roadside curbs, sheet flow becomes channelized along the low side of the road (gutter flow). The algorithm automatically detects the grid points on the downstream boundary on which the flow is kinematic or the water surface is flat due to the channelization. Then either zero-depth gradient B.C. or kinematic B.C. is selectively applied on the downstream boundary cells.

4.2.3 Numerical Model Development

Equation (4.2.5) has no analytical solution due to the nonlinear diffusion coefficient; therefore only approximate solutions are available through numerical computation. For the numerical computation, all geometric properties of the curvilinear grids (physical space) described in Section 4.1 are transformed into rectangular grids (computational space) as shown in Figure 4.11. In this figure, ξ represents the longitudinal direction of roadway and η the transverse direction, both in the computation space representation. Indices i and j range from $(1,1)$ to (N_x,N_y). The curvilinear shape of the physical domain is normalized to a rectangular shape in the computational domain. Geometric properties are conserved through the transformation properties.

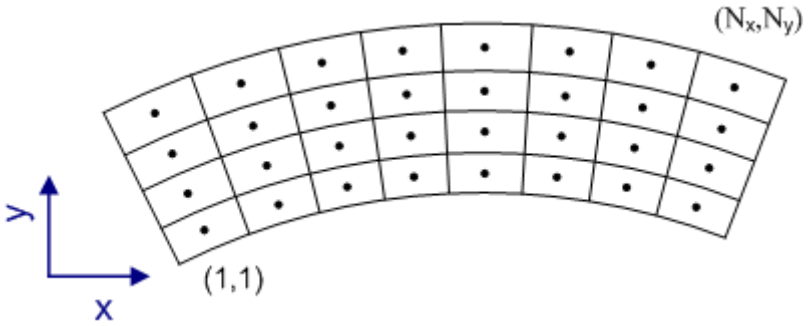

(a) Curvilinear grids in physical space (x,y)

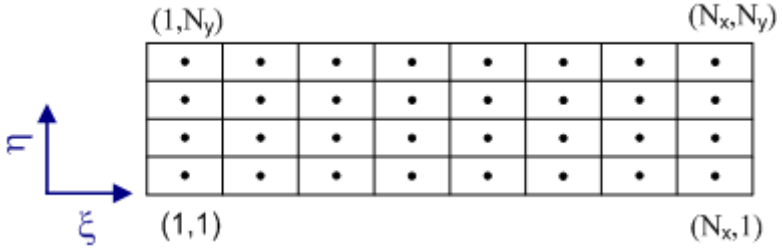

(b) Rectangular grids in computational space (ξ,η)

Figure 4.11: Transformation of grid space

The finite volume method (FVM) is used to develop the numerical model equations as it more easily provides local mass balance on nonuniform grids compared with other finite-grid schemes. For space discretization, 3-point central differencing is used and the Crank-Nicolson method is employed for time differencing. The equation development is formulated for the computational grid cell shown in Figure 4.12.

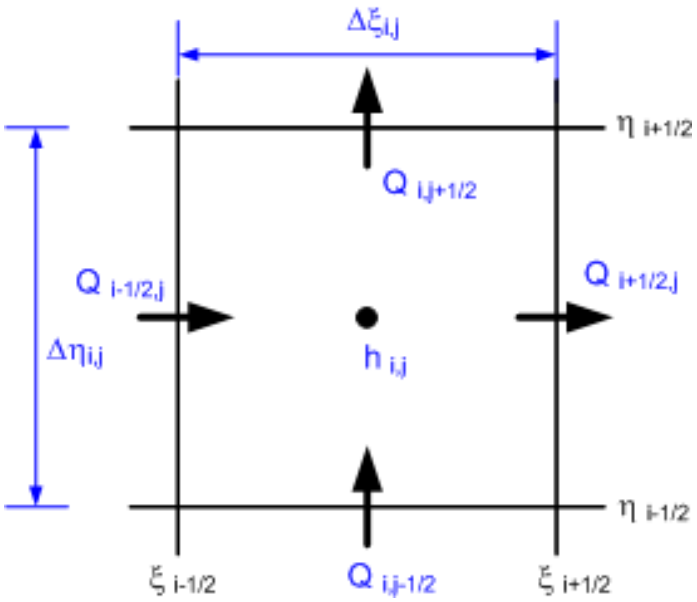

Figure 4.12: Transformed grid for cell (i,j)

When applied to the i,j-grid cell shown in Figure 4.12 the continuity equation (4.2.1) is written

$$\frac{dh_{i,j}}{dt} + \frac{1}{A_{i,j}}\left(Q_{i,j-1/2} + Q_{i-1/2,j} + Q_{i,j+1/2} + Q_{i+1/2,j}\right) = r \qquad (4.2.19)$$

In equation (4.2.19), $h_{i,j}$ is the depth in the cell [the total head $H_{i,j}$ could equally be used as the primary variable], $A_{i,j}$ is the grid cell area, the Q's are the volume discharges outward across the grid cell boundary, and r is the constant rainfall rate. Within the transformed coordinate system, the main variable, depth (h), is evaluated at the center of cell, while the flux (Q) is estimated at the cell boundaries. Each cell has four boundaries facing the neighboring cells. The longitudinal fluxes (ξ-axis) associated with the cell (i,j) may be discretized as follows.

$$Q_{i-1/2,j} = -\frac{2\,D_{i-1/2,j}}{\Delta\xi_{i-1,j} + \Delta\xi_{i,j}}\Delta\eta_{i,j}\left(H_{i-1,j} - H_{i,j}\right)$$

$$Q_{i+1/2,j} = -\frac{2\,D_{i+1/2,j}}{\Delta\xi_{i,j} + \Delta\xi_{i+1,j}}\Delta\eta_{i,j}\left(H_{i+1,j} - H_{i,j}\right) \qquad (4.2.20a)$$

Similarly, fluxes in the transverse direction (η-axis) take the following form.

$$Q_{i,j-1/2} = -\frac{2\,D_{i,j-1/2}}{\Delta\eta_{i,j-1} + \Delta\eta_{i,j}}\Delta\xi_{i,j}\left(H_{i,j-1} - H_{i,j}\right)$$

$$Q_{i,j+1/2} = -\frac{2\,D_{i,j+1/2}}{\Delta\eta_{i,j} + \Delta\eta_{i,j+1}}\Delta\xi_{i,j}\left(H_{i,j+1} - H_{i,j}\right) \qquad (4.2.20b)$$

In order to implement the model, equation (4.2.19) must be transformed back to the prototype data space. The transformation to the roadway grid system requires transformation of boundary and area sections. To parameterize the cell transformation one may introduce "cell conductance" coefficients ($C_{i,j}$), which vary in space and time. First, the boundary discharge terms from

equation (4.2.20) are divided by the cell area (see equation 4.2.19) and the resulting cell conductance terms are defined by

$$\left(C_\xi\right)_{i-1/2,j} = \frac{2\,D_{i-1/2,j}}{\Delta\xi_{i,j}\left(\Delta\xi_{i-1,j}+\Delta\xi_{i,j}\right)}$$

$$\left(C_\xi\right)_{i+1/2,j} = \frac{2\,D_{i+1/2,j}}{\Delta\xi_{i,j}\left(\Delta\xi_{i,j}+\Delta\xi_{i+1,j}\right)}$$

$$\left(C_\eta\right)_{i,j-1/2} = \frac{2\,D_{i,j-1/2}}{\Delta\eta_{i,j}\left(\Delta\eta_{i,j-1}+\Delta\eta_{i,j}\right)}$$

$$\left(C_\eta\right)_{i,j+1/2} = \frac{2\,D_{i,j+1/2}}{\Delta\eta_{i,j}\left(\Delta\eta_{i,j}+\Delta\eta_{i,j+1}\right)} \qquad (4.2.21)$$

When transformed to the roadway grid using equation (4.1.17) these terms become

$$\left(C_\xi\right)_{i-1/2,j} = \frac{2\,D_{i-1/2,j}}{\ell_{i,j}\left(\ell_{i-1,j}+\ell_{i,j}\right)}$$

$$\left(C_\xi\right)_{i+1/2,j} = \frac{2\,D_{i+1/2,j}}{\ell_{i,j}\left(\ell_{i+1,j}+\ell_{i,j}\right)^2}$$

$$\left(C_\eta\right)_{i,j-1/2} = \frac{2\,D_{i,j-1/2}}{w_{i,j}\left(w_{i,j-1}+w_{i,j}\right)}$$

$$\left(C_\eta\right)_{i,j+1/2} = \frac{2\,D_{i,j+1/2}}{w_{i,j}\left(w_{i,j}+w_{i,j+1}\right)} \qquad (4.2.22)$$

In equation (4.2.22) $\ell_{i,j}$ and $w_{i,j}$ are the length and width of cell-(i,j) as defined in equation (4.1.17). The ranges of (i,j) indices are $1 \le i \le N_x$ and $1 \le j \le N_y$ where N_x is the number of grid points in the ξ direction and N_y is that in the η direction over the entire domain. The effective nonlinear diffusion coefficient is calculated using the interpolated values of the flow depth and friction slope at the center of the boundary between the cells. For example, the water depth at the interface between cells (i,j) and (i+1,j) is calculated from

$$h_{i+1/2,j} = \frac{h_{i,j}\ell_{i+1,j} + h_{i+1,j}\ell_{i,j}}{\ell_{i+1,j}+\ell_{i,j}} \qquad (4.2.23)$$

For the ξ-component of the friction slope the longitudinal gradient is discretized on the boundary of cells. For instance, the friction slope between the cells (i,j) and (i+1,j) is approximated by

$$\left(S_{f\xi}\right)_{i+1/2,j} = \frac{2\left(H_{i,j}-H_{i+1,j}\right)}{\ell_{i,j}+\ell_{i+1,j}} \qquad (4.2.24)$$

The η-component of the friction slope ($S_{f\eta}$) for the transverse gradient can be calculated using expressions similar to equation (4.2.24). The average transverse gradient at the boundary between cell (i,j) and (i+1,j) requires values of $(S_{f\eta})_{i,j+1/2}$, $(S_{f\eta})_{i+1,j+1/2}$, $(S_{f\eta})_{i+1,j-1/2}$, and $(S_{f\eta})_{i,j-1/2}$. The interpolated value of the η-component at the center of the ξ-face of the cell is then calculated using

$$\left(S_{f\eta}\right)_{i+1/2,j} = \frac{\left[\left(S_{f\eta}\right)_{i,j+1/2}+\left(S_{f\eta}\right)_{i,j-1/2}\right]\ell_{i+1,j}+\left[\left(S_{f\eta}\right)_{i+1,j+1/2}+\left(S_{f\eta}\right)_{i+1,j-1/2}\right]\ell_{i,j}}{2\left(\ell_{i+1,j}+\ell_{i,j}\right)} \qquad (4.2.25)$$

The magnitude of the friction slope at the interface is calculated using

$$\left(S_f\right)_{i+1/2,j} = \sqrt{\left(S_{f\xi}\right)^2_{i+1/2,j} + \left(S_{f\eta}\right)^2_{i+1/2,j}} \tag{4.2.26}$$

With equations (4.2.23) through (4.2.26), the discrete form of the diffusion coefficient on the cell interface takes the form

$$D_{i+1/2,j} = \frac{h^{5/3}_{i+1/2,j}}{n_{i,j}\sqrt{\left(S_f\right)_{i+1/2,j}}} \tag{4.2.27}$$

With equations (4.2.23), (4.2.26), and (4.2.27), the conveyance coefficient can be evaluated from equation (4.2.22). Combining all of the terms, equation (4.2.19) may be written

$$\frac{dh_{i,j}}{dt} + f(h) + f(z) - r = 0 \tag{4.2.28}$$

In equation (4.2.28)

$$\begin{aligned} f(h) &= \left(\left(C_\xi\right)_{i-1/2,j} + \left(C_\eta\right)_{i,j-1/2} + \left(C_\xi\right)_{i+1/2,j} + \left(C_\eta\right)_{i,j+1/2}\right)h_{i,j} - \left(C_\xi\right)_{i-1/2,j}h_{i-1,j} \\ &\quad - \left(C_\xi\right)_{i+1/2,j}h_{i+1,j} - \left(C_\eta\right)_{i,j-1/2}h_{i,j-1} - \left(C_\eta\right)_{i,j+1/2}h_{i,j+1} \\ f(z) &= \left(\left(C_\xi\right)_{i-1/2,j} + \left(C_\eta\right)_{i,j-1/2} + \left(C_\xi\right)_{i+1/2,j} + \left(C_\eta\right)_{i,j+1/2}\right)z_{i,j} - \left(C_\xi\right)_{i-1/2,j}z_{i-1,j} \\ &\quad - \left(C_\xi\right)_{i+1/2,j}z_{i+1,j} - \left(C_\eta\right)_{i,j-1/2}z_{i,j-1} - \left(C_\eta\right)_{i,j+1/2}z_{i,j+1} \end{aligned} \tag{4.2.29}$$

In practical applications, the water surface elevation (H) is usually several digits larger than water depth (h) in order-of-magnitude. Therefore, the water depth term is used as the main variable to reduce truncation error, which may be caused by the difference between water depth and surface elevation in the order of magnitude ($h/z \sim 10^{-6}$). Use the notation ${h_{i,j}}^k$ for cell location (i,j) and time level k. The final system of equations is evaluated using the Crank-Nicolson method (Ferziger and Peric, 2002), which gives

$$\frac{{h_{i,j}}^{k+1} - {h_{i,j}}^{k}}{\Delta t} + \frac{1}{2}\left(f(h) + f(z)\right)^{k+1} + \frac{1}{2}\left(f(h) + f(z)\right)^{k} - r = 0 \tag{4.2.30}$$

The superscript refers to the time level at which the variable and coefficients are evaluated. The system of equations is solved iteratively using a conjugate gradient method solver with an inner loop for updating the nonlinear coefficients and outer loop for convergence check.

4.2.4 Solution Process

The transformed grid is shown in Figure 4.13. There are a total of NR rows and NC columns in the domain. The model system of equation should be formulated:

$$\underline{\underline{A}} \cdot \underline{x} = \underline{f} \tag{4.2.31}$$

The unknown vector x has global components of $N = N_R \cdot N_C$.

$$\begin{aligned} \underline{x} &= \left[h_{1,1}\ \ h_{1,2}\ \ \ldots\ \ h_{1,N_R}\ \ h_{2,1}\ \ \ldots\ \ h_{N_C,N_R-1}\ \ h_{N_C,N_R}\right]^T \\ x_n &= h_{i,j} \qquad where\ n = i \cdot N_R + j \end{aligned} \tag{4.2.32}$$

The local unknown $h_{i,j}$ is located as global component x_n. The matrix A is a square N by N matrix with components $a_{m,n}$ where $1 \le m \le N$, $1 \le n \le N$. The column vector f is numbered the same as the unknown vector x.

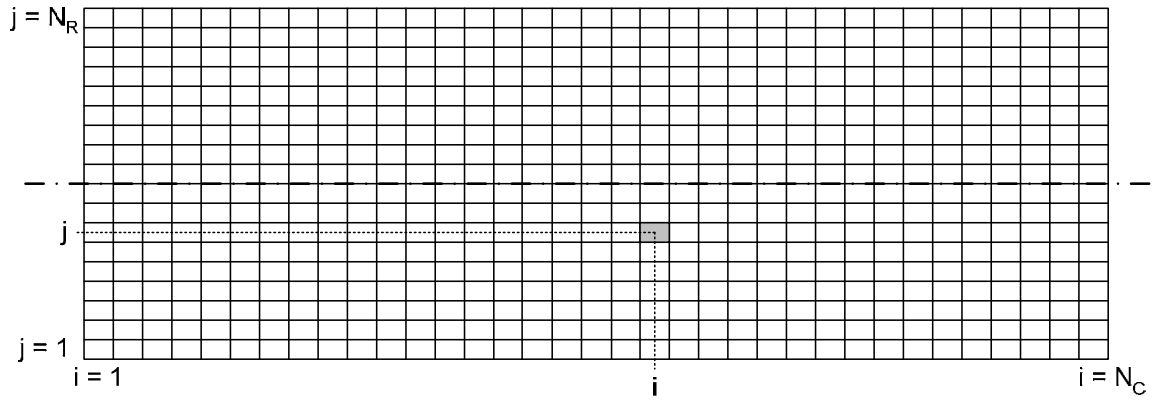

Figure 4.13: Transformed model grid

With the row-column numbering system, equation (4.2.28) may be written

$$a_n x_{n-N_R}^{k+1} + b_n x_{n-1}^{k+1} + c_n x_n^{k+1} + d_n x_{n+1}^{k+1} + e_n x_{n+N_R}^{k+1} = f_n \tag{4.2.33}$$

For the set of equations discretized in 2D space shown in equation (4.2.33), the coefficient matrix A becomes pentadiagonal, which means there are two upper diagonals and two lower diagonals with main diagonal band. For the index notation defined in equation (4.2.33) the components of the matrix A are

$$\begin{aligned}
a_n &= -\left(C_\xi\right)_{i-1/2,j}^{k+1} \\
b_n &= -\left(C_\eta\right)_{i,j-1/2}^{k+1} \\
c_n &= \left(C_\xi\right)_{i-1/2,j}^{k+1} + \left(C_\eta\right)_{i,j-1/2}^{k+1} + \left(C_\xi\right)_{i+1/2,j}^{k+1} + \left(C_\eta\right)_{i,j+1/2}^{k+1} + 2/\Delta t \\
d_n &= -\left(C_\eta\right)_{i,j+1/2}^{k+1} \\
e_n &= -\left(C_\xi\right)_{i+1/2,j}^{k+1}
\end{aligned} \tag{4.2.34}$$

The RHS vector f is

$$\begin{aligned}
f_n &= \left(2/\Delta t\right)h_{i,j}^k + 2r \\
&- \left(C_\xi\right)_{i-1/2,j}^{k+1}\left(z_{Bi,j} - z_{Bi-1,j}\right) - \left(C_\xi\right)_{i+1/2,j}^{k+1}\left(z_{Bi,j} - z_{Bi+1,j}\right) \\
&- \left(C_\eta\right)_{i,j-1/2}^{k+1}\left(z_{Bi,j} - z_{Bi,j-1}\right) - \left(C_\eta\right)_{i,j+1/2}^{k+1}\left(z_{Bi,j} - z_{Bi,j+1}\right) \\
&- \left(C_\xi\right)_{i-1/2,j}^{k}\left(H_{i,j}^k - H_{i-1,j}^k\right) - \left(C_\xi\right)_{i+1/2,j}^{k}\left(H_{i,j}^k - H_{i+1,j}^k\right) \\
&- \left(C_\eta\right)_{i,j-1/2}^{k}\left(H_{i,j}^k - H_{i,j-1}^k\right) - \left(C_\eta\right)_{i,j+1/2}^{k}\left(H_{i,j}^k - H_{i,j+1}^k\right)
\end{aligned} \tag{4.2.35}$$

The pentadiagonal matrix system for equation (4.2.33) is shown in Figure 4.14. The matrix A is symmetric, banded, and sparse.

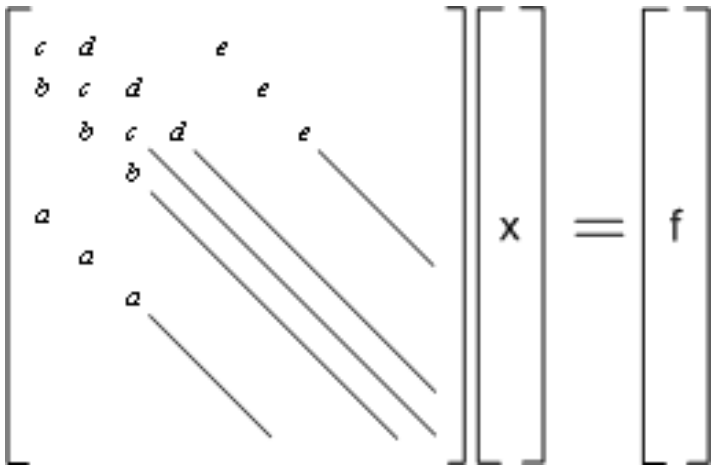

Figure 4.14: Pentadiagonal matrix systems

As shown in equations (4.2.22) and (4.2.27), the indices of the coefficient matrix (which actually are conductance terms) are dependent on the solution vector of the system, making the system nonlinear. Strictly, the coefficient matrix cannot be defined unless the unknown vector is solved. Linearization is necessary to solve a nonlinear problem. Newton's method is known as the master method for solving nonlinear equations due to its fast convergence speed. However, the cost of generating the Jacobian of transformation and solving the system by Gauss elimination may be high so that the overall cost is greater than that of other iterative methods (Ferziger and Peric, 2002). A Picard iteration method used by Feng and Molz (1997) is used for the linearization. The nonlinear terms at the time level k+1 are linearized by approximating the conductance terms with the solutions at the time level k. Then, the system of linear equations is solved and the coefficient matrix is updated with new solutions at k+1 level. The solution of the next nonlinear iteration step (m+1) is compared to the previous nonlinear iteration step (m) solution for the convergence check (until the difference becomes small enough and the solution process converges). The solution process for nonlinear iteration is outlined as follows:

(1) At time level k+1, conductance terms are computed with k level solution. e.g. $\left(C_{\xi}\right)_{i+1/2,j}^{k}$

(2) The matrix system is solved for the vector x. e.g. $h_{i,j}^{k+1,m}$

(3) Update the matrix A. e.g. $\left(C_{\xi}\right)_{i+1/2,j}^{k+1,m+1}$.

(4) Update solution vector. e.g. $h_{i,j}^{k+1,m+1}$

(5) Check the convergence of the solution

(6) Repeat (3), (4) and (5) until the solution converges

(7) Go to next time level

The number of iterations for this linearization depends on the time interval and the rate of change in the conductance terms between time steps. In this model, the time series solution is computed for a rising hydrograph. The algorithm adopted from the implicit Conjugate Gradient method preconditioned with the Modified Incomplete Cholesky Decomposition (MICCG) proposed by

Cooley (1992) solves the system of equations iteratively. The solution process starts by creating a computational grid space based on the input road surface geometry. Boundary conditions are updated at each time step, and the MICCG solver iterates until current time step solution converges. At each time step, nonlinear diffusion coefficients are found by iterating the inner loop of MICCG solver. The solution process repeats as time step advances until the flow reaches steady state condition. Figure 4.15 outlines this procedure through a flow chart.

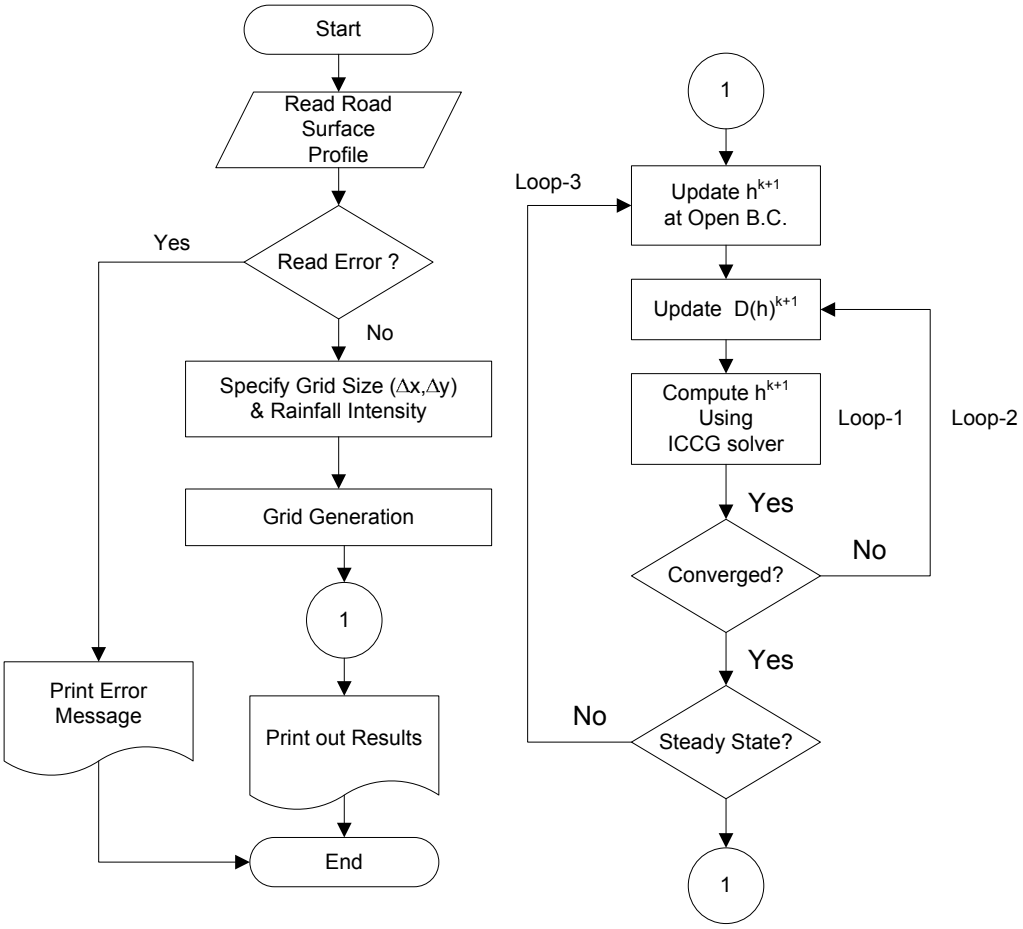

Figure 4.15: Solution Process

4.3 Model Testing and Evaluation

Model testing involves evaluation of stability, convergence, and comparison with known analytical solutions based on the kinematic wave model. Model stability is discussed by Jeong (2008) who shows that the linearized model equations are unconditionally stable. The following subsections describe investigations of model convergence and comparison with known analytical solutions.

4.3.1 Evaluation of Model Convergence

Theoretically the numerical solution x_i^k should approach the exact solution of the differential equation when the spatial and temporal intervals tend to zero. For a well-posed and

consistent discretization scheme, stability is the necessary and sufficient condition for convergence (Hirsch, 1998). From the practical point of view, it is important to specify appropriate stopping criteria to guarantee the solution to be reasonable. Vector norms are frequently used to check the convergence of iterative methods. There are three loops that iterate the solution procedure. The first inner most DO-loop iterates to seek for the solutions for any given condition using the CG solver. The second loop compares the linearized model solutions to generate the approximate nonlinear solution at each time step. The last outer most loop stops only when the solution reaches steady state. L_2 norm and L_∞ norms are used as stopping criteria in the model. To eliminate the 'order of magnitude' related truncation errors, the norms are normalized by the solution itself such that

$$\|x\|_2^{\,n} = \frac{\sqrt{\sum_{i=1}^{N_x}\sum_{j=1}^{N_y}\left|\left(h_{i,j}^{\,k}\right)^n - \left(h_{i,j}^{\,k}\right)^{n-1}\right|^2}}{\left(h_{avg}^{k}\right)^n}$$

$$\|x\|_\infty^{\,n} = \max_{i,j}\left|\frac{\left(h_{i,j}^{\,k}\right)^n - \left(h_{i,j}^{\,k}\right)^{n-1}}{\left(h_{i,j}^{\,k}\right)^n}\right| \qquad (4.3.1)$$

In equation (4.3.1) n represents the n^{th} iteration and k the time step. In the loop for nonlinearity, n represents the number of nonlinear iterations. Therefore, the actual number of iterations becomes $n_{inner} \times n_{outer}$. The difference in solutions between the current and previous iterations is compared and the process iterates until the norms becomes smaller than the stopping criteria. The solution is considered to be converged only when (1) the difference in the solution between iterations is small (L_2 norm) and (2) the residual at the current iteration is small (L_∞ norm).

$$\|x\|_2^{\,n} < \varepsilon_2 \quad and \quad \|x\|_\infty^{\,n} < \varepsilon_\infty \qquad (4.3.2)$$

In equation (4.3.2) the parameters ε_2 and ε_∞ are the stopping criteria with magnitudes such as 10^{-5}. Figure 4.16 shows an example of convergence of the numerical solution of the CG solver. Both L_2 and L_∞ norms decrease exponentially as the number of iteration increases during an iterative solution process.

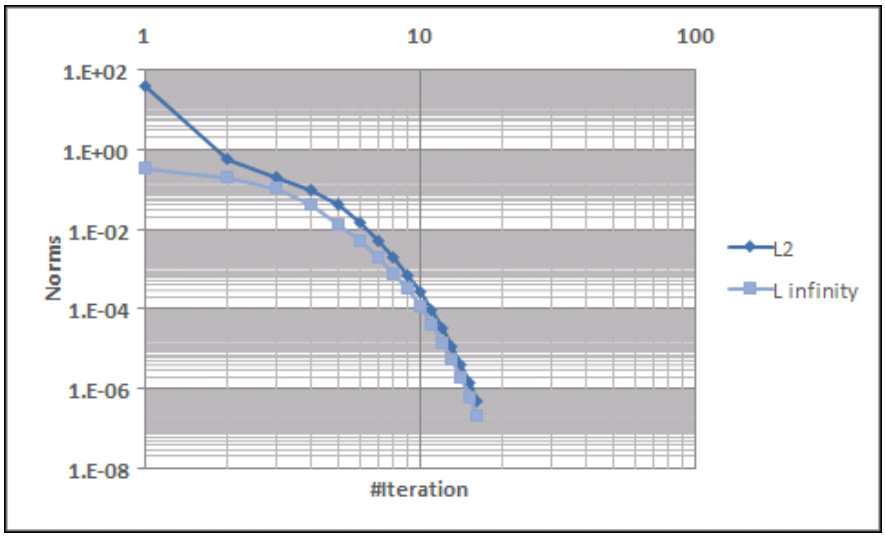

Figure 4.16: Convergence speed of MICCG solver measured by L_2 and L_∞ norms.

A problem with one-dimensional flow is simulated with the following variables: L = 15 m (50 ft), r = 250 mm/hr and S_x = 1%. The solution with N_x = 1000 (Δx = 0.015 m) is used as the exact solution. Figure 4.17(a) shows the variation of the water depth as the grid is refined for the central differencing scheme (CDS). The grid was refined from N_x = 10 to N_x = 500. On the coarsest grid, the model does not produce a meaningful solution. As the grid is refined, the model result converges monotonically towards a grid-independent solution.

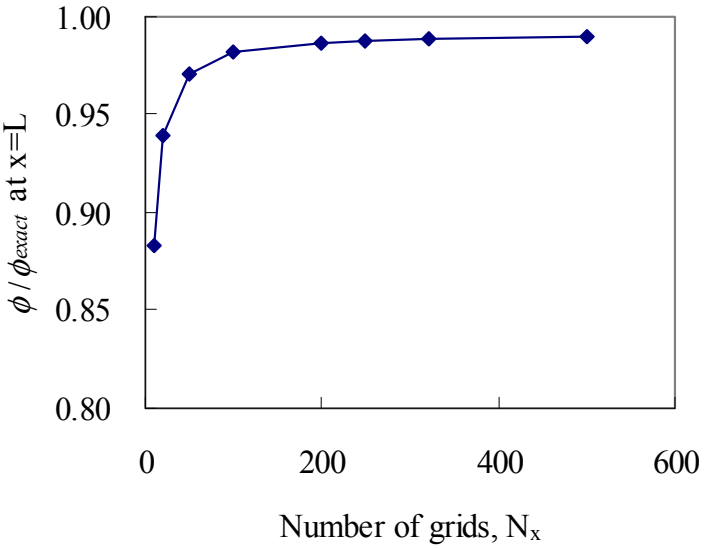

(a) Convergence of downstream water depth

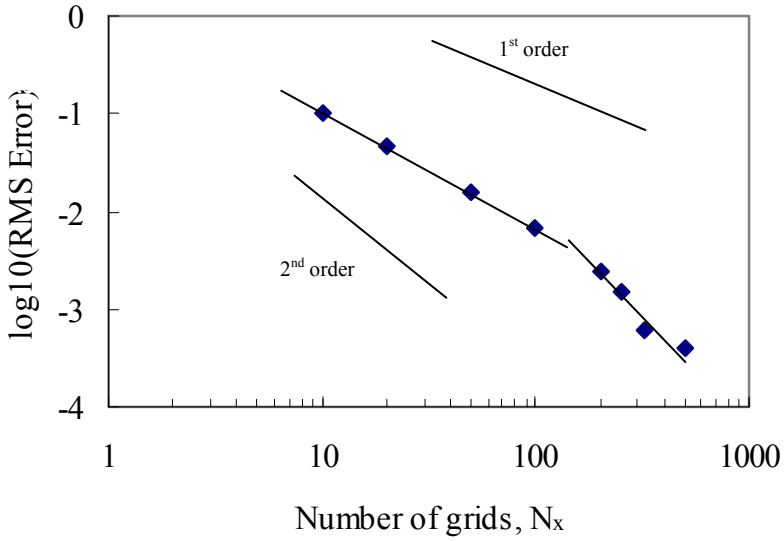

(b) Error in computed water depth

Figure 4.17: Convergence and errors in 1D simulation as a function of the number of grids

The normalized RMSE errors are plotted with respect to the normalized grid size on the bottom of Figure 4.17(b). The expected first- and second-order are also shown. The slope of the error curve is expected a second-order as the model is written in CDS; however, the error shows irregular behavior on coarse grids with the slope of the first-order convergence. As the grid is refined, the error reduces to second-order. This irregular behavior is not clearly explained with the theory. Research shows the numerical stability of implicit methods does not guarantee the numerical accuracy at large Courant-Friedrichs-Lewy (CFL) numbers (Hodges, 2004). He found

the second-order accuracy of the Crank-Nicolson method for unsteady flows was not assured for CFL less than unity. Similarly, if the error associated with time interval dominates the error of the model solution at coarse grids, the slope of error may not be of the second-order. As the grid is refined, the slope of error becomes second-order as the influence of the time interval related error becomes negligible.

Similar behavior is observed in a 2D error simulation. An inclined rectangular domain is used for 2D simulation with the variables as follow: L = 30 m, W = 15 m, r = 250 mm/hr, and S_x = S_y = 0.01. The steepest surface slope goes diagonally from the north-west corner to the south-east corner. In Figure 4.18, the error with respect to the number of grids is plotted in the log-log scale.

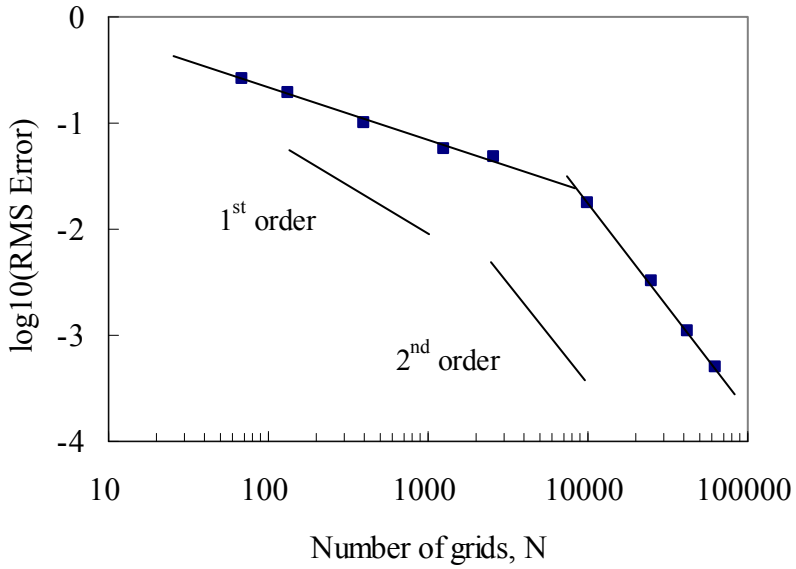

Figure 4.18: Errors in 2D simulation with different cell sizes

Ferziger and Peric (2002) suggests that the solution of an implicit method will be bounded if the time interval (Δt) is smaller than twice of the maximum Δt of an explicit scheme limited by CFL condition. Figure 4.19 shows the error in 1D flow simulation with respect to time interval. To assess the influence of nonlinear iteration, the model is modified so that the diffusion coefficient is constant (Case 1), and the original nonlinear model is simulated for comparison (Case 2).

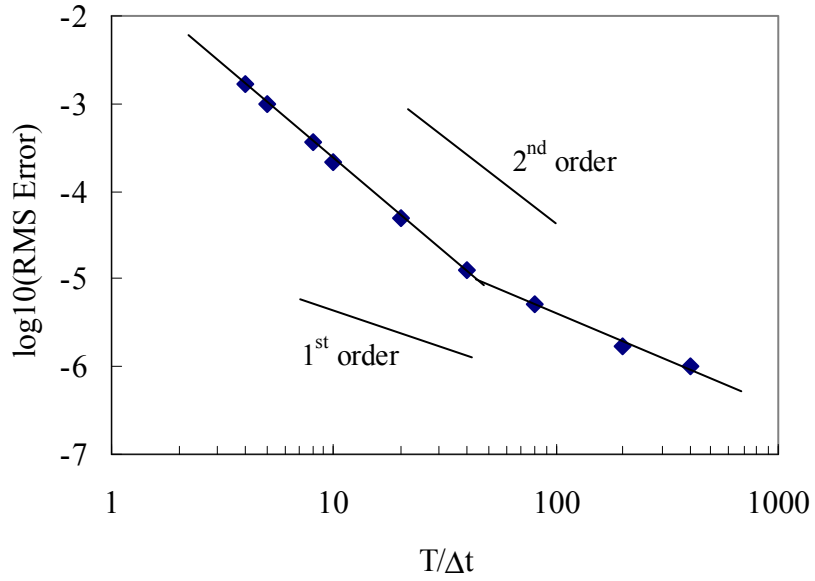

(a) Case 1: linear model

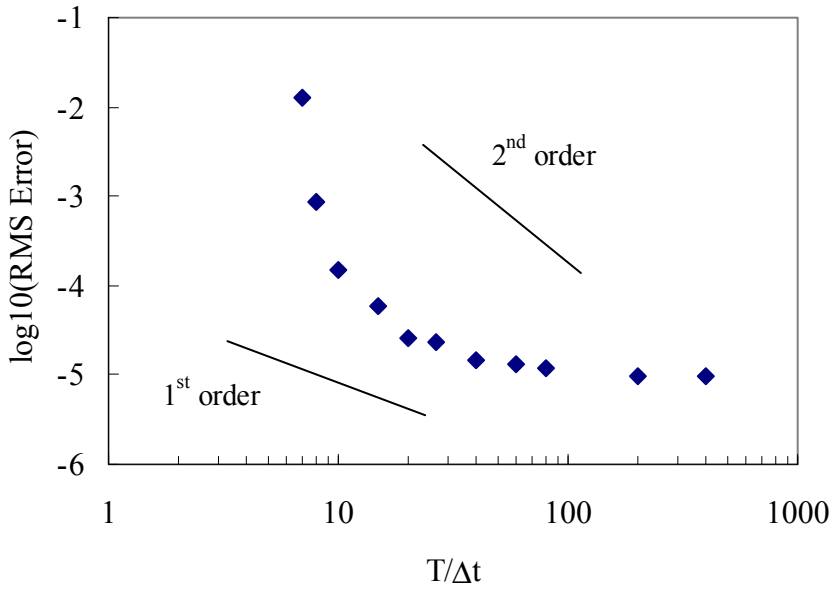

(b) Case 2: nonlinear model

Figure 4.19: Error in the solution for 1D flow with different time intervals for (a) linear model and (b) nonlinear model

The model solutions are bounded within the simulated range of time intervals. The error of the linear model is piecewise linear: second-order on large time intervals and first-order on small intervals. Meanwhile, the error of the nonlinear model shows similar pattern to the linear model while it is more rounded in shape. Also, the rate of error reduction as a function of time interval is very slow at small time intervals. The error generated from nonlinear iteration or the error generated from relatively large space interval may cause the result not to be second-order of CN method as the resolution of time interval increases.

As time step increases the solution eventually reaches steady state. Thereafter, any further simulation is trivial under constant rainfall intensity because the solution does not change with increasing time step. Therefore, the model stops running when the difference in solutions between time steps becomes small. The L_2 and L_∞ norms are defined such that they compare the solutions between two time steps.

$$\|x\|_2^{\,k} = \frac{\sqrt{\sum_{i=1}^{Nx}\sum_{j=1}^{N_y}\left|h_{i,j}^{\,k} - h_{i,j}^{\,k-1}\right|^2}}{h_{avg}^{k}}$$

$$\|x\|_\infty^{\,n} = \max_{i,j}\left|\frac{h_{i,j}^{\,k} - h_{i,j}^{\,k-1}}{h_{i,j}^{\,k}}\right| \qquad (4.3.3)$$

When the L_2 and L_∞ norms become smaller than the stopping criteria, the solution is considered to have reached steady state. It should be noted that the stopping criteria need to be determined carefully so numerical errors do not propagate during the solution procedure. Because the norms are normalized by average numbers, tolerance values for CG solver and nonlinear iteration used in the model simulation are 0.001 for CG iteration and 0.005 for nonlinear iteration. These values balance the accuracy in the solution and the computing time most efficiently. Same criteria applies to L_2 and L_∞ norms such that the iteration continues until both norms become smaller than the tolerance values.

Computation time increases proportionally as the size of a domain increases. Average computation time for sheet flow to reach steady state on different widths of roads is presented in Table 4.1. The model is run on personal computers with Intel(R) Pentium(R) 4 CPU 2.80GHz and 1GB RAM. As the number of lanes doubles, the average computing time also increases by nearly a factor of two.

Table 4.1: Computation time with respect to number of lanes

Number of lanes*	Number of cells**	t_{avg} (min)***
4	26,220	37.1
6	35,343	51.7
8	44,460	65.0

* Number for both sides of a road

** L = 230 m, $W_{each\ lane}$ = 3.7 m, $W_{shoulder}$ = 3 m , Δx = 0.6 m, Δy = 0.3 m, Δt = 0.4 sec

*** Time to reach steady state condition

4.3.2 Evaluation of Boundary Condition Implementation

The open boundary conditions at upstream end and downstream ends are evaluated by simulating sheet flow on a plane tilted surface. The upstream and downstream boundary values are compared with those within the domain. For this comparison, cell values at the same location in the transverse direction are compared. A diagonally slanted asphalt-type surface with L = 30 m, W = 15 m, S_y = 2.0%, r = 250 mm/hr is used in this test. Because the surface slope is constant everywhere, the ponding depth should be constant in the longitudinal direction at any

cross section within the domain including boundaries. For the comparison, steady state solution at a station in the middle of domain is used as reference (i.e. exact solution).

Table 4.2: Errors in the upstream boundary condition

S_x (%)	0.1	1.0	2.0	4.0
RMS (mm)	0.023	0.064	0.072	0.079
$\|d\|_{max}$[a] (mm)	0.073	0.122	0.169	0.216
$\|d\|_{min}$ (mm)	0.000	0.000	0.000	0.000
$\|d\|_{avg}$ (mm)	0.021	0.058	0.063	0.059

[a] Difference in upstream boundary values between those estimated by the open B.C and exact solution

As shown in Table 4.2 the error of the upstream boundary condition increases as the longitudinal slope increases. Extended flow paths that contribute to the inflow to upstream end result in the increase in error. However, the estimated error is overall very small such that the error is negligible. The estimated error in the downstream boundary condition is summarized in Table 4.3. Again, the estimated error is small enough to be ignored. No trend is found in the error with respect to longitudinal slope.

Table 4.3: Errors in the downstream boundary condition

S_x (%)	0.1	1.0	2.0	4.0
RMS (mm)	0.018	0.005	0.004	0.029
$\|d\|_{max}$[a] (mm)	0.034	0.026	0.018	0.057
$\|d\|_{min}$ (mm)	0.000	0.000	0.000	0.000
$\|d\|_{avg}$ (mm)	0.017	0.003	0.002	0.019

[a] Difference in downstream boundary values between those estimated by the open B.C and exact solution

4.3.3 Model Verification

One advantage of the proposed computer model is versatility in application. As long as the geometry file is written such that the model can read, the proposed model generates a grid space and computes the sheet flow depth and discharge on the domain. In this section, the model solution for one dimensional flow will be compared to the kinematic wave model solution to validate the accuracy of the model. The model equation shown in equation (4.2.5) does not have an analytical solution, so the numerical solution of the proposed model cannot be directly compared to the exact solution for validation; instead, the model solution is compared with an analytical solution of the kinematic wave (KW) model for a case of 1D flow. A mild slope surface (S_o = 1%) and a steep slope surface (S_o = 5%) are used for the simulation. The results are shown in Figure 4.20 (mild on left side, steep on right side).

In Figure 4.20, the RMS errors between the numerical and the analytical solutions at steady state are 0.043% and 0.023%, respectively on 1% and 5% slope. The no-through flow

boundary condition at the upstream end in the proposed diffusion wave model makes a difference in the steady state solution. Consequently, about 50% of the error occurs at the 5 grid points on the upstream end and the accuracy of the model solution is even better than it appears in the RMS errors.

Time series solutions are compared in Figure 4.21. The KW analytical solution and the DW numerical solution are in good agreement on a rising hydrograph. A smooth transition in DW solution near the peak is observed. As Kazezyılmaz-Alhan and Medina (2007) noted, the pressure gradient term in the rising part of the DW model affects the solution being smooth near the peak. It is also observed that the DW model slightly overestimates the flow rate at the steady state compared to the kinematic wave solution. Based on the spatial and temporal comparisons, we can conclude that the proposed DW model gives reliable solutions for 1D flow and may be extended to 2D flow problems.

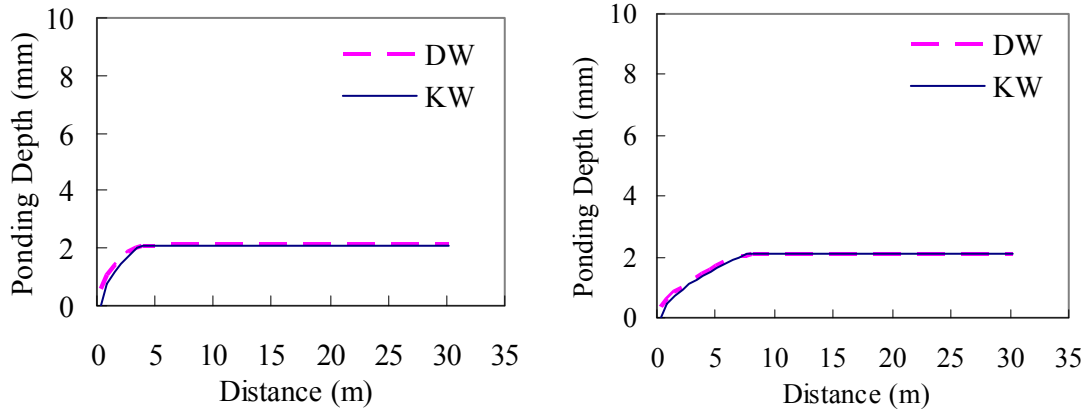

(a) at t = 30 seconds

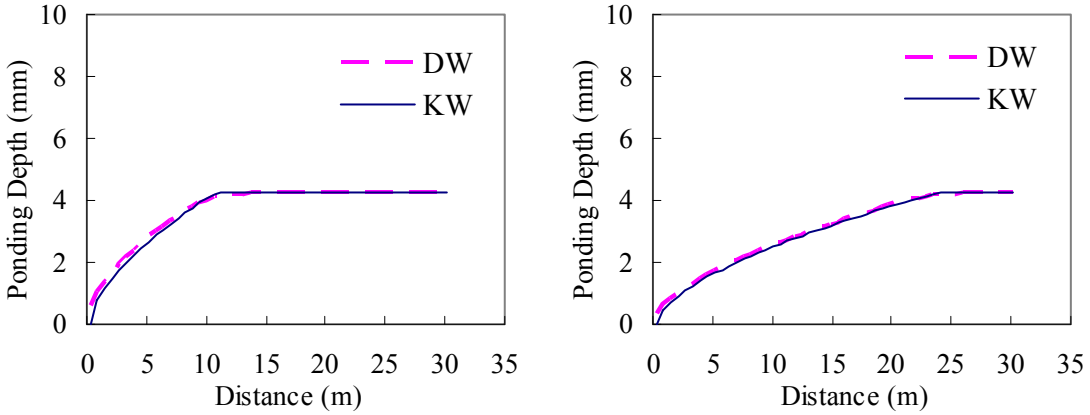

(b) at t = 60 seconds

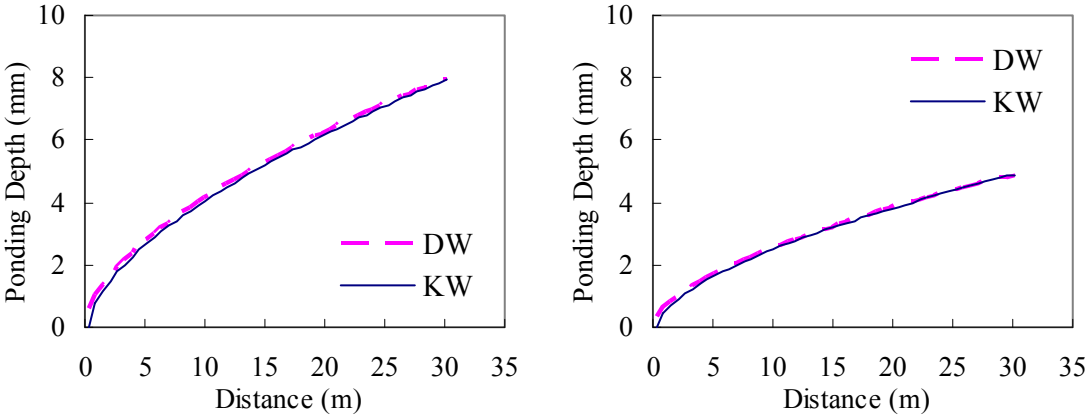

(c) at steady state ($T_{c,KW}$ = 120 sec, $T_{c,DW}$ = 70 sec)

Figure 4.20: Comparison of the model solutions with kinematic wave model solutions at different time levels.
r = 250 mm/hr, n = 0.015, L = 30 m, Δx = 0.6 m, Nx = 50. (S_o=1% shown on the left, 5% on the right)

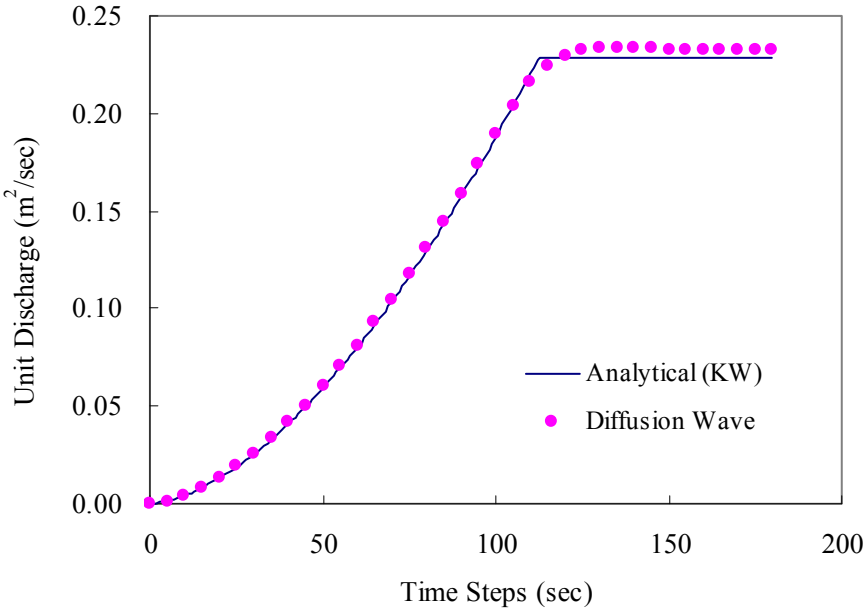

Figure 4.21: Rising hydrograph of the diffusion wave model for a 1D flow: So = 1%, Manning coefficient = 0.015, r = 200 mm/hr, L = 30m

4.4 Algorithm for Curb-opening Inlets

This subsection describes algorithms that have been developed to simulate flow near curb-opening inlets. Curb-opening inlets are commonly installed along the curb side of highways. The interval between inlets and the inlet size are determined based on the amount of stormwater runoff for a certain design rainfall intensity. A typical curb-opening inlet configuration is shown in Figure 4.22.

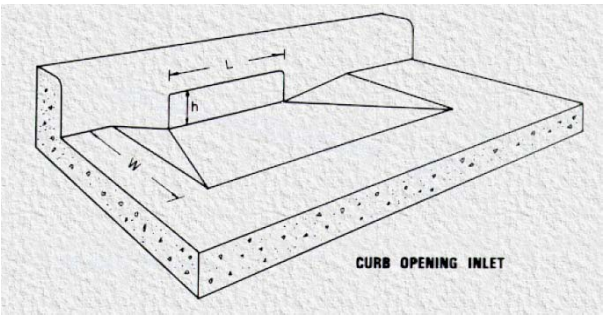

Figure 4.22: Schematic view of a depressed curb-opening inlet (HEC12)

A curb-opening inlet places the inlet on the wall of the roadside curb; therefore, it is reasonable to design an algorithm such that the inlet is located at the outside of roadside boundary cells. The schematic at the cell scale is shown in Figure 4.23. The critical flow condition applies on the outside interface of a boundary cell. Thus, the proposed algorithm does not consider lateral flooding over inlets.

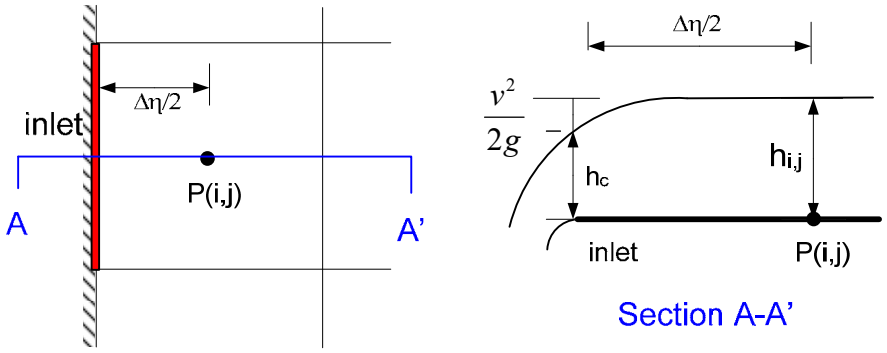

Figure 4.23: Schematic of the cell scale configuration of a curb-opening inlet

For the critical flow condition, the Froude number is forced to be one. Then one gets a relationship between flow rate and water depth.

$$Fr = \frac{v}{\sqrt{gh}} = 1 \quad \Rightarrow \quad v_c = \sqrt{gh_c} \tag{4.4.1}$$

Assuming that the flow depth at the cell center corresponds to the available specific energy for lateral flow into the curb inlet, one may use the critical flow condition at the inlet to determine the inlet depth as a function of flow depth at the center of the cell (at critical flow, one-third of the specific energy is associated with flow velocity and two-thirds is associated with flow depth)

$$\left(h_c^{\,k+1}\right)^{m+1} = \frac{2}{3}\left(h_{i,j}^{k+1}\right)^m \tag{4.4.2}$$

In equation (4.4.2) the index m denotes the m^{th} step of the nonlinear iteration. The critical depth at the current nonlinear iteration step is estimated based on the values computed at the previous iteration. The diffusion coefficient for the flow coming into the inlet opening is estimated as follows.

$$\left(D_\eta\right)_{inlet} = \frac{h_c^{\,5/3}}{n\sqrt{S_f}} \text{ where } S_f = \frac{H_{i,j} - \left(z_{inlet} + h_c\right)}{w_{i,j}/2} \tag{4.4.3}$$

In equation (4.4.3) $w_{i,j}$ is the width of the cell-(i,j). The conveyance on the inlet boundary is

$$\left(C_\eta\right)_{inlet} = \frac{2\left(D_\eta\right)_{inlet}}{w_{i,j}^{\,2}} \tag{4.4.4}$$

There are two possible scenarios in this case concerning the placement of the inlet.

Case I. Inlet is located at $(i,1)$. The discrete equation for this case takes the form

$$\begin{aligned}&\left(\left(C_\xi\right)_{i-1/2,1} + \left(\boldsymbol{C_\eta}\right)_{\boldsymbol{inlet}} + \left(C_\xi\right)_{i+1/2,1} + \left(C_\eta\right)_{i,1+1/2} + 2/\Delta t\right)h_{i,1}^{k+1} - \left(C_\xi\right)_{i-1/2,1}h_{i-1,1}^{k+1} \\ &\quad - \left(C_\xi\right)_{i+1/2,1}h_{i+1,1}^{k+1} - \left(C_\eta\right)_{i,1+1/2}h_{i,2}^{k+1} = f_{i,1}\end{aligned} \tag{4.4.5}$$

In equation (4.4.5) the forcing term is defined by

$$
\begin{aligned}
& f_{i,1} = (2/\Delta t)h_{i,1}^{k} + 2r \\
& -\left(C_{\xi}\right)_{i-1/2,1}^{k+1}\left(z_{i,1} - z_{i-1,1}\right) - \left(C_{\xi}\right)_{i+1/2,1}^{k+1}\left(z_{i,1} - z_{i+1,1}\right) \\
& -\left(C_{\eta}\right)_{inlet}^{k+1}\left(z_{i,1} - z_{inlet}\right) - \left(C_{\eta}\right)_{i,1+1/2}^{k+1}\left(z_{i,1} - z_{i,2}\right) + \left(C_{\eta}\right)_{inlet}^{k+1} h_{inlet}^{k+1} \\
& -\left(C_{\xi}\right)_{i-1/2,1}^{k}\left(H_{i,1}^{k} - H_{i-1,1}^{k}\right) - \left(C_{\xi}\right)_{i+1/2,1}^{k}\left(H_{i,1}^{k} - H_{i+1,1}^{k}\right) \\
& -\left(C_{\eta}\right)_{inlet}^{k}\left(H_{i,1}^{k} - H_{inlet}^{k}\right) - \left(C_{\eta}\right)_{i,1+1/2}^{k}\left(H_{i,1}^{k} - H_{i,2}^{k}\right)
\end{aligned}
\tag{4.4.6}
$$

Case II. Inlet is on the side of (i,N_y)

$$
\begin{aligned}
& \left(\left(C_{\xi}\right)_{i-1/2,Ny} + \left(\boldsymbol{C_{\eta}}\right)_{\boldsymbol{inlet}} + \left(C_{\xi}\right)_{i+1/2,Ny} + \left(C_{\eta}\right)_{i,Ny-1/2} + 2/\Delta t\right) H_{i,Ny}^{k+1} - \left(C_{\xi}\right)_{i-1/2,Ny} H_{i-1,Ny}^{k+1} \\
& -\left(C_{\xi}\right)_{i+1/2,Ny} H_{i+1,1}^{k+1} - \left(C_{\eta}\right)_{i,Ny-1/2} H_{i,Ny-1}^{k+1} = f_{i,Ny}
\end{aligned}
\tag{4.4.7}
$$

In equation (4.4.7) the forcing term takes the form

$$
\begin{aligned}
& f_{i,N_y} = (2/\Delta t)h_{i,1}^{k} + 2r \\
& -\left(C_{\xi}\right)_{i-1/2,N_y}^{k+1}\left(z_{i,N_y} - z_{i-1,N_y}\right) - \left(C_{\xi}\right)_{i+1/2,N_y}^{k+1}\left(z_{i,N_y} - z_{i+1,N_y}\right) \\
& -\left(C_{\eta}\right)_{i,N_y-1/2}^{k+1}\left(z_{i,N_y} - z_{i,N_y-1}\right) - \left(C_{\eta}\right)_{i,inlet}^{k+1}\left(z_{i,N_y} - z_{inlet}\right) + \left(C_{\eta}\right)_{inlet}^{k+1} h_{inlet}^{k+1} \\
& -\left(C_{\xi}\right)_{i-1/2,N_y}^{k}\left(H_{i,N_y}^{k} - H_{i-1,N_y}^{k}\right) - \left(C_{\xi}\right)_{i+1/2,N_y}^{k}\left(H_{i,N_y}^{k} - H_{i+1,N_y}^{k}\right) \\
& -\left(C_{\eta}\right)_{inlet}^{k}\left(H_{i,N_y}^{k} - H_{inlet}^{k}\right) - \left(C_{\eta}\right)_{inlet}^{k}\left(H_{i,N_y}^{k} - H_{inlet}^{k}\right)
\end{aligned}
\tag{4.4.8}
$$

The following example is considered: A 3-meter long curb inlet is placed at d_{in} = 3 m from the zero cross slope section as shown in Figure 4.24. Three different pavement surfaces with 2%, 4%, and 6% longitudinal slopes are simulated. After 120 seconds, the profile of water depth in the transverse direction at the station where the curb-opening inlet is placed shows depression of water surface near the curb, especially on the right side in Figure 4.25.

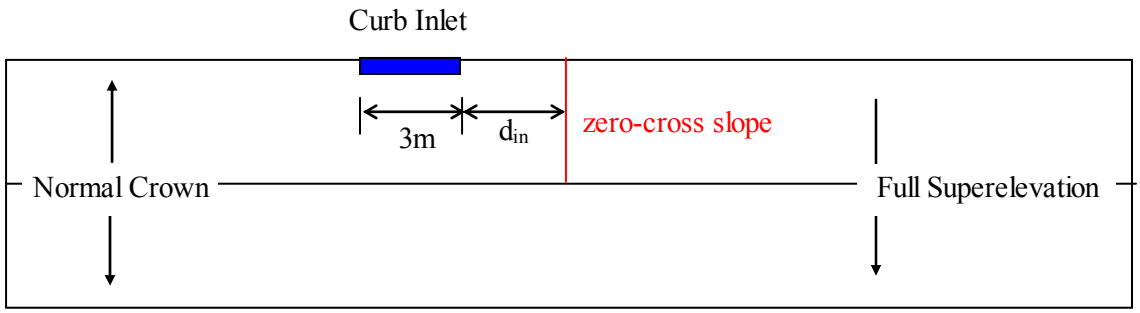

Figure 4.24: Scenario for curb-opening inlet simulation

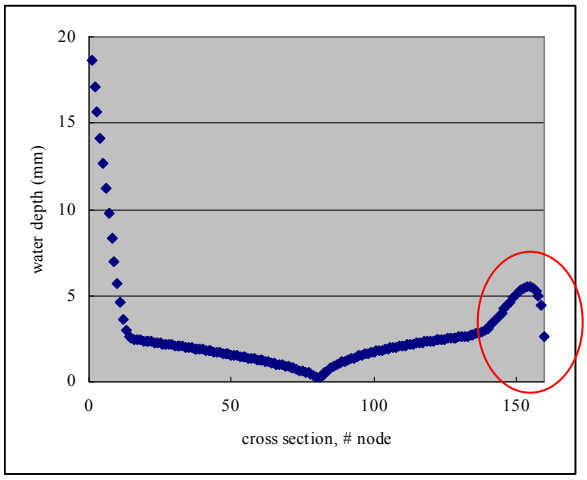

Figure 4.25: Depression in ponding depth at the inlet

The longitudinal profile of water depth along the road direction at the center of the left half of the road near the curb-opening is shown in Figure 4.26. Water depth is large for mild slope and decreases as the slope increases. The existence of curb inlet resulted in decreasing the water depth on traffic lanes by 1 ~ 2 mm.

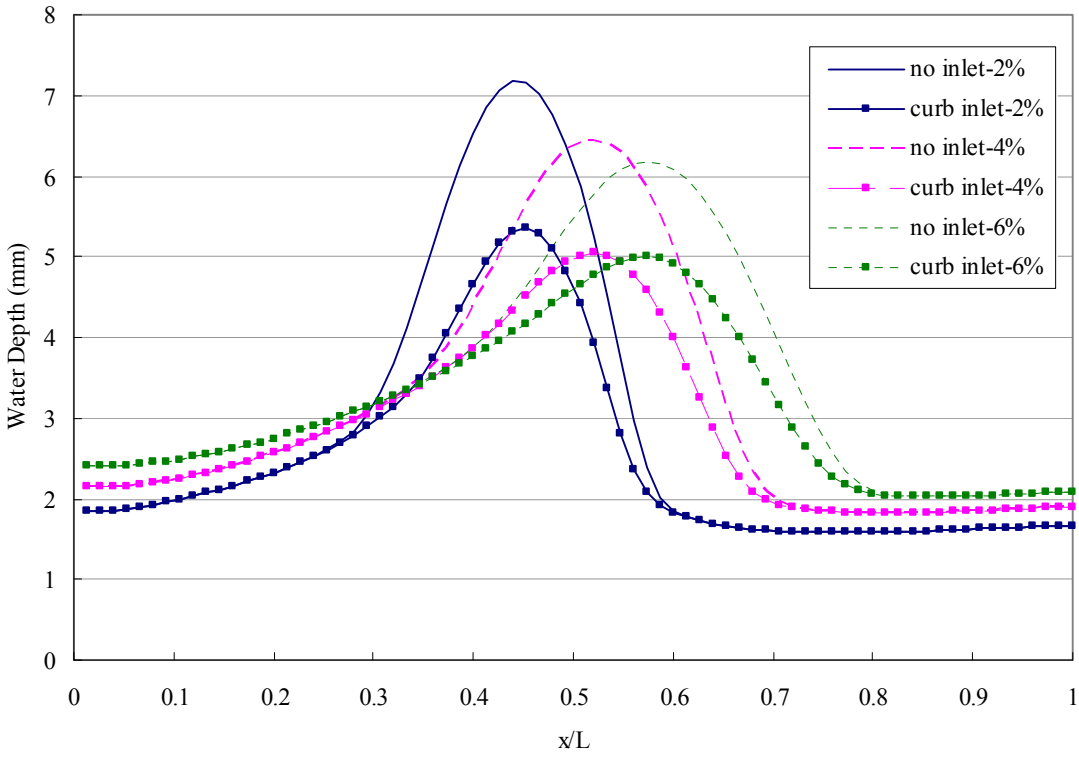

Figure 4.26: Performance of curb-opening inlet

Chapter 5. Model Application and Results

5.1 Stormwater Drainage under Normal Crown Conditions

Design of highway drainage systems is an iterative process, described briefly as follows. Potential inlet locations are identified and contributing drainage areas are calculated along with surface slopes, runoff coefficients, and surface roughness (Manning's n). The design discharge is calculated using the rational method. For the rational method, the rainfall intensity is calculated from the intensity-duration-frequency function for the area (county) with duration based on the time of concentration. The kinematic wave model is recommended for calculation of the time of concentration (FHWA HEC-12). TxDOT specifies a minimum duration (usually 10 minutes), which sets an upper limit on the rainfall intensity. Gutter flow is calculated using Manning's equation in the form presented by Izzard (1946), and the water spread across the gutter and roadway surface is calculated from the discharge. The resulting spread is compared with the limiting design spread, and the inlet spacing is adjusted. Equations are available for estimating inlet bypass for inlets on grade, and this additional discharge is added to the runoff from the rational method. TxDOT highway drainage projects are usually designed and analyzed using the *WinStorm* program package. *WinStorm* (Version 3) is a Windows-based computer application that represents the drainage network through drainage areas, nodes (inlets, junctions, manholes) and the links (conveyance channels, conduits, culverts) between nodes. Only a single longitudinal and transverse slope may be specified for a drainage area, and if a zero cross slope is specified, an infinite ponding width is calculated. Thus, in its present form, *WinStorm* is not applicable for design of superelevation transitions where the cross slope passes through zero.

Stormwater runoff behavior is modeled using Manning's equation. For normal crown conditions, the runoff depth increases with lateral distance from the crown location. In addition to lateral station location, runoff depth is a function of pavement type (roughness), lateral slope, longitudinal slope, and rainfall intensity. Tables 5.1 (concrete-type pavement roughness) and 5.2 (asphalt-type pavement roughness) present water film thickness (WFT) values at center and transverse edge-of-lane stations based on a lane width 3.66 m (12 feet) for different values of longitudinal slope (S_o). Lane 1 is closest to the roadway centerline. Depth calculations are made using kinematic wave theory. These WFT values are presented for comparison with superelevation transition runoff depth distributions calculated using the numerical model described in Chapter 4.

Table 5.1: WFT (mm) at different lateral stations for cross slope = 0.02 with Manning coefficient = 0.012. Effective rainfall intensity = 100 mm/hr (4 in/hr)

	Longitudinal Slope, S_o							
	0	0.005	0.01	0.02	0.03	0.04	0.05	0.06
Lane 1 Center	0.61	0.61	0.63	0.68	0.73	0.78	0.82	0.86
Lane 1 Edge	0.92	0.93	0.96	1.02	1.10	1.18	1.24	1.30
Lane 2 Center	1.18	1.19	1.22	1.31	1.41	1.50	1.59	1.66
Lane 2 Edge	1.40	1.41	1.45	1.55	1.67	1.78	1.88	1.98
Lane 3 Center	1.60	1.62	1.66	1.78	1.91	2.04	2.15	2.26
Lane 3 Edge	1.79	1.80	1.85	1.98	2.13	2.27	2.40	2.52

Table 5.2: WFT (mm) at different lateral stations for cross slope = 0.02 with Manning coefficient = 0.015. Effective rainfall intensity = 100 mm/hr (4 in/hr)

	Longitudinal Slope, S_o							
	0	0.005	0.01	0.02	0.03	0.04	0.05	0.06
Lane 1 Center	0.70	0.70	0.72	0.77	0.83	0.89	0.94	0.98
Lane 1 Edge	1.06	1.07	1.09	1.17	1.26	1.34	1.42	1.49
Lane 2 Center	1.35	1.36	1.39	1.49	1.61	1.71	1.81	1.90
Lane 2 Edge	1.60	1.62	1.66	1.78	1.91	2.04	2.15	2.26
Lane 3 Center	1.83	1.85	1.89	2.03	2.18	2.33	2.46	2.58
Lane 3 Edge	2.04	2.06	2.11	2.27	2.44	2.60	2.75	2.88

5.2 Description of Numerical Model Experiments

Road surface geometry and rainfall intensity are the major variables that affect stormwater runoff depth from pavement surfaces. The sensitivity of sheet flow to these variables is investigated through a series of numerical experiments on various road sections with different geometric configurations and rainfall intensity. Various shapes of asphalt concrete pavement (ACP) surfaces were designed with GEOPAK with the following variables: L = 460 m (1,500 ft), R = 610 m (2,000 ft), design speed = 100 km/hr, maximum superelevation rate = 4% (based on TxDOT design manual). The estimated time of concentration is less than three minutes in all cases, so the time series solution at t = 3 minutes is considered the steady state solution. Sensitivity of stormwater runoff is tested on 270 scenarios covering the following cases:

1. 2, 3, and 4 traffic lanes in one direction (i.e. 4, 6, and 8 lanes on both directions) with 3-meter roadside shoulder.
2. 15 longitudinal slopes 0.1%, 0.2%, 0.3%, … , 0.9%, 1.0%, 2.0%, …, 5.0%, 6%.
3. The patterns of sheet flow on the surface are categorized into two types based on the geometry of the road. As shown in Figure 5.1a, *Type-I* starts with the normal crown on the upstream end and finishes with full superelevation on the downstream end. *Type-II* starts with full superelevation and finishes with the normal crown (see Figure 5.1b).
4. Rainfall intensity of 100 mm/hr, 150 mm/hr, 200 mm/hr, and 250 mm/hr.

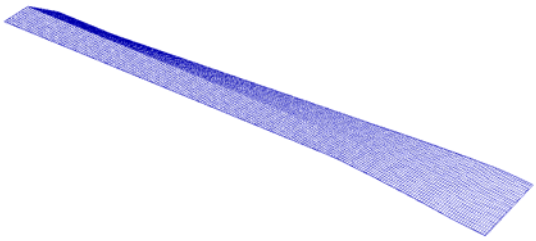

Type-I: Transition from normal crown to superelevation

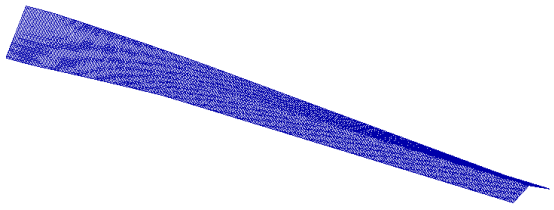

Type-II: Transition from superelevation to normal crown

Figure 5.1: Types of the roadway surfaces used in the numerical experiments

From the geometric point of view, *Type-I* and *Type-II* roads comprise a curved section, so the two sections face each other at full superelevation. In other words, *Type-I* is the entrance to a curvature and *Type-II* is the exit to a straight section from the curved section. Even though they can be treated as a whole section combined, their geometries induce different sheet flow behaviors, and they need to be analyzed separately.

The cross slope of *Type-1* road begins with normal crown and gradually changes to full superelevation toward the downstream end as shown in Figure 5.2. Due to the transition of cross slope from the negative normal crown to the positive full superelevation, there exists a zero cross slope (ZCS) section on the outside-lanes of the road. For the case shown in Figure 5.2, the ZCS section is located at 122m on the outside lanes.

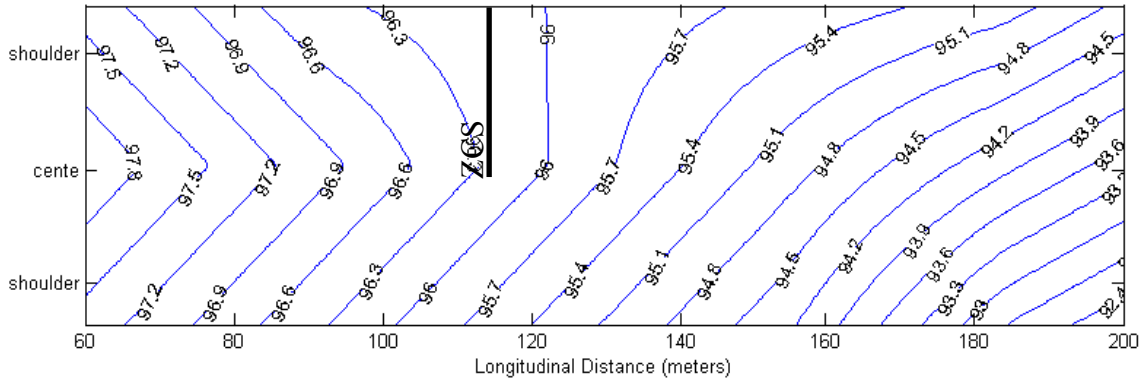

Figure 5.2: Contour plot of the surface elevation of a Type-I road (4-lane, S_x = 1.0%, ZCS at 122 meter station)

The cross slope of *Type-II* road begins with full superelevation and gradually turns into normal crown as the roadway continues to a straight section at the downstream end as shown in Figure 5.3. The ZCS section exists on the outside lanes due to the transition in cross slope.

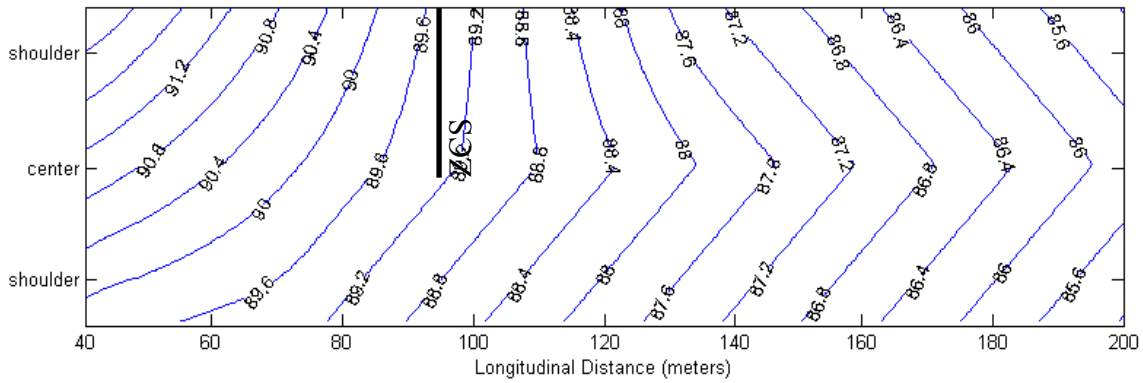

Figure 5.3: Contour plot of the surface elevation of a Type-II road (4-lane road, S_x = 1.0%, ZCS at 103 meter station)

5.3 Presentation and Analysis of Numerical Experiment Results

5.3.1 *Type-I* Configuration

"Mild" slope surfaces are defined as the surfaces on which the transition in the cross slope compromises the base slope, causing the longitudinal slope at the road side to be positive (uphill) or flat while the center line slope is negative (downhill). The profile of water depth on a mild slope surface is shown in Figure 5.4a labeled S_x = 0.1%. On this surface, the cross slope changes from the normal crown (-2%) to a full superelevation (+3.8%). As one can see from the figure, there is an accumulation of the stormwater at the outside-lane edge near the location of zero cross slope (ZCS). Due to the positive longitudinal slope of the outside-edge, the stormwater drainage occurs toward the upstream direction (left direction in Figure 5.4a) of the zero cross slope section (also see Figure 5.5a). For larger longitudinal slopes, the accumulated water at the outside-edge tends to flow inward towards the center of the road rather than draining to road side. On medium longitudinal slopes such as 1.0%, the sheet flow drains over the center of the road near the ZCS section. The flow forms a pond as it flows over the center of road near the ZCS section because of the sharp edge of the road center. On steep longitudinal slopes (e.g. 6.0%) the flow path becomes longer and the flow passes the road center far downstream from the ZCS section as steep longitudinal slope dictates the overall surface slope (see Figures 5.4c, 5.5c). The accumulated flow on these surfaces is typically continuous in profile with gradually increasing depth and size. Therefore, the maximum depth and flow rate occur at the downstream end (e.g., near 180m at the inside-lane edge in Figure 5.5c).

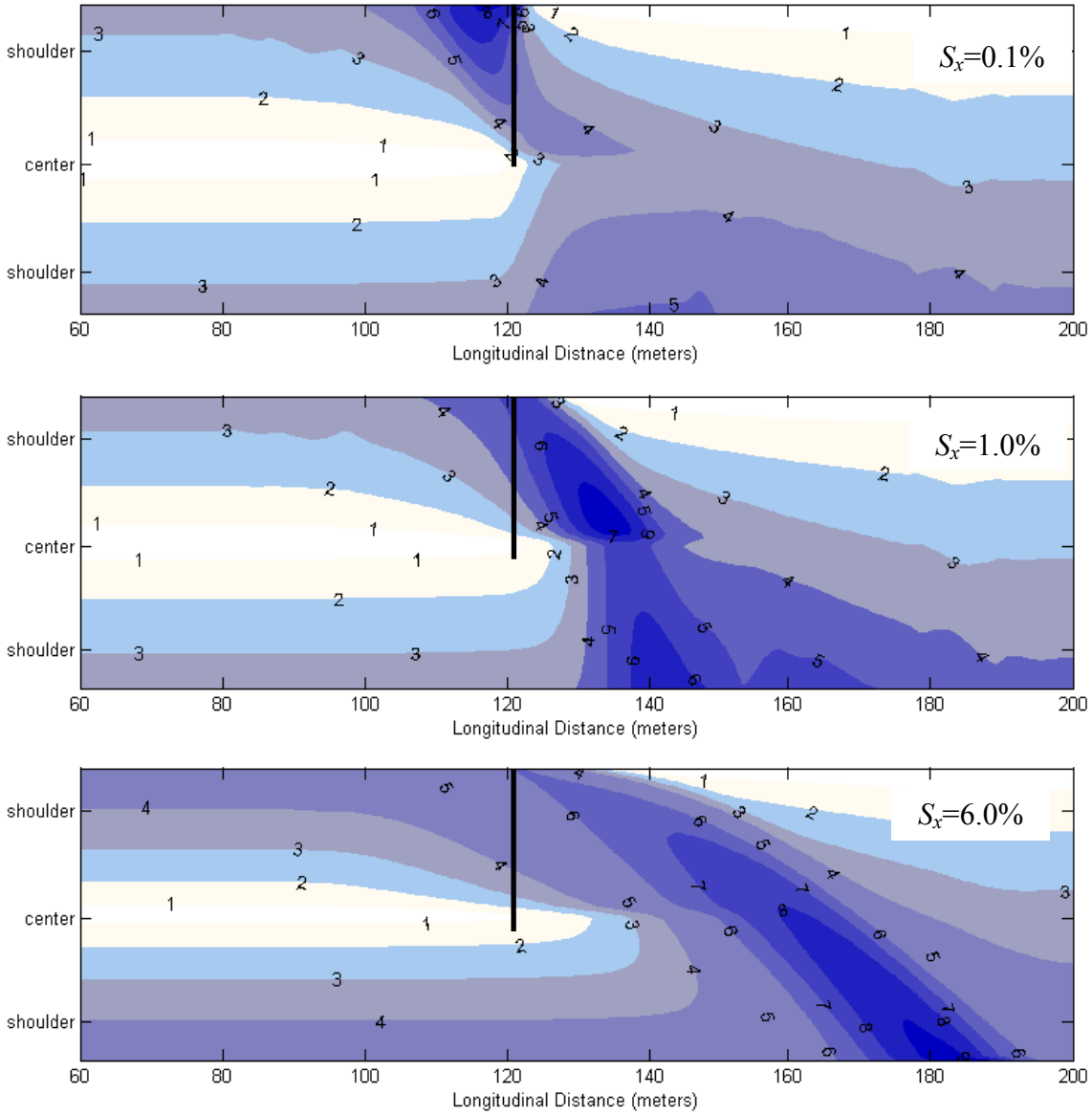

Figure 5.4: The profile of water depth at the steady state condition (Type-I, r = 250 mm/hr, 4-lane road)

Figure 5.5 shows the flow vector plots corresponding to the three runoff depth plots shown in Figure 5.4. In Figure 5.5a one may identify flow paths originating on the upper boundary, downstream side of the ZCS station that flow upstream and towards the roadway centerline, and then curve towards the upper boundary at the ZCS station, finally discharging from the roadway at the location with greatest ponding depth. The gradient along these flow paths is very small. In Figure 5.5b the flow paths with greatest depth originate near the roadway centerline on the upstream side of the ZCS station. These paths turn near the upper boundary at the ZCS station, and then cross all traffic lanes before discharging at the lower boundary. The largest depth accumulation is near the roadway centerline, before the flow 'spills' over the centerline and moves rapidly to the lower boundary. The behavior shown in Figure 5.5c is

similar to Figure 5.5b, except that the longitudinal slope dominates and there is no significant accumulation near the roadway centerline.

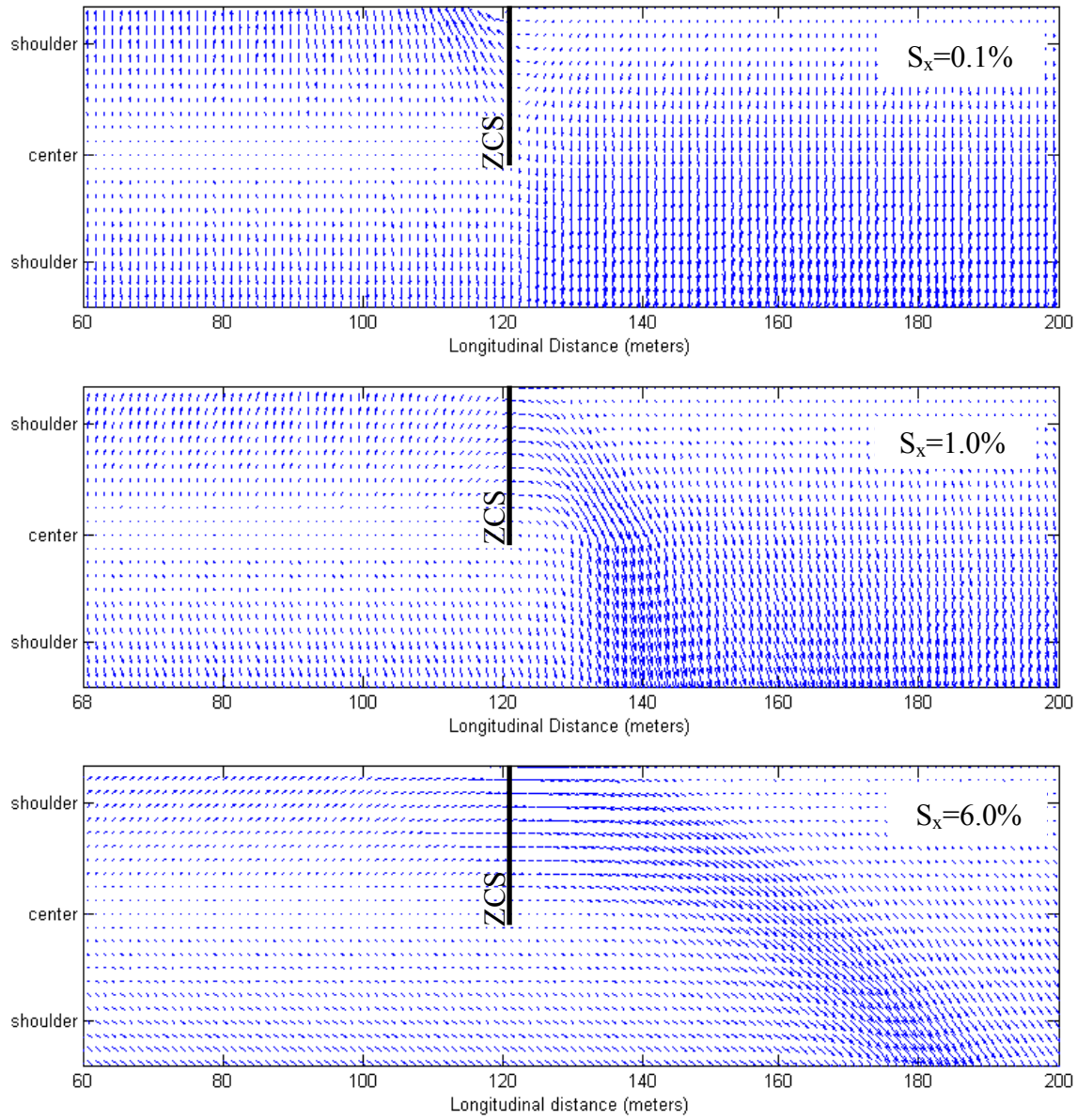

Figure 5.5: Vector plots of the unit flow rate at the steady state condition (Type-I, r = 250mm/hr, 4-lane road)

The different patterns of sheet flow on *Type-I* surfaces are mostly related to base longitudinal slopes. This will be discussed in greater detail later in this section under sensitivity analysis.

5.3.2 *Type-II* Configuration

The cross slope of *Type-II* roads changes from full superelevation to normal crown. As the cross slope of the outer half of the road changes from positive (full superelevation) to

negative (normal crown), the stormwater runoff flowing inward (toward the road center) on the upstream gradually turns outward along the direction of the steepest slope. As shown in Figure 5.6, the trail of concentrated flow grows larger and longer as the longitudinal slope increases.

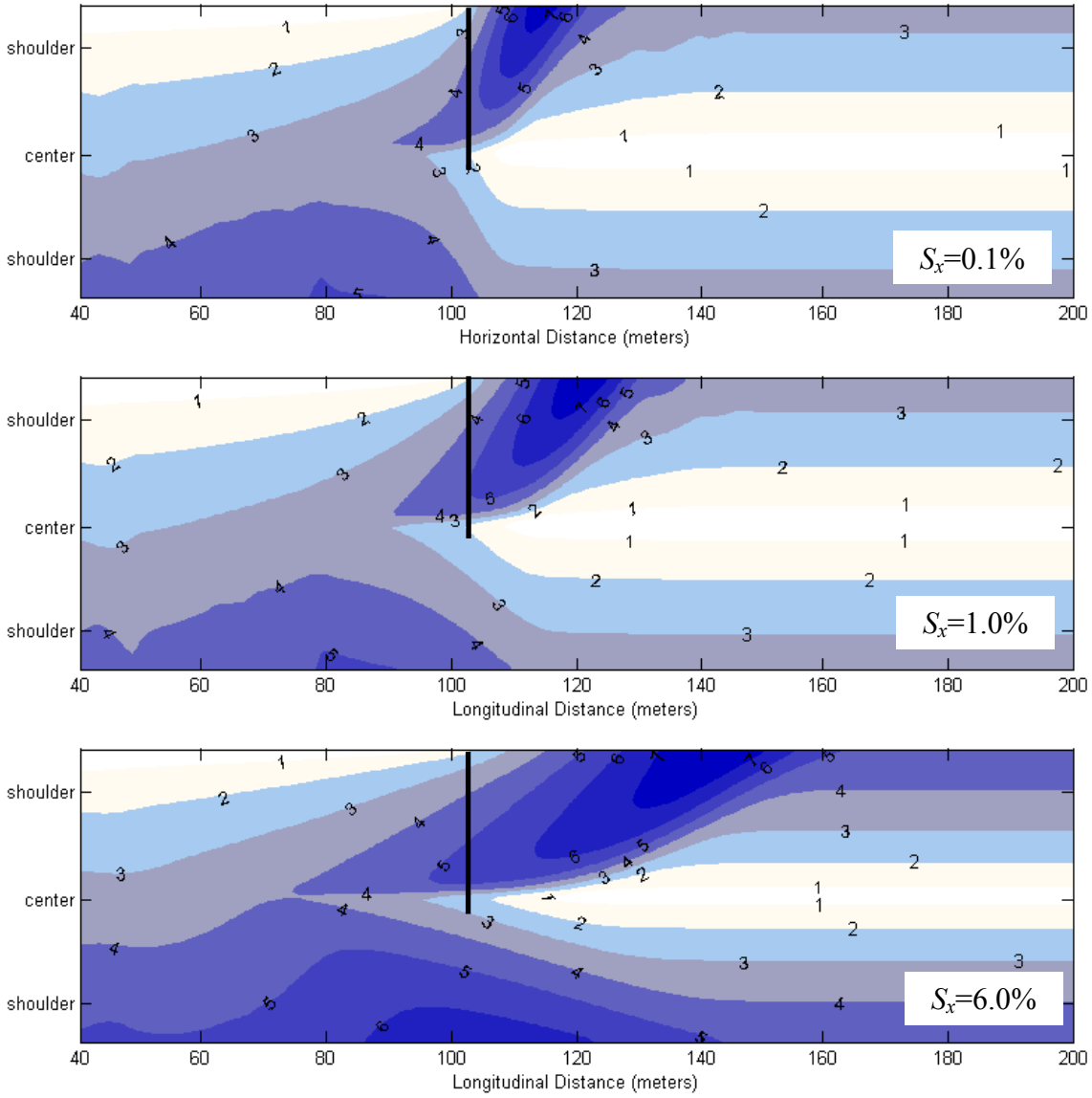

Figure 5.6: The profile of water depth at the steady state condition (Type-II, r = 250 mm/hr, 4-lane road)

Vector plots of unit flow (see Figure 5.7) show the direction of sheet flow near the ZCS section on *Type-II* surfaces. In all cases the flow direction on the outside lanes is parallel to the traffic direction at the ZCS as it transitions from flowing inward to outward, but the concentrated flow reaches the outside-lane edge farther downstream on greater longitudinal slopes.

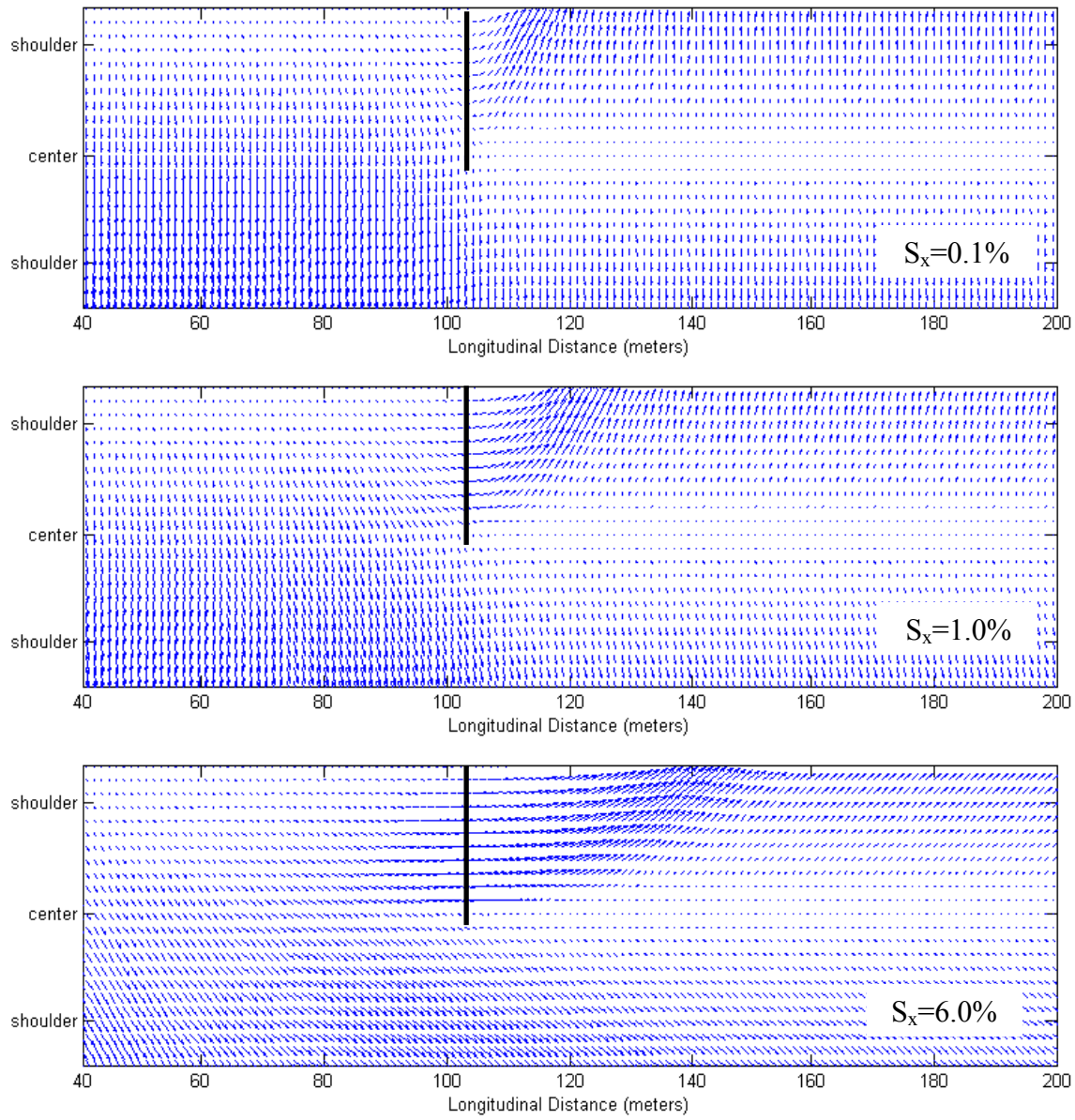

Figure 5.7: Vector plots of the unit flow rate at the steady state condition (Type-II, r = 250 mm/hr, 4-lane road)

The numerical tests show that the maximum depth is barely affected by longitudinal slope. On *Type-II* surfaces with longitudinal slopes varying from 0.1% to 6.0%, the estimated maximum depths were almost the same. This implies that the tendency of "spread" due to lateral gradient of water surface compromises the tendency of "accumulation" on these surfaces. Accordingly, the variation in the maximum depth on the *Type-II* surfaces in the numerical experiment is limited to less than one millimeter while the longitudinal slope varies from 0.1% to 6.0% as shown in Figure 5.8. Meanwhile, the size (width) and length of the accumulated flow increase as the longitudinal slope gets steeper.

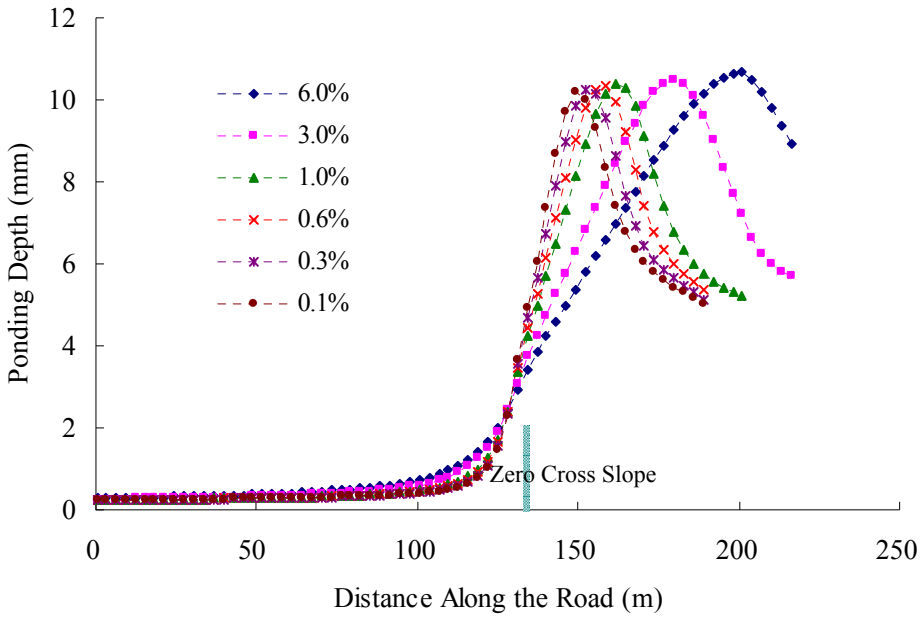

Figure 5.8: Longitudinal profile of ponding depth at the inside end of 8-lane road under 250 mm/hr rainfall (Type-II roads)

The area on the traffic lanes flooded by a certain depth or greater is much more on steep slope roads. In Figure 5.8, the distance along the road covered with 9 mm or greater depth is approximately 10 m on the 0.1% road. On the 6.0% road, a much greater distance (~35 meters) is flooded with the same depth of water. This implies that there tends to be more water ponded on the road surface on longitudinally steep roads. In conclusion, a near-flat longitudinal slope is recommended as the optimal longitudinal slope for *Type-II* roads, under the condition that it does not deteriorate the drainage along the roadside in case roadside curbs exist.

5.4 Sensitivity Analysis

5.4.1 Longitudinal Slope

In this chapter, the degree of storm water accumulation and spread based on the level of longitudinal slope is investigated. Different longitudinal slopes affect the direction of the downhill slope of road surfaces and pattern of the flow. As mentioned in section 5.3, model simulation on *Type-I* surfaces shows interesting results when different longitudinal slopes are used. The accumulation of sheet flow on the 0.1% slope is limited to the outside-lane edge near the ZCS section. The positive (uphill) longitudinal slope toward downstream at the outside-lane edge generates reverse flow in this area. Because the flow paths lead to the road side edge, the accumulated flow does not propagate to the inside lanes. On 1.0% slope, there exists no positive longitudinal slope within the domain because the base longitudinal slope is larger than the compromising uphill slope generated by the superelevation transition. Therefore, the accumulated water at the outside-lane edge flows inward as it passes the ZCS section. The flow ponds near the center of road and spreads out as it flows over the center line. The geometric interpretation of these results based on the relative gradient (G) is discussed in Section 2.6.

Flow responses on different longitudinal slopes, 0.1%, 1.0%, and 6.0%, are directly compared at several locations as shown in Figure 5.9. The sections are at different longitudinal stations. The selected locations include the normal crown and the stations where the maximum depth occurs on each longitudinal slope: 0.1% road at 118 m, 1.0% at 135 m, and 6.0% at 185 m. At normal crown, the profile of water depth on 0.1% road is slightly lower than 1.0% road, but there is little difference between the two. The profile on 6.0% road appears apparently higher than the other slopes. Assuming that the water flows along the steepest slope, the flow lengths on a 7.3 m width (from the road center to side edge) road is 7.388 m, 8.138 m, and 23.10 m for 0.1%, 1.0%, and 6.0 % roads, respectively. Flow depth is proportional to the length of flow, but is inversely proportional to surface slope. Considering the relative significance of flow length and surface slope, one can expect the extent of the differences in the water depth profiles at normal crown shown in Figure 5.9a.

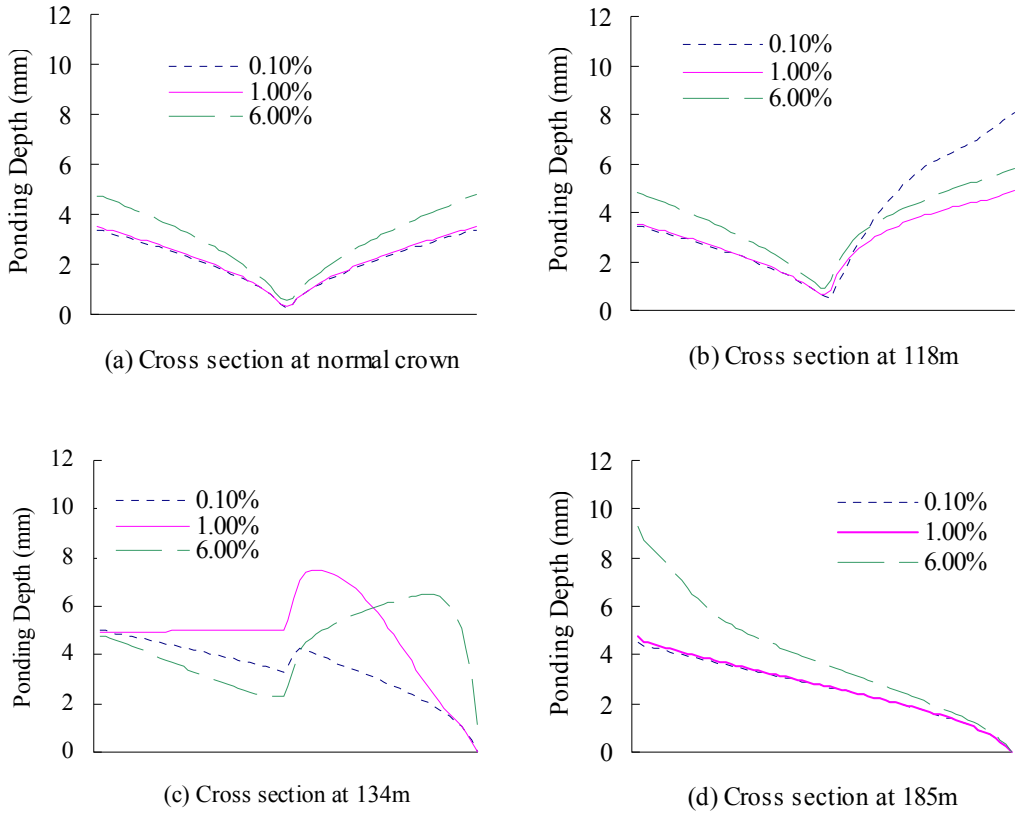

Figure 5.9: Cross sectional profile of water depth at different locations of the Type-I roads shown in Figure 5.4

The 1.0% road at x = 134 m has a fairly uniform depth of 5 mm on all the inside lanes, and the peak depth occurs on the outside lanes; therefore, almost three quarters of the cross section is flooded with at least 5 mm depth of water. Water depth on the outside-lane edge becomes nearly zero as the cross slope turns positive (uphill) toward the outside edge after passing the ZCS, and the accumulation of water moves to inside lanes.

The longitudinal slope of the road affects the dynamics of the flow. As shown in Figure 5.10, the location of the maximum depth moves downstream as the base longitudinal slope of the road increases.

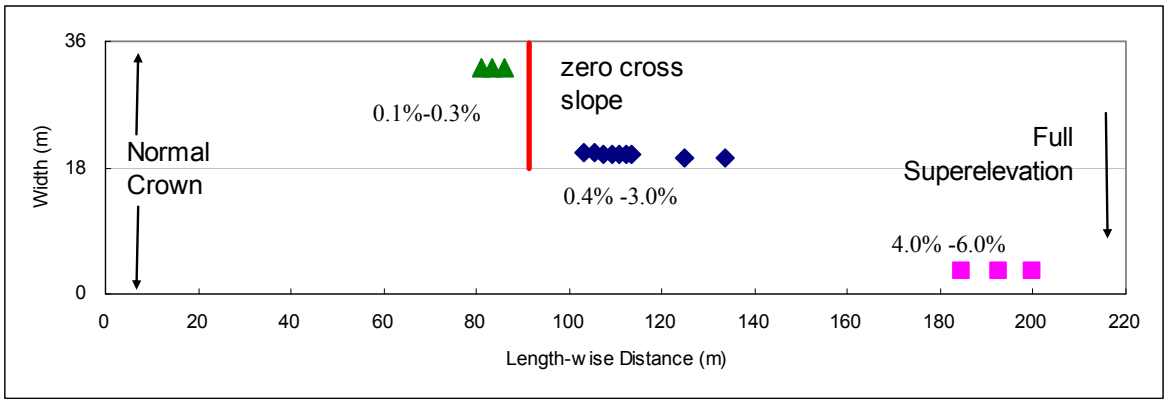

Figure 5.10: Locations of peak depth for steady state conditions on various longitudinal slope surfaces (Type-I roads)

On mild slope surfaces (S_x=0.1%-0.3%), the maximum depths are located at the outside-lane edge near the zero cross slope section (triangles). However, the location of the maximum depth jumps to the center of road as the longitudinal slope increases to S_x=0.4%-3.0% (diamonds). For longitudinal slope larger than 4.0%, the location of the maximum depth occurs at the inside edge far downstream from the zero cross slope section (squares). The relative change in the longitudinal slope at the outside-lane edge and the abrupt change in the cross slope at the center of may create such discontinuities. On mild longitudinal slopes, the increase in surface elevation due to the transition in cross slope overcomes the base longitudinal slope. As a result, the longitudinal slope of the outside-lane edge becomes positive while the center line and inside-lane edge have negative slopes. Because of these opposite slopes, there exists a stagnation point on the road, where the road surface forms a plateau, and the surface shape is similar to a saddle. A stagnation point may also be called a saddle point. Figure 5.11 shows an example of a stagnation point on a 0.1% slope road. Due to hyperbolic shape of the surface near the stagnation point, the flow diverges near the stagnation point to two opposite directions.

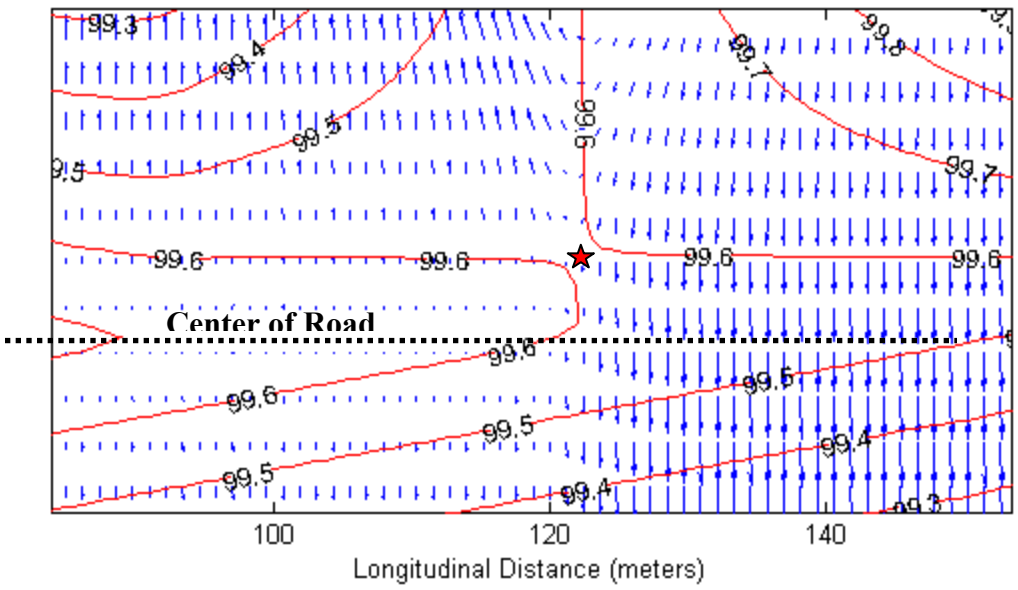

Figure 5.11: Saddle point at the ZCS section on a 0.1% slope road.
Contours show surface elevation and arrows represent the direction and magnitude of unit flow on the surface at steady state

The location of the stagnation point is affected by longitudinal slope. If the base longitudinal slope is small, the stagnation point is located near the center of road at the ZCS section as shown in Figure 5.11. On larger longitudinal slopes, the location of the stagnation point moves to the outside-lane edge, and if the base longitudinal slope is large enough to make the slope of the outside-lane edge remain negative, it eventually disappears (see Figure 5.12). The gap between the locations of the peak water depths on 0.3% and 0.4% roads shown in Figure 5.10 can now be explained by this concept. The location of the stagnation point on the 0.4% must be close to the road side enough to make the diverged flow flowing toward the center larger than the flow going to the outside-lane edge.

The center of the road is the axis of rotation for normal crown shapes or superelevation transitions; therefore, the center is theoretically sharply angled in the transverse direction. As a result, the inside lanes on a superelevation transition section have steeper cross slope than outside lanes with the center of road sharply angled. Once the base longitudinal slope becomes large enough for the stagnation point to move off the road, the location of the maximum depth moves toward the center of road as water flows inward after passing the ZCS section. The accumulated water near the center of road spreads out quickly as it flows over the center line due to "weir" effect of the center of road.

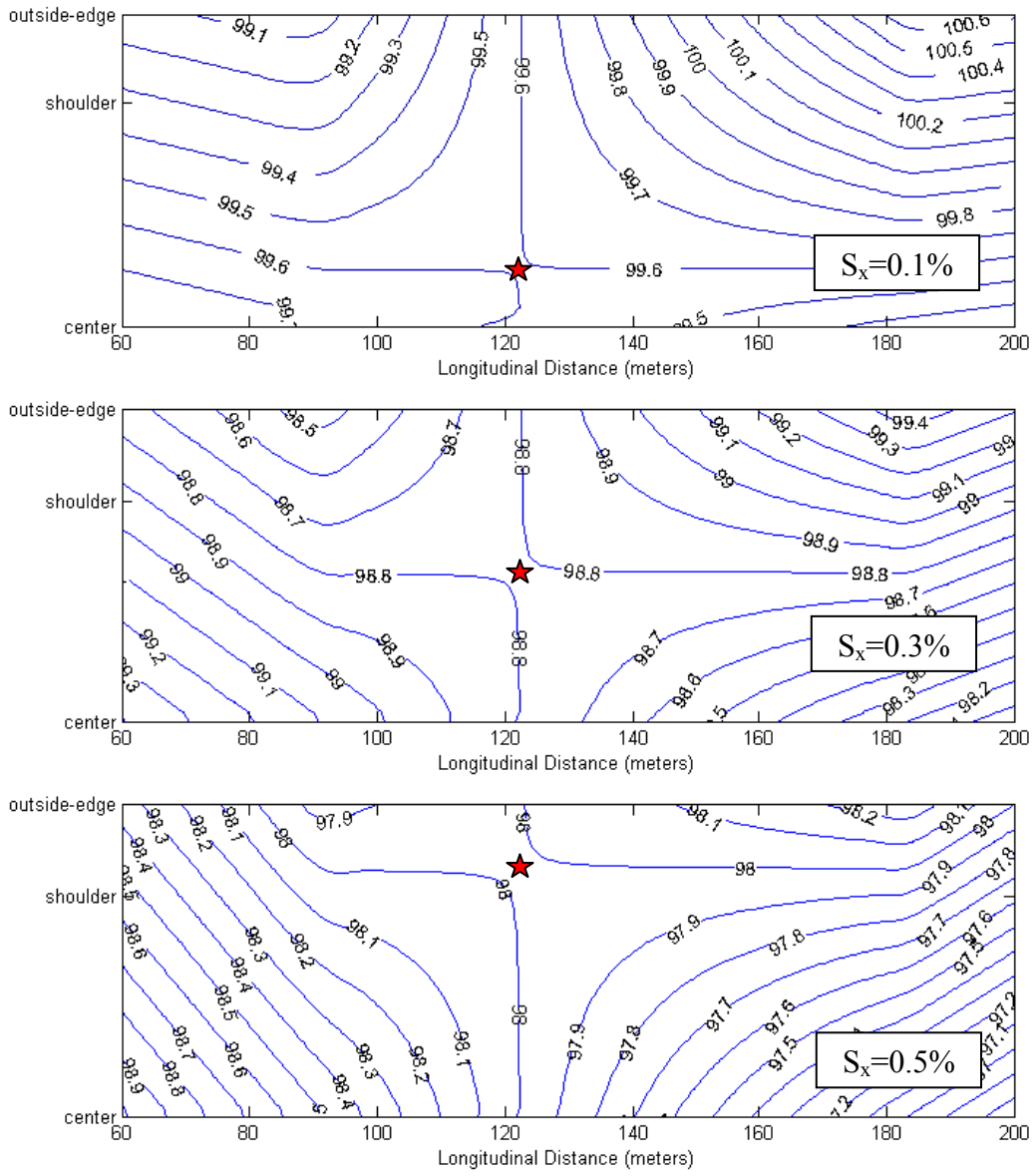

Figure 5.12: Contour of the surface elevation near the stagnation point (red star) on different slopes (Type-I roads)

On steep surfaces, the accumulated water flows far downstream from the ZCS section, where the shape of the center of road becomes much smoother as the cross slope turns to full superelevation. Therefore, there is little "weir" effect at the road center and the accumulated flow keeps its shape extending to the edge of inside-lane.

5.4.2 Rainfall Intensity

Sensitivity of the maximum depth on rainfall intensity is investigated. The maximum depths on different widths and longitudinal slopes under the rainfall intensity of 150 mm/hr, 200 mm/hr, and 250 mm/hr are compared. Result shows that the maximum ponding depth is fairly

linear with respect to different rainfall intensity values with $R^2 > 0.99$. However, the slope and intercept of linear regression vary with respect to the number of lanes and longitudinal slope. Nevertheless, with these linear relationships, one can simply interpolate the maximum depth on a superelevation transition section for any desired rainfall intensity. The slope and intercept values are summarized in Table 5.3. Figure 5.13 shows an example of the maximum ponding depth as a function of rainfall intensity on 4-, 6-, and 8-lane roads with $S_x = 1.0\%$.

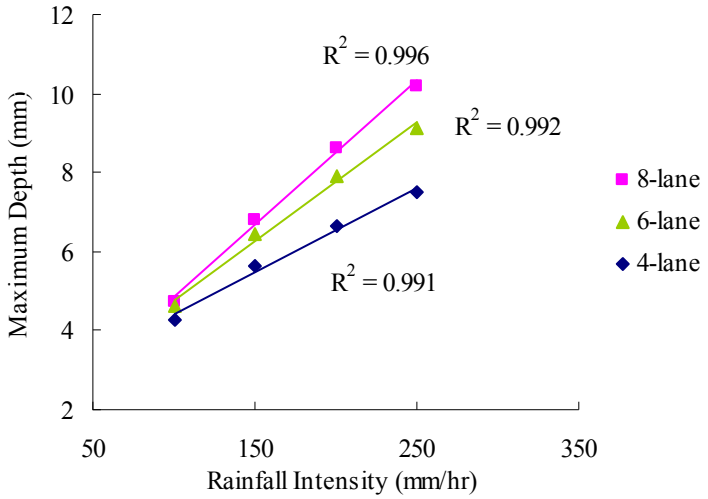

Figure 5.13: Linearity in the maximum ponding depth with respect to rainfall intensity (S_x = 1.0%)

Table 5.3: Variables for linear regression of the maximum water depth w.r.t. rainfall intensity

Type	Sx (%)	4-lane road			6-lane road			8-lane road		
		slope	intercept	R^2	slope	intercept	R^2	slope	intercept	R^2
I	0.1	0.019	1.945	0.997	0.025	2.334	0.999	0.031	2.242	0.999
	0.3	0.018	1.724	1.000	0.024	1.972	0.999	0.029	1.913	0.999
	0.6	0.019	2.279	0.994	0.023	2.771	0.998	0.029	2.517	0.998
	1.0	0.021	2.269	0.991	0.030	1.801	0.992	0.036	1.231	0.996
	3.0	0.024	2.089	0.991	0.031	1.941	0.995	0.039	0.823	0.999
	6.0	0.030	1.587	0.985	0.038	0.840	0.999	0.041	0.631	1.000
II	0.1	0.018	2.222	0.993	0.023	2.732	0.998	0.029	2.445	0.998
	0.3	0.020	2.249	0.990	0.027	2.298	0.994	0.037	0.948	0.998
	0.6	0.019	2.254	0.990	0.025	2.559	0.996	0.033	1.825	0.998
	1.0	0.019	2.257	0.990	0.026	2.483	0.996	0.034	1.551	0.998
	3.0	0.020	2.249	0.990	0.027	2.298	0.994	0.037	0.948	0.998
	6.0	0.021	2.215	0.989	0.029	2.099	0.993	0.039	0.619	0.999

($h_{max}=ar+b$, *r: rainfall intensity [mm/hr],* h_{max}*: maximum water depth [mm], a: slope, b: intercept*)

5.4.3 Number of Traffic Lanes

According to AASHTO Green Book (2004), the length of superelevation runoff is proportional to the number of lanes on either side of the center. For instance, the runoff length is twice longer on an 8-lane road (4 lanes each side) than on a 4-lane road if other variables are the same. The sensitivity of the maximum depth to the number of lanes cannot be directly measured because the increase of number of lanes is equivalent to increase of drainage area. Therefore, one should be careful when interpreting the result such as those shown in Figures 5.14 and 5.15 because the roads have different superelevation runoff lengths and drainage areas.

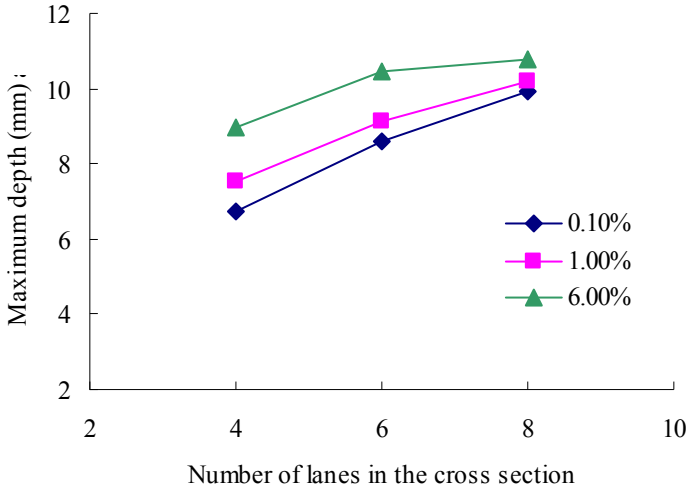

(a) *Type-I* roads

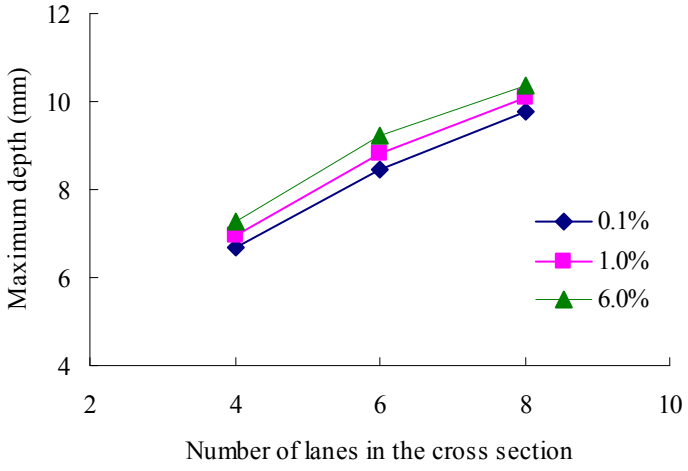

(b) *Type-II* roads

Figure 5.14: Maximum ponding depths on the traffic lanes (r = 250 mm/hr)

As expected, the roads with larger width and steeper longitudinal slope have more ponding depths than the others. On *Type I* roads, the impact of longitudinal slope is significant on the 4-lane road, but the gap becomes narrower as the number of lanes increases. As discussed

in Section 5.4.1, the location of the maximum depth and flow pattern vary with respect to longitudinal slope; thus, converging trend on *Type-I* roads shown in Figure 5.14(a) is considered trivial.

On both road types, the maximum depth shows a trend of curvature with respect to number of lanes. This can be explained theoretically by kinematic wave theory in which water depth is proportional to flow length in a nonlinear style ($\sim L^{3/5}$). It is very likely that the overall trend of maximum depth over number of lanes comes from this relationship. Figure 5.15 gives another perspective for the analysis: the maximum depths on the entire traffic lanes, inside-lane edge, outside-lane edge, and the center of the roads with different widths are presented. In these figures, positive and negative values of longitudinal slope denote the *Type-I* and *Type-II* roads, respectively.

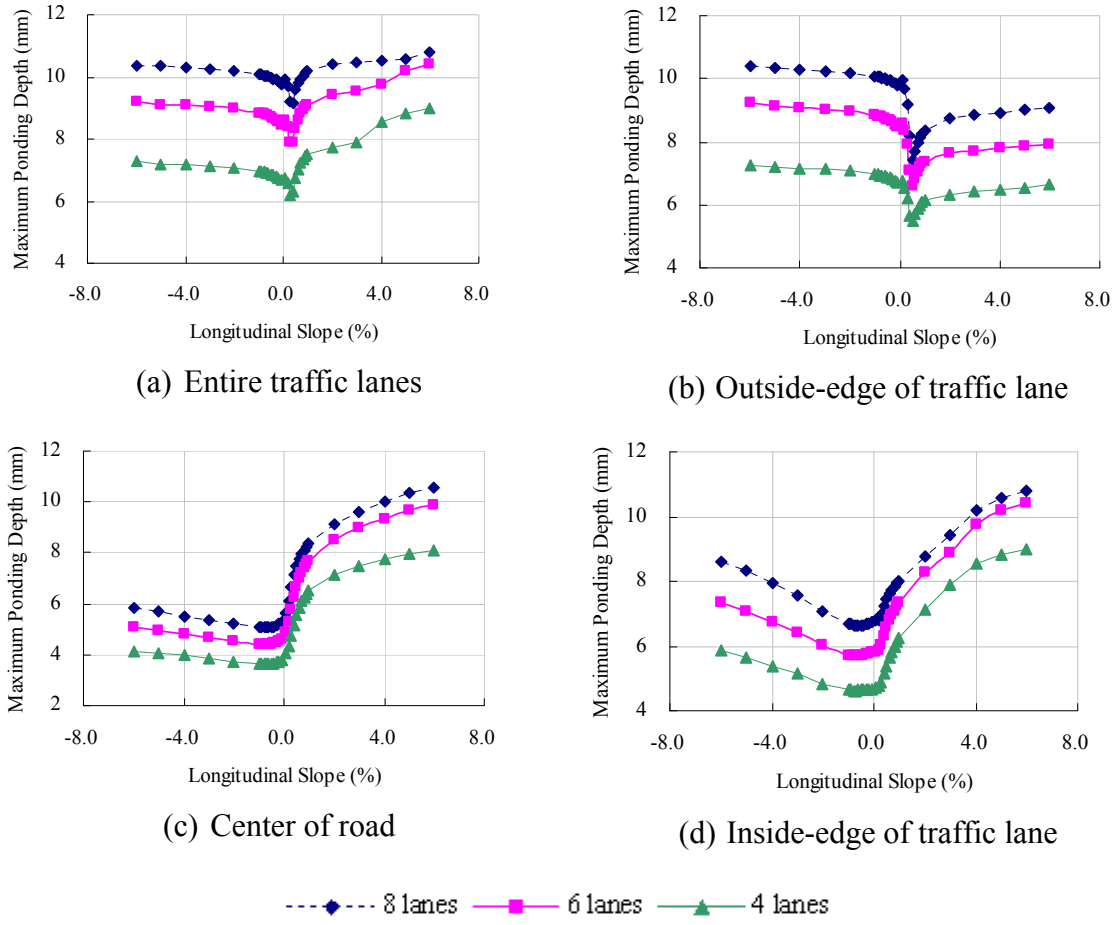

Figure 5.15: Maximum ponding depth (r = 250 mm/hr)

It is interesting that the profile of maximum depth at the center of road is similar to that of the inside-edge of lanes. The curved profile observed in Figure 5.15 consistently repeats in this figure. The gap in the profile between 8-lane and 6-lane roads is overall less than that between 6-lane and 4-lane roads, and is especially significant at the center and inside-edge of *Type-I* road.

5.4.4 Residence Time of Stormwater Runoff

The extended drainage flow path associated with superelevation transitions results in an increase of residence time, T_r, of stormwater runoff near the location of ZCS. In this chapter, impact of superelevation transition is studied by estimating residence time of stormwater runoff near ZCS sections. Relative differences of estimated T_r values for superelevation transitions and normal crown sections are compared. Stormwater runoff residence time is estimated by T_r = Volume/Discharge. To make the calculation, a section of roadway that includes the ZCS station is selected. Then, using the steady-state depth in each cell, the cell storage volume is calculated from the cell depth and area. The volumes for cells within the roadway section are then added over the selected domain to get the total volume of water. The discharge is calculated using Discharge = ∑(Cell Area x Rainfall Intensity). The residence time for normal crown is calculated analytically using kinematic wave theory. Figure 5.16 shows the difference in residence time between a superelevation transition section and a normal crown section for the following variables: n = 0.015, r = 250 mm/hr, number of lanes is 4, 6, and 8, shoulder width = 3 m, and variable base longitudinal slopes. The difference in residence time shown in Figure 5.16 is purely due to the difference in geometry of the roads; there is approximately a thirty percent increase in T_r values associated with the greater water depth on the roadway.

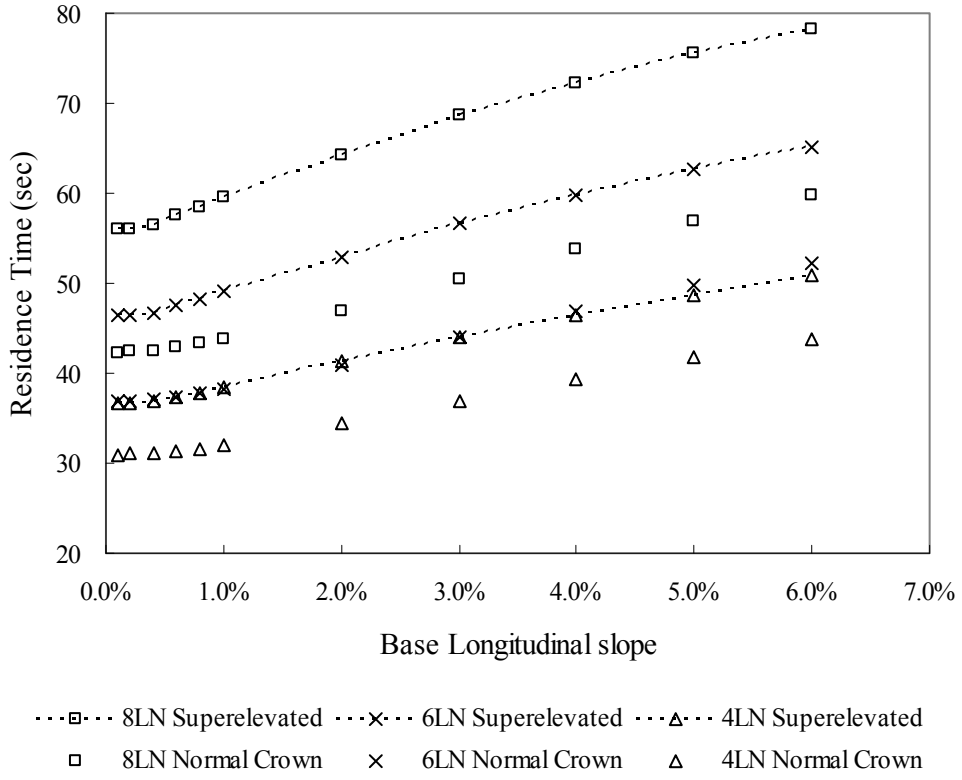

Figure 5.16: Residence time of stormwater runoff

Results show that the residence time increases as the base longitudinal slope increases. This implies that more water exists on the roadway on longitudinally steep grades than on flat sections. More importantly, residence time is always larger on superelevation transition sections compared with normal crown sections. The difference in residence time with respect to base

longitudinal slope is fairly consistent; however, the magnitude of the difference increases as the number of traffic lanes increases. This may be observed more clearly in Figure 5.17, which shows the box-plot of the difference in residence time (T_r) between superelevation transition and normal crown sections. The trend of the box-plot shows that the difference in residence time becomes larger as the number of traffic lanes increases. Furthermore, the variation of the difference increases as the number of lanes increases.

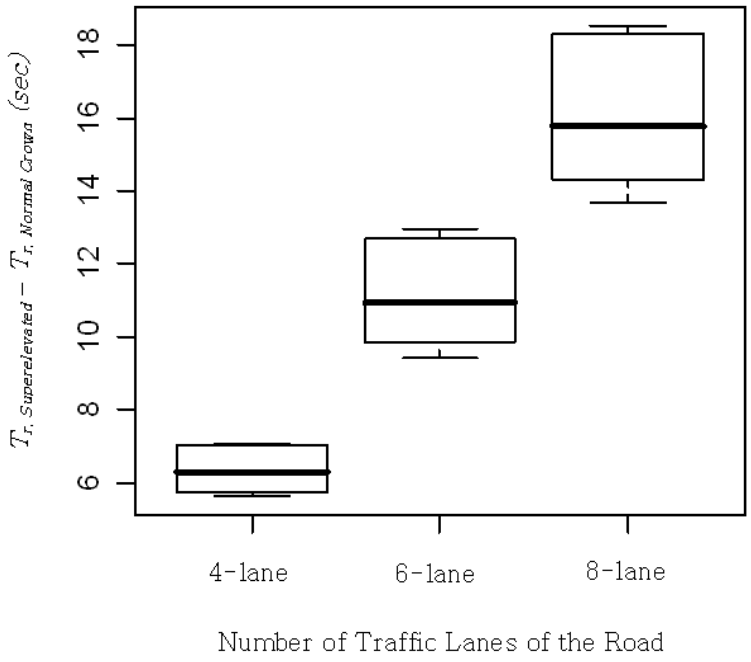

Figure 5.17: Box-plot of the difference in residence time between superelevation transition and normal crown sections

Impact of superelevation transition length on residence time is investigated. Table 5.4 shows the relative difference of residence time between normal crown and superelevation transition sections with S_x = 0.02, n = 0.015, r = 250 mm/hr. On the normal crown sections, residence time does not change with respect to the length of road, while it increases as the length of superelevation transition increases. The relative difference is estimated as 24.2% for 30.5 m road to 34.5% for 91.4 m roadway section length.

Table 5.4: Estimated difference in residence time of stormwater runoff between normal crown and superelevation transition sections

Length of Road		Residence Time (sec)		Relative difference (%)
(ft)	(m)	Normal Crown	Superelevation	
100	30.5	28.13	37.10	24.2
200	61.0	28.13	41.73	32.6
300	91.4	28.13	42.94	34.5

5.4.5 Location of Curb-opening Inlets

A curb-opening inlet is often used to collect gutter flow on the highway pavement when roadside curbs exist. HEC 22 (FHWA, 1996) recommends placing an inlet immediately upstream of the location of zero cross slope. In this subsection, flow response with respect to the location of a curb-opening inlet is investigated. A 3-meter (10-ft) long curb-opening inlet is placed on the outside-lane edge at the location of zero cross slope and at subsequent stations upstream at 0.6 meter (2 ft) increments from the ZCS section (schematic drawing is presented in Figure 4.22). Results are presented in Figure 5.18 where horizontal axis represents the distance of the downstream-side end of the inlet from the ZCS section and vertical axis denotes the maximum ponding depth within the domain (entire traffic lanes of a superelevation transition section). As shown in the figure, the location of inlet affects the maximum ponding depth within the domain: the maximum depth decreases as the location of the inlet moves toward upstream from ZCS section, then reaches a lower limit at 1.5 m, and then increases as the location of inlet is moved farther from the ZCS section.

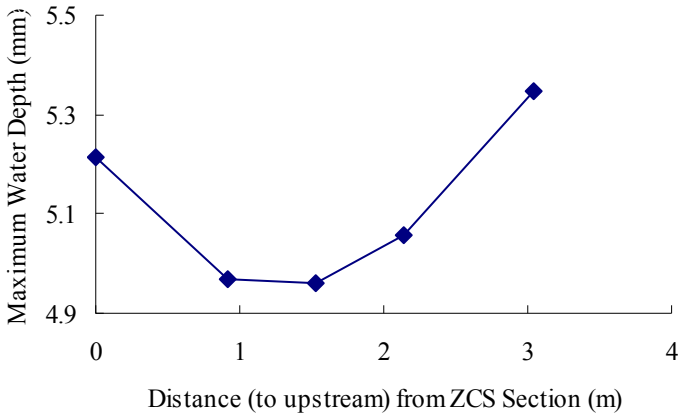

Figure 5.18: Maximum ponding depths on the traffic lanes (shoulder area excluded) on Type-I roads (r = 250 mm/hr)

The results shown in Figure 5.18 implies that the inlet efficiency is greatest with the inlet located 1.5 m upstream from ZCS section because the gutter flow on the roadside starts to spread out before it reaches the ZCS section. Even though cross slope is still downhill to the outside-lane edge, the gradient of water surface promotes a lateral flow into traffic lanes. As the location of inlet is moved farther upstream, the inlet becomes inefficient because it fails to capture the flow coming from the main road accumulating between the inlet and ZCS section. However, one cannot claim that the optimal location of inlet (1.5 m in this case) does have significant meaning in terms of flow control on the road, for the difference in the maximum depth between the locations of an inlet at ZCS section and 1.5 meter (5 ft) away is less than 1 mm. Additional simulations with different sizes of inlets on various surfaces would help toward understanding the significance of curb-opening inlet placement effects. Moreover, grate inlets are another type of inlet that is often used for highway drainage. An investigation for finding the optimal locations of these inlets or for comparing the efficiencies of different inlets is left to future work.

Chapter 6. Summary and Conclusions

This research program has addressed issues associated with highway drainage at superelevation transitions through combined physical modeling and mathematical modeling investigations. The research objectives focused on four major questions: 1) whether literature characterization of sheet flow mechanics provides appropriate models for application to highway drainage; 2) whether kinematic or diffusion wave models are applicable for simulation of highway runoff near superelevation transitions; 3) how the pattern of pavement drainage at superelevation transitions is influenced by longitudinal grade; and 4) whether design guidance can be developed to minimize stormwater ponding through control of longitudinal grade at superelevation transitions.

As discussed in Chapter 2, the literature on overland flow (sheet flow) is vast. The primary interest for this research is the effects of surface roughness and rainfall intensity, and how these may be represented through hydraulic models such as Manning's equation, possibly with parameters that are flow-dependent. The physical modeling program described in Chapter 3 has shown that conventional models from fluid mechanics (logarithmic boundary layer theory) can be used to describe sheet flow behavior on rough surfaces with a primary variable that is directly related to surface roughness (equivalent sand roughness). Significantly, the much simpler Manning equation provides a model that is equally capable of representing the experimental data, as evaluated statistically from the standard error of measurement. Estimated magnitudes of roughness height determined using the logarithmic boundary layer model and Manning's equation are very similar and correspond directly to the material characteristics that were used to create the three different experiment surfaces. The effective flow depth should be measured from near the top of the roughness element height, and this effective flow depth corresponds to the depth that is significant in determining hydroplaning potential. Manning coefficient values are consistent with literature values, and when effective flow depth is used in the flow calculation, the Manning coefficient value does not depend on flow rate (Reynolds number). While there is large uncertainty in predictions for small flow rates, the lack of Reynolds number dependence on the primary flow parameter (Manning coefficient) is different than found in other recent highway-related research studies and greatly simplifies model development and application. Finally, for sheet flow over rough surfaces, the effect of rainfall at intensity of approximately 100 mm/hr does not have a consistent effect on flow behavior. Apparently, the chaotic effects of raindrops do not significantly affect flow behavior beyond that caused by the surface roughness. Rainfall intensity need not be directly included when selecting hydraulic model parameters for estimating stormwater runoff. The data from the experimental program described in Chapter 3 is listed in Appendix B.

Both kinematic and diffusion wave numerical simulation models have been developed as part of this research program. For regular (flat) surfaces, these models give equivalent results. However, with irregular roadway sections such as found near superelevation transitions, the kinematic wave model formulation cannot be used because transverse (between adjacent flow paths) head gradients can become significant. In contrast, the diffusion wave model formulation is capable of addressing all flow conditions that would be expected. Diffusion wave model formulation is much simpler than full dynamic wave models, and solution methods are much easier to develop and apply. The diffusion wave model formulation was successfully used during this research program. Model development is documented in Chapter 4.

The primary features that influence pavement drainage and ponding of stormwater runoff near superelevation transitions are the combined effects of the change from negative to positive lateral grade for the outside lanes of a curve near the transition and the longitudinal slope. For a roadway without curbs under normal crown conditions, the greatest ponding depth occurs near the roadway edge and increases with roadway width (number of traffic lanes), rainfall intensity, surface roughness (characterized by the Manning coefficient), and longitudinal slope. There is approximately a forty percent increase in maximum flow depth at the roadway edge as the longitudinal slope increases from zero to six percent under normal crown conditions (both for concrete and asphalt type pavement surfaces). The situation is quite different for superelevation transition sections. The magnitude of the maximum flow depth increases compared to normal crown conditions and the location of maximum depth changes with longitudinal slope. For transitions entering a superelevated section with positive longitudinal grade (down slope), which correspond to *Type-I* configuration in Section 5.2, the location of maximum depth is near the outside edge of pavement for slopes up to 0.4 percent (which corresponds approximately to the relative gradient, G, for a design speed of 100 km/hr). For longitudinal slope values between about 0.4 and 3 percent, the location of maximum ponding depth is located near the roadway centerline, but on the outside lanes. For longitudinal slope values greater than about 3 percent, the location of maximum flow depth is located on the inside edge of pavement at a distance downstream from the zero cross slope (ZCS) station. For a *Type-II* configuration, which corresponds to a roadway exiting a superelevated section with positive slope, the location of maximum flow depth is always located near the outside edge of pavement at a distance downstream of the ZCS station that increases with longitudinal grade. For both *Type-I* and *Type-II* configurations, the magnitude of the maximum flow depth changes very little with longitudinal grade. Simulation results for different roadway configurations and variable sensitivity are discussed in Chapter 5.

Development of design guidance to minimize ponding depth as a function of longitudinal grade is difficult. A draft guidance document is provided in Appendix A, though this did not prove very helpful to TxDOT design engineers who reviewed the document for possible use within the districts. The primary difficulty is that the maximum ponding depth on the roadway surface is not very sensitive to longitudinal grade. What is possibly more significant is the observation that the location of maximum ponding depth is sensitive to longitudinal grade. As noted in the previous paragraph and in Chapter 5, the maximum depth occurs near the center of the roadway for moderate longitudinal slopes (0.4 to 3 percent). Other issues that are possibly important for vehicle safety include lateral variation in ponding depth, which may cause torque on the vehicle due to differential drag on tires, and the longitudinal rate-of-change in ponding depth, which could serve to initiate hydroplaning. While such issues could be addressed using the tools developed through this research effort, we are not aware of existing criteria that could be used to provide limiting conditions and thus serve as a basis for development of design guidance. These are issues that should be considered in future research.

References

Akan, A.O., Schafran, G.C., Pommerenk, P., and Harrell, L.J. (2000). Modeling storm-water runoff quantity and quality from marine drydocks. *Journal of Environmental Engineering, ASCE, 126*(1), 5-11.

Anderson, D.A., Huebner, R.S., Reed, J.R., Warner, J.C., and Henry, J.J. (1998). Improved Surface Drainage of Pavements, Final Report. National Cooperative Highway Research Program (NCHRP) Web Document 16.

ASTM (2006). Standard test method for measuring pavement macrotexture depth using a volumetric technique, Designation: E 965 – 96. ASTM International.

Barros, A.P. and Colello, J.D. (2001). Surface roughness for shallow overland flow on crushed stone surfaces. *J. Hydraulic Engineering, ASCE*, 127, 38-52.

Bayazit, M. (1976). Free surface flow in a channel of large relative roughness, *Journal of Hydraulic Research, 14*(2), 115-126.

Brown, S.A., Stein, S.M., and Warner, J.C. (2001). Urban Drainage Design Manual, Hydraulic Engineering Circular 22, Second Edition, FHWA-NHI-01-21, HEC-22, Federal Highway Administration, Washington, D.C.

Charbeneau, R.J., Jeong, J., Reeder, E., and Chan, W.S. (2007). Physical modeling of sheet flow on highway pavement surfaces. Presented at the 32nd Congress of IAHR, Venice, Italy, July 1-6, 2007, International Association of Hydraulic Engineering and Research.

Chien, N. and Wan, Z. (1999). *Mechanics of Sediment Transport*. ASCE Press, Reston, Virginia.

Chow, V.T., Maidment, D.R., and Mays, L.W. (1988). *Applied Hydrology*. McGraw-Hill, New York.

Christiansen, J. (1942). Irrigation by sprinkling. *Bull. No. 670*, California Agricultural Experiment Station, Berkeley, Calif., 110-116.

Cooley, R. L (1992). A Modular Finite-Element Model (MODFE) for Areal and Axisymmetric Groundwater Flow Problems, Part 2: Derivation of Finite-Element Equations and Comparisons with Analytical Solutions. USGS Book 6, Chapter A4.

Cristina, C. M. and Sansalone, J.J. (2003). Kinematic wave model of urban pavement rainfall-runoff subject to traffic loadings. *Journal of Environmental Engineering, ASCE, 129*(7), 629-636.

Daluz Vieira, J.H. (1983). Conditions governing the use of approximations for the Saint-Venant equations for shallow surface water flow. *Journal of Hydrology, 60*, 43-58.

Einstein, H.A. and El-Samni, E.S. (1949), Hydrodynamic forces on a rough wall, *Reviews of Modern Physics, 21*(3), 520-524.

Engman, E.T. (1986). Roughness coefficients for routing surface runoff. *J. Irrigation and Drainage, ASCE, 112*, 39-53.

Emmett, W.W. (1970). The hydraulics of overland flow on hillslopes. Geological Survey Professional Paper 662-A, U.S. Government Printing Office, Washington.

Feng, K. and Molz, F.J. (1997). A 2-D, diffusion-based, wetland flow model. *Journal of Hydrology*, *196*(1-4), 230-250.

Ferziger, J.H. and Peric, M. (2002). *Computational Methods for Fluid Dynamics*. Springer, Berlin.

Goldstein, S. (1938). *Modern Developments in Fluid Dynamics, Volume II*. Oxford University Press, Oxford.

Govindaraju, R.S., Jones, S.E., and Kavvas, M.L. (1988a). On the diffusion wave model for overland-flow: 1. Solution for steep slopes. *Water Resources Research, 24*(5), 734-744.

Govindaraju, R.S., Jones, S.E., and Kavvas, M.L. (1988b). On the diffusion wave model for overland-flow: 2. Steady-state analysis. *Water Resources Research, 24*(5), 745-754.

Grayson, R. B., Moore, I. D., and McMahon, T. A. (1992). Physically Based Hydrologic Modeling: 2. Is the Concept Realistic? *Water Resourc. Res., 26*, 2659–2666.

Henderson, F.M. (1966). *Open Channel Flow*. Macmillan Company, New York.

Henderson, F.M. and Wooding, R.A. (1964). Overland flow and groundwater flow from a steady rainfall of finite duration. *J. Geophysical Research*, *69*(8), 1531-1540.

Hicks, W.I. (1944). A method of computing urban runoff. *Transactions, ASCE, 109*, 1217-1268.

Hinze, J.O. (1975). *Turbulence*. Second Edition, McGraw-Hill, New York.

Hirsch, Ch. (1988). *Numerical Computation of Internal & External Flows*. Volume 1, John Wiley & Sons Ltd..

Hodges, B. R. (2004). Accuracy order of Crank-Nicolson discretization for hydrostatic free-surface flow. *Journal of Engineering Mechanics, ASCE, 130*(8), 904-910.

Horton, R.E., Leach, H.R., Van Vliet, R. (1934). Laminar sheet flow. *Transactions of the American Geophysical Union*, *2*, 393-404.

Hromadka, T.V. and Yen, C.C. (1986). A diffusion hydrodynamic model (DHM). *Advances in Water Resources*, *9*(3), 118-170.

Huebner, R.S., Reed, J.R., and Henry, J.J. (1986). Criteria for predicting hydroplaning potential. *J. Transportation Engineering, ASCE, 112*(5), 549-553.

Iwagaki, Y. (1955). Fundamental studies of the runoff analysis by characteristics. *Kyoto Univ. Disaster Prevention Res. Inst*., Japan, Bull., 10, 1-25.

Izzard, C.F. (1944). The surface profile of overland flow. *Transactions, Am. Geophysical Union*, Part VI, 959-968.

Izzard, C.F. (1946). Hydraulics of runoff from developed surfaces. *Proceedings of the Highway Research Board, 26*, 129-146.

Jain, M.K. and Singh, V.P. (2005). DEM-based modeling of surface runoff using diffusion wave equation. *Journal of Hydrology*, *302*(1-4), 107-126.

Jeffreys, H.J. (1925). The flow of water in an inclined channel of rectangular section. *Philos. Mag., 6*(49), 793-807.

Jeong, J. (2008). A hydrodynamic diffusion wave model for stormwater runoff on highway surfaces at superelevation transitions. Ph.D. Dissertation, The University of Texas at Austin.

Katz, D.M., Watts, F.J., and Burroughs, E.R. (1995). Effects of surface roughness and rainfall impact on overland flow. *J. Hydraulic Engineering, ASCE, 121*, 546-553.

Kazezyilmaz-Alhan, C.M. and Medina, M.A. (2007). Kinematic and diffusion waves: analytical and numerical solutions to overland and channel flow. *Journal of Hydraulic Engineering, ASCE, 133*(2), 217-228.

Keulegan, G.H. (1938). Laws of turbulent flow in open channels. *Journal of the National Bureau of Standards, 21*, 707-741.

Keulegan, G.H. (1944). Spatially variable discharge over a sloping plane. *Transactions, Am. Geophysical Union*, Part VI, 956-959.

Lal, A.M.W. (1998). Weighted implicit finite-volume model for overland flow. *Journal of Hydraulic Engineering, ASCE*, *124*(9), 941-950.

Lawrence, D.S.L. (2000). Hydraulic resistance in overland flow during partial and marginal surface inundation: experimental observations and modeling. *Water Resources Research, 36*(8), 2381-2393.

Li, G. and Abrahams, A.D. (1997). Effect of saltating sediment load on the determination of the mean velocity of overland flow. *Water Resources Research*, *33*, 341-347.

Li, G., Abrahams, A.D. and Atkinson, J.F. (1996). Correction factors in the determination of mean velocity of overland flow. *Earth Surface Processes and Landforms*, *21*, 509-515.

Liggett, J.A. and Woolhiser, D.A. (1967). Difference solutions of the shallow-water equation. *Journal of the Engineering Mechanics Division*, EM2, 39-71.

Lighthill, M.J. and Whitham, G.B. (1955). On kinematic waves, 1. Flood movement in long rivers. *Proc. Roy. Soc. London, A, 229*, 281-316.

Luk, S.H. and Merz, W. (1992). Use of the salt tracing technique to determine the velocity of overland flow. *Soil Technology*, *5*, 289-301.

Monin, A.S. and Yaglom, A.M. (1971). *Statistical Fluid Mechanics, Volume 1*. MIT Press, Cambridge.

Phelps, H.O. (1975). Shallow laminar flows over rough granular surfaces. *J. Hydraulics Division, ASCE, 101*, 367-384.

Ponce, V.M. (1990). Generalized diffusion wave-equation with inertial effects. *Water Resources Research, 26*(5), 1099-1101.

Robertson, A.F., Turner, A.K., Crow, F.R. and Ree, W.O. (1966). Runoff from impervious surfaces under conditions of simulated rainfall. *Transactions of the ASAE*, 343-351.

Savat, J. (1977). The hydraulics of sheet flow on a smooth surface and the effect of simulated rainfall. *Earth Surface Processes and Landforms, 2*, 125-140.

Savat, J. (1980). Resistance to flow in rough supercritical sheet flow. *Earth Surface Processes and Landforms, 5*, 103-122.

Schlichting, H. (1968). *Boundary-Layer Theory*, 6th Ed. McGraw-Hill, New York.

Schneider, Lauren (2006). Physical models of rainfall runoff for superelevation transition. M.S. Thesis. The University of Texas at Austin.

Shen, H.W. and Li, R-M. (1973). Rainfall effect on sheet flow over smooth surface. *J. Hydraulics Division, ASCE, 99*, 771-792.

Sherman, L.K. (1932). Streamflow from rainfall by the unit-graph method. *Eng. News Rec., 108*, 501-505.

Singh, V.P. (1996). *Kinematic Wave Modeling in Water Resources*. Wiley-Interscience, New York.

Singh, V.P. and Aravamuthan, V. (1996). Errors of kinematic-wave and diffusion-wave approximations for steady-state overland flows. *Catena, 27*(3-4), 209-227.

Sturm, T.W. (2001). *Open Channel Hydraulics*. McGraw-Hill, Boston.

Taylor, J.R. (1982). *An Introduction to Error Analysis, The Study of Uncertainties in Physical Measurements*, University Science Books, Oxford University Press, Mill Valley, CA.

Tisdale, T. S. and Yu, J.M.H.L. (1999). Kinematic wave analysis of sheet flow using topography fitted coordinates. *Journal of Hydrologic Engineering, ASCE, 4*(4).

Tsai, T. L. and J. C. Yang (2005). Kinematic wave modeling of overland flow using characteristics method with cubic-spline interpolation. *Advances in Water Resources 28*(7), 661-670.

Villard, Julien (2005). Minimum longitudinal grade at zero cross slope in superelevation transition. M.S. Thesis. The University of Texas at Austin.

Woolhiser, D.A. and Liggett, J.A. (1967). Unsteady one-dimensional flow over a plane: the rising hydrograph. *Water Resources Research, 3*(3), 753-771.

Yalin, M.S. (1977). *Mechanics of Sediment Transport*, 2nd Ed., Pergamon Press, Oxford.

Yoon, Y.N. and Wenzel, H.G, Jr. (1971). Mechanics of sheet flow under simulated rainfall. *J. Hydraulics Division, ASCE, 97*, 1367-86.

Yu, Y.S. and McNown, J.S. (1964). Runoff from impervious surfaces, *J. Hydraulics Research*, *2*(1), 3-24.

Appendix A. Design Guidance for Roadway Drainage at Superelevation Transitions

Introduction: TxDOT Project 0-4875 has an objective to develop design guidance on longitudinal grade at superelevation transitions, as it impacts stormwater runoff behavior and hydroplaning potential. Because of changes in cross slope at superelevation transitions, drainage path lengths can be considerably longer than under normal crown conditions, resulting in larger runoff depths and increased longitudinal and lateral variation in runoff depth. This guidance provides estimates of maximum stormwater runoff depth and maximum changes in depth at superelevation transitions as a function of longitudinal grade.

Background: Vehicle speed at incipient hydroplaning (HPS) depends on stormwater runoff depth, tire pressure, tire tread depth, average pavement texture depth, and other factors. Stormwater runoff depth (water film thickness, WFT) is the primary variable. Figure A1 shows results from model equations of HPS as a function of WFT. There is a great deal of uncertainty associated with the curve shown in Figure A1. Furthermore, with regard to vehicle safety at superelevation transitions, it is not clear whether the magnitudes of WFT or changes in WFT in the longitudinal and lateral directions are the more critical variables.

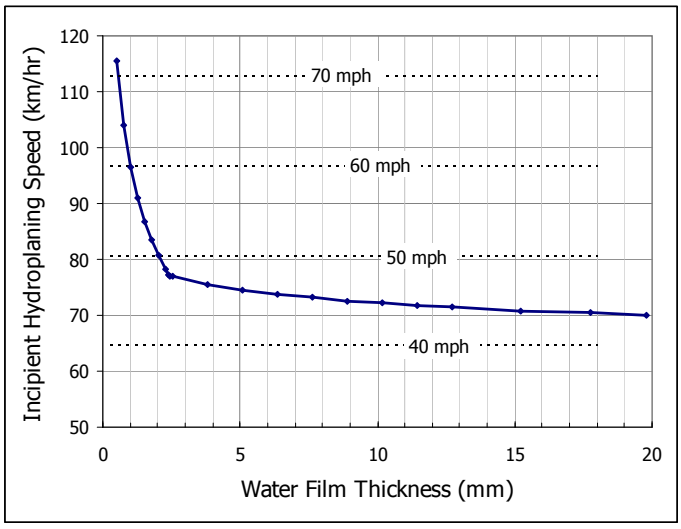

Figure A1. Model results for vehicle speed at incipient hydroplaning
Note: Figure A1 based on Huebner, R.S., J.R. Reed, and J.J. Henry (1986). Criteria for predicting hydroplaning potential. ASCE J. Transportation Engineering, 112(5), 549-553.

Guidance Development: Guidance development is based on results from numerical simulation of stormwater runoff on pavement surfaces. Roadway alignment is taken from GEOPAK geometry files that specify the (x,y,z) coordinates of right, center, and left ends of traffic lanes at regular longitudinal station intervals. The geometry file values are interpolated to develop a curvilinear modeling grid for numerical simulation of roadway runoff using the diffusion wave model formulation and the finite volume numerical method. Model results provide estimates of the

runoff depth and flow rate within the simulation domain as a function of time. Steady state values (corresponding to the time of concentration) are used for guidance development.

Runoff under Normal Crown Conditions: Stormwater runoff behavior is modeled using Manning's equation. For normal crown conditions, the runoff depth increases with lateral distance from the crown location. In addition to lateral station location, runoff depth is a function of pavement type (roughness), lateral slope, longitudinal slope, and rainfall intensity. Tables A1 (concrete-type pavement roughness) and A2 (asphalt-type pavement roughness) present WFT values at center and transverse edge-of-lane stations based on a lane width 3.66 m (12 feet) for different values of longitudinal slope (S_o). Lane 1 is closest to the roadway centerline.

Table A1. WFT (mm) at different lateral stations for cross slope = 0.02 with Manning coefficient = 0.012. Effective rainfall intensity = 100 mm/hr (4 in/hr)

	Longitudinal Slope, S_o							
	0	0.005	0.01	0.02	0.03	0.04	0.05	0.06
Lane 1 Center	0.61	0.61	0.63	0.68	0.73	0.78	0.82	0.86
Lane 1 Edge	0.92	0.93	0.96	1.02	1.10	1.18	1.24	1.30
Lane 2 Center	1.18	1.19	1.22	1.31	1.41	1.50	1.59	1.66
Lane 2 Edge	1.40	1.41	1.45	1.55	1.67	1.78	1.88	1.98
Lane 3 Center	1.60	1.62	1.66	1.78	1.91	2.04	2.15	2.26
Lane 3 Edge	1.79	1.80	1.85	1.98	2.13	2.27	2.40	2.52

Table A2. WFT (mm) at different lateral stations for cross slope = 0.02 with Manning coefficient = 0.015. Effective rainfall intensity = 100 mm/hr (4 in/hr)

	Longitudinal Slope, S_o							
	0	0.005	0.01	0.02	0.03	0.04	0.05	0.06
Lane 1 Center	0.70	0.70	0.72	0.77	0.83	0.89	0.94	0.98
Lane 1 Edge	1.06	1.07	1.09	1.17	1.26	1.34	1.42	1.49
Lane 2 Center	1.35	1.36	1.39	1.49	1.61	1.71	1.81	1.90
Lane 2 Edge	1.60	1.62	1.66	1.78	1.91	2.04	2.15	2.26
Lane 3 Center	1.83	1.85	1.89	2.03	2.18	2.33	2.46	2.58
Lane 3 Edge	2.04	2.06	2.11	2.27	2.44	2.60	2.75	2.88

Alignment at Superelevation Transitions: Roadway alignment is based on design guidance for maximum longitudinal rate of rotation of pavement slope, as a function of vehicle design speed, as provided in the TxDOT Roadway Design Manual (October, 2006), Chapter 2 (Basic Design Criteria), Section 4 (Horizontal Alignment). The minimum superelevation runoff travel length depends on the width of travel lanes, the design superelevation cross slope, and the relative gradient (G) that depends on the vehicle design speed (Table 2.8 shows that G varies from 0.8 percent at design speed 20 km/hr to 0.35 percent at design speed 130 km/hr). AASHTO guidance includes an additional factor that depends on the number of travel lanes, which allows reduction of the minimum superelevation runoff length. Figure A2 provides a schematic view of a superelevation transition with superelevation runoff length L_2 and tangent runoff length L_1. The upper part of this figure is a plan view of the pavement surface, while the lower part shows the

cross slope as a function of longitudinal station. A linear longitudinal change in cross slope is shown. The relative gradient (G) is the primary determinant of vertical alignment near superelevation transitions; the superelevation runoff length depends directly on the design superelevation cross slope, but the roadway configuration near the zero cross slope station does not depend on the superelevation cross slope. It is the drainage characteristics near the zero cross slope (ZCS) station that are most critical for hydroplaning potential.

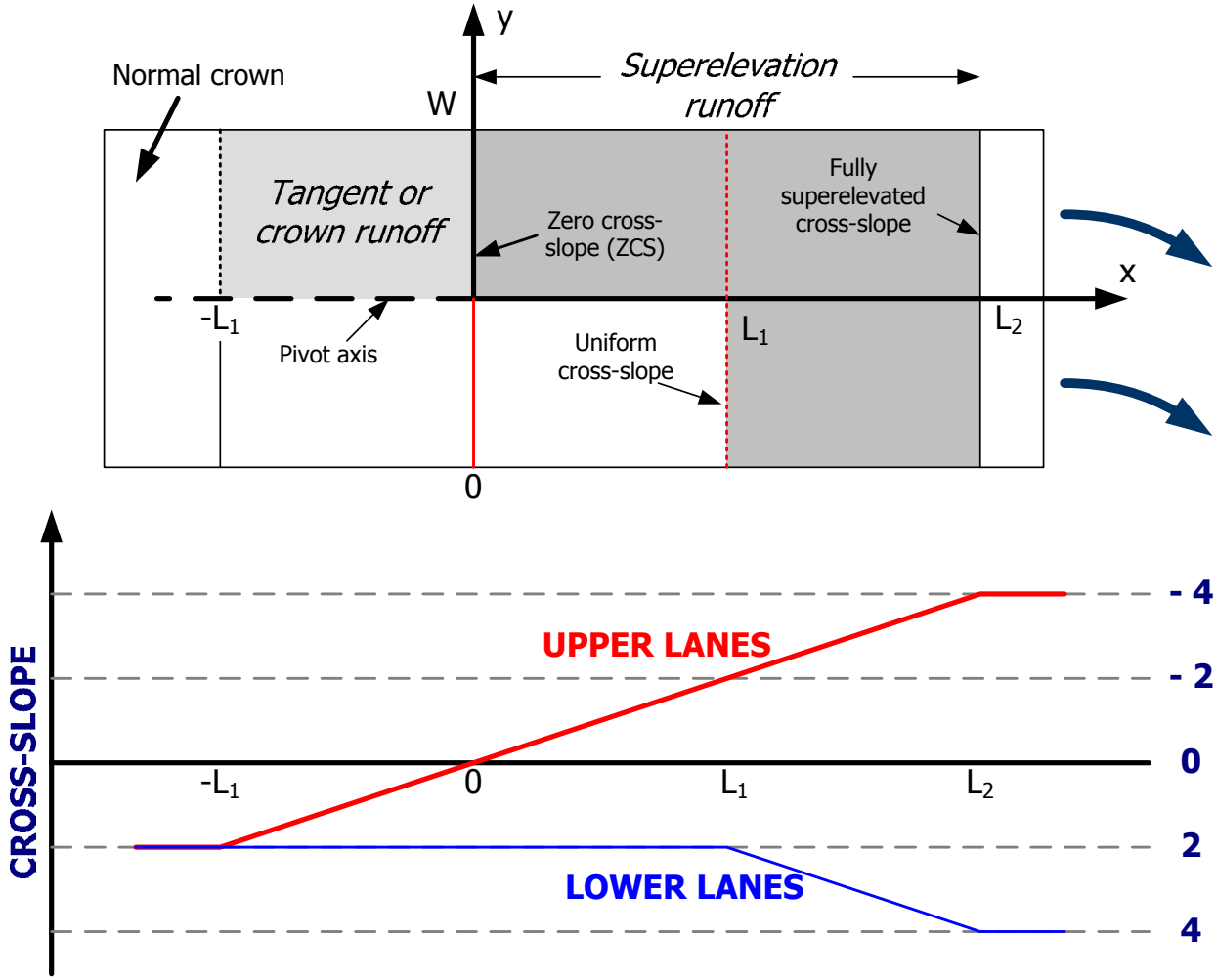

Figure A2. Lateral alignment at superelevation transition with superelevation cross slope = 4%

Distribution of runoff depth: Maximum runoff depth (water film thickness, WFT) was estimated using numerical simulation modeling for different roadway configurations (2, 4, and 6 travel lanes plus a one-lane shoulder on each side, and longitudinal slope). Example results are shown for a roadway with 4 travel lanes. Asphalt-type roadway surface is assumed (Manning n = 0.015) and the rainfall intensity is 100 mm/hr (4 in/hr). The roadway alignment is based on a design speed of 96.6 km/hr (60 mph), which corresponds to a Maximum Relative Gradient G = 0.45 percent. Figures A3 and A4 show the simulated WFT profiles along the center of each travel lane, and within the centerline of the shoulder on each side. The 'zero' distance corresponds to the Zero Cross Slope (ZCS) station.

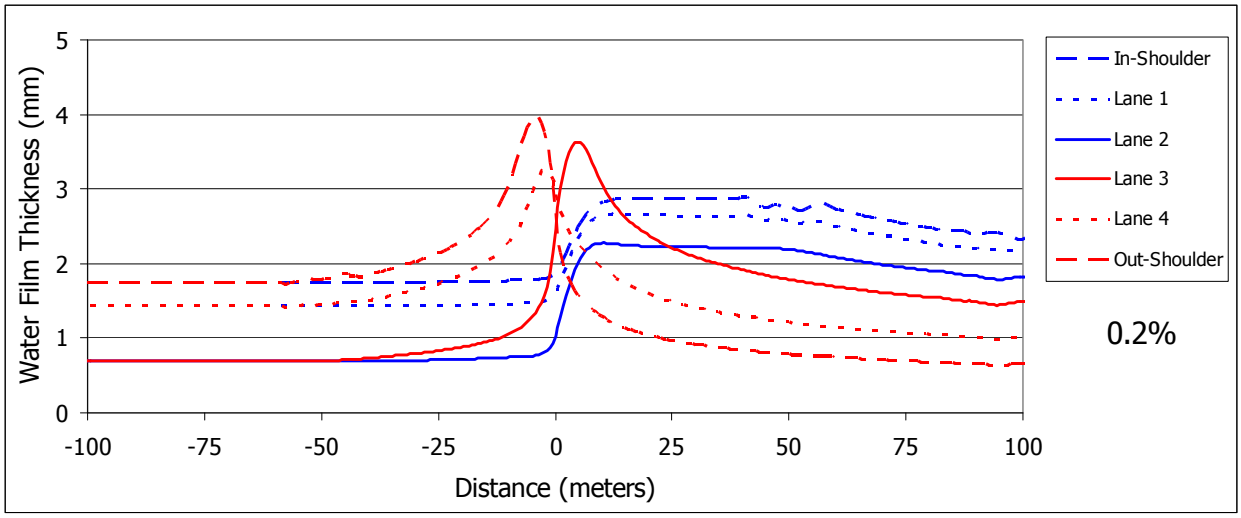

(a) Longitudinal Slope = 0.2 Percent

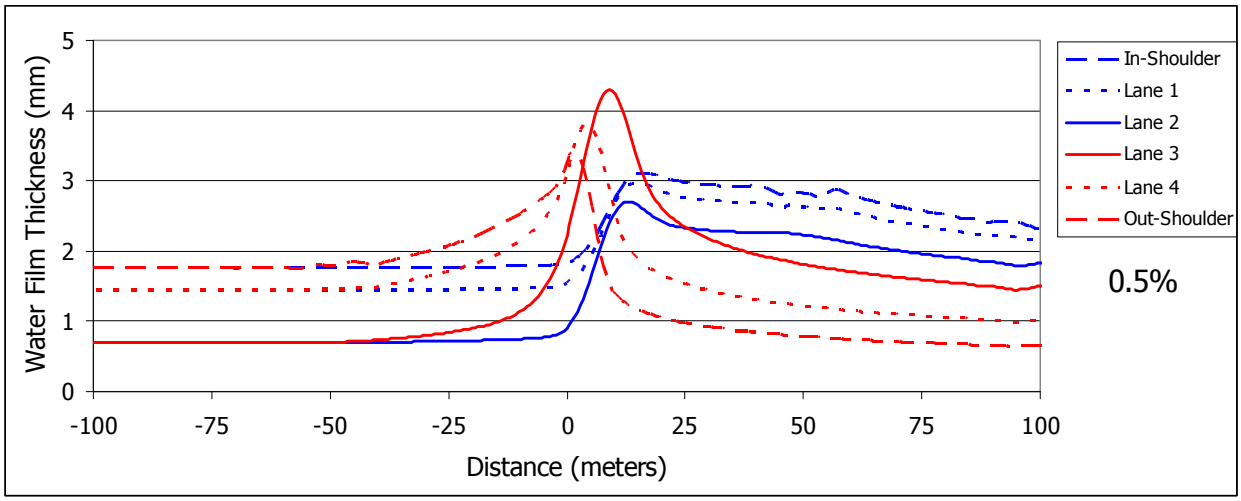

(b) Longitudinal Slope = 0.5 Percent

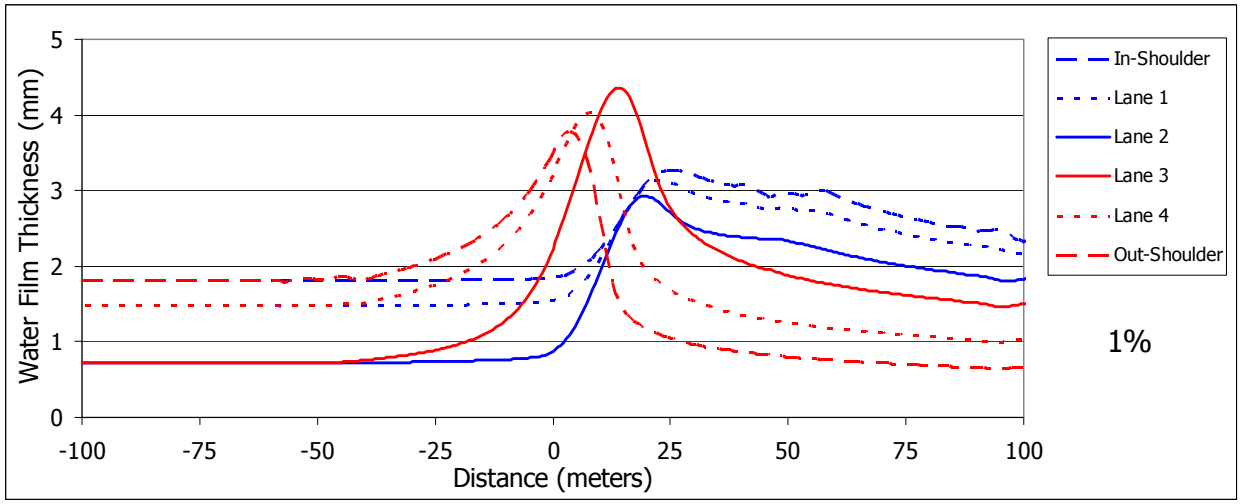

(c) Longitudinal Slope = 1.0 Percent

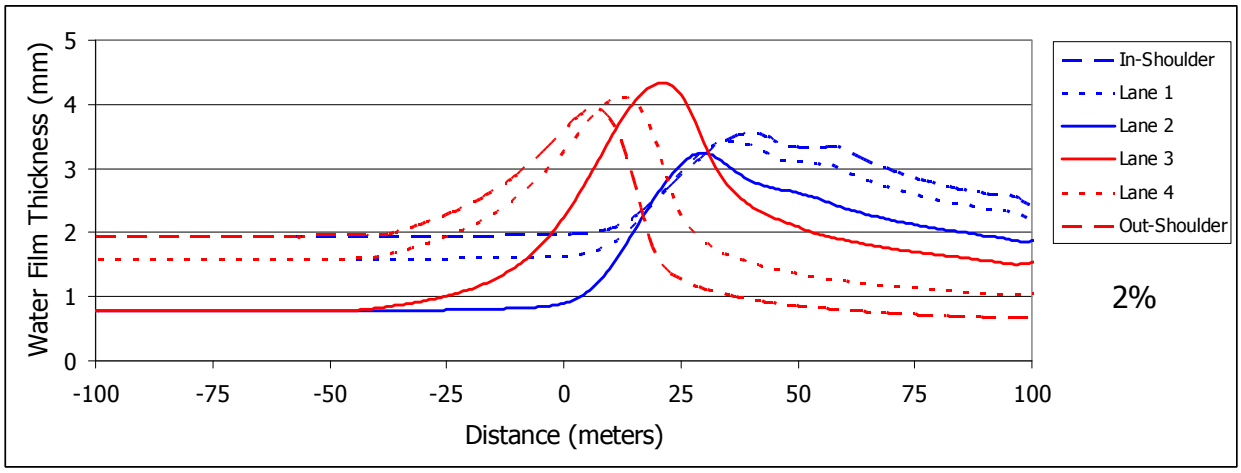

(d) Longitudinal Slope = 2.0 Percent

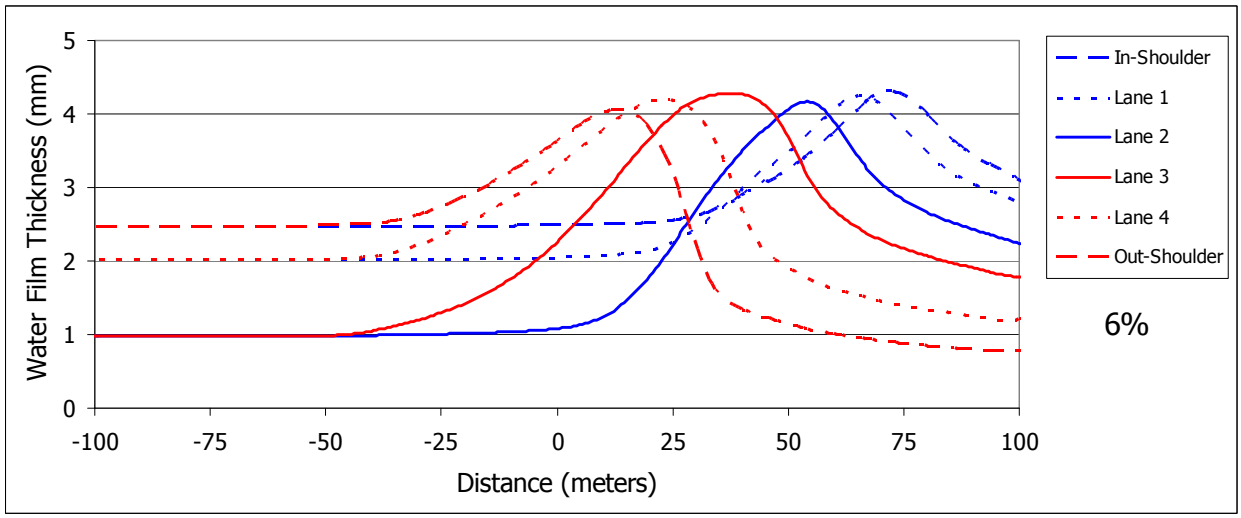

(e) Longitudinal Slope = 6.0 Percent

Figure A3. Water Film Thickness (WFT) profiles for roadway with four travel lanes and downward longitudinal slope in left-to-right direction.

Note: The roadway alignment corresponds to Figure A2 with profiles shown in blue color corresponding to vehicle travel from left-to-right, and profiles shown in red color corresponding to vehicle travel from right-to-left. The primary variables are Manning's n = 0.015, normal crown cross slope Sx = 2 percent, and rainfall intensity = 100 mm/hr (4 in/hr).

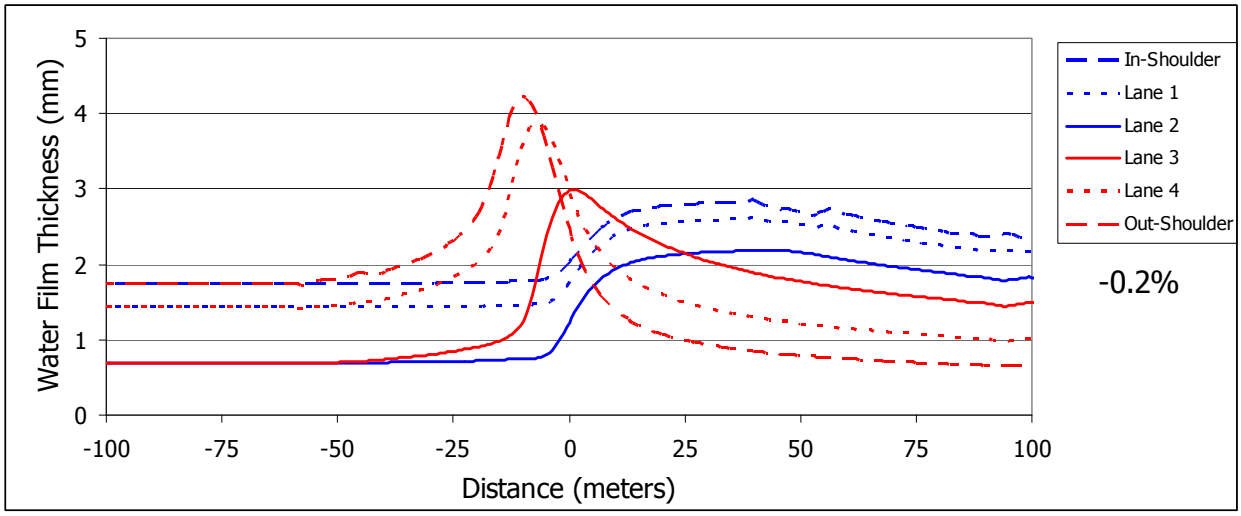

(a) Longitudinal Slope = -0.2 Percent

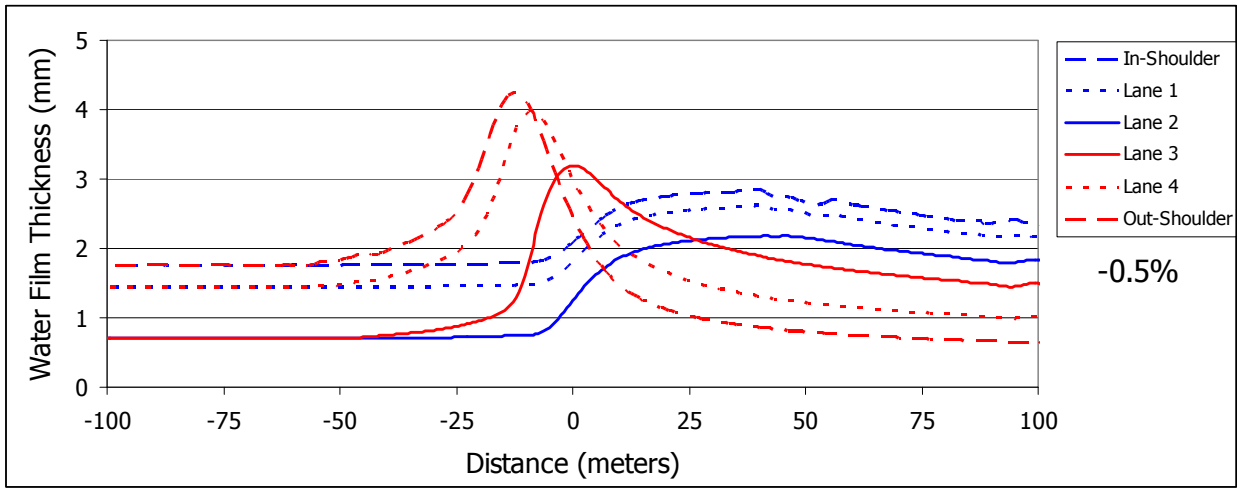

(b) Longitudinal Slope = -0.5 Percent

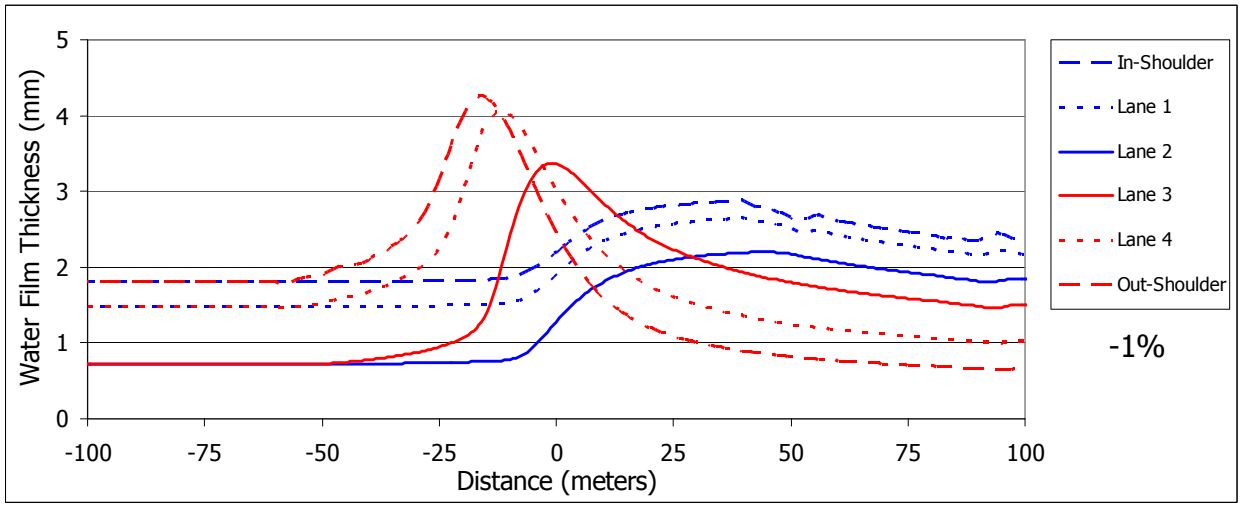

(c) Longitudinal Slope = -1.0 Percent

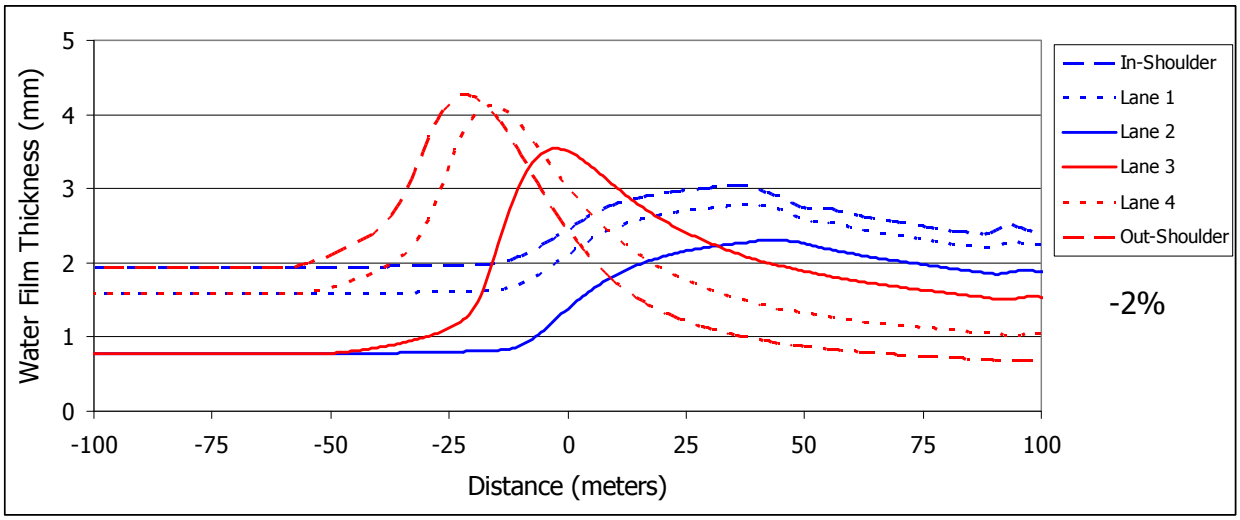

(d) Longitudinal Slope = -2.0 Percent

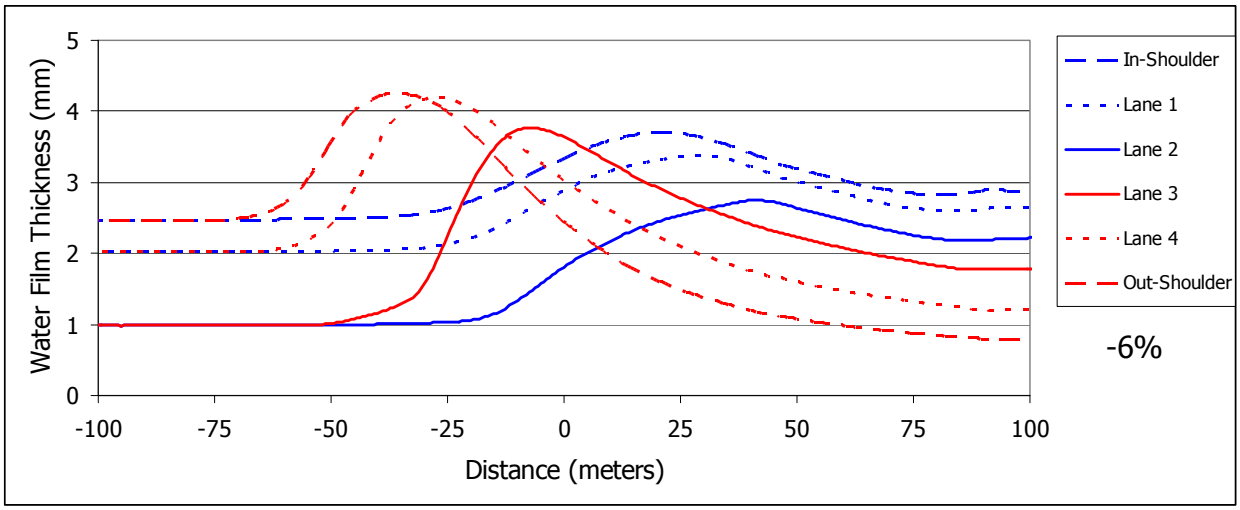

(e) Longitudinal Slope = -6.0 Percent

Figure A4. Water Film Thickness (WFT) profiles for roadway with four travel lanes and upward longitudinal slope in left-to-right direction.

Note: The roadway alignment corresponds to Figure A2 with profiles shown in blue color corresponding to vehicle travel from left-to-right, and profiles shown in red color corresponding to vehicle travel from right-to-left. The primary variables are Manning's n = 0.015, normal crown cross slope Sx = 2 percent, and rainfall intensity = 100 mm/hr (4 in/hr).

Discussion: Figures A3 and A4 clearly show that runoff depth (WFT) distribution is nonuniform and irregular through superelevation transitions, and that most of the irregular variation in WFT is located near the ZCS station. For positive longitudinal grade (Figure A3) the maximum WFT within the travel lanes occurs near the roadway centerline in Lane 3 (outer lanes). Except for very small (0.1 and 0.2 percent) and large (5 and 6 percent) grades, this is the largest WFT on the entire roadway surface. However, the variation in maximum WFT with grade is not significant. Of greater interest is the variation of WFT in the longitudinal direction (along the travel lanes).

There are significant (1 to 3 mm) variations in runoff depth over short (25 to 50 meter) distances. The 'rate' of depth variation is greater for smaller longitudinal grades. Similar results are found for negative grades (Figure A4), except that the largest WFT is always located on the outer shoulder and the largest WFT within the travel lanes is always located on the outer part of Lane 4. Figure A5 shows the variation with maximum WFT on the travel lanes and roadway as a function of longitudinal grade for a roadway surface with G = 0.45 percent.

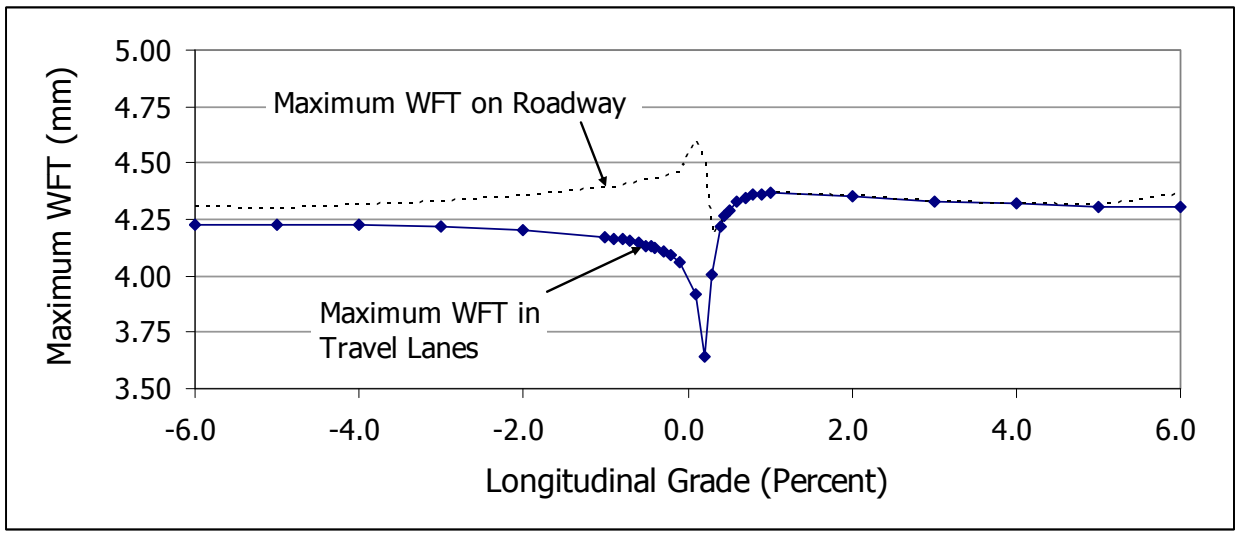

Figure A5. Variation in maximum Water Film Thickness (WFT) with longitudinal grade for a roadway surface with relative gradient G = 0.45 percent.

Longitudinal Alignment: The WFT profiles shown in Figures A3 and A4 are based on a roadway longitudinal alignment corresponding to a roadway curve-to-the-right as one moves from left-to-right in Figure A2. Identical profiles will be found for a curve-to-the-left, except that the direction of traffic flow will be reversed. The red profiles correspond to vehicle traffic from left-to-right, while the blue profiles correspond to vehicle traffic from right-to-left. The longitudinal variation in WFT for the outer lanes (red) is more significant for this case. The condition with greatest longitudinal variation in WFT occurs in Lane 3 for a longitudinal slope = G (0.45 percent for this case) with a 'curve-to-the-left'.

Design Guidance Summary: Literature on hydroplaning potential clearly shows that WFT is a significant variable. There is little literature guidance on the effects of longitudinal and transverse variations in WFT on hydroplaning potential, and these variations may be more significant than the magnitude of WFT through superelevation transitions. If minimization of WFT is the primary objective in design, and if the natural longitudinal grade is small (less than the maximum relative gradient specified in TxDOT Roadway Design manual, Table 2.8), then the maximum WFT can be minimized by selecting a relative gradient (G) equal to the longitudinal grade at a superelevation transition, as shown in Figure A5. However, the advantage in design is not large, and greater depths occur on the roadway shoulders. Generally for superelevation transitions, larger longitudinal gradients result in larger regions with ponded water on the roadway surface, while smaller longitudinal grades result in larger variations in WFT in the direction of traffic flow.

Appendix B. Experimental Data

Experimental data are listed in this appendix for the three surfaces considered. Data includes temperature, unit discharge and flow depth. For each experiment, unit discharge and flow depth are reported for each of the three sample ports and represent average values from three repetitive measurements.

Kinematic viscosity is calculated from measured temperature using the following empirical model.

$$\ln\left(\frac{\nu}{\nu_0}\right) = a + b\left(\frac{T_0}{T}\right) + c\left(\frac{T_0}{T}\right)^2$$

Tabulated kinematic viscosity values at temperatures ranging from 0 to 50 degrees Celsius were used to find best-fit parameter values with base values $\nu_0 = 1.792(10^{-6})$ m^2/s at T_0 = 0 Celsius = 273.16 Kelvin. The resulting model equation is

$$10^6\,\nu = 1.792\exp\left(2.443 - 14.146\left(\frac{273.16}{273.16 + C}\right) + 11.701\left(\frac{273.16}{273.16 + C}\right)^2\right)$$

The model curve and tabular data are shown in Figure B1 and Table B1.

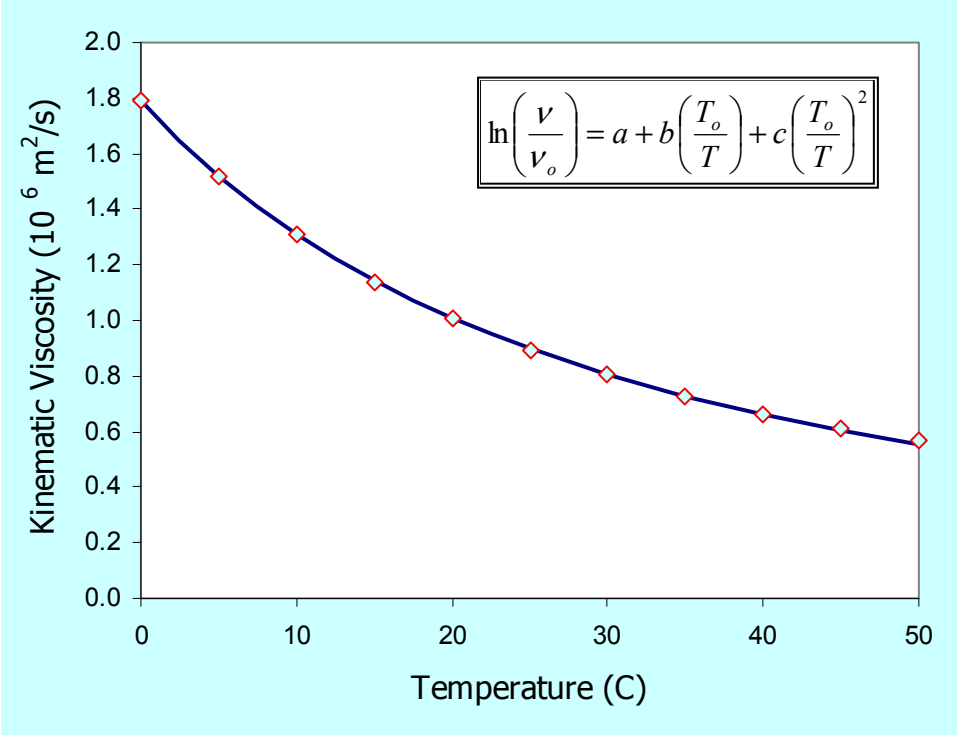

Figure B1: Model curve

The shaded data in the following table correspond to the potential outliers identified in Figures 3.22 to 3.24.

Table B1: Tabular data

Surface 1 Data

Test No.	*Condition*	Slope	Temp. (C^o)	Kin.Visc. (ν) 10^6 (m^2/s)	Discharge (q) (m^2/s)	Depth (h) (m)
1.1.1	*NR*	0.01	22.2	0.953	0.00198	0.00730
1.1.2	*NR*	0.01	22.2	0.953	0.00160	0.00549
1.1.3	*NR*	0.01	22.2	0.953	0.00100	0.00613
1.2.1	*NR*	0.01	23.3	0.929	0.00159	0.00699
1.2.2	*NR*	0.01	23.3	0.929	0.00127	0.00549
1.2.3	*NR*	0.01	23.3	0.929	0.00072	0.00565
1.3.1	*NR*	0.01	23.3	0.929	0.00134	0.00651
1.3.2	*NR*	0.01	23.3	0.929	0.00112	0.00533
1.3.3	*NR*	0.01	23.3	0.929	0.00048	0.00501
1.4.1	*NR*	0.01	23.9	0.916	0.00118	0.00619
1.4.2	*NR*	0.01	23.9	0.916	0.00101	0.00555
1.4.3	*NR*	0.01	23.9	0.916	0.00040	0.00507
1.5.1	*NR*	0.01	22.8	0.940	0.00170	0.00784
1.5.2	*NR*	0.01	22.8	0.940	0.00143	0.00795
1.5.3	*NR*	0.01	22.8	0.940	0.00103	0.00624
1.6.1	*NR*	0.01	22.8	0.940	0.00128	0.00640
1.6.2	*NR*	0.01	22.8	0.940	0.00103	0.00683
1.6.3	*NR*	0.01	22.8	0.940	0.00067	0.00533
1.7.1	*NR*	0.01	24.4	0.906	0.00104	0.00560
1.7.2	*NR*	0.01	24.4	0.906	0.00081	0.00576
1.7.3	*NR*	0.01	24.4	0.906	0.00046	0.00449
1.8.1	*NR*	0.01	24.4	0.906	0.00160	0.00699
1.8.2	*NR*	0.01	24.4	0.906	0.00129	0.00725
1.8.3	*NR*	0.01	24.4	0.906	0.00093	0.00560
1.9.1	*NR*	0.01	25.0	0.894	0.00066	0.00416
1.9.2	*NR*	0.01	25.0	0.894	0.00056	0.00437
1.9.3	*NR*	0.01	25.0	0.894	0.00013	0.00336
1.10.1	*NR*	0.01	22.2	0.953	0.00093	0.00523
1.10.2	*NR*	0.01	22.2	0.953	0.00076	0.00544
1.10.3	*NR*	0.01	22.2	0.953	0.00030	0.00421
1.11.1	*NR*	0.01	23.3	0.929	0.00120	0.00667

Test No.	*Condition*	Slope	Temp. (C^o)	Kin.Visc. (ν) 10^6 (m^2/s)	Discharge (q) (m^2/s)	Depth (h) (m)
1.11.2	*NR*	0.01	23.3	0.929	0.00105	0.00677
1.11.3	*NR*	0.01	23.3	0.929	0.00067	0.00517
1.12.1	*NR*	0.01	24.4	0.906	0.00089	0.00523
1.12.2	*NR*	0.01	24.4	0.906	0.00070	0.00507
1.12.3	*NR*	0.01	24.4	0.906	0.00022	0.00395
1.13.1	*NR*	0.01	25.6	0.882	0.00297	0.01056
1.13.2	*NR*	0.01	25.6	0.882	0.00288	0.01051
1.13.3	*NR*	0.01	25.6	0.882	0.00225	0.00848
1.14.1	*NR*	0.01	30.0	0.802	0.00104	0.00576
1.14.2	*NR*	0.01	30.0	0.802	0.00072	0.00549
1.14.3	*NR*	0.01	30.0	0.802	0.00023	0.00389
1.15.1	*NR*	0.01	30.6	0.793	0.00158	0.00731
1.15.2	*NR*	0.01	30.6	0.793	0.00105	0.00677
1.15.3	*NR*	0.01	30.6	0.793	0.00051	0.00453
1.16.1	*NR*	0.01	30.6	0.793	0.00107	0.00624
1.16.2	*NR*	0.01	30.6	0.793	0.00073	0.00565
1.16.3	*NR*	0.01	30.6	0.793	0.00020	0.00389
1.17.1	*NR*	0.01	28.9	0.821	0.00101	0.00587
1.17.2	*NR*	0.01	28.9	0.821	0.00070	0.00517
1.17.3	*NR*	0.01	28.9	0.821	0.00017	0.00352
1.18.1	*NR*	0.01	30.0	0.802	0.00092	0.00549
1.18.2	*NR*	0.01	30.0	0.802	0.00066	0.00517
1.18.3	*NR*	0.01	30.0	0.802	0.00015	0.00373
1.19.1	*R*	0.01	22.2	0.953	0.00089	0.00480
1.19.2	*R*	0.01	22.2	0.953	0.00074	0.00464
1.19.3	*R*	0.01	22.2	0.953	0.00020	0.00411
1.20.1	*R*	0.01	24.2	0.910	0.00094	0.00539
1.20.2	*R*	0.01	24.2	0.910	0.00078	0.00475
1.20.3	*R*	0.01	24.2	0.910	0.00020	0.00400
1.21.1	*R*	0.01	25.6	0.882	0.00085	0.00480
1.21.2	*R*	0.01	25.6	0.882	0.00074	0.00533
1.21.3	*R*	0.01	25.6	0.882	0.00034	0.00421
1.22.1	*R*	0.01	26.7	0.861	0.00080	0.00453
1.22.2	*R*	0.01	26.7	0.861	0.00069	0.00507
1.22.3	*R*	0.01	26.7	0.861	0.00027	0.00405
1.23.1	*R*	0.01	25.6	0.882	0.00079	0.00485
1.23.2	*R*	0.01	25.6	0.882	0.00070	0.00544
1.23.3	*R*	0.01	25.6	0.882	0.00021	0.00405

Test No.	*Condition*	Slope	Temp. (C^o)	Kin.Visc. (ν) 10^6 (m^2/s)	Discharge (q) (m^2/s)	Depth (h) (m)
1.24.1	*R*	0.01	28.9	0.821	0.00060	0.00469
1.24.2	*R*	0.01	28.9	0.821	0.00042	0.00485
1.24.3	*R*	0.01	28.9	0.821	0.00010	0.00309
1.25.1	*R*	0.01	26.7	0.861	0.00074	0.00480
1.25.2	*R*	0.01	26.7	0.861	0.00052	0.00459
1.25.3	*R*	0.01	26.7	0.861	0.00018	0.00352
1.26.1	*R*	0.01	27.8	0.840	0.00075	0.00464
1.26.2	*R*	0.01	27.8	0.840	0.00052	0.00480
1.26.3	*R*	0.01	27.8	0.840	0.00018	0.00379
1.27.1	*R*	0.01	25.6	0.882	0.00070	0.00448
1.27.2	*R*	0.01	25.6	0.882	0.00048	0.00416
1.27.3	*R*	0.01	25.6	0.882	0.00013	0.00309
1.28.1	*R*	0.01	26.1	0.872	0.00056	0.00389
1.28.2	*R*	0.01	26.1	0.872	0.00037	0.00400
1.28.3	*R*	0.01	26.1	0.872	0.00007	0.00331
1.29.1	*R&HB*	0.01	17.2	1.077	0.00267	0.00837
1.29.2	*R&HB*	0.01	17.2	1.077	0.00206	0.00715
1.29.3	*R&HB*	0.01	17.2	1.077	0.00252	0.00613
1.30.1	*R&HB*	0.01	16.4	1.099	0.00124	0.00587
1.30.2	*R&HB*	0.01	16.4	1.099	0.00127	0.00496
1.30.3	*R&HB*	0.01	16.4	1.099	0.00088	0.00432
1.31.1	*R&HB*	0.01	17.8	1.061	0.00109	0.00496
1.31.2	*R&HB*	0.01	17.8	1.061	0.00115	0.00437
1.31.3	*R&HB*	0.01	17.8	1.061	0.00074	0.00411
1.32.1	*R&HB*	0.01	17.8	1.061	0.00263	0.00821
1.32.2	*R&HB*	0.01	17.8	1.061	0.00214	0.00715
1.32.3	*R&HB*	0.01	17.8	1.061	0.00127	0.00603
1.33.1	*R&HB*	0.01	25.6	0.882	0.00157	0.00704
1.33.2	*R&HB*	0.01	25.6	0.882	0.00142	0.00763
1.33.3	*R&HB*	0.01	25.6	0.882	0.00091	0.00581
1.34.1	*R&HB*	0.01	25.6	0.882	0.00112	0.00597
1.34.2	*R&HB*	0.01	25.6	0.882	0.00101	0.00613
1.34.3	*R&HB*	0.01	25.6	0.882	0.00053	0.00480
1.35.1	*R&HB*	0.01	25.6	0.882	0.00156	0.00773
1.35.2	*R&HB*	0.01	25.6	0.882	0.00139	0.00747
1.35.3	*R&HB*	0.01	25.6	0.882	0.00091	0.00581
1.36.1	*R&HB*	0.01	23.3	0.929	0.00121	0.00640
1.36.2	*R&HB*	0.01	23.3	0.929	0.00109	0.00629

Test No.	*Condition*	Slope	Temp. (C^o)	Kin.Visc. (ν) 10^6 (m^2/s)	Discharge (q) (m^2/s)	Depth (h) (m)
1.36.3	*R&HB*	0.01	23.3	0.929	0.00063	0.00480
1.37.1	*R&HB*	0.01	29.7	0.807	0.00255	0.00880
1.37.2	*R&HB*	0.01	29.7	0.807	0.00200	0.00875
1.37.3	*R&HB*	0.01	29.7	0.807	0.00134	0.00667
1.38.1	*R&HB*	0.01	30.5	0.794	0.00331	0.00981
1.38.2	*R&HB*	0.01	30.5	0.794	0.00271	0.01024
1.38.3	*R&HB*	0.01	30.5	0.794	0.00193	0.00816
1.39.1	*R&HB*	0.01	25.6	0.882	0.00076	0.00491
1.39.2	*R&HB*	0.01	25.6	0.882	0.00054	0.00480
1.39.3	*R&HB*	0.01	25.6	0.882	0.00014	0.00384
1.40.1	*R&HB*	0.01	28.9	0.821	0.00093	0.00555
1.40.2	*R&HB*	0.01	28.9	0.821	0.00063	0.00512
1.40.3	*R&HB*	0.01	28.9	0.821	0.00022	0.00373
1.41.1	*R&HB*	0.01	28.3	0.832	0.00100	0.00555
1.41.2	*R&HB*	0.01	28.3	0.832	0.00074	0.00544
1.41.3	*R&HB*	0.01	28.3	0.832	0.00030	0.00416
1.42.1	*R&HB*	0.01	28.9	0.821	0.00100	0.00613
1.42.2	*R&HB*	0.01	28.9	0.821	0.00072	0.00608
1.42.3	*R&HB*	0.01	28.9	0.821	0.00027	0.00448
1.43.1	*R&HB*	0.01	30.5	0.794	0.00120	0.00629
1.43.2	*R&HB*	0.01	30.5	0.794	0.00087	0.00565
1.43.3	*R&HB*	0.01	30.5	0.794	0.00038	0.00384
1.44.1	*R&HB*	0.01	31.1	0.785	0.00110	0.00592
1.44.2	*R&HB*	0.01	31.1	0.785	0.00076	0.00576
1.44.3	*R&HB*	0.01	31.1	0.785	0.00030	0.00443
1.45.1	*NR*	0.02	12.8	1.210	0.00108	0.00501
1.45.2	*NR*	0.02	12.8	1.210	0.00135	0.00581
1.45.3	*NR*	0.02	12.8	1.210	0.00110	0.00619
1.46.1	*NR*	0.02	12.8	1.210	0.00028	0.00251
1.46.2	*NR*	0.02	12.8	1.210	0.00044	0.00395
1.46.3	*NR*	0.02	12.8	1.210	0.00032	0.00384
1.47.1	*NR*	0.02	12.8	1.210	0.00048	0.00352
1.47.2	*NR*	0.02	12.8	1.210	0.00060	0.00485
1.47.3	*NR*	0.02	12.8	1.210	0.00060	0.00448
1.48.1	*NR*	0.02	12.8	1.210	0.00138	0.00608
1.48.2	*NR*	0.02	12.8	1.210	0.00168	0.00640
1.48.3	*NR*	0.02	12.8	1.210	0.00144	0.00827

Test No.	*Condition*	Slope	Temp. (C^o)	Kin.Visc. (ν) 10^6 (m^2/s)	Discharge (q) (m^2/s)	Depth (h) (m)
1.49.1	*NR*	0.02	12.8	1.210	0.00084	0.00512
1.49.2	*NR*	0.02	12.8	1.210	0.00109	0.00608
1.49.3	*NR*	0.02	12.8	1.210	0.00085	0.00675
1.50.1	*NR*	0.02	12.8	1.210	0.00092	0.00555
1.50.2	*NR*	0.02	12.8	1.210	0.00119	0.00523
1.50.3	*NR*	0.02	12.8	1.210	0.00095	0.00533
1.51.1	*NR*	0.02	11.1	1.268	0.00124	0.00576
1.51.2	*NR*	0.02	11.1	1.268	0.00154	0.00544
1.51.3	*NR*	0.02	11.1	1.268	0.00128	0.00608
1.52.1	*NR*	0.02	11.7	1.247	0.00124	0.00635
1.52.2	*NR*	0.02	11.7	1.247	0.00152	0.00613
1.52.3	*NR*	0.02	11.7	1.247	0.00127	0.00640
1.53.1	*NR*	0.02	13.3	1.193	0.00180	0.00709
1.53.2	*NR*	0.02	13.3	1.193	0.00225	0.00699
1.53.3	*NR*	0.02	13.3	1.193	0.00191	0.00741
1.54.1	*NR*	0.02	27.8	0.840	0.00098	0.00395
1.54.2	*NR*	0.02	27.8	0.840	0.00058	0.00373
1.54.3	*NR*	0.02	27.8	0.840	0.00024	0.00299
1.55.1	*NR*	0.02	28.3	0.832	0.00366	0.00752
1.55.2	*NR*	0.02	28.3	0.832	0.00293	0.00651
1.55.3	*NR*	0.02	28.3	0.832	0.00197	0.00640
1.56.1	*NR*	0.02	26.1	0.872	0.00107	0.00443
1.56.2	*NR*	0.02	26.1	0.872	0.00064	0.00453
1.56.3	*NR*	0.02	26.1	0.872	0.00036	0.00347
1.57.1	*NR*	0.02	27.2	0.851	0.00242	0.00672
1.57.2	*NR*	0.02	27.2	0.851	0.00181	0.00623
1.57.3	*NR*	0.02	27.2	0.851	0.00127	0.00581
1.58.1	*NR*	0.02	26.1	0.872	0.00371	0.00805
1.58.2	*NR*	0.02	26.1	0.872	0.00299	0.00725
1.58.3	*NR*	0.02	26.1	0.872	0.00209	0.00693
1.59.1	*NR*	0.02	28.9	0.821	0.00092	0.00368
1.59.2	*NR*	0.02	28.9	0.821	0.00054	0.00373
1.59.3	*NR*	0.02	28.9	0.821	0.00036	0.00315
1.60.1	*NR*	0.02	29.4	0.813	0.00129	0.00459
1.60.2	*NR*	0.02	29.4	0.813	0.00083	0.00512
1.60.3	*NR*	0.02	29.4	0.813	0.00053	0.00427
1.61.1	*NR*	0.02	28.3	0.832	0.00212	0.00587
1.61.2	*NR*	0.02	28.3	0.832	0.00153	0.00549

Test No.	*Condition*	Slope	Temp. (C^o)	Kin.Visc. (ν) 10^6 (m^2/s)	Discharge (q) (m^2/s)	Depth (h) (m)
1.61.3	*NR*	0.02	28.3	0.832	0.00111	0.00491
1.62.1	*NR*	0.02	28.3	0.832	0.00082	0.00411
1.62.2	*NR*	0.02	28.3	0.832	0.00048	0.00389
1.62.3	*NR*	0.02	28.3	0.832	0.00022	0.00325
1.63.1	*NR*	0.02	28.9	0.821	0.00100	0.00432
1.63.2	*NR*	0.02	28.9	0.821	0.00060	0.00448
1.63.3	*NR*	0.02	28.9	0.821	0.00034	0.00336
1.64.1	*NR*	0.02	28.9	0.821	0.00088	0.00405
1.64.2	*NR*	0.02	28.9	0.821	0.00056	0.00405
1.64.3	*NR*	0.02	28.9	0.821	0.00029	0.00309
1.65.1	*NR*	0.02	29.4	0.813	0.00111	0.00459
1.65.2	*NR*	0.02	29.4	0.813	0.00075	0.00459
1.65.3	*NR*	0.02	29.4	0.813	0.00045	0.00331
1.66.1	*NR*	0.02	30.0	0.802	0.00058	0.00309
1.66.2	*NR*	0.02	30.0	0.802	0.00040	0.00309
1.66.3	*NR*	0.02	30.0	0.802	0.00011	0.00256
1.67.1	*NR*	0.02	30.5	0.794	0.00067	0.00363
1.67.2	*NR*	0.02	30.5	0.794	0.00046	0.00352
1.67.3	*NR*	0.02	30.5	0.794	0.00015	0.00299
1.68.1	*NR*	0.02	31.7	0.775	0.00065	0.00379
1.68.2	*NR*	0.02	31.7	0.775	0.00044	0.00363
1.68.3	*NR*	0.02	31.7	0.775	0.00014	0.00288
1.69.1	*NR*	0.02	29.4	0.813	0.00084	0.00395
1.69.2	*NR*	0.02	29.4	0.813	0.00055	0.00373
1.69.3	*NR*	0.02	29.4	0.813	0.00020	0.00304
1.70.1	*NR*	0.02	30.0	0.802	0.00079	0.00405
1.70.2	*NR*	0.02	30.0	0.802	0.00051	0.00416
1.70.3	*NR*	0.02	30.0	0.802	0.00017	0.00299
1.71.1	*NR*	0.02	32.2	0.768	0.00075	0.00363
1.71.2	*NR*	0.02	32.2	0.768	0.00050	0.00352
1.71.3	*NR*	0.02	32.2	0.768	0.00016	0.00288
1.72.1	*NR*	0.02	32.8	0.758	0.00106	0.00427
1.72.2	*NR*	0.02	32.8	0.758	0.00071	0.00427
1.72.3	*NR*	0.02	32.8	0.758	0.00042	0.00331
1.73.1	*NR*	0.02	30.0	0.802	0.00082	0.00373
1.73.2	*NR*	0.02	30.0	0.802	0.00052	0.00357
1.73.3	*NR*	0.02	30.0	0.802	0.00023	0.00299
1.74.1	*NR*	0.02	30.5	0.794	0.00075	0.00363

Test No.	*Condition*	Slope	Temp. (C^o)	Kin.Visc. (ν) 10^6 (m^2/s)	Discharge (q) (m^2/s)	Depth (h) (m)
1.74.2	*NR*	0.02	30.5	0.794	0.00047	0.00352
1.74.3	*NR*	0.02	30.5	0.794	0.00017	0.00277
1.75.1	*NR*	0.02	31.7	0.775	0.00105	0.00432
1.75.2	*NR*	0.02	31.7	0.775	0.00065	0.00448
1.75.3	*NR*	0.02	31.7	0.775	0.00038	0.00379
1.76.1	*NR*	0.02	29.4	0.813	0.00068	0.00347
1.76.2	*NR*	0.02	29.4	0.813	0.00041	0.00341
1.76.3	*NR*	0.02	29.4	0.813	0.00013	0.00272
1.77.1	*R*	0.02	14.4	1.159	0.00062	0.00283
1.77.2	*R*	0.02	14.4	1.159	0.00056	0.00395
1.77.3	*R*	0.02	14.4	1.159	0.00030	0.00320
1.78.1	*R*	0.02	14.4	1.159	0.00042	0.00405
1.78.2	*R*	0.02	14.4	1.159	0.00059	0.00517
1.78.3	*R*	0.02	14.4	1.159	0.00031	0.00411
1.79.*	*R*	0.02	14.4	1.159	0.00037	0.00245
1.80.1	*R*	0.02	14.4	1.159	0.00060	0.00256
1.80.2	*R*	0.02	14.4	1.159	0.00064	0.00331
1.80.3	*R*	0.02	14.4	1.159	0.00038	0.00341
1.81.1	*R*	0.02	14.4	1.159	0.00041	0.00304
1.81.2	*R*	0.02	14.4	1.159	0.00059	0.00331
1.81.3	*R*	0.02	14.4	1.159	0.00041	0.00395
1.82.1	*R*	0.02	14.4	1.159	0.00045	0.00267
1.82.2	*R*	0.02	14.4	1.159	0.00059	0.00363
1.82.3	*R*	0.02	14.4	1.159	0.00039	0.00411
1.83.1	*R*	0.02	14.4	1.159	0.00038	0.00293
1.83.2	*R*	0.02	14.4	1.159	0.00053	0.00373
1.83.3	*R*	0.02	14.4	1.159	0.00040	0.00384
1.84.1	*R*	0.02	14.4	1.159	0.00040	0.00299
1.84.2	*R*	0.02	14.4	1.159	0.00056	0.00469
1.84.3	*R*	0.02	14.4	1.159	0.00041	0.00485
1.85.1	*R*	0.02	15.5	1.125	0.00042	0.00293
1.85.2	*R*	0.02	15.5	1.125	0.00056	0.00432
1.85.3	*R*	0.02	15.5	1.125	0.00040	0.00432
1.86.1	*R*	0.02	16.1	1.108	0.00041	0.00309
1.86.2	*R*	0.02	16.1	1.108	0.00055	0.00416
1.86.3	*R*	0.02	16.1	1.108	0.00038	0.00432
1.87.1	*R*	0.02	15.5	1.125	0.00048	0.00245
1.87.2	*R*	0.02	15.5	1.125	0.00058	0.00395

Test No.	*Condition*	Slope	Temp. (C^o)	Kin.Visc. (ν) 10^6 (m^2/s)	Discharge (q) (m^2/s)	Depth (h) (m)
1.87.3	*R*	0.02	15.5	1.125	0.00044	0.00363
1.88.1	*R*	0.02	15.5	1.125	0.00047	0.00309
1.88.2	*R*	0.02	15.5	1.125	0.00057	0.00427
1.88.3	*R*	0.02	15.5	1.125	0.00046	0.00384
1.89.1	*R*	0.02	29.2	0.816	0.00076	0.00363
1.89.2	*R*	0.02	29.2	0.816	0.00049	0.00368
1.89.3	*R*	0.02	29.2	0.816	0.00031	0.00357
1.90.1	*R*	0.02	27.8	0.840	0.00080	0.00341
1.90.2	*R*	0.02	27.8	0.840	0.00050	0.00347
1.90.3	*R*	0.02	27.8	0.840	0.00035	0.00341
1.91.1	*R*	0.02	28.6	0.826	0.00070	0.00331
1.91.2	*R*	0.02	28.6	0.826	0.00043	0.00363
1.91.3	*R*	0.02	28.6	0.826	0.00025	0.00341
1.92.1	*R*	0.02	28.3	0.832	0.00061	0.00325
1.92.2	*R*	0.02	28.3	0.832	0.00039	0.00363
1.92.3	*R*	0.02	28.3	0.832	0.00020	0.00336
1.93.1	*R*	0.02	26.7	0.861	0.00061	0.00315
1.93.2	*R*	0.02	26.7	0.861	0.00042	0.00363
1.93.3	*R*	0.02	26.7	0.861	0.00026	0.00331
1.94.1	*R*	0.02	27.5	0.846	0.00069	0.00341
1.94.2	*R*	0.02	27.5	0.846	0.00045	0.00379
1.94.3	*R*	0.02	27.5	0.846	0.00030	0.00331
1.95.1	*R*	0.02	30.5	0.794	0.00057	0.00363
1.95.2	*R*	0.02	30.5	0.794	0.00038	0.00384
1.95.3	*R*	0.02	30.5	0.794	0.00021	0.00363
1.96.1	*R*	0.02	30.8	0.789	0.00050	0.00320
1.96.2	*R*	0.02	30.8	0.789	0.00033	0.00352
1.96.3	*R*	0.02	30.8	0.789	0.00015	0.00320
1.97.1	*R*	0.02	30.8	0.789	0.00052	0.00286
1.97.2	*R*	0.02	30.8	0.789	0.00033	0.00328
1.97.3	*R*	0.02	30.8	0.789	0.00017	0.00304
1.98.1	*R*	0.02	30.0	0.802	0.00041	0.00288
1.98.2	*R*	0.02	30.0	0.802	0.00028	0.00296
1.98.3	*R*	0.02	30.0	0.802	0.00012	0.00272
1.99.1	*R*	0.02	31.7	0.775	0.00045	0.00280
1.99.2	*R*	0.02	31.7	0.775	0.00031	0.00296
1.99.3	*R*	0.02	31.7	0.775	0.00016	0.00272
1.100.1	*R*	0.02	26.7	0.861	0.00046	0.00232

Test No.	*Condition*	Slope	Temp. (C^o)	Kin.Visc. (ν) 10^6 (m^2/s)	Discharge (q) (m^2/s)	Depth (h) (m)
1.100.2	*R*	0.02	26.7	0.861	0.00031	0.00264
1.100.3	*R*	0.02	26.7	0.861	0.00014	0.00232
1.101.1	*R*	0.02	26.7	0.861	0.00051	0.00256
1.101.2	*R*	0.02	26.7	0.861	0.00034	0.00288
1.101.3	*R*	0.02	26.7	0.861	0.00018	0.00280
1.102.1	*R*	0.02	32.2	0.768	0.00040	0.00272
1.102.2	*R*	0.02	32.2	0.768	0.00030	0.00320
1.102.3	*R*	0.02	32.2	0.768	0.00014	0.00320
1.103.1	*R*	0.02	28.3	0.832	0.00081	0.00304
1.103.2	*R*	0.02	28.3	0.832	0.00060	0.00352
1.103.3	*R*	0.02	28.3	0.832	0.00036	0.00336
1.104.1	*R&HB*	0.02	14.4	1.159	0.00093	0.00443
1.104.2	*R&HB*	0.02	14.4	1.159	0.00118	0.00523
1.104.3	*R&HB*	0.02	14.4	1.159	0.00092	0.00533
1.105.1	*R&HB*	0.02	16.7	1.091	0.00102	0.00571
1.105.2	*R&HB*	0.02	16.7	1.091	0.00131	0.00587
1.105.3	*R&HB*	0.02	16.7	1.091	0.00107	0.00544
1.106.1	*R&HB*	0.02	16.7	1.091	0.00101	0.00565
1.106.2	*R&HB*	0.02	16.7	1.091	0.00130	0.00565
1.106.3	*R&HB*	0.02	16.7	1.091	0.00110	0.00565
1.107.1	*R&HB*	0.02	19.4	1.019	0.00110	0.00597
1.107.2	*R&HB*	0.02	19.4	1.019	0.00133	0.00629
1.107.3	*R&HB*	0.02	19.4	1.019	0.00121	0.00597
1.108.1	*R&HB*	0.02	20.6	0.990	0.00082	0.00501
1.108.2	*R&HB*	0.02	20.6	0.990	0.00103	0.00571
1.108.3	*R&HB*	0.02	20.6	0.990	0.00090	0.00512
1.109.1	*R&HB*	0.02	20.0	1.004	0.00076	0.00475
1.109.2	*R&HB*	0.02	20.0	1.004	0.00093	0.00565
1.109.3	*R&HB*	0.02	20.0	1.004	0.00082	0.00523
1.110.1	*R&HB*	0.02	19.4	1.019	0.00052	0.00395
1.110.2	*R&HB*	0.02	19.4	1.019	0.00069	0.00496
1.110.3	*R&HB*	0.02	19.4	1.019	0.00060	0.00432
1.111.1	*R&HB*	0.02	19.4	1.019	0.00200	0.00747
1.111.2	*R&HB*	0.02	19.4	1.019	0.00232	0.00709
1.111.3	*R&HB*	0.02	19.4	1.019	0.00206	0.00800
1.112.1	*R&HB*	0.02	28.3	0.832	0.00141	0.00475
1.112.2	*R&HB*	0.02	28.3	0.832	0.00099	0.00517
1.112.3	*R&HB*	0.02	28.3	0.832	0.00073	0.00459

Test No.	*Condition*	Slope	Temp. (C^o)	Kin.Visc. (ν) 10^6 (m^2/s)	Discharge (q) (m^2/s)	Depth (h) (m)
1.113.1	*R&HB*	0.02	25.6	0.882	0.00157	0.00501
1.113.2	*R&HB*	0.02	25.6	0.882	0.00115	0.00512
1.113.3	*R&HB*	0.02	25.6	0.882	0.00083	0.00437
1.114.1	*R&HB*	0.02	26.7	0.861	0.00293	0.00709
1.114.2	*R&HB*	0.02	26.7	0.861	0.00225	0.00656
1.114.3	*R&HB*	0.02	26.7	0.861	0.00160	0.00640
1.115.1	*R&HB*	0.02	26.7	0.861	0.00294	0.00756
1.115.2	*R&HB*	0.02	26.7	0.861	0.00228	0.00661
1.115.3	*R&HB*	0.02	26.7	0.861	0.00165	0.00608
1.116.1	*R&HB*	0.02	28.9	0.821	0.00381	0.00848
1.116.2	*R&HB*	0.02	28.9	0.821	0.00328	0.00763
1.116.3	*R&HB*	0.02	28.9	0.821	0.00229	0.00731
1.117.1	*R&HB*	0.02	31.1	0.785	0.00262	0.00640
1.117.2	*R&HB*	0.02	31.1	0.785	0.00192	0.00581
1.117.3	*R&HB*	0.02	31.1	0.785	0.00147	0.00533
1.118.1	*R&HB*	0.02	31.7	0.775	0.00209	0.00576
1.118.2	*R&HB*	0.02	31.7	0.775	0.00152	0.00565
1.118.3	*R&HB*	0.02	31.7	0.775	0.00109	0.00507
1.119.1	*R&HB*	0.02	30.6	0.793	0.00398	0.00795
1.119.2	*R&HB*	0.02	30.6	0.793	0.00320	0.00683
1.119.3	*R&HB*	0.02	30.6	0.793	0.00223	0.00651
1.120.1	*R&HB*	0.02	31.9	0.772	0.00253	0.00640
1.120.2	*R&HB*	0.02	31.9	0.772	0.00189	0.00592
1.120.3	*R&HB*	0.02	31.9	0.772	0.00139	0.00544
1.121.1	*R&HB*	0.02	32.2	0.768	0.00390	0.00816
1.121.2	*R&HB*	0.02	32.2	0.768	0.00320	0.00699
1.121.3	*R&HB*	0.02	32.2	0.768	0.00218	0.00672
1.122.1	*R&HB*	0.02	30.0	0.802	0.00136	0.00495
1.122.2	*R&HB*	0.02	30.0	0.802	0.00098	0.00507
1.122.3	*R&HB*	0.02	30.0	0.802	0.00066	0.00405
1.123.1	*R&HB*	0.02	30.0	0.802	0.00179	0.00555
1.123.2	*R&HB*	0.02	30.0	0.802	0.00129	0.00533
1.123.3	*R&HB*	0.02	30.0	0.802	0.00090	0.00448
1.124.1	*R&HB*	0.02	31.1	0.785	0.00226	0.00613
1.124.2	*R&HB*	0.02	31.1	0.785	0.00164	0.00597
1.124.3	*R&HB*	0.02	31.1	0.785	0.00119	0.00528
1.125.1	*R&HB*	0.02	28.8	0.823	0.00303	0.00736
1.125.2	*R&HB*	0.02	28.8	0.823	0.00247	0.00656

Test No.	*Condition*	Slope	Temp. (C^o)	Kin.Visc. (ν) 10^6 (m^2/s)	Discharge (q) (m^2/s)	Depth (h) (m)
1.125.3	*R&HB*	0.02	28.8	0.823	0.00170	0.00619
1.126.1	*NR*	0.03	25.0	0.894	0.00121	0.00544
1.126.2	*NR*	0.03	25.0	0.894	0.00089	0.00421
1.126.3	*NR*	0.03	25.0	0.894	0.00075	0.00448
1.127.1	*NR*	0.03	25.5	0.884	0.00110	0.00496
1.127.2	*NR*	0.03	25.5	0.884	0.00077	0.00411
1.127.3	*NR*	0.03	25.5	0.884	0.00065	0.00384
1.128.1	*NR*	0.03	26.1	0.872	0.00178	0.00603
1.128.2	*NR*	0.03	26.1	0.872	0.00139	0.00464
1.128.3	*NR*	0.03	26.1	0.872	0.00116	0.00485
1.129.1	*NR*	0.03	26.4	0.866	0.00230	0.00661
1.129.2	*NR*	0.03	26.4	0.866	0.00187	0.00512
1.129.3	*NR*	0.03	26.4	0.866	0.00145	0.00357
1.130.1	*NR*	0.03	27.8	0.840	0.00278	0.00725
1.130.2	*NR*	0.03	27.8	0.840	0.00228	0.00560
1.130.3	*NR*	0.03	27.8	0.840	0.00180	0.00539
1.131.1	*NR*	0.03	28.6	0.826	0.00049	0.00277
1.131.2	*NR*	0.03	28.6	0.826	0.00037	0.00299
1.131.3	*NR*	0.03	28.6	0.826	0.00013	0.00224
1.132.1	*NR*	0.03	26.7	0.861	0.00064	0.00379
1.132.2	*NR*	0.03	26.7	0.861	0.00046	0.00389
1.132.3	*NR*	0.03	26.7	0.861	0.00032	0.00304
1.133.1	*NR*	0.03	27.2	0.851	0.00140	0.00453
1.133.2	*NR*	0.03	27.2	0.851	0.00103	0.00395
1.133.3	*NR*	0.03	27.2	0.851	0.00081	0.00373
1.134.1	*NR*	0.03	27.2	0.851	0.00066	0.00331
1.134.2	*NR*	0.03	27.2	0.851	0.00045	0.00325
1.134.3	*NR*	0.03	27.2	0.851	0.00030	0.00277
1.135.1	*NR*	0.03	27.8	0.840	0.00056	0.00315
1.135.2	*NR*	0.03	27.8	0.840	0.00035	0.00315
1.135.3	*NR*	0.03	27.8	0.840	0.00017	0.00272
1.136.1	*NR*	0.03	28.9	0.821	0.00109	0.00459
1.136.2	*NR*	0.03	28.9	0.821	0.00074	0.00400
1.136.3	*NR*	0.03	28.9	0.821	0.00064	0.00389
1.137.1	*R*	0.03	23.9	0.916	0.00063	0.00357
1.137.2	*R*	0.03	23.9	0.916	0.00048	0.00336
1.137.3	*R*	0.03	23.9	0.916	0.00051	0.00309

Test No.	*Condition*	Slope	Temp. (C^o)	Kin.Visc. (ν) 10^6 (m^2/s)	Discharge (q) (m^2/s)	Depth (h) (m)
1.138.1	*R*	0.03	24.4	0.906	0.00069	0.00363
1.138.2	*R*	0.03	24.4	0.906	0.00050	0.00341
1.138.3	*R*	0.03	24.4	0.906	0.00050	0.00325
1.139.1	*R*	0.03	25.3	0.888	0.00063	0.00331
1.139.2	*R*	0.03	25.3	0.888	0.00045	0.00347
1.139.3	*R*	0.03	25.3	0.888	0.00044	0.00293
1.140.1	*R*	0.03	24.4	0.906	0.00058	0.00405
1.140.2	*R*	0.03	24.4	0.906	0.00042	0.00395
1.140.3	*R*	0.03	24.4	0.906	0.00040	0.00363
1.141.1	*R*	0.03	29.4	0.813	0.00062	0.00309
1.141.2	*R*	0.03	29.4	0.813	0.00046	0.00352
1.141.3	*R*	0.03	29.4	0.813	0.00046	0.00315
1.142.1	*R*	0.03	26.7	0.861	0.00052	0.00304
1.142.2	*R*	0.03	26.7	0.861	0.00039	0.00336
1.142.3	*R*	0.03	26.7	0.861	0.00036	0.00315
1.143.1	*R*	0.03	27.5	0.846	0.00050	0.00283
1.143.2	*R*	0.03	27.5	0.846	0.00036	0.00352
1.143.3	*R*	0.03	27.5	0.846	0.00032	0.00325
1.144.1	*R&HB*	0.03	25.5	0.884	0.00197	0.00645
1.144.2	*R&HB*	0.03	25.5	0.884	0.00158	0.00501
1.144.3	*R&HB*	0.03	25.5	0.884	0.00131	0.00496
1.145.1	*R&HB*	0.03	26.7	0.861	0.00138	0.00485
1.145.2	*R&HB*	0.03	26.7	0.861	0.00105	0.00400
1.145.3	*R&HB*	0.03	26.7	0.861	0.00089	0.00357
1.146.1	*R&HB*	0.03	23.3	0.929	0.00139	0.00523
1.146.2	*R&HB*	0.03	23.3	0.929	0.00105	0.00421
1.146.3	*R&HB*	0.03	23.3	0.929	0.00088	0.00405
1.147.1	*R&HB*	0.03	28.9	0.821	0.00263	0.00725
1.147.2	*R&HB*	0.03	28.9	0.821	0.00217	0.00560
1.147.3	*R&HB*	0.03	28.9	0.821	0.00175	0.00565
1.148.1	*R&HB*	0.03	28.3	0.832	0.00370	0.00699
1.148.2	*R&HB*	0.03	28.3	0.832	0.00317	0.00613
1.148.3	*R&HB*	0.03	28.3	0.832	0.00251	0.00619

Surface 2 Data

Test No.	*Condition*	Slope	Temp. (C^o)	Kin.Visc. (ν) 10^6 (m^2/s)	Discharge (q) (m^2/s)	Depth (h) (m)
2.1.1	*NR*	0.01	27.8	0.840	0.00253	0.01218
2.1.2	*NR*	0.01	27.8	0.840	0.00229	0.01157
2.1.3	*NR*	0.01	27.8	0.840	0.00106	0.00965
2.2.1	*NR*	0.01	28.9	0.821	0.00380	0.01461
2.2.2	*NR*	0.01	28.9	0.821	0.00318	0.01376
2.2.3	*NR*	0.01	28.9	0.821	0.00193	0.01157
2.3.1	*NR*	0.01	32.2	0.768	0.00186	0.01040
2.3.2	*NR*	0.01	32.2	0.768	0.00195	0.00976
2.3.3	*NR*	0.01	32.2	0.768	0.00089	0.00821
2.4.1	*NR*	0.01	34.4	0.735	0.00142	0.00992
2.4.2	*NR*	0.01	34.4	0.735	0.00143	0.00960
2.4.3	*NR*	0.01	34.4	0.735	0.00061	0.00789
2.5.1	*NR*	0.01	26.7	0.861	0.00090	0.00741
2.5.2	*NR*	0.01	26.7	0.861	0.00080	0.00683
2.5.3	*NR*	0.01	26.7	0.861	0.00021	0.00629
2.6.1	*NR*	0.01	27.8	0.840	0.00084	0.00715
2.6.2	*NR*	0.01	27.8	0.840	0.00075	0.00683
2.6.3	*NR*	0.01	27.8	0.840	0.00009	0.00656
2.7.1	*NR*	0.01	27.2	0.851	0.00073	0.00747
2.7.2	*NR*	0.01	27.2	0.851	0.00074	0.00667
2.7.3	*NR*	0.01	27.2	0.851	0.00038	0.00587
2.8.1	*NR*	0.01	27.8	0.840	0.00116	0.00853
2.8.2	*NR*	0.01	27.8	0.840	0.00111	0.00779
2.8.3	*NR*	0.01	27.8	0.840	0.00050	0.00672
2.9.1	*NR*	0.01	26.7	0.861	0.00105	0.00773
2.9.2	*NR*	0.01	26.7	0.861	0.00104	0.00725
2.9.3	*NR*	0.01	26.7	0.861	0.00034	0.00640
2.10.1	*NR*	0.01	27.8	0.840	0.00090	0.00875
2.10.2	*NR*	0.01	27.8	0.840	0.00092	0.00731
2.10.3	*NR*	0.01	27.8	0.840	0.00025	0.00635
2.11.1	*NR*	0.01	27.8	0.840	0.00107	0.00933
2.11.2	*NR*	0.01	27.8	0.840	0.00110	0.00848
2.11.3	*NR*	0.01	27.8	0.840	0.00035	0.00736
2.12.1	*NR*	0.01	29.4	0.813	0.00394	0.01611

Test No.	*Condition*	Slope	Temp. (C^o)	Kin.Visc. (ν) 10^6 (m^2/s)	Discharge (q) (m^2/s)	Depth (h) (m)
2.12.2	*NR*	0.01	29.4	0.813	0.00361	0.01536
2.12.3	*NR*	0.01	29.4	0.813	0.00240	0.01648
2.13.1	*NR*	0.01	30.0	0.802	0.00066	0.00747
2.13.2	*NR*	0.01	30.0	0.802	0.00075	0.00677
2.13.3	*NR*	0.01	30.0	0.802	0.00025	0.00613
2.14.1	*NR*	0.01	31.7	0.775	0.00125	0.00976
2.14.2	*NR*	0.01	31.7	0.775	0.00141	0.00891
2.14.3	*NR*	0.01	31.7	0.775	0.00057	0.00779
2.15.1	*NR*	0.01	30.0	0.802	0.00093	0.00704
2.15.2	*NR*	0.01	30.0	0.802	0.00099	0.00683
2.15.3	*NR*	0.01	30.0	0.802	0.00042	0.00603
2.16.1	*NR*	0.01	29.4	0.813	0.00047	0.00670
2.16.2	*NR*	0.01	29.4	0.813	0.00053	0.00597
2.16.3	*NR*	0.01	29.4	0.813	0.00012	0.00538
2.17.1	*NR*	0.01	31.1	0.785	0.00140	0.00965
2.17.2	*NR*	0.01	31.1	0.785	0.00138	0.00912
2.17.3	*NR*	0.01	31.1	0.785	0.00064	0.00805
2.18.1	*NR*	0.01	31.7	0.775	0.00104	0.00880
2.18.2	*NR*	0.01	31.7	0.775	0.00113	0.00821
2.18.3	*NR*	0.01	31.7	0.775	0.00046	0.00731
2.19.1	*NR*	0.01	30.0	0.802	0.00383	0.01612
2.19.2	*NR*	0.01	30.0	0.802	0.00401	0.01451
2.19.3	*NR*	0.01	30.0	0.802	0.00236	0.01337
2.20.1	*NR*	0.01	32.2	0.768	0.00086	0.00843
2.20.2	*NR*	0.01	32.2	0.768	0.00099	0.00747
2.20.3	*NR*	0.01	32.2	0.768	0.00041	0.00699
2.21.1	*NR*	0.01	29.4	0.813	0.00392	0.01691
2.21.2	*NR*	0.01	29.4	0.813	0.00391	0.01483
2.21.3	*NR*	0.01	29.4	0.813	0.00257	0.01328
2.22.1	*NR*	0.01	31.1	0.785	0.00277	0.01376
2.22.2	*NR*	0.01	31.1	0.785	0.00272	0.01259
2.22.3	*NR*	0.01	31.1	0.785	0.00136	0.01147
2.23.1	*NR*	0.01	33.3	0.751	0.00296	0.01355
2.23.2	*NR*	0.01	33.3	0.751	0.00292	0.01280
2.23.3	*NR*	0.01	33.3	0.751	0.00154	0.01077
2.24.1	*NR*	0.01	35.6	0.719	0.00295	0.01312
2.24.2	*NR*	0.01	35.6	0.719	0.00293	0.01248
2.24.3	*NR*	0.01	35.6	0.719	0.00147	0.01088

Test No.	*Condition*	Slope	Temp. (C^o)	Kin.Visc. (ν) 10^6 (m^2/s)	Discharge (q) (m^2/s)	Depth (h) (m)
2.25.1	*NR*	0.01	32.2	0.768	0.00402	0.01700
2.25.2	*NR*	0.01	32.2	0.768	0.00415	0.01580
2.25.3	*NR*	0.01	32.2	0.768	0.00261	0.01405
2.26.1	*NR*	0.01	32.2	0.768	0.00373	0.01722
2.26.2	*NR*	0.01	32.2	0.768	0.00417	0.01601
2.26.3	*NR*	0.01	32.2	0.768	0.00262	0.01426
2.27.1	*NR*	0.01	30.0	0.802	0.00256	0.01146
2.27.2	*NR*	0.01	30.0	0.802	0.00214	0.01041
2.27.3	*NR*	0.01	30.0	0.802	0.00088	0.00909
2.28.1	*NR*	0.01	30.0	0.802	0.00109	0.00650
2.28.2	*NR*	0.01	30.0	0.802	0.00091	0.00614
2.28.3	*NR*	0.01	30.0	0.802	0.00022	0.00541
2.29.1	*NR*	0.01	29.4	0.813	0.00068	0.00570
2.29.2	*NR*	0.01	29.4	0.813	0.00055	0.00566
2.29.3	*NR*	0.01	29.4	0.813	0.00014	0.00493
2.30.1	*NR*	0.01	30.0	0.802	0.00230	0.01114
2.30.2	*NR*	0.01	30.0	0.802	0.00195	0.01036
2.30.3	*NR*	0.01	30.0	0.802	0.00090	0.00898
2.31.1	*R*	0.01	27.8	0.840	0.00104	0.00832
2.31.2	*R*	0.01	27.8	0.840	0.00098	0.00779
2.31.3	*R*	0.01	27.8	0.840	0.00043	0.00704
2.35.1	*R*	0.01	28.9	0.821	0.00104	0.00848
2.35.2	*R*	0.01	28.9	0.821	0.00101	0.00763
2.35.3	*R*	0.01	28.9	0.821	0.00046	0.00667
2.36.1	*R*	0.01	27.8	0.840	0.00101	0.00853
2.36.2	*R*	0.01	27.8	0.840	0.00102	0.00752
2.36.3	*R*	0.01	27.8	0.840	0.00044	0.00656
2.37.1	*R*	0.01	29.4	0.813	0.00051	0.00587
2.37.2	*R*	0.01	29.4	0.813	0.00057	0.00560
2.37.3	*R*	0.01	29.4	0.813	0.00016	0.00539
2.38.1	*R*	0.01	32.8	0.758	0.00076	0.00720
2.38.2	*R*	0.01	32.8	0.758	0.00083	0.00640
2.38.3	*R*	0.01	32.8	0.758	0.00035	0.00603
2.39.1	*R*	0.01	33.3	0.751	0.00049	0.00448
2.39.2	*R*	0.01	33.3	0.751	0.00059	0.00480
2.39.3	*R*	0.01	33.3	0.751	0.00019	0.00501
2.40.1	*R*	0.01	28.3	0.832	0.00069	0.00704
2.40.2	*R*	0.01	28.3	0.832	0.00075	0.00683

Test No.	*Condition*	Slope	Temp. (C^o)	Kin.Visc. (ν) 10^6 (m^2/s)	Discharge (q) (m^2/s)	Depth (h) (m)
2.40.3	*R*	0.01	28.3	0.832	0.00032	0.00672
2.41.1	*R*	0.01	28.9	0.821	0.00072	0.00720
2.41.2	*R*	0.01	28.9	0.821	0.00079	0.00677
2.41.3	*R*	0.01	28.9	0.821	0.00034	0.00651
2.42.1	*R*	0.01	29.4	0.813	0.00073	0.00795
2.42.2	*R*	0.01	29.4	0.813	0.00089	0.00656
2.42.3	*R*	0.01	29.4	0.813	0.00037	0.00683
2.43.1	*R*	0.01	29.4	0.813	0.00070	0.00731
2.43.2	*R*	0.01	29.4	0.813	0.00076	0.00640
2.43.3	*R*	0.01	29.4	0.813	0.00034	0.00619
2.44.1	*R*	0.01	25.6	0.882	0.00110	0.00954
2.44.2	*R*	0.01	25.6	0.882	0.00102	0.00902
2.44.3	*R*	0.01	25.6	0.882	0.00042	0.00797
2.45.1	*R&HB*	0.01	29.7	0.807	0.00239	0.01259
2.45.2	*R&HB*	0.01	29.7	0.807	0.00238	0.01147
2.45.3	*R&HB*	0.01	29.7	0.807	0.00119	0.00960
2.46.1	*R&HB*	0.01	29.4	0.813	0.00379	0.01563
2.46.2	*R&HB*	0.01	29.4	0.813	0.00417	0.01451
2.46.3	*R&HB*	0.01	29.4	0.813	0.00239	0.01264
2.47.1	*R&HB*	0.01	30.0	0.802	0.00460	0.01557
2.47.2	*R&HB*	0.01	30.0	0.802	0.00322	0.01419
2.47.3	*R&HB*	0.01	30.0	0.802	0.00253	0.01243
2.48.1	*R&HB*	0.01	33.9	0.742	0.00190	0.01088
2.48.2	*R&HB*	0.01	33.9	0.742	0.00184	0.01013
2.48.3	*R&HB*	0.01	33.9	0.742	0.00087	0.00896
2.49.1	*R&HB*	0.01	30.0	0.802	0.00131	0.00997
2.49.2	*R&HB*	0.01	30.0	0.802	0.00139	0.00949
2.49.3	*R&HB*	0.01	30.0	0.802	0.00064	0.00821
2.50.1	*R&HB*	0.01	30.6	0.793	0.00150	0.01088
2.50.2	*R&HB*	0.01	30.6	0.793	0.00160	0.00971
2.50.3	*R&HB*	0.01	30.6	0.793	0.00078	0.00869
2.51.1	*R&HB*	0.01	32.2	0.768	0.00100	0.00864
2.51.2	*R&HB*	0.01	32.2	0.768	0.00109	0.00773
2.51.3	*R&HB*	0.01	32.2	0.768	0.00048	0.00688
2.52.1	*R&HB*	0.01	35.0	0.727	0.00089	0.00629
2.52.2	*R&HB*	0.01	35.0	0.727	0.00097	0.00640
2.52.3	*R&HB*	0.01	35.0	0.727	0.00039	0.00597

Test No.	*Condition*	Slope	Temp. (C^o)	Kin.Visc. (ν) 10^6 (m^2/s)	Discharge (q) (m^2/s)	Depth (h) (m)
2.53.1	*R&HB*	0.01	33.3	0.751	0.00170	0.01120
2.53.2	*R&HB*	0.01	33.3	0.751	0.00172	0.01008
2.53.3	*R&HB*	0.01	33.3	0.751	0.00083	0.00912
2.54.1	*R&HB*	0.01	32.2	0.768	0.00389	0.01744
2.54.2	*R&HB*	0.01	32.2	0.768	0.00459	0.01563
2.54.3	*R&HB*	0.01	32.2	0.768	0.00271	0.01429
2.55.1	*R&HB*	0.01	29.4	0.813	0.00490	0.01691
2.55.2	*R&HB*	0.01	29.4	0.813	0.00455	0.01509
2.55.3	*R&HB*	0.01	29.4	0.813	0.00276	0.01397
2.56.1	*R&HB*	0.01	29.4	0.813	0.00530	0.01851
2.56.2	*R&HB*	0.01	29.4	0.813	0.00331	0.01749
2.56.3	*R&HB*	0.01	29.4	0.813	0.00320	0.01520
2.57.1	*R&HB*	0.01	30.6	0.793	0.00482	0.01834
2.57.2	*R&HB*	0.01	30.6	0.793	0.00453	0.01708
2.57.3	*R&HB*	0.01	30.6	0.793	0.00303	0.01533
2.58.1	*R&HB*	0.01	30.0	0.802	0.00307	0.01492
2.58.2	*R&HB*	0.01	30.0	0.802	0.00283	0.01398
2.58.3	*R&HB*	0.01	30.0	0.802	0.00153	0.01245
2.59.1	*R&HB*	0.01	30.0	0.802	0.00207	0.01263
2.59.2	*R&HB*	0.01	30.0	0.802	0.00198	0.01180
2.59.3	*R&HB*	0.01	30.0	0.802	0.00099	0.01069
2.60.1	*NR*	0.02	31.1	0.785	0.00362	0.01397
2.60.2	*NR*	0.02	31.1	0.785	0.00389	0.01387
2.60.3	*NR*	0.02	31.1	0.785	0.00234	0.01369
2.61.1	*NR*	0.02	32.8	0.758	0.00468	0.01344
2.61.2	*NR*	0.02	32.8	0.758	0.00367	0.01349
2.61.3	*NR*	0.02	32.8	0.758	0.00228	0.01189
2.62.1	*NR*	0.02	30.0	0.802	0.00402	0.01408
2.62.2	*NR*	0.02	30.0	0.802	0.00373	0.01392
2.62.3	*NR*	0.02	30.0	0.802	0.00226	0.01227
2.63.1	*NR*	0.02	31.1	0.785	0.00374	0.01365
2.63.2	*NR*	0.02	31.1	0.785	0.00351	0.01349
2.63.3	*NR*	0.02	31.1	0.785	0.00224	0.01221
2.64.1	*NR*	0.02	31.1	0.785	0.00344	0.01371
2.64.2	*NR*	0.02	31.1	0.785	0.00331	0.01333
2.64.3	*NR*	0.02	31.1	0.785	0.00206	0.01173
2.65.1	*NR*	0.02	31.1	0.785	0.00288	0.01291

Test No.	*Condition*	Slope	Temp. (C^o)	Kin.Visc. (ν) 10^6 (m^2/s)	Discharge (q) (m^2/s)	Depth (h) (m)
2.65.2	*NR*	0.02	31.1	0.785	0.00302	0.01232
2.65.3	*NR*	0.02	31.1	0.785	0.00179	0.01083
2.66.1	*NR*	0.02	30.6	0.793	0.00204	0.01040
2.66.2	*NR*	0.02	30.6	0.793	0.00178	0.01024
2.66.3	*NR*	0.02	30.6	0.793	0.00104	0.00885
2.67.1	*NR*	0.02	31.7	0.775	0.00265	0.01173
2.67.2	*NR*	0.02	31.7	0.775	0.00235	0.01136
2.67.3	*NR*	0.02	31.7	0.775	0.00135	0.01040
2.68.1	*NR*	0.02	32.8	0.758	0.00403	0.01387
2.68.2	*NR*	0.02	32.8	0.758	0.00346	0.01360
2.68.3	*NR*	0.02	32.8	0.758	0.00215	0.01195
2.69.1	*NR*	0.02	28.9	0.821	0.00067	0.00901
2.69.2	*NR*	0.02	28.9	0.821	0.00074	0.00843
2.69.3	*NR*	0.02	28.9	0.821	0.00038	0.00784
2.70.1	*NR*	0.02	30.0	0.802	0.00089	0.00939
2.70.2	*NR*	0.02	30.0	0.802	0.00096	0.00896
2.70.3	*NR*	0.02	30.0	0.802	0.00050	0.00763
2.71.1	*NR*	0.02	30.6	0.793	0.00322	0.01189
2.71.2	*NR*	0.02	30.6	0.793	0.00312	0.01280
2.71.3	*NR*	0.02	30.6	0.793	0.00169	0.01152
2.72.1	*NR*	0.02	30.6	0.793	0.00361	0.01360
2.72.2	*NR*	0.02	30.6	0.793	0.00340	0.01333
2.72.3	*NR*	0.02	30.6	0.793	0.00187	0.00885
2.73.1	*NR*	0.02	31.1	0.785	0.00194	0.01147
2.73.2	*NR*	0.02	31.1	0.785	0.00205	0.01109
2.73.3	*NR*	0.02	31.1	0.785	0.00104	0.00992
2.74.1	*NR*	0.02	28.9	0.821	0.00085	0.00869
2.74.2	*NR*	0.02	28.9	0.821	0.00098	0.00837
2.74.3	*NR*	0.02	28.9	0.821	0.00044	0.00741
2.75.1	*NR*	0.02	29.4	0.813	0.00118	0.00928
2.75.2	*NR*	0.02	29.4	0.813	0.00120	0.00880
2.75.3	*NR*	0.02	29.4	0.813	0.00056	0.00811
2.76.1	*NR*	0.02	32.2	0.768	0.00400	0.01355
2.76.2	*NR*	0.02	32.2	0.768	0.00374	0.01349
2.76.3	*NR*	0.02	32.2	0.768	0.00220	0.01211
2.77.1	*NR*	0.02	28.9	0.821	0.00416	0.01424
2.77.2	*NR*	0.02	28.9	0.821	0.00402	0.01349
2.77.3	*NR*	0.02	28.9	0.821	0.00229	0.01237

Test No.	*Condition*	Slope	Temp. (C^o)	Kin.Visc. (ν) 10^6 (m^2/s)	Discharge (q) (m^2/s)	Depth (h) (m)
2.78.1	*NR*	0.02	31.1	0.785	0.00375	0.01333
2.78.2	*NR*	0.02	31.1	0.785	0.00346	0.01301
2.78.3	*NR*	0.02	31.1	0.785	0.00205	0.01195
2.79.1	*NR*	0.02	31.7	0.775	0.00316	0.01259
2.79.2	*NR*	0.02	31.7	0.775	0.00305	0.01237
2.79.3	*NR*	0.02	31.7	0.775	0.00170	0.01115
2.80.1	*NR*	0.02	29.4	0.813	0.00089	0.00837
2.80.2	*NR*	0.02	29.4	0.813	0.00086	0.00779
2.80.3	*NR*	0.02	29.4	0.813	0.00041	0.00736
2.81.1	*NR*	0.02	28.9	0.821	0.00046	0.00635
2.81.2	*NR*	0.02	28.9	0.821	0.00039	0.00597
2.81.3	*NR*	0.02	28.9	0.821	0.00017	0.00549
2.82.1	*NR*	0.02	28.9	0.821	0.00023	0.00544
2.82.2	*NR*	0.02	28.9	0.821	0.00023	0.00539
2.82.3	*NR*	0.02	28.9	0.821	0.00009	0.00496
2.83.1	*R*	0.02	34.4	0.735	0.00083	0.00728
2.83.1	*R*	0.02	34.4	0.735	0.00066	0.00728
2.83.3	*R*	0.02	34.4	0.735	0.00040	0.00688
2.84.1	*R*	0.02	31.7	0.775	0.00061	0.00760
2.84.2	*R*	0.02	31.7	0.775	0.00071	0.00752
2.84.3	*R*	0.02	31.7	0.775	0.00040	0.00712
2.85.1	*R*	0.02	26.7	0.861	0.00052	0.00688
2.85.2	*R*	0.02	26.7	0.861	0.00059	0.00680
2.85.3	*R*	0.02	26.7	0.861	0.00032	0.00680
2.86.1	*R&HB*	0.02	30.0	0.802	0.00460	0.01419
2.86.2	*R&HB*	0.02	30.0	0.802	0.00374	0.01392
2.86.3	*R&HB*	0.02	30.0	0.802	0.00271	0.01243
2.87.1	*R&HB*	0.02	32.8	0.758	0.00402	0.01440
2.87.2	*R&HB*	0.02	32.8	0.758	0.00362	0.01419
2.87.3	*R&HB*	0.02	32.8	0.758	0.00259	0.01259
2.88.1	*R&HB*	0.02	31.1	0.785	0.00362	0.01424
2.88.2	*R&HB*	0.02	31.1	0.785	0.00346	0.01376
2.88.3	*R&HB*	0.02	31.1	0.785	0.00225	0.01227
2.89.1	*R&HB*	0.02	31.1	0.785	0.00319	0.01408
2.89.2	*R&HB*	0.02	31.1	0.785	0.00328	0.01344
2.89.3	*R&HB*	0.02	31.1	0.785	0.00209	0.01189
2.90.1	*R&HB*	0.02	29.4	0.813	0.00259	0.01168

Test No.	*Condition*	Slope	Temp. (C^o)	Kin.Visc. (ν) 10^6 (m^2/s)	Discharge (q) (m^2/s)	Depth (h) (m)
2.90.2	*R&HB*	0.02	29.4	0.813	0.00227	0.01157
2.90.3	*R&HB*	0.02	29.4	0.813	0.00135	0.01035
2.91.1	*R&HB*	0.02	33.3	0.751	0.00410	0.01493
2.91.2	*R&HB*	0.02	33.3	0.751	0.00388	0.01461
2.91.3	*R&HB*	0.02	33.3	0.751	0.00259	0.01317
2.92.1	*R&HB*	0.02	33.3	0.751	0.00386	0.01365
2.92.2	*R&HB*	0.02	33.3	0.751	0.00343	0.01371
2.92.3	*R&HB*	0.02	33.3	0.751	0.00220	0.01205
2.93.1	*R&HB*	0.02	30.5	0.794	0.00391	0.01429
2.93.2	*R&HB*	0.02	30.5	0.794	0.00351	0.01408
2.93.3	*R&HB*	0.02	30.5	0.794	0.00206	0.01253
2.94.1	*R&HB*	0.02	30.5	0.794	0.00308	0.01312
2.94.2	*R&HB*	0.02	30.5	0.794	0.00279	0.01285
2.94.3	*R&HB*	0.02	30.5	0.794	0.00167	0.01147
2.95.1	*R&HB*	0.02	28.0	0.837	0.00117	0.01035
2.95.2	*R&HB*	0.02	28.0	0.837	0.00127	0.01003
2.95.3	*R&HB*	0.02	28.0	0.837	0.00068	0.00864
2.96.1	*R&HB*	0.02	31.1	0.785	0.00355	0.01403
2.96.2	*R&HB*	0.02	31.1	0.785	0.00347	0.01376
2.96.3	*R&HB*	0.02	31.1	0.785	0.00190	0.01248
2.97.1	*R&HB*	0.02	27.8	0.840	0.00051	0.00741
2.97.2	*R&HB*	0.02	27.8	0.840	0.00058	0.00741
2.97.3	*R&HB*	0.02	27.8	0.840	0.00030	0.00736
2.98.1	*R&HB*	0.02	31.7	0.775	0.00410	0.01451
2.98.2	*R&HB*	0.02	31.7	0.775	0.00439	0.01419
2.98.3	*R&HB*	0.02	31.7	0.775	0.00237	0.01291
2.99.1	*R&HB*	0.02	28.9	0.821	0.00413	0.01440
2.99.2	*R&HB*	0.02	28.9	0.821	0.00425	0.01387
2.99.3	*R&HB*	0.02	28.9	0.821	0.00279	0.01323
2.100.1	*R&HB*	0.02	31.1	0.785	0.00400	0.01413
2.100.2	*R&HB*	0.02	31.1	0.785	0.00385	0.01381
2.100.3	*R&HB*	0.02	31.1	0.785	0.00232	0.01253
2.101.1	*NR*	0.03	31.1	0.785	0.00356	0.01248
2.101.2	*NR*	0.03	31.1	0.785	0.00364	0.01264
2.101.3	*NR*	0.03	31.1	0.785	0.00257	0.01141
2.102.1	*NR*	0.03	30.6	0.793	0.00354	0.01285
2.102.2	*NR*	0.03	30.6	0.793	0.00370	0.01280

Test No.	*Condition*	Slope	Temp. (C^o)	Kin.Visc. (ν) 10^6 (m^2/s)	Discharge (q) (m^2/s)	Depth (h) (m)
2.102.3	*NR*	0.03	30.6	0.793	0.00261	0.01157
2.103.1	*NR*	0.03	28.9	0.821	0.00264	0.01046
2.103.2	*NR*	0.03	28.9	0.821	0.00264	0.01099
2.103.3	*NR*	0.03	28.9	0.821	0.00184	0.01003
2.104.1	*NR*	0.03	28.9	0.821	0.00117	0.00805
2.104.2	*NR*	0.03	28.9	0.821	0.00124	0.00880
2.104.3	*NR*	0.03	28.9	0.821	0.00095	0.00779
2.105.1	*NR*	0.03	33.3	0.751	0.00324	0.01173
2.105.2	*NR*	0.03	33.3	0.751	0.00345	0.01211
2.105.3	*NR*	0.03	33.3	0.751	0.00236	0.01040
2.106.1	*NR*	0.03	31.1	0.785	0.00343	0.01243
2.106.2	*NR*	0.03	31.1	0.785	0.00347	0.01291
2.106.3	*NR*	0.03	31.1	0.785	0.00238	0.01125
2.107.1	*NR*	0.03	30.0	0.802	0.00143	0.00912
2.107.2	*NR*	0.03	30.0	0.802	0.00148	0.00923
2.107.3	*NR*	0.03	30.0	0.802	0.00103	0.00843
2.108.1	*NR*	0.03	35.0	0.727	0.00241	0.01040
2.108.2	*NR*	0.03	35.0	0.727	0.00242	0.01120
2.108.3	*NR*	0.03	35.0	0.727	0.00153	0.00987
2.109.1	*NR*	0.03	32.8	0.758	0.00330	0.01173
2.109.2	*NR*	0.03	32.8	0.758	0.00329	0.01211
2.109.3	*NR*	0.03	32.8	0.758	0.00213	0.01024
2.110.1	*NR*	0.03	32.2	0.768	0.00366	0.01232
2.110.2	*NR*	0.03	32.2	0.768	0.00366	0.01275
2.110.3	*NR*	0.03	32.2	0.768	0.00243	0.01088
2.111.1	*NR*	0.03	30.0	0.802	0.00391	0.01280
2.111.2	*NR*	0.03	30.0	0.802	0.00389	0.01328
2.111.3	*NR*	0.03	30.0	0.802	0.00271	0.01104
2.112.1	*NR*	0.03	30.6	0.793	0.00295	0.01120
2.112.2	*NR*	0.03	30.6	0.793	0.00288	0.01173
2.112.3	*NR*	0.03	30.6	0.793	0.00194	0.01013
2.113.1	*NR*	0.03	30.0	0.802	0.00048	0.00624
2.113.2	*NR*	0.03	30.0	0.802	0.00049	0.00672
2.113.3	*NR*	0.03	30.0	0.802	0.00033	0.00629
2.114.1	*NR*	0.03	30.6	0.793	0.00058	0.00635
2.114.2	*NR*	0.03	30.6	0.793	0.00057	0.00672
2.114.3	*NR*	0.03	30.6	0.793	0.00039	0.00619
2.115.1	*R&HB*	0.03	30.0	0.802	0.00393	0.01323

Test No.	*Condition*	Slope	Temp. (C^o)	Kin.Visc. (ν) 10^6 (m^2/s)	Discharge (q) (m^2/s)	Depth (h) (m)
2.115.2	*R&HB*	0.03	30.0	0.802	0.00406	0.01333
2.115.3	*R&HB*	0.03	30.0	0.802	0.00210	0.01227
2.116.1	*R&HB*	0.03	31.7	0.775	0.00384	0.01291
2.116.2	*R&HB*	0.03	31.7	0.775	0.00399	0.01312
2.116.3	*R&HB*	0.03	31.7	0.775	0.00290	0.01184
2.117.1	*R&HB*	0.03	26.7	0.861	0.00114	0.00821
2.117.2	*R&HB*	0.03	26.7	0.861	0.00120	0.00821
2.117.3	*R&HB*	0.03	26.7	0.861	0.00095	0.00768
2.118.1	*R&HB*	0.03	27.2	0.851	0.00050	0.00672
2.118.2	*R&HB*	0.03	27.2	0.851	0.00060	0.00709
2.118.3	*R&HB*	0.03	27.2	0.851	0.00042	0.00688
2.119.1	*R&HB*	0.03	29.4	0.813	0.00378	0.01317
2.119.2	*R&HB*	0.03	29.4	0.813	0.00392	0.01333
2.119.3	*R&HB*	0.03	29.4	0.813	0.00271	0.01232
2.120.1	*R&HB*	0.03	31.1	0.785	0.00360	0.01301
2.120.2	*R&HB*	0.03	31.1	0.785	0.00374	0.01333
2.120.3	*R&HB*	0.03	31.1	0.785	0.00266	0.01189
2.121.1	*R&HB*	0.03	28.3	0.832	0.00157	0.00896
2.121.2	*R&HB*	0.03	28.3	0.832	0.00160	0.00928
2.121.3	*R&HB*	0.03	28.3	0.832	0.00113	0.00885
2.123.1	*R&HB*	0.03	28.3	0.832	0.00192	0.00907
2.123.2	*R&HB*	0.03	28.3	0.832	0.00195	0.01003
2.123.3	*R&HB*	0.03	28.3	0.832	0.00130	0.00896
2.124.1	*R&HB*	0.03	31.7	0.775	0.00387	0.01296
2.124.2	*R&HB*	0.03	31.7	0.775	0.00397	0.01333
2.124.3	*R&HB*	0.03	31.7	0.775	0.00272	0.01184
2.125.1	*R&HB*	0.03	31.7	0.775	0.00359	0.01248
2.125.2	*R&HB*	0.03	31.7	0.775	0.00361	0.01280
2.125.3	*R&HB*	0.03	31.7	0.775	0.00250	0.01099
2.126.1	*R&HB*	0.03	28.9	0.821	0.00287	0.01093
2.126.2	*R&HB*	0.03	28.9	0.821	0.00276	0.01168
2.126.3	*R&HB*	0.03	28.9	0.821	0.00191	0.01019
2.127.1	*R&HB*	0.03	32.2	0.768	0.00296	0.01083
2.127.2	*R&HB*	0.03	32.2	0.768	0.00288	0.01163
2.127.3	*R&HB*	0.03	32.2	0.768	0.00192	0.01045
2.128.1	*R&HB*	0.03	30.6	0.793	0.00413	0.01317
2.128.2	*R&HB*	0.03	30.6	0.793	0.00411	0.01307
2.128.3	*R&HB*	0.03	30.6	0.793	0.00278	0.01189

Test No.	*Condition*	Slope	Temp. (C^o)	Kin.Visc. (ν) 10^6 (m^2/s)	Discharge (q) (m^2/s)	Depth (h) (m)
2.129.1	*R&HB*	0.03	30.3	0.798	0.00331	0.01195
2.129.2	*R&HB*	0.03	30.3	0.798	0.00322	0.01221
2.129.3	*R&HB*	0.03	30.3	0.798	0.00208	0.01109

Surface 3 Data

Test No.	Condition	Slope	Temp. (C^o)	Kin.Visc. (ν) 10^6 (m^2/s)	Discharge (q) (m^2/s)	Depth (h) (m)
3.1.1	NR	0.01	28.9	0.821	0.00231	0.01306
3.1.2	NR	0.01	28.9	0.821	0.00129	0.01158
3.1.3	NR	0.01	28.9	0.821	0.00072	0.01042
3.2.1	NR	0.01	27.8	0.840	0.00239	0.01279
3.2.2	NR	0.01	27.8	0.840	0.00112	0.01196
3.2.3	NR	0.01	27.8	0.840	0.00031	0.01079
3.3.1	NR	0.01	27.8	0.840	0.00127	0.01018
3.3.2	NR	0.01	27.8	0.840	0.00062	0.00945
3.3.3	NR	0.01	27.8	0.840	0.00015	0.00893
3.4.1	NR	0.01	27.8	0.840	0.00332	0.01455
3.4.2	NR	0.01	27.8	0.840	0.00206	0.01350
3.4.3	NR	0.01	27.8	0.840	0.00129	0.01165
3.5.1	NR	0.01	27.8	0.840	0.00068	0.00757
3.5.2	NR	0.01	27.8	0.840	0.00022	0.00693
3.5.3	NR	0.01	27.8	0.840	0.00004	0.00679
3.6.1	NR	0.01	28.9	0.821	0.00165	0.01119
3.6.2	NR	0.01	28.9	0.821	0.00089	0.01025
3.6.3	NR	0.01	28.9	0.821	0.00049	0.00941
3.7.1	NR	0.01	27.8	0.840	0.00516	0.01780
3.7.2	NR	0.01	27.8	0.840	0.00358	0.01644
3.7.3	NR	0.01	27.8	0.840	0.00236	0.01437
3.8.1	NR	0.01	27.8	0.840	0.00235	0.01367
3.8.2	NR	0.01	27.8	0.840	0.00138	0.01238
3.8.3	NR	0.01	27.8	0.840	0.00080	0.01095
3.9.1	NR	0.01	28.3	0.831	0.00116	0.00895
3.9.2	NR	0.01	28.3	0.831	0.00055	0.00849
3.9.3	NR	0.01	28.3	0.831	0.00012	0.00807
3.10.1	NR	0.01	25.6	0.883	0.00172	0.01178
3.10.2	NR	0.01	25.6	0.883	0.00088	0.01057
3.10.3	NR	0.01	25.6	0.883	0.00045	0.00930
3.11.1	NR	0.01	18.9	1.032	0.00814	0.01995
3.11.2	NR	0.01	18.9	1.032	0.00591	0.01744
3.11.3	NR	0.01	18.9	1.032	0.00498	0.01499
3.12.1	NR	0.01	18.9	1.032	0.00833	0.01995
3.12.2	NR	0.01	18.9	1.032	0.00598	0.01792
3.12.3	NR	0.01	18.9	1.032	0.00513	0.01524

Test No.	Condition	Slope	Temp. (C^o)	Kin.Visc. (ν) 10^6 (m^2/s)	Discharge (q) (m^2/s)	Depth (h) (m)
3.13.1	NR	0.01	14.4	1.159	0.00083	0.00731
3.13.2	NR	0.01	14.4	1.159	0.00060	0.00667
3.13.3	NR	0.01	14.4	1.159	0.00040	0.00656
3.14.1	NR	0.01	13.3	1.193	0.00176	0.01013
3.14.2	NR	0.01	13.3	1.193	0.00119	0.00917
3.14.3	NR	0.01	13.3	1.193	0.00083	0.00816
3.15.1	NR	0.01	13.9	1.174	0.00094	0.00699
3.15.2	NR	0.01	13.9	1.174	0.00051	0.00624
3.15.3	NR	0.01	13.9	1.174	0.00027	0.00581
3.16.1	NR	0.01	15.5	1.125	0.00073	0.00613
3.16.2	NR	0.01	15.5	1.125	0.00040	0.00597
3.16.3	NR	0.01	15.5	1.125	0.00028	0.00555
3.17.1	NR	0.01	13.3	1.193	0.00229	0.01131
3.17.2	NR	0.01	13.3	1.193	0.00163	0.01068
3.17.3	NR	0.01	13.3	1.193	0.00136	0.00955
3.18.1	NR	0.01	11.1	1.268	0.00103	0.00805
3.18.2	NR	0.01	11.1	1.268	0.00091	0.00789
3.18.3	NR	0.01	11.1	1.268	0.00047	0.00832
3.19.1	NR	0.01	12.2	1.230	0.00103	0.00843
3.19.2	NR	0.01	12.2	1.230	0.00088	0.00821
3.19.3	NR	0.01	12.2	1.230	0.00049	0.00800
3.20.1	NR	0.01	12.2	1.230	0.00596	0.01819
3.20.2	NR	0.01	12.2	1.230	0.00416	0.01739
3.20.3	NR	0.01	12.2	1.230	0.00398	0.01648
3.21.1	NR	0.01	12.8	1.210	0.00609	0.01824
3.21.2	NR	0.01	12.8	1.210	0.00408	0.01749
3.21.3	NR	0.01	12.8	1.210	0.00388	0.01648
3.22.1	NR	0.01	13.3	1.193	0.00300	0.01259
3.22.2	NR	0.01	13.3	1.193	0.00214	0.01216
3.22.3	NR	0.01	13.3	1.193	0.00182	0.01131
3.23.1	NR	0.01	13.3	1.193	0.00309	0.01248
3.23.2	NR	0.01	13.3	1.193	0.00208	0.01184
3.23.3	NR	0.01	13.3	1.193	0.00172	0.01131
3.24.1	NR	0.01	7.8	1.396	0.00385	0.01557
3.24.2	NR	0.01	7.8	1.396	0.00299	0.01429
3.24.3	NR	0.01	7.8	1.396	0.00236	0.01269
3.25.1	NR	0.01	7.8	1.396	0.00380	0.01547
3.25.2	NR	0.01	7.8	1.396	0.00230	0.01451
3.25.3	NR	0.01	7.8	1.396	0.00235	0.01280
3.26.1	NR	0.01	16.7	1.091	0.01551	0.02507

Test No.	Condition	Slope	Temp. (C^o)	Kin.Visc. (ν) 10^6 (m^2/s)	Discharge (q) (m^2/s)	Depth (h) (m)
3.26.2	NR	0.01	16.7	1.091	0.00990	0.02304
3.26.3	NR	0.01	16.7	1.091	0.00745	0.02251
3.27.1	NR	0.01	16.7	1.091	0.01536	0.02517
3.27.2	NR	0.01	16.7	1.091	0.01000	0.02304
3.27.3	NR	0.01	16.7	1.091	0.00759	0.02240
3.28.1	NR	0.01	16.7	1.091	0.01929	0.02837
3.28.2	NR	0.01	16.7	1.091	0.01335	0.02379
3.28.3	NR	0.01	16.7	1.091	0.01073	0.02400
3.29.1	NR	0.01	16.1	1.108	0.01901	0.02869
3.29.2	NR	0.01	16.1	1.108	0.01317	0.02400
3.29.3	NR	0.01	16.1	1.108	0.01084	0.02400
3.30.1	NR	0.01	16.7	1.091	0.00374	0.01355
3.30.2	NR	0.01	16.7	1.091	0.00235	0.01291
3.30.3	NR	0.01	16.7	1.091	0.00128	0.01163
3.31.1	NR	0.01	16.7	1.091	0.00373	0.01344
3.31.2	NR	0.01	16.7	1.091	0.00214	0.01237
3.31.3	NR	0.01	16.7	1.091	0.00135	0.01141
3.32.1	NR	0.01	17.2	1.077	0.00169	0.00885
3.32.2	NR	0.01	17.2	1.077	0.00076	0.00800
3.32.3	NR	0.01	17.2	1.077	0.00041	0.00736
3.33.1	NR	0.01	17.2	1.077	0.00168	0.00885
3.33.2	NR	0.01	17.2	1.077	0.00076	0.00800
3.33.3	NR	0.01	17.2	1.077	0.00043	0.00736
3.34.1	NR	0.01	14.0	1.171	0.00789	0.02059
3.34.2	NR	0.01	14.0	1.171	0.00575	0.01867
3.34.3	NR	0.01	14.0	1.171	0.00409	0.01664
3.35.1	NR	0.01	14.0	1.171	0.00793	0.02059
3.35.2	NR	0.01	14.0	1.171	0.00573	0.01856
3.35.3	NR	0.01	14.0	1.171	0.00409	0.01664
3.36.1	NR	0.01	16.7	1.091	0.01469	0.02523
3.36.2	NR	0.01	16.7	1.091	0.01053	0.02288
3.36.3	NR	0.01	16.7	1.091	0.00849	0.02171
3.37.1	NR	0.01	16.7	1.091	0.01503	0.02512
3.37.2	NR	0.01	16.7	1.091	0.01035	0.02261
3.37.3	NR	0.01	16.7	1.091	0.00857	0.02197
3.38.1	NR	0.01	16.7	1.091	0.00993	0.02197
3.38.2	NR	0.01	16.7	1.091	0.00751	0.01931
3.38.3	NR	0.01	16.7	1.091	0.00574	0.01856
3.39.1	NR	0.01	17.2	1.077	0.00987	0.02197
3.39.2	NR	0.01	17.2	1.077	0.00747	0.01931

Test No.	Condition	Slope	Temp. (C^o)	Kin.Visc. (ν) 10^6 (m^2/s)	Discharge (q) (m^2/s)	Depth (h) (m)
3.39.3	NR	0.01	17.2	1.077	0.00573	0.01856
3.40.1	NR	0.01	17.2	1.077	0.01276	0.02421
3.40.2	NR	0.01	17.2	1.077	0.00937	0.02155
3.40.3	NR	0.01	17.2	1.077	0.00722	0.02080
3.41.1	NR	0.01	17.2	1.077	0.01229	0.02421
3.41.2	NR	0.01	17.2	1.077	0.00938	0.02155
3.41.3	NR	0.01	17.2	1.077	0.00728	0.02080
3.42.1	R	0.01	26.1	0.872	0.00101	0.00826
3.42.2	R	0.01	26.1	0.872	0.00046	0.00785
3.42.3	R	0.01	26.1	0.872	0.00008	0.00765
3.43.1	R	0.01	29.4	0.812	0.00099	0.00881
3.43.2	R	0.01	29.4	0.812	0.00047	0.00809
3.43.3	R	0.01	29.4	0.812	0.00008	0.00797
3.44.1	R	0.01	27.8	0.841	0.00151	0.01082
3.44.2	R	0.01	27.8	0.841	0.00075	0.00964
3.44.3	R	0.01	27.8	0.841	0.00037	0.00917
3.45.1	R	0.01	14.0	1.171	0.00079	0.00640
3.45.2	R	0.01	14.0	1.171	0.00052	0.00656
3.45.3	R	0.01	14.0	1.171	0.00030	0.00656
3.46.1	R&HB	0.01	27.8	0.840	0.00307	0.01450
3.46.2	R&HB	0.01	27.8	0.840	0.00180	0.01302
3.46.3	R&HB	0.01	27.8	0.840	0.00117	0.01138
3.47.1	R&HB	0.01	27.8	0.840	0.00577	0.01844
3.47.2	R&HB	0.01	27.8	0.840	0.00396	0.01713
3.47.3	R&HB	0.01	27.8	0.840	0.00144	0.01522
3.48.1	R&HB	0.01	26.7	0.861	0.00575	0.01632
3.48.2	R&HB	0.01	26.7	0.861	0.00439	0.01456
3.48.3	R&HB	0.01	26.7	0.861	0.00281	0.01184
3.49.1	R&HB	0.01	26.7	0.861	0.00845	0.02027
3.49.2	R&HB	0.01	26.7	0.861	0.00650	0.01819
3.49.3	R&HB	0.01	26.7	0.861	0.00538	0.01563
3.50.1	R&HB	0.01	18.9	1.032	0.00843	0.02000
3.50.2	R&HB	0.01	18.9	1.032	0.00658	0.01792
3.50.3	R&HB	0.01	18.9	1.032	0.00555	0.01563
3.51.1	R&HB	0.01	15.0	1.140	0.00145	0.00883
3.51.2	R&HB	0.01	15.0	1.140	0.00107	0.00827
3.51.3	R&HB	0.01	15.0	1.140	0.00082	0.00782
3.52.1	R&HB	0.01	15.5	1.125	0.00158	0.00907
3.52.2	R&HB	0.01	15.5	1.125	0.00101	0.00827
3.52.3	R&HB	0.01	15.5	1.125	0.00077	0.00757

Test No.	Condition	Slope	Temp. (C^o)	Kin.Visc. (ν) 10^6 (m^2/s)	Discharge (q) (m^2/s)	Depth (h) (m)
3.53.1	R&HB	0.01	14.4	1.159	0.00179	0.01056
3.53.2	R&HB	0.01	14.4	1.159	0.00132	0.01024
3.53.3	R&HB	0.01	14.4	1.159	0.00106	0.00955
3.54.1	R&HB	0.01	12.2	1.230	0.00219	0.01184
3.54.2	R&HB	0.01	12.2	1.230	0.00174	0.01109
3.54.3	R&HB	0.01	12.2	1.230	0.00128	0.01045
3.55.1	R&HB	0.01	12.2	1.230	0.00222	0.01184
3.55.2	R&HB	0.01	12.2	1.230	0.00171	0.01109
3.55.3	R&HB	0.01	12.2	1.230	0.00128	0.01045
3.56.1	R&HB	0.01	13.3	1.193	0.00357	0.01387
3.56.2	R&HB	0.01	13.3	1.193	0.00272	0.01344
3.56.3	R&HB	0.01	13.3	1.193	0.00224	0.01216
3.57.1	R&HB	0.01	13.3	1.193	0.00346	0.01376
3.57.2	R&HB	0.01	13.3	1.193	0.00270	0.01291
3.57.3	R&HB	0.01	13.3	1.193	0.00224	0.01216
3.58.1	R&HB	0.01	13.9	1.174	0.00611	0.01835
3.58.2	R&HB	0.01	13.9	1.174	0.00472	0.01707
3.58.3	R&HB	0.01	13.9	1.174	0.00404	0.01611
3.59.1	R&HB	0.01	13.3	1.193	0.00627	0.01824
3.59.2	R&HB	0.01	13.3	1.193	0.00474	0.01717
3.59.3	R&HB	0.01	13.3	1.193	0.00407	0.01600
3.60.1	R&HB	0.01	17.8	1.061	0.01415	0.02709
3.60.2	R&HB	0.01	17.8	1.061	0.01108	0.02485
3.60.3	R&HB	0.01	17.8	1.061	0.00815	0.02432
3.61.1	R&HB	0.01	17.8	1.061	0.01443	0.02709
3.61.2	R&HB	0.01	17.8	1.061	0.01110	0.02379
3.61.3	R&HB	0.01	17.8	1.061	0.00837	0.02224
3.62.1	R&HB	0.01	17.8	1.061	0.00525	0.01600
3.62.2	R&HB	0.01	17.8	1.061	0.00361	0.01483
3.62.3	R&HB	0.01	17.8	1.061	0.00215	0.01365
3.63.1	R&HB	0.01	17.8	1.061	0.00532	0.01600
3.63.2	R&HB	0.01	17.8	1.061	0.00361	0.01483
3.63.3	R&HB	0.01	17.8	1.061	0.00212	0.01344
3.64.1	NR	0.02	23.9	0.916	0.00214	0.00827
3.64.2	NR	0.02	23.9	0.916	0.00155	0.00736
3.64.3	NR	0.02	23.9	0.916	0.00163	0.00773
3.65.1	NR	0.02	24.4	0.905	0.00214	0.00821
3.65.2	NR	0.02	24.4	0.905	0.00155	0.00736
3.65.3	NR	0.02	24.4	0.905	0.00163	0.00773
3.66.1	NR	0.02	25.0	0.894	0.00140	0.00731

Test No.	Condition	Slope	Temp. (C^o)	Kin.Visc. (ν) 10^6 (m^2/s)	Discharge (q) (m^2/s)	Depth (h) (m)
3.66.2	NR	0.02	25.0	0.894	0.00089	0.00725
3.66.3	NR	0.02	25.0	0.894	0.00106	0.00656
3.67.1	NR	0.02	25.6	0.883	0.00143	0.00725
3.67.2	NR	0.02	25.6	0.883	0.00089	0.00731
3.67.3	NR	0.02	25.6	0.883	0.00103	0.00667
3.68.1	NR	0.02	26.1	0.872	0.00248	0.00960
3.68.2	NR	0.02	26.1	0.872	0.00172	0.00875
3.68.3	NR	0.02	26.1	0.872	0.00191	0.00880
3.69.1	NR	0.02	26.7	0.861	0.00249	0.00981
3.69.2	NR	0.02	26.7	0.861	0.00172	0.00875
3.69.3	NR	0.02	26.7	0.861	0.00193	0.00896
3.70.1	NR	0.02	27.2	0.851	0.00106	0.00608
3.70.2	NR	0.02	27.2	0.851	0.00059	0.00624
3.70.3	NR	0.02	27.2	0.851	0.00070	0.00565
3.71.1	NR	0.02	27.8	0.841	0.00100	0.00608
3.71.2	NR	0.02	27.8	0.841	0.00061	0.00624
3.71.3	NR	0.02	27.8	0.841	0.00069	0.00571
3.72.1	NR	0.02	13.3	1.193	0.01038	0.01872
3.72.2	NR	0.02	13.3	1.193	0.01032	0.01904
3.72.3	NR	0.02	13.3	1.193	0.00981	0.01808
3.73.1	NR	0.02	13.3	1.193	0.01062	0.01877
3.73.2	NR	0.02	13.3	1.193	0.01037	0.01904
3.73.3	NR	0.02	13.3	1.193	0.00974	0.01819
3.74.1	NR	0.02	7.2	1.421	0.01277	0.01931
3.74.2	NR	0.02	7.2	1.421	0.01135	0.02064
3.74.3	NR	0.02	7.2	1.421	0.01099	0.01819
3.75.1	NR	0.02	7.2	1.421	0.01282	0.01920
3.75.2	NR	0.02	7.2	1.421	0.01106	0.02064
3.75.3	NR	0.02	7.2	1.421	0.01101	0.01829
3.76.1	NR	0.02	7.2	1.421	0.00767	0.01504
3.76.2	NR	0.02	7.2	1.421	0.00657	0.01552
3.76.3	NR	0.02	7.2	1.421	0.00638	0.01392
3.77.1	NR	0.02	7.8	1.396	0.00779	0.01515
3.77.2	NR	0.02	7.8	1.396	0.00658	0.01552
3.77.3	NR	0.02	7.8	1.396	0.00625	0.01392
3.78.1	NR	0.02	8.3	1.375	0.00646	0.01333
3.78.2	NR	0.02	8.3	1.375	0.00462	0.01301
3.78.3	NR	0.02	8.3	1.375	0.00419	0.01280
3.79.1	NR	0.02	8.3	1.375	0.00645	0.01323
3.79.2	NR	0.02	8.3	1.375	0.00465	0.01280

Test No.	Condition	Slope	Temp. (C^o)	Kin.Visc. (ν) 10^6 (m^2/s)	Discharge (q) (m^2/s)	Depth (h) (m)
3.79.3	NR	0.02	8.3	1.375	0.00425	0.01280
3.80.1	NR	0.02	8.3	1.375	0.01086	0.01696
3.80.2	NR	0.02	8.3	1.375	0.00774	0.01771
3.80.3	NR	0.02	8.3	1.375	0.00716	0.01653
3.81.1	NR	0.02	8.3	1.375	0.01076	0.01696
3.81.2	NR	0.02	8.3	1.375	0.00785	0.01749
3.81.3	NR	0.02	8.3	1.375	0.00722	0.01643
3.82.1	NR	0.02	10.0	1.309	0.01348	0.02101
3.82.2	NR	0.02	10.0	1.309	0.01151	0.02123
3.82.3	NR	0.02	10.0	1.309	0.01031	0.01920
3.83.1	NR	0.02	10.0	1.309	0.01369	0.02112
3.83.2	NR	0.02	10.0	1.309	0.01179	0.02144
3.83.3	NR	0.02	10.0	1.309	0.01049	0.01952
3.84.1	NR	0.02	10.0	1.309	0.01233	0.01867
3.84.2	NR	0.02	10.0	1.309	0.00940	0.01931
3.84.3	NR	0.02	10.0	1.309	0.00844	0.01739
3.85.1	NR	0.02	10.0	1.309	0.01212	0.01856
3.85.2	NR	0.02	10.0	1.309	0.00926	0.01920
3.85.3	NR	0.02	10.0	1.309	0.00827	0.01739
3.86.1	NR	0.02	10.0	1.309	0.01090	0.01696
3.86.2	NR	0.02	10.0	1.309	0.00800	0.01792
3.86.3	NR	0.02	10.0	1.309	0.00680	0.01632
3.87.1	NR	0.02	10.0	1.309	0.01090	0.01696
3.87.2	NR	0.02	10.0	1.309	0.00803	0.01792
3.87.3	NR	0.02	10.0	1.309	0.00681	0.01632
3.88.1	NR	0.02	10.0	1.309	0.00641	0.01376
3.88.2	NR	0.02	10.0	1.309	0.00458	0.01333
3.88.3	NR	0.02	10.0	1.309	0.00403	0.01301
3.89.1	NR	0.02	10.0	1.309	0.00626	0.01365
3.89.2	NR	0.02	10.0	1.309	0.00463	0.01323
3.89.3	NR	0.02	10.0	1.309	0.00391	0.01312
3.90.1	NR	0.02	10.0	1.309	0.01351	0.02192
3.90.2	NR	0.02	10.0	1.309	0.01124	0.02117
3.90.3	NR	0.02	10.0	1.309	0.01020	0.01904
3.91.1	NR	0.02	10.0	1.309	0.01329	0.02112
3.91.2	NR	0.02	10.0	1.309	0.01114	0.02091
3.91.3	NR	0.02	10.0	1.309	0.01020	0.01893
3.92.1	NR	0.02	10.0	1.309	0.00827	0.01632
3.92.2	NR	0.02	10.0	1.309	0.00603	0.01568
3.92.3	NR	0.02	10.0	1.309	0.00498	0.01461

Test No.	Condition	Slope	Temp. (C^o)	Kin.Visc. (ν) 10^6 (m^2/s)	Discharge (q) (m^2/s)	Depth (h) (m)
3.93.1	NR	0.02	10.0	1.309	0.00841	0.01632
3.93.2	NR	0.02	10.0	1.309	0.00602	0.01557
3.93.3	NR	0.02	10.0	1.309	0.00485	0.01461
3.94.1	NR	0.02	15.5	1.125	0.00228	0.00864
3.94.2	NR	0.02	15.5	1.125	0.00132	0.00704
3.94.3	NR	0.02	15.5	1.125	0.00089	0.00768
3.95.1	NR	0.02	15.5	1.125	0.00229	0.00864
3.95.2	NR	0.02	15.5	1.125	0.00130	0.00736
3.95.3	NR	0.02	15.5	1.125	0.00087	0.00768
3.96.1	NR	0.02	16.7	1.091	0.00134	0.00757
3.96.2	NR	0.02	16.7	1.091	0.00067	0.00747
3.96.3	NR	0.02	16.7	1.091	0.00031	0.00619
3.97.1	NR	0.02	16.7	1.091	0.00152	0.00800
3.97.2	NR	0.02	16.7	1.091	0.00075	0.00736
3.97.3	NR	0.02	16.7	1.091	0.00033	0.00672
3.98.1	R&HB	0.02	24.4	0.905	0.00275	0.00939
3.98.2	R&HB	0.02	24.4	0.905	0.00203	0.00757
3.98.3	R&HB	0.02	24.4	0.905	0.00226	0.00565
3.99.1	R&HB	0.02	24.4	0.905	0.00273	0.00939
3.99.2	R&HB	0.02	24.4	0.905	0.00203	0.00747
3.99.3	R&HB	0.02	24.4	0.905	0.00226	0.00560
3.100.1	R&HB	0.02	23.3	0.928	0.00204	0.00811
3.100.2	R&HB	0.02	23.3	0.928	0.00139	0.00789
3.100.3	R&HB	0.02	23.3	0.928	0.00154	0.00784
3.101.1	R&HB	0.02	23.3	0.928	0.00204	0.00800
3.101.2	R&HB	0.02	23.3	0.928	0.00142	0.00784
3.101.3	R&HB	0.02	23.3	0.928	0.00154	0.00779
3.102.1	R&HB	0.02	20.0	1.004	0.00312	0.01019
3.102.2	R&HB	0.02	20.0	1.004	0.00225	0.00843
3.102.3	R&HB	0.02	20.0	1.004	0.00246	0.00944
3.103.1	R&HB	0.02	20.0	1.004	0.00311	0.01029
3.103.2	R&HB	0.02	20.0	1.004	0.00225	0.00837
3.103.3	R&HB	0.02	20.0	1.004	0.00252	0.00949
3.104.1	R&HB	0.02	20.0	1.004	0.00292	0.00992
3.104.2	R&HB	0.02	20.0	1.004	0.00213	0.00800
3.104.3	R&HB	0.02	20.0	1.004	0.00233	0.00923
3.105.1	R&HB	0.02	20.0	1.004	0.00293	0.00992
3.105.2	R&HB	0.02	20.0	1.004	0.00214	0.00800
3.105.3	R&HB	0.02	20.0	1.004	0.00236	0.00917
3.106.1	R&HB	0.02	20.6	0.991	0.00161	0.00736

Test No.	Condition	Slope	Temp. (C^o)	Kin.Visc. (ν) 10^6 (m^2/s)	Discharge (q) (m^2/s)	Depth (h) (m)
3.106.2	R&HB	0.02	20.6	0.991	0.00111	0.00720
3.106.3	R&HB	0.02	20.6	0.991	0.00129	0.00635
3.107.1	R&HB	0.02	20.6	0.991	0.00163	0.00720
3.107.2	R&HB	0.02	20.6	0.991	0.00111	0.00720
3.107.3	R&HB	0.02	20.6	0.991	0.00129	0.00640
3.108.1	R&HB	0.02	20.0	1.004	0.00188	0.00784
3.108.2	R&HB	0.02	20.0	1.004	0.00140	0.00752
3.108.3	R&HB	0.02	20.0	1.004	0.00139	0.00763
3.109.1	R&HB	0.02	20.0	1.004	0.00187	0.00800
3.109.2	R&HB	0.02	20.0	1.004	0.00139	0.00763
3.109.3	R&HB	0.02	20.0	1.004	0.00139	0.00763
3.110.1	R&HB	0.02	19.4	1.018	0.00106	0.00613
3.110.2	R&HB	0.02	19.4	1.018	0.00066	0.00624
3.110.3	R&HB	0.02	19.4	1.018	0.00068	0.00576
3.111.1	R&HB	0.02	18.9	1.032	0.00105	0.00608
3.111.2	R&HB	0.02	18.9	1.032	0.00066	0.00613
3.111.3	R&HB	0.02	18.9	1.032	0.00069	0.00576
3.112.1	R&HB	0.02	13.3	1.193	0.01036	0.01915
3.112.2	R&HB	0.02	13.3	1.193	0.01053	0.01920
3.112.3	R&HB	0.02	13.3	1.193	0.01040	0.01835
3.113.1	R&HB	0.02	13.3	1.193	0.01014	0.01909
3.113.2	R&HB	0.02	13.3	1.193	0.01039	0.01920
3.113.3	R&HB	0.02	13.3	1.193	0.01022	0.01824
3.114.1	R&HB	0.02	8.3	1.375	0.00415	0.01173
3.114.2	R&HB	0.02	8.3	1.375	0.00381	0.01141
3.114.3	R&HB	0.02	8.3	1.375	0.00376	0.01200
3.115.1	R&HB	0.02	8.3	1.375	0.00436	0.01195
3.115.2	R&HB	0.02	8.3	1.375	0.00380	0.01157
3.115.3	R&HB	0.02	8.3	1.375	0.00386	0.01205
3.116.1	R&HB	0.02	7.8	1.396	0.00824	0.01493
3.116.2	R&HB	0.02	7.8	1.396	0.00715	0.01584
3.116.3	R&HB	0.02	7.8	1.396	0.00687	0.01520
3.117.1	R&HB	0.02	7.8	1.396	0.00839	0.01483
3.117.2	R&HB	0.02	7.8	1.396	0.00714	0.01573
3.117.3	R&HB	0.02	7.8	1.396	0.00697	0.01520
3.118.1	R&HB	0.02	8.3	1.375	0.01085	0.01728
3.118.2	R&HB	0.02	8.3	1.375	0.00830	0.01792
3.118.3	R&HB	0.02	8.3	1.375	0.00757	0.01675
3.119.1	R&HB	0.02	8.9	1.351	0.01129	0.01728
3.119.2	R&HB	0.02	8.9	1.351	0.00825	0.01792

Test No.	Condition	Slope	Temp. (C^o)	Kin.Visc. (ν) 10^6 (m^2/s)	Discharge (q) (m^2/s)	Depth (h) (m)
3.119.3	R&HB	0.02	8.9	1.351	0.00763	0.01685
3.120.1	R&HB	0.02	10.0	1.309	0.01373	0.02123
3.120.2	R&HB	0.02	10.0	1.309	0.01217	0.02165
3.120.3	R&HB	0.02	10.0	1.309	0.01071	0.01995
3.121.1	R&HB	0.02	10.0	1.309	0.01345	0.02123
3.121.2	R&HB	0.02	10.0	1.309	0.01157	0.02155
3.121.3	R&HB	0.02	10.0	1.309	0.01064	0.01941
3.122.1	R&HB	0.02	10.0	1.309	0.01015	0.01632
3.122.2	R&HB	0.02	10.0	1.309	0.00744	0.01696
3.122.3	R&HB	0.02	10.0	1.309	0.00645	0.01568
3.123.1	R&HB	0.02	10.0	1.309	0.01020	0.01643
3.123.2	R&HB	0.02	10.0	1.309	0.00752	0.01696
3.123.3	R&HB	0.02	10.0	1.309	0.00647	0.01568
3.124.1	R&HB	0.02	10.0	1.309	0.01377	0.02069
3.124.2	R&HB	0.02	10.0	1.309	0.01159	0.02091
3.124.3	R&HB	0.02	10.0	1.309	0.01023	0.01899
3.125.1	R&HB	0.02	10.0	1.309	0.01353	0.02069
3.125.2	R&HB	0.02	10.0	1.309	0.01143	0.02101
3.125.3	R&HB	0.02	10.0	1.309	0.01029	0.01899
3.126.1	R&HB	0.02	10.0	1.309	0.01126	0.01760
3.126.2	R&HB	0.02	10.0	1.309	0.00829	0.01792
3.126.3	R&HB	0.02	10.0	1.309	0.00736	0.01685
3.127.1	R&HB	0.02	10.0	1.309	0.01122	0.01749
3.127.2	R&HB	0.02	10.0	1.309	0.00845	0.01792
3.127.3	R&HB	0.02	10.0	1.309	0.00736	0.01664
3.128.1	R&HB	0.02	10.0	1.309	0.01336	0.02160
3.128.2	R&HB	0.02	10.0	1.309	0.01159	0.02112
3.128.3	R&HB	0.02	10.0	1.309	0.01063	0.01920
3.129.1	R&HB	0.02	10.0	1.309	0.01308	0.02144
3.129.2	R&HB	0.02	10.0	1.309	0.01156	0.02123
3.129.3	R&HB	0.02	10.0	1.309	0.01040	0.01915
3.130.1	R&HB	0.02	16.1	1.108	0.00170	0.00736
3.130.2	R&HB	0.02	16.1	1.108	0.00089	0.00651
3.130.3	R&HB	0.02	16.1	1.108	0.00054	0.00629
3.131.1	R&HB	0.02	16.1	1.108	0.00174	0.00736
3.131.2	R&HB	0.02	16.1	1.108	0.00097	0.00640
3.131.3	R&HB	0.02	16.1	1.108	0.00053	0.00640
3.132.1	NR	0.03	26.7	0.861	0.00396	0.01293
3.132.2	NR	0.03	26.7	0.861	0.00256	0.01151
3.132.3	NR	0.03	26.7	0.861	0.00258	0.01241

Test No.	Condition	Slope	Temp. (C^o)	Kin.Visc. (ν) 10^6 (m^2/s)	Discharge (q) (m^2/s)	Depth (h) (m)
3.133.1	NR	0.03	24.4	0.905	0.00204	0.00957
3.133.2	NR	0.03	24.4	0.905	0.00108	0.00852
3.133.3	NR	0.03	24.4	0.905	0.00110	0.00905
3.134.1	NR	0.03	27.2	0.851	0.00069	0.00507
3.134.2	NR	0.03	27.2	0.851	0.00029	0.00452
3.134.3	NR	0.03	27.2	0.851	0.00021	0.00418
3.135.1	NR	0.03	27.2	0.851	0.00311	0.00971
3.135.2	NR	0.03	27.2	0.851	0.00204	0.00768
3.135.3	NR	0.03	27.2	0.851	0.00203	0.00875
3.136.1	NR	0.03	27.8	0.840	0.00172	0.00795
3.136.2	NR	0.03	27.8	0.840	0.00101	0.00688
3.136.3	NR	0.03	27.8	0.840	0.00132	0.00715
3.137.1	NR	0.03	26.7	0.861	0.00082	0.00533
3.137.2	NR	0.03	26.7	0.861	0.00038	0.00539
3.137.3	NR	0.03	26.7	0.861	0.00061	0.00469
3.138.1	NR	0.03	25.6	0.882	0.00179	0.00779
3.138.2	NR	0.03	25.6	0.882	0.00112	0.00677
3.138.3	NR	0.03	25.6	0.882	0.00136	0.00704
3.139.1	NR	0.03	25.6	0.882	0.00184	0.00779
3.139.2	NR	0.03	25.6	0.882	0.00116	0.00677
3.139.3	NR	0.03	25.6	0.882	0.00138	0.00704
3.140.1	NR	0.03	13.3	1.193	0.00935	0.01536
3.140.2	NR	0.03	13.3	1.193	0.00676	0.01472
3.140.3	NR	0.03	13.3	1.193	0.00536	0.01344
3.141.1	NR	0.03	13.3	1.193	0.00948	0.01536
3.141.2	NR	0.03	13.3	1.193	0.00678	0.01472
3.141.3	NR	0.03	13.3	1.193	0.00535	0.01344
3.142.1	NR	0.03	13.3	1.193	0.01287	0.01824
3.142.2	NR	0.03	13.3	1.193	0.00972	0.01696
3.142.3	NR	0.03	13.3	1.193	0.00783	0.01568
3.143.1	NR	0.03	13.3	1.193	0.01258	0.01835
3.143.2	NR	0.03	13.3	1.193	0.00963	0.01696
3.143.3	NR	0.03	13.3	1.193	0.00769	0.01568
3.144.1	NR	0.03	8.9	1.351	0.00915	0.01504
3.144.2	NR	0.03	8.9	1.351	0.00612	0.01408
3.144.3	NR	0.03	8.9	1.351	0.00509	0.01344
3.145.1	NR	0.03	8.9	1.351	0.00905	0.01504
3.145.2	NR	0.03	8.9	1.351	0.00618	0.01408
3.145.3	NR	0.03	8.9	1.351	0.00510	0.01344
3.146.1	NR	0.03	8.9	1.351	0.01528	0.02016

Test No.	Condition	Slope	Temp. (C^o)	Kin.Visc. (ν) 10^6 (m^2/s)	Discharge (q) (m^2/s)	Depth (h) (m)
3.146.2	NR	0.03	8.9	1.351	0.01135	0.01856
3.146.3	NR	0.03	8.9	1.351	0.00915	0.01792
3.147.1	NR	0.03	8.9	1.351	0.01542	0.02016
3.147.2	NR	0.03	8.9	1.351	0.01142	0.01824
3.147.3	NR	0.03	8.9	1.351	0.00934	0.01792
3.148.1	NR	0.03	8.9	1.351	0.01805	0.02187
3.148.2	NR	0.03	8.9	1.351	0.01332	0.01995
3.148.3	NR	0.03	8.9	1.351	0.01166	0.01952
3.149.1	NR	0.03	8.9	1.351	0.01818	0.02176
3.149.2	NR	0.03	8.9	1.351	0.01397	0.01973
3.149.3	NR	0.03	8.9	1.351	0.01167	0.01963
3.150.1	NR	0.03	8.9	1.351	0.01496	0.01984
3.150.2	NR	0.03	8.9	1.351	0.01111	0.01824
3.150.3	NR	0.03	8.9	1.351	0.00901	0.01781
3.151.1	NR	0.03	8.9	1.351	0.01476	0.01984
3.151.2	NR	0.03	8.9	1.351	0.01100	0.01813
3.151.3	NR	0.03	8.9	1.351	0.00873	0.01781
3.152.1	NR	0.03	7.8	1.396	0.01084	0.01664
3.152.2	NR	0.03	7.8	1.396	0.00779	0.01536
3.152.3	NR	0.03	7.8	1.396	0.00649	0.01440
3.153.1	NR	0.03	7.8	1.396	0.01064	0.01664
3.153.2	NR	0.03	7.8	1.396	0.00781	0.01536
3.153.3	NR	0.03	7.8	1.396	0.00630	0.01440
3.154.1	NR	0.03	8.3	1.375	0.00449	0.01056
3.154.2	NR	0.03	8.3	1.375	0.00283	0.00853
3.154.3	NR	0.03	8.3	1.375	0.00241	0.00939
3.155.1	NR	0.03	8.3	1.375	0.00453	0.01088
3.155.2	NR	0.03	8.3	1.375	0.00283	0.00864
3.155.3	NR	0.03	8.3	1.375	0.00242	0.00960
3.156.1	NR	0.03	8.9	1.351	0.00277	0.00853
3.156.2	NR	0.03	8.9	1.351	0.00151	0.00597
3.156.3	NR	0.03	8.9	1.351	0.00116	0.00747
3.157.1	NR	0.03	8.9	1.351	0.00276	0.00811
3.157.2	NR	0.03	8.9	1.351	0.00151	0.00608
3.157.3	NR	0.03	8.9	1.351	0.00117	0.00789
3.158.1	NR	0.03	8.9	1.351	0.00145	0.00576
3.158.2	NR	0.03	8.9	1.351	0.00057	0.00480
3.158.3	NR	0.03	8.9	1.351	0.00038	0.00512
3.159.1	NR	0.03	8.9	1.351	0.00144	0.00576
3.159.2	NR	0.03	8.9	1.351	0.00039	0.00480

Test No.	Condition	Slope	Temp. (C^o)	Kin.Visc. (ν) 10^6 (m^2/s)	Discharge (q) (m^2/s)	Depth (h) (m)
3.159.3	NR	0.03	8.9	1.351	0.00038	0.00512
3.160.1	NR	0.03	15.0	1.140	0.00299	0.00917
3.160.2	NR	0.03	15.0	1.140	0.00169	0.00672
3.160.3	NR	0.03	15.0	1.140	0.00138	0.00864
3.161.1	NR	0.03	14.4	1.159	0.00297	0.00917
3.161.2	NR	0.03	14.4	1.159	0.00163	0.00672
3.161.3	NR	0.03	14.4	1.159	0.00134	0.00864
3.162.1	NR	0.03	14.4	1.159	0.00394	0.01024
3.162.2	NR	0.03	14.4	1.159	0.00241	0.00789
3.162.3	NR	0.03	14.4	1.159	0.00199	0.00949
3.163.1	NR	0.03	13.9	1.174	0.00391	0.01024
3.163.2	NR	0.03	13.9	1.174	0.00242	0.00800
3.163.3	NR	0.03	13.9	1.174	0.00205	0.00928
3.164.1	NR	0.03	13.9	1.174	0.00656	0.01312
3.164.2	NR	0.03	13.9	1.174	0.00445	0.01152
3.164.3	NR	0.03	13.9	1.174	0.00357	0.01163
3.165.1	NR	0.03	13.9	1.174	0.00652	0.01301
3.165.2	NR	0.03	13.9	1.174	0.00445	0.01152
3.165.3	NR	0.03	13.9	1.174	0.00359	0.01152
3.166.1	NR	0.03	15.0	1.140	0.01641	0.02112
3.166.2	NR	0.03	15.0	1.140	0.01263	0.01952
3.166.3	NR	0.03	15.0	1.140	0.01083	0.01888
3.167.1	NR	0.03	15.0	1.140	0.01640	0.02112
3.167.2	NR	0.03	15.0	1.140	0.01275	0.01952
3.167.3	NR	0.03	15.0	1.140	0.01083	0.01888
3.168.1	NR	0.03	15.0	1.140	0.01822	0.02197
3.168.2	NR	0.03	15.0	1.140	0.01403	0.02016
3.168.3	NR	0.03	15.0	1.140	0.01183	0.01952
3.169.1	NR	0.03	15.0	1.140	0.01832	0.02208
3.169.2	NR	0.03	15.0	1.140	0.01396	0.02016
3.169.3	NR	0.03	15.0	1.140	0.01201	0.01931
3.170.1	NR	0.03	15.6	1.122	0.01335	0.01899
3.170.2	NR	0.03	15.6	1.122	0.00993	0.01696
3.170.3	NR	0.03	15.6	1.122	0.00798	0.01632
3.171.1	NR	0.03	15.6	1.122	0.01341	0.01888
3.171.2	NR	0.03	15.6	1.122	0.00992	0.01696
3.171.3	NR	0.03	15.6	1.122	0.00805	0.01632
3.172.1	R	0.03	22.2	0.952	0.00093	0.00491
3.172.2	R	0.03	22.2	0.952	0.00041	0.00491
3.172.3	R	0.03	22.2	0.952	0.00050	0.00448

Test No.	Condition	Slope	Temp. (C^o)	Kin.Visc. (ν) 10^6 (m^2/s)	Discharge (q) (m^2/s)	Depth (h) (m)
3.173.1	R	0.03	27.2	0.851	0.00075	0.00485
3.173.2	R	0.03	27.2	0.851	0.00037	0.00458
3.173.3	R	0.03	27.2	0.851	0.00042	0.00450
3.174.1	R	0.03	17.2	1.077	0.00092	0.00640
3.174.2	R	0.03	17.2	1.077	0.00048	0.00448
3.174.3	R	0.03	17.2	1.077	0.00019	0.00480
3.175.1	R	0.03	17.2	1.077	0.00080	0.00427
3.175.2	R	0.03	17.2	1.077	0.00039	0.00427
3.175.3	R	0.03	17.2	1.077	0.00016	0.00448
3.176.1	R	0.03	17.8	1.061	0.00087	0.00427
3.176.2	R	0.03	17.8	1.061	0.00043	0.00427
3.176.3	R	0.03	17.8	1.061	0.00029	0.00459
3.177.1	R	0.03	18.3	1.047	0.00088	0.00427
3.177.2	R	0.03	18.3	1.047	0.00043	0.00437
3.177.3	R	0.03	18.3	1.047	0.00019	0.00416
3.178.1	R&HB	0.03	26.1	0.872	0.00287	0.01063
3.178.2	R&HB	0.03	26.1	0.872	0.00184	0.00943
3.178.3	R&HB	0.03	26.1	0.872	0.00194	0.01102
3.179.1	R&HB	0.03	26.7	0.861	0.00402	0.01045
3.179.2	R&HB	0.03	26.7	0.861	0.00256	0.00821
3.179.3	R&HB	0.03	26.7	0.861	0.00263	0.00912
3.180.1	R&HB	0.03	26.1	0.872	0.00221	0.00859
3.180.2	R&HB	0.03	26.1	0.872	0.00150	0.00656
3.180.3	R&HB	0.03	26.1	0.872	0.00195	0.00811
3.181.1	R&HB	0.03	26.7	0.861	0.00220	0.00864
3.181.2	R&HB	0.03	26.7	0.861	0.00149	0.00640
3.181.3	R&HB	0.03	26.7	0.861	0.00196	0.00816
3.182.1	R&HB	0.03	24.4	0.905	0.00137	0.00661
3.182.2	R&HB	0.03	24.4	0.905	0.00076	0.00629
3.182.3	R&HB	0.03	24.4	0.905	0.00116	0.00619
3.183.1	R&HB	0.03	24.4	0.905	0.00140	0.00651
3.183.2	R&HB	0.03	24.4	0.905	0.00077	0.00624
3.182.3	R&HB	0.03	24.4	0.905	0.00116	0.00629
3.183.1	R&HB	0.03	25.6	0.883	0.00235	0.00843
3.183.2	R&HB	0.03	25.6	0.883	0.00165	0.00651
3.183.3	R&HB	0.03	25.6	0.883	0.00207	0.00800
3.184.1	R&HB	0.03	25.6	0.883	0.00239	0.00843
3.184.2	R&HB	0.03	25.6	0.883	0.00167	0.00667
3.184.3	R&HB	0.03	25.6	0.883	0.00209	0.00795
3.185.1	R&HB	0.03	12.2	1.230	0.00952	0.01536

Test No.	Condition	Slope	Temp. (C^o)	Kin.Visc. (ν) 10^6 (m^2/s)	Discharge (q) (m^2/s)	Depth (h) (m)
3.185.2	R&HB	0.03	12.2	1.230	0.00656	0.01493
3.185.3	R&HB	0.03	12.2	1.230	0.00544	0.01344
3.186.1	R&HB	0.03	12.2	1.230	0.00946	0.01536
3.186.2	R&HB	0.03	12.2	1.230	0.00668	0.01472
3.186.3	R&HB	0.03	12.2	1.230	0.00552	0.01365
3.187.1	R&HB	0.03	13.3	1.193	0.00912	0.01547
3.187.2	R&HB	0.03	13.3	1.193	0.00689	0.01472
3.187.3	R&HB	0.03	13.3	1.193	0.00537	0.01333
3.188.1	R&HB	0.03	13.3	1.193	0.00930	0.01536
3.188.2	R&HB	0.03	13.3	1.193	0.00697	0.01472
3.188.3	R&HB	0.03	13.3	1.193	0.00661	0.01344
3.189.1	R&HB	0.03	16.1	1.108	0.00621	0.01280
3.189.2	R&HB	0.03	16.1	1.108	0.00417	0.01120
3.189.3	R&HB	0.03	16.1	1.108	0.00340	0.01099
3.190.1	R&HB	0.03	16.1	1.108	0.00619	0.01280
3.190.2	R&HB	0.03	16.1	1.108	0.00416	0.01109
3.190.3	R&HB	0.03	16.1	1.108	0.00342	0.01109
3.191.1	R&HB	0.03	16.1	1.108	0.01860	0.02176
3.191.2	R&HB	0.03	16.1	1.108	0.01446	0.02005
3.191.3	R&HB	0.03	16.1	1.108	0.01179	0.01941
3.192.1	R&HB	0.03	16.1	1.108	0.01784	0.02165
3.192.2	R&HB	0.03	16.1	1.108	0.01435	0.02016
3.192.3	R&HB	0.03	16.1	1.108	0.01146	0.01920
3.193.1	R&HB	0.03	16.1	1.108	0.01709	0.02080
3.193.2	R&HB	0.03	16.1	1.108	0.01311	0.01952
3.193.3	R&HB	0.03	16.1	1.108	0.01023	0.01824
3.194.1	R&HB	0.03	16.1	1.108	0.01732	0.02080
3.194.2	R&HB	0.03	16.1	1.108	0.01285	0.01931
3.194.3	R&HB	0.03	16.1	1.108	0.01026	0.01824
3.195.1	R&HB	0.03	16.1	1.108	0.00923	0.01504
3.195.2	R&HB	0.03	16.1	1.108	0.00627	0.01408
3.195.3	R&HB	0.03	16.1	1.108	0.00485	0.01344
3.196.1	R&HB	0.03	16.7	1.091	0.00894	0.01515
3.196.2	R&HB	0.03	16.7	1.091	0.00628	0.01408
3.196.3	R&HB	0.03	16.7	1.091	0.00487	0.01344
3.197.1	R&HB	0.03	16.7	1.091	0.00574	0.01259
3.197.2	R&HB	0.03	16.7	1.091	0.00388	0.01088
3.197.3	R&HB	0.03	16.7	1.091	0.00287	0.01120
3.198.1	R&HB	0.03	16.7	1.091	0.00572	0.01248
3.198.2	R&HB	0.03	16.7	1.091	0.00384	0.01088

Test No.	Condition	Slope	Temp. (C^o)	Kin.Visc. (ν) 10^6 (m^2/s)	Discharge (q) (m^2/s)	Depth (h) (m)
3.198.3	R&HB	0.03	16.7	1.091	0.00290	0.01120
3.199.1	R&HB	0.03	17.8	1.061	0.00192	0.00704
3.199.2	R&HB	0.03	17.8	1.061	0.00104	0.00512
3.199.3	R&HB	0.03	17.8	1.061	0.00074	0.00640
3.200.1	R&HB	0.03	17.8	1.061	0.00189	0.00693
3.200.2	R&HB	0.03	17.8	1.061	0.00102	0.00512
3.200.3	R&HB	0.03	17.8	1.061	0.00069	0.00597
3.201.1	R&HB	0.03	17.2	1.077	0.00204	0.00736
3.201.2	R&HB	0.03	17.2	1.077	0.00107	0.00715
3.201.3	R&HB	0.03	17.2	1.077	0.00072	0.00640
3.202.1	R&HB	0.03	17.2	1.077	0.00177	0.00640
3.202.2	R&HB	0.03	17.2	1.077	0.00089	0.00544
3.202.3	R&HB	0.03	17.2	1.077	0.00051	0.00565
3.203.1	R&HB	0.03	17.2	1.077	0.00393	0.00939
3.203.2	R&HB	0.03	17.2	1.077	0.00255	0.00768
3.203.3	R&HB	0.03	17.2	1.077	0.00179	0.00896
3.204.1	R&HB	0.03	17.2	1.077	0.00396	0.00939
3.204.2	R&HB	0.03	17.2	1.077	0.00262	0.00768
3.204.3	R&HB	0.03	17.2	1.077	0.00179	0.00896